Inertia- and elasticity-driven turbulence in viscoelastic fluids with high levels of drag reduction

INERTIA- AND ELASTICITY-DRIVEN TURBULENCE IN VISCOELASTIC FLUIDS WITH HIGH LEVELS OF DRAG REDUCTION

BY

LU ZHU, M.Eng., B.Eng.

A THESIS

SUBMITTED TO THE DEPARTMENT OF CHEMICAL ENGINEERING

AND THE SCHOOL OF GRADUATE STUDIES

OF MCMASTER UNIVERSITY

IN PARTIAL FULFILMENT OF THE REQUIREMENTS

FOR THE DEGREE OF

DOCTOR OF PHILOSOPHY

Doctor of Philosophy(2019) McMaster University

(Chemical Engineering) Hamilton, Ontario, Canada

TITLE:	Inertia- and elasticity-driven turbulence in viscoelastic fluids with high levels of drag reduction
AUTHOR:	Lu Zhu M.Eng., (Mechanical and Power Engineering) East China Univ. of Sci. & Tech., Shanghai, China
SUPERVISOR:	Dr. Li Xi
NUMBER OF PAGES:	xxvii,260

Lay Abstract

Turbulence is known to consume kinetic energy in a fluid system. To enhance the efficiency of fluid transportation, various techniques are developed. Especially, it was found that a small amount of polymers in turbulent flows can significantly suppress turbulent activity and cause considerable friction drag reduction (DR). Extraordinary progress has been made to study this phenomenon, however, some questions still remain elusive. This dissertation tries to address some fundamental questions that relate to the two typical polymeric turbulent motions: the inertia- (IDT) and elasticity-driven turbulence (EDT). In IDT, mechanisms of transitions between the intermediate stages are investigated from the perspective of vortex dynamics. The different effects of polymers at each stage of the flow lead to different flow behaviors. Particularly, starting from the low- to high-extent DR transition, the lift-up process of vortices is suppressed by polymers. The regeneration cycles of turbulence are thus modified, which results in qualitative changes of flow statistics. Numerical study on EDT is enabled by a newly developed hybrid pseudo-spectral/finite-difference scheme. A systematic investigation of the parameter space indicates that EDT is one self-contain turbulence driven purely by the elastic force. It can also interact with IDT and lead to a dynamical flow state in which EDT and IDT can alternatively occur.

Abstract

In dilute polymer solution, polymers are able to change the flow structures and suppress the intensity of turbulence, resulting in a considerable friction drag reduction (DR). Despite the extraordinary progress made in the past few decades, some critical questions remain unanswered. This dissertation will try to address two fundamental questions in dilute polymeric turbulence: (I) interactions between polymers and turbulent motions during the qualitative low-extent to high-extent drag reduction (LDR and HDR) transition in inertia-driven turbulence, (II) roles of the inertia- and elasticity-driven turbulent motions in the dynamics of high elasticity polymeric flows.

Many studies in the area of DR turbulence have been focused on the onset of DR and the maximum drag rection (MDR) asymptote. Between these two distinct stages, polymeric turbulent flows can also be classified into the qualitative LDR and HDR stages. Understanding the polymer-turbulence interactions during the drastic LDR-HDR transition is of vital importance for the development of efficient flow control technology. However, knowledge regarding this qualitative transition is still limited. In our DNS (direct numerical simulation) study, differences between the LDR and HDR stages are presented by a number of sharp changes in flow structures and statistics. Drag reduction in the flows is thus governed by two different mechanisms. The first is introduced at the onset of DR, which has been well explained by the

indiscriminate suppression of turbulent fluctuations during the coil-stretch transition of polymers. The second mechanism starts at the LDR-HDR transition but its physical origin is not clear. Based on instantaneous observations and indirect statistical evidence, we proposed that polymers, after the LDR-HDR transition, could suppress the lift-up process of the near-wall vortices and modify the turbulent regeneration cycles. However, direct evidence to support this hypothesis is not available without a statistical analysis of the vortex configurations. Therefore, a new vortex tracking algorithm – VATIP (vortex axis tracking by iterative propagation) – is developed to analyze statistically the configurations and distribution of vortices. Implementing this method in the polymeric turbulence demonstrates that the lift-up process of streamwise vortices in the buffer layer is restrained at HDR, while the generation of hairpins and other three-dimensional vortices is suppressed. In addition, the characteristic lifting angle of conditional eddies extracted by a conditional sampling method is found to be larger in HDR than in the Newtonian turbulence. These observations all support our hypothesis about the mechanism of LDR-HDR transition.

Research on the low elasticity turbulence usually considered the flow motions to be Newtonian-like. Turbulence here is driven by the inertial force (and hence called "inertia-driven" turbulence (IDT)) while polymers are responsible for dissipating turbulent kinetic energy. In the high elasticity turbulence, recent studies found a completely different turbulent flow type in which turbulence is driven by the elastic force and polymers could also feed energy to the flow. The behaviors of this "elasticity-driven" turbulence (EDT) are of significant interest in this area because of its potential connection to the MDR asymptote. However, EDT is difficult to capture by the traditional pseudo-spectral DNS scheme (SM) as a global artificial diffusion (GAD) term

is involved in the polymer constitutive equation to stabilize the simulation. In our study, a new hybrid pseudo-spectral/finite-difference scheme is developed to simulate the polymeric turbulence without requiring a GAD. All of the spatial derivative terms are still discretized by the Fourier-Chebyshev-Fourier pseudo-spectral projection except for the convection term in the constitutive equation which is discretized using a conservative second-order upwind TVD (total variation diminishing) finite difference scheme. The numerical study using the hybrid scheme suggests that turbulent flows can be either driven by the inertial or the elastic forces and respectively result in the IDT and EDT flows. A dynamical flow state is also found in the high elasticity flow regime in which IDT and EDT can be sustained alternatively.

Acknowledgements

I would first like to express my sincere thanks to my advisor, Dr. Li Xi, for his enthusiasm, motivation, inspiration, and continuous support throughout the entire period of my PhD study. I would not have accomplished what I have today without his wise and patient guidance.

I would also like to thank my supervisory committee: Dr. Christopher Swartz and Dr. Bartosz Protas for their insightful encouragement and comments. Their questions incented me to widen my research from various perspectives. I would like to thank my TA instructor Dr. David Latulippe for his great help in the past four years. His expertise and way of teaching are quite fantastic. A very special gratitude goes out to all down at NSERC for providing the funding for this work and Compute/Calcul Canada for the allocation of computing resources.

I am also grateful to my fellow labmates and my friends that met in the past four years. Many thanks to Dongyang Li, Navven Kumar Vasudevan, Oluseye Adeyemi, Ali Heydari Beni, Ziqi Gao, Feng Lu, JieJiang, Evan Krushelnycky, Kushal Panchal, Xue Bai, Shimiao Zhang, Yuanhua Li, Fengyan Wang, Hongfeng Zhang and Jinlei Li. It was awesome to have this chance to work and cheer with you.

My great thanks goes to my parents for the through moral and wholeheartedly support they provide me during these years and throughout all my life.

My biggest appreciation goes to Qianqian Zhang, my deepest love and my original motivation of this journey. It is the greatest happiness of my life to meet you. Thank you for accompanying and supporting me all the way in the past seven years.

Contents

List of Tables

List of Figures

Notation and abbreviations

AD	artificial diffusion
A_p	perturbation amplitude
A_s	magnitude of the spanwise undulation
A^*_{25}	instantaneous log-law slope of the mean velocity profiles at $y^* = 25$
A^*_{20-30}	instantaneous log-law slope of the mean velocity profiles in the layer $20 \leq y^* \leq 30$
b	maximum extensibility parameter
BDAB3	third-order semi-implicit backward-differentiation/Adams-Bashforth scheme
$\tilde{\boldsymbol{C}}$	constant term in momentum equations
$\boldsymbol{C}_p$	constant term in FENE-P equations
CFL	Courant–Friedrichs–Lewy
COG	center of gravity
CUD3	compact upwind scheme
C_{xx}, C_{yy}, C_{zz}	three diagonal components of polymer convection term
c	signals in benchmark problem

DNS	direct numerical simulation
DR	drag reduction
DR%	magnitude of DR
D_{xx}, D_{yy}, D_{zz}	three diagonal components of artificial polymer diffusion term
EDT	elasto-driven turbulence
EIT	elasto-inertial turbulence
$E_{\alpha,b}, E_{u,b}$	bulk one-dimensional energy spectra of the x-diagonal component of the polymer conformation tensor and the streamwise velocity
$\boldsymbol{e_x}, \boldsymbol{e_y}, \boldsymbol{e_z}$	unit vector in the x-, y-, and z-directions
$\mathrm{FFT}, \mathrm{FFT}^{-1}$	forward and reverse Fourier transform
FDM	finite-difference method
FENE-P	finitely extensible nonlinear elastic dumbbell model with the Peterlin approximation
FENE	finitely extensible nolinear elastic
$\mathrm{FFT}, \mathrm{FFT}^{-1}$	forward and reverse Fourier transform
F, F_{ijk}	numerical flux on direction k
$F_{ijk,q-1/2}, F_{ijk,q+1/2}$	numerical fluxes at the upstream/downstream boundaries of the virtual cell q
GAD	global artificial diffusion
$g(y)$	the wall-normal dependence function
HDR	high-extent drag reduction
HM	hybrid pseudo-spectral/finite-difference method
IDT	inertial-driven turbulence

$k_i\%$	percentage of TKE contained in all vortices of type i
L	domain size of the benchmark problem
$\tilde{\boldsymbol{L}}$	linear terms in momentum equations
LAD	local artificial diffusion
LDR	low-extent drag reduction
LFFS	Lax-Friedrichs flux splitting
L_x, L_z	streamwise/spanwise period of the computational domain
L_x^+, L_z^+	streamwise/spanwise period of computational domain in inner scales
l	half-channel height
l_x^+, l_y^+, l_z^+	average length of a vortex in x-, y-, and z-directions
$\max(l_{z,z\mathrm{ap}}^+)$	length of the longest spanwise segment in the axis-line of a vortex
MDR	maximum drag reduction
$\tilde{\boldsymbol{N}}$	inertial nonlinear terms in momentum equations
$\boldsymbol{N}_p$	nonlinear terms in FENE-P equations
N_x, N_y, N_z	number of gridpoints in x-, y-, and z-directions
$N_{x\mathrm{ap}}$	number of x-axis-points in each yz-planes
$\bar{\mathcal{P}}^k$	bulk-average production of the TKE budget
$P_x(X)$	percentage of yz-planes that satisfy the condition X
Q	Q quantity to identify vortex
$\boldsymbol{Q}$	end-to-end vector of each polymer dumbbell
Q_{rms}	root-mean-square of Q
Re	Reynolds number

Re_τ	friction Reynolds number
r_v	average radius of the streamwise vortex tube
$r, r^+_{q+1/2}, r^-_{q+1/2}$	successive gradient ratio
$\boldsymbol{S}$	strain-rate tensor
$mathrmSc$	Schmidt number
SM	pseudo-spectral method
$\tilde{\boldsymbol{S}}_p$	polymer nonlinear terms in momentum equations
SS	steady-state
TKE	turbulent kinetic energy
TVD	total variation diminish
U^+	mean flow velocity at each y^+
U_b, V_b, W_b	x-, y-, and z-components of the STG base flow
U_c	laminar centerline velocity
UD2	2nd-order upwind scheme
U_m	mean velocity profile of a steady-state DNS
VATIP	vortex axis tracking by iterative propagation
$V_i\%$	percentage of volume occupied by all vortices of type i
$\boldsymbol{v}$	velocity vector
$v_{k,\max}$	maximum velocity along k direction
$\lvert\langle v'^*_x v'^*_y\rangle\rvert$	peak of the instantaneous Reynolds shear stress profile
v'^+_x, v'^+_y, v'^+_z	velocity fluctuations in x-, y-, and z-directions normalized by the viscous length scale
WENO	weighted essentially non-oscillating
Wi	Weissenberg number

$x_{\mathrm{COG},x\mathrm{ap}}, x_{\mathrm{COG},z\mathrm{ap}}$	x-coordinate of COG of all x-/z-axis-points
$x_{\mathrm{COG},N_{x\mathrm{ap}}>1}$	COG. of the branched portion of a vortex
$x_{\text{max-}D_z}$	x-coordinate with the maximum spanwise span of a vortex
x_q	location of the grid point q
y^+	distance from the wall normalized by the viscous length scale
$y^+_{\max}, y^+_{\min}$	maximum/minimum y^+ coordinates of the vortex axis-line
α_p	streamwise wave number
$\boldsymbol{\alpha}$	polymer conformation tensor
β	ratio of the solvent viscosity to the total solution viscosity
β_s	spanwise streak spacing of STG base flow
$\dot{\gamma}$	characteristic shear rate of the flow
Δ_k	grid spacing on k-direction
Δ_k, q	size of the virtual cell q on k-direction
δ_x^+, δ_x^+	grid spacing in the x- and z-directions
$\delta^+_{y,\min}, \delta^+_{y,\max}$	minimum/maximum grid size
$\bar{\epsilon}^k$	bulk-average dissipation of the TKE budget
η	total solution viscosity
η_s	solvent viscosity
κ	coefficient for the magnitude of LAD
λ	polymer relaxation time
ρ	density
ς, a_j, b_j	numerical coefficients of the AB3 scheme
$\boldsymbol{\tau}_p$	polymer stress tensor
τ^+_{xy}	total shear stress normalized by the viscous length scale

$\bar{\chi}^k$	bulk-average polymer work of the TKE budget
$\mathbf{\Omega}$	vorticity tensor

Chapter 1

Introduction

Turbulence represents a broad range of flows that are random in details but coherent in statistics. Studies on turbulence usually involve self-sustaining mechanism, i.e., turbulence can reproduce itself in the absence of external disturbance. The "vortical structures" – typical recurrent flow structures in the turbulent flows – are believed to play the key role in the self-sustaining of turbulence (Cantwell, 1981; Robinson, 1991; Panton, 2001). Based on the concept of vortex, a number of theories for the dynamics of turbulence were proposed in the past (Brooke and Hanratty, 1993; Bernard *et al.*, 1993; Hamilton *et al.*, 1995; Schoppa and Hussain, 2002).

When adding a small amount of polymers into the Newtonian turbulence, the self-sustaining dynamics of the flows are modified and distinct drag reduction (DR) is observed (Graham, 2018). Several qualitative different stages are found in the DR turbulence. Especially, the flow can be driven by the inertial and elastic forces, leading to the fundamentally different flow states: the inertia- and elasticity-driven turbulence.

1.1 Turbulence and coherent structures

Turbulent flows exist everywhere. They occur when wind blows into the room, when cars travel on the road and even when people stir their coffee. Although it is intuitive to accept this concept, turbulence, in fact, is far from been fully understood after hundreds years of studies (Pope, 2000; Mathieu and Scott, 2000). It is even difficult to precisely define turbulence due to its highly chaotic nature. Intuitively, turbulence represents a broad range of flows that share some common features: they are random in details but highly coherent in statistics, they are made up by correlated flow structures with a wide range of scales, and they are responsible for intensive energy exchanging and dissipation (Mathieu and Scott, 2000). Despite such abundant types of turbulence, we will only focus on the wall-bounded turbulent flows.

A wide range of the engineering turbulence interacts with the walls, e.g., those flows over wings of an aircraft or inside a pipeline. When in contact with the walls, friction drag is induced as the walls try to retard the flow which consumes a large amount of kinetic energy. In the meantime, turbulence could be triggered which enhances the consumption of energy by opening another pathway: the fluid kinetic energy is extracted from the mean flow and continuously transferred to smaller and smaller turbulent eddies until it is eventually dissipated into the internal heat at the Kolmogorov scale (Pope, 2000). The process described above is self-sustaining, i.e., reproduction of turbulence by itself in the absence of external disturbance. Study on how turbulence sustains is of significant importance for developing new flow control strategies in practice (Mullin, 2011). In the past century, much progress has been made to reveal the physics of the self-sustaining process of turbulence. Particularly, the so-called "coherent structures" (Corrsin, 1943; Einstein and Li, 1956) – spatial

and temporal coherent structures that repetitively occur in turbulence – are intensively discussed and are believed to have a key role in the self-sustaining process of turbulence (Cantwell, 1981; Robinson *et al.*, 1989; Panton, 2001; Jiménez, 2018).

The concept of coherent structures involves various types of structures, e.g. the near-wall quasi-streamwise streaks and vortices, which are difficult to be fully addressed. The readers are referred to those high impact papers (Robinson, 1991; Panton, 2001; Adrian, 2007; Jiménez, 2018) for a more comprehensive overview of the entire area. In this dissertation, we will mostly focus on the vortex structures which represent a class of rotating flow motions that broadly distribute in the turbulent flows (Robinson, 1991; Panton, 2001). Vortex is usually regarded as the fundamental element in many proposed theories to explain the self-sustaining dynamics of turbulence. Schoppa and Hussain (2002) roughly summarized those theories into two categories: (i) the "parent-offspring" mechanism in which the lifted-up "parent" vortex can generate a new "offspring" vortex around its two ends in the streamwise direction (Brooke and Hanratty, 1993; Bernard *et al.*, 1993), and (ii) the "streak-instability" mechanism in which new vortices are generated through interactions between the old vortices and the near-wall streaks (Hamilton *et al.*, 1995; Schoppa and Hussain, 2002). These two types of mechanisms could both exist and regenerate vortices in turbulent flows, but their importance will depend on flow conditions.

The shape of vortices can be greatly different in the wall-bounded turbulence. In the near-wall region, the quasi-streamwise vortices were frequently observed in experiments (Kim *et al.*, 1971; Smith and Schwartz, 1983) and simulations (Bernard *et al.*, 1993). This type of vortices is inclined in the quasi-streamwise direction, their downstream head can occasionally lift up towards the outer layer. The dominant

population of the quasi-streamwise vortices in the near-wall region (Schoppa and Hussain, 2002) brings it to the central of a number of proposed mechanisms (Bernard *et al.*, 1993; Hamilton *et al.*, 1995; Schoppa and Hussain, 2002) to explain the self-sustaining of turbulence. In the meantime, another type of vortex with more complex configuration is found outside the buffer layer (Robinson, 1991). This so-called "hairpin" (aka "horseshoe" (Theodorsen, 1952)) vortex usually has a Ω- or Λ-shape with the head (i.e. the top of the arc of Ω) oriented in the downstream direction and drastically lifting up towards the outer layer of the turbulent flows. Although the concept of the hairpin vortex was raised some 80 years ago (Theodorsen, 1952), direct visualization of this structure is not available until fairly recent direct numerical simulation implemented by Wu and Moin (2009). Compared with the well-known quasi-streamwise vortices, the role of hairpin vortices in turbulence is less understood and still controversial. Some studies (Smith, 1984; Adrian *et al.*, 2000; Zhou *et al.*, 1999; Adrian, 2007) suggested that hairpin is important for the self-sustaining of turbulence. Adrian (2007) proposed that hairpin in the wall-bounded turbulence could rapidly regenerate themselves and form the so-called "vortex packets". The alignment of the vortex packets also offers an explanation for the large-scale-motion (LSM) and very-large-scale motion (VLSM) that observed in high-Re experiments. Meanwhile, some other studies (Schlatter *et al.*, 2014; Morris *et al.*, 2007; Jiménez, 2013) suspected the critical roles of the hairpin vortices in high Re turbulence.

The debate on the role of hairpin vortex in the self-sustaining process of turbulence is partially due to the lack of an efficient vortex tracking algorithm to extract the configuration information of individual vortices from the vortex fields (Marusic *et al.*, 2010). In general, two steps are required to extract the vortex configuration:

(1) determining vortex regions by an identification criterion, and (2) grouping the vortex regions to individual vortex objects by a vortex tracking algorithm. An intuitive option for the identification of vortex is the vorticity $\boldsymbol{\omega} \equiv \boldsymbol{\nabla} \times \boldsymbol{v}$ which defines the angular velocity of fluid elements. However, the limitation of vorticity soon becomes clear as it cannot efficiently distinguish between pure shear and real swirling motion (Jeong *et al.*, 1997). Instead, invariant vortex identification techniques are commonly adopted. In this thesis, we adopt one of the invariant criterion – the Q-criterion (Hunt *et al.*, 1988) – which is defined by

$$Q = \frac{1}{2}(\|\boldsymbol{\Omega}\|^2 - \|\boldsymbol{S}\|^2). \tag{1.1}$$

Here, $\boldsymbol{\Omega} \equiv \left(\boldsymbol{\nabla v} - \boldsymbol{\nabla v}^T\right)/2$ and $\boldsymbol{S} \equiv \left(\boldsymbol{\nabla v} + \boldsymbol{\nabla v}^T\right)/2$ are the vorticity and rate of strain tensors. Beyond the Q-criterion, other criteria, such as the λ_2-criterion (Jeong and Hussain, 1995) and Δ-criterion (Chong *et al.*, 1990), were also designed for vortex identification in the literature. Despite their different mathematical definitions, it is widely agreed that vortex fields obtained by these criteria are largely equivalent in practice (Chakraborty *et al.*, 2005; Chen *et al.*, 2015).

Identification criteria enable the visualization of vortex fields but do not differentiate the identity of individual vortices. In order to quantitatively analyze the topology of vortices, another tracking step is required to automatically disintegrate the vortex fields and capture each vortex. However, development on this front is limited. One classical method for this was developed by Jeong *et al.* (1997), which represents the vortex tubes by their axis-lines. In their method, the axis-lines are obtained by connecting the planar maximum of each (y, z) cross-sectional plane through a so-called "cone detective" algorithm. However, the Jeong *et al.* (1997) approach was designed

only for the detection of the quasi-streamwise vortices.

Inspired by Jeong *et al.* (1997), we developed a new vortex tracking algorithm – VATIP (vortex axis tracking by iterative propagation) – which iteratively searches for planar maxima in all directions. VATIP is then applied to the vortex fields identified by any scalar vortex identification criteria (e.g., Q-criterion or λ_2-criterion) and is capable of efficiently tracking the configuration of highly curved vortices, e.g., the hairpin vortices. It is also adopted, in this dissertation, to understand the influence of vortex dynamics and self-sustaining mechanism in the polymeric flows. A detailed discussion will be presented in chapters 3 and 4.

1.2 Dilute polymeric turbulence

1.2.1 Drag reduction turbulence

The influence of polymers on the turbulent flows has long been observed since the 20th century. Especially, in the dilute polymer solution ("dilute" indicates solutions in which the polymer-polymer interactions are negligible), a small amount of flexible linear polymer chains could significantly change the dynamics of turbulent coherent structures and lead to significant friction drag reduction (Toms, 1948; Virk, 1975). This phenomenon has great practical implications for the development of flow control methods that can imitate these effects for friction drag reduction. In particular, it can help us break the ceiling of the maximum drag reduction in DR flows.

In dilute polymeric turbulence, the configuration of individual polymers is constantly changed by the flows. Depending on the immediate configurations and flow

conditions, a polymer can be either stretched or recoiled. The feedback of the polymer to surrounding flow can be expressed as additional polymer stress that appears in the momentum balance (governed by the Navier–Stokes equations) of the flow. The dynamics of polymers and their contributions to the flows can be well captured by the FENE-P (finite extension nonlinear elastic model with Peterlin closure approximation) constitutive equations (Bird *et al.*, 1987) in which polymers are mimicked as the finitely extensible nonlinear elastic dumbbells. The mean configuration of polymers in the FENE-P model is described by the polymer conformation tensor $\boldsymbol{\alpha} \equiv \langle \boldsymbol{QQ} \rangle$ (where $\boldsymbol{Q}$ stands for the end-to-end vector of each polymer dumbbell). As polymers are extended in the flow, it has the tendency to relax and approach to the equilibrium. The time required by the polymers to relax reflects the "memory" of the fluid, i.e., the elasticity. In the FENE-P model, the elasticity is measured by the non-dimensional parameter: Weissenberg number Wi which is defined by the ratio of the polymer relaxation time λ and the flow deformation time $1/\dot{\gamma}$ (where $\dot{\gamma}$ is the characteristic shear rate of the flow).

Depending on the relative magnitudes of inertial and elastic forces (measured respectively by the Reynolds number Re and Wi), polymeric flows could exhibit completely different behaviors, some of which will not be entirely covered by this dissertation. Instead, we will only focus on the viscoelastic flows at a moderate Re that near the laminar-turbulence transition of Newtonian flows. As have been reported by a number of investigations (Xi and Graham, 2010; Li *et al.*, 2005; Housiadas *et al.*, 2005; Owolabi *et al.*, 2017), polymeric turbulence in this regime would exhibit distinct DR which has obviously practical and academic interests. In particular, several qualitatively different stages are sequentially observed when increasing Wi in

the DR turbulence. Differences between these stages can be clearly demonstrated by the schematic mean velocity profiles (fig. 1.1). At a low Wi (Wi $\leq$ 10 (Housiadas and Beris, 2003; Xi and Graham, 2010; Li *et al.*, 2015)), the influence of polymers is negligible and the flow behaves the same as the Newtonian turbulence. Further raising Wi rephrases into the low-extent drag reduction (LDR) stage where polymers' effects on the flow statistics concentrate in the buffer layer ($y^+ \lesssim 30$ in Newtonian turbulence, where y is the distance from the wall and "+" indicates quantities in turbulent inner scales (Pope, 2000)). As a result, the turbulent intensity in this layer becomes weaker and the layer becomes thicker, which is referred to as the "elastic sublayer" (Virk *et al.*, 1967). Continuously increasing Wi leads to the high-extent drag reduction (HDR) stage at which the influence zone of polymers extends to the log-law layer ($y^+ \gtrsim 30$). As shown in fig. 1.1, the slope of the velocity profile increases in the log-law layer (Warholic *et al.*, 1999) at HDR but is almost equivalent to the Newtonian turbulence at LDR. From the pre-onset of DR to the HDR, the level of DR successively increases but cannot infinitely grow and will eventually converge to an asymptotic upper bound. Moreover, experimental and numerical studies (Virk, 1975; Warholic *et al.*, 1999; Xi and Graham, 2010; Housiadas and Beris, 2013) found that this so-called maximum drag reduction (MDR) asymptote is identical in solutions with different rheological properties.

Despite the qualitatively different flow statistics between these stages, the in-depth mechanisms behind still remain puzzling in many respects. It has been gradually accepted that the complex interactions between polymer and turbulence could suppress the critical near-wall vortical structures and result in the reduction of turbulent intensity (Dubief *et al.*, 2005; Li and Graham, 2007; Kim *et al.*, 2007). This effect is related

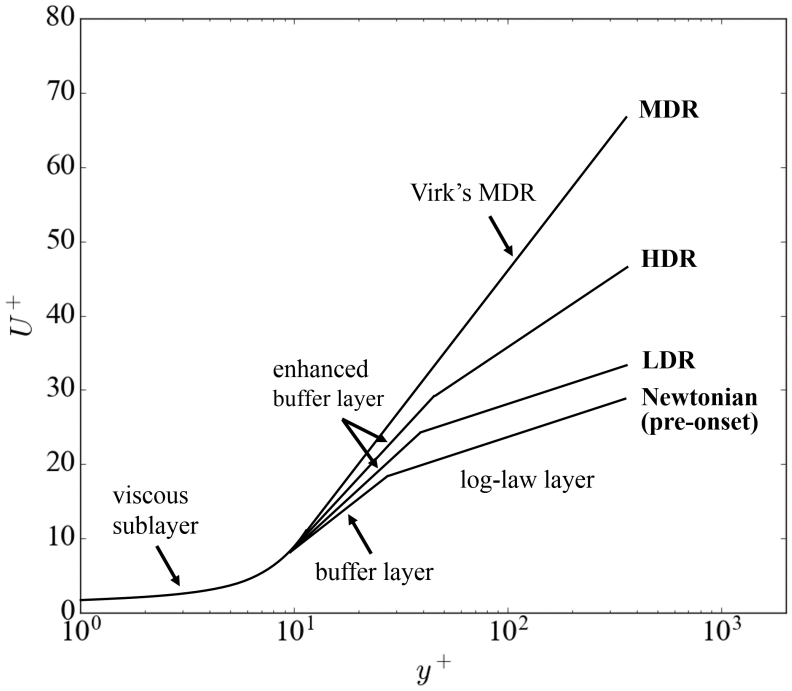

Figure 1.1: Schematic of mean velocity profiles (mean streamwise velocity as a function of the distance from the wall) at different stages of DR. Reprinted with permission from (Zhu *et al.*, 2018).Copyright (2018) Elsevier.

to the onset of DR as it appears during the coil-stretch transition of polymers (Li *et al.*, 2015). In addition to the relatively well-established theory for the onset of DR, mechanisms for the qualitative LDR-HDR and HDR-MDR transitions are still waiting to be uncovered. Understanding of the MDR transition is undoubtedly the heart of this field. Intuitively, the universality of this stage indicates the existence of a unique mechanism that does not completely eliminate turbulence but pushes it to a steady turbulent status (Zhu *et al.*, 2019). However, a consistent theory to explain this universal upper limit is still not available as contradictory evidence was found in the literature (White and Mungal, 2008; Procaccia *et al.*, 2008; Xi and Graham, 2012b).

Comparing with the long-known LDR and MDR stages, the concept of HDR is more recent. Flow statistics, e.g. the mean velocity profile, in this stage are considerably different from the LDR, indicating the existence of two-stage interactions between polymers and turbulence in the DR flows: one starts at the onset while the other at the LDR-HDR transition (Zhu *et al.*, 2018). Studying the turbulent dynamics of HDR is pivotal for the understanding of MDR, in the sense that it is immediately followed by the MDR and thus highly correlated. Recent work by Xi and Graham (2012b,a) in the minimal flow unit suggested that the alternation of the two turbulence phases, active and hibernating phases, may correspond to the qualitative LDR-HDR transition. In Xi and Graham (2012b)'s work, the increasing DR in HDR stage is accompanied by the reducing fraction of the stronger turbulent phase (i.e. the active phase) that resembles the Newtonian turbulence, and the increasing fraction of the weaker phase (i.e. the hibernation phase). This theory was recently supported by Wang *et al.* (2017); Zhu *et al.* (2018) in a large simulation domain at various Re.

Study on the HDR turbulence is meaningful due to its direct connection to both the LDR (and hence the onset of DR) and the MDR. In this dissertation, following the active-hibernating protocol, we investigate the underlying dynamics of turbulent coherent structures in the DR turbulence and propose a hypothesis that relates the alternation of turbulent phases in HDR to the modification of vortex shapes and regeneration mechanisms. Our hypothesis is supported by the statistical analysis of vortices using the self-design vortex tracking algorithm – VATIP.

1.2.2 Inertia- and elasticity-driven turbulence

In most of the studies on DR turbulence (Housiadas and Beris, 2003; Kim *et al.*, 2008; Li *et al.*, 2006; Xi and Graham, 2010), flows are driven by the inertial force, leading to inertia-driven turbulence (IDT). Although modified by polymers, the flow structures and statistics of IDT still share tremendous similarities with the Newtonian turbulence. For instance, it has the Newtonian-like quasi-streamwise vortices and streaks (Robinson, 1991; Zhu *et al.*, 2018). The contribution of polymers to the turbulent kinetic energy is mostly negative, indicating the suppression effect of polymers on the turbulent flows. On the other hand, when elasticity rises to a certain level, the Newtonian-like turbulent structures may be erased by polymers and a new type of turbulent motions, i.e., the so-called elasticity-driven turbulence (EDT) can occur and dominate the flows. Dallas *et al.* (2010) found that the contribution of polymers to the turbulent kinetic energy becomes positive in EDT flows. That is, polymers are responsible for the generation of turbulence. Meanwhile, EDT flow is dominated by spanwise vortices and sheet-like polymer structures (Dubief *et al.*, 2013; Samanta *et al.*, 2013), which is drastically different in comparison with IDT. Also, the strictly

two-dimensional (2D) nature of EDT allows it to sustain in a 2D flow geometry (Sid *et al.*, 2018). The concept of EDT is comparatively new, but soon attracted great attention due to its potential relation to MDR (Dubief *et al.*, 2013). In addition, it may be related to the elastic turbulence – an inertia-less turbulent flow that occurs in curved streamline geometry (Groisman and Steinberg, 2000).

It is well accepted that EDT is governed by small-scale structures that are driven by the elastic forces (Sid *et al.*, 2018). However, the detailed dynamics of this flow and its role in the DR turbulence are still highly controversial. Dubief *et al.* (2013) suggested that EDT plays a critical role in the dynamics of DR turbulence. They proposed that the elastic structures can dominate HDR stage of polymeric turbulence and eventually connect to MDR. On the other hand, the occurrence of the elastic structures is not captured by some previously numerical studies (Xi and Graham, 2010; Li *et al.*, 2006; Housiadas *et al.*, 2005), and the flow relaminarizes once the IDT structures cannot sustain. Sid *et al.* (2018) suggested that the absence of the EDT structures in those numerical studies is due to the addition of a global artificial diffusion term (GAD) when solving the polymer constitutive equations. As will be discussed in this dissertation, with a newly developed hybrid pseudo-spectral/finite-difference algorithm, sustained IDT is also obtained at HDR without a GAD. The elastic structures only become dominant after the IDT structures are mostly eliminated by polymers. Moreover, based on a careful investigation on the initial conditions and parameters, we find a dynamical flow state existing in the polymeric turbulence in which IDT and EDT are coexistence.

1.3 Objectives

The phenomenon of polymer additives drag reduction has been used in many industry areas. Compared with its wide applications, fundamental understanding of this phenomenon is still not completed. In particular, as the elasticity of the polymeric turbulence gradually increases, several qualitatively different stages are observed which indicate the multiple complex effects of polymers on the turbulent flows. In this thesis, we attempt to numerically study the polymeric turbulence and understand these interactions. There are five specific objectives:

- To find the qualitative changes of flow statistics and dynamics during the LDR-HDR transition of IDT.
- To understand the beneath polymer-turbulence interactions during the LDR-HDR transition from the vortex perspective.
- To develop a vortex tracking algorithm for the analysis of vortex statistics in the LDR and HDR stage.
- To develop an artificial-diffusion-free DNS method for accurate and efficient simulation of high elasticity polymeric turbulence.
- To study the roles of IDT and EDT in the dynamics of high elasticity polymeric turbulence.

1.4 Dissertation outline

This dissertation is targeted to address questions in the dilute polymeric solution. Essentially, polymeric turbulence can be driven by the inertial or the elastic forces

which respectively result in the drastically different inertia- and elasticity-driven turbulence. The inertia-driven turbulence occurs at a relatively low elasticity in which Newtonian-like turbulent motions still dominate the flow. A series of intermediate states (e.g., the pre-onset of DR, LDR, and HDR) can be sequentially observed as the elasticity gradually increases in IDT. The complex polymer-turbulence interactions that lead to the transitions between these intermediate stages, are still not fully understood and are attempted to be addressed in Chapters 2-5. On the other hand, elasticity-driven turbulence is found at a higher elasticity. The numerical method to capture this type of turbulence and the study on its role in DR turbulence will be the focus of Chapter 6 and 7.

As illustrated in fig. 1.2, the dissertation will be divided into two parts. The first part (Chapters 2-5) will focus on the inertia-driven polymeric turbulence in the low and intermediate elasticity regime. In Chapter 2, we present the distinct differences between the LDR and the HDR stages. A hypothesis based on the dynamics of vortical structures is proposed for the qualitative LDR-HDR transition. To support this hypothesis, an efficient vortex tracking scheme – VATIP – is developed to capture vortices in turbulent flows (Chapter 3). This tracking scheme allows the statistical analysis of vortex shapes and their distribution in the flows. It is then applied to the polymeric turbulence to study the influence of polymers on the flow structures at the LDR and HDR stages (Chapter 4). In Chapter 5, a conditional sampling algorithm is employed to analyze the characteristic features of vortices in the HDR stage. Results from the vortex analysis are consistent with our hypothesis for the mechanism of LDR-HDR transition in Chapter 2.

In the second part (Chapters 6 and 7), we will extend our knowledge to the

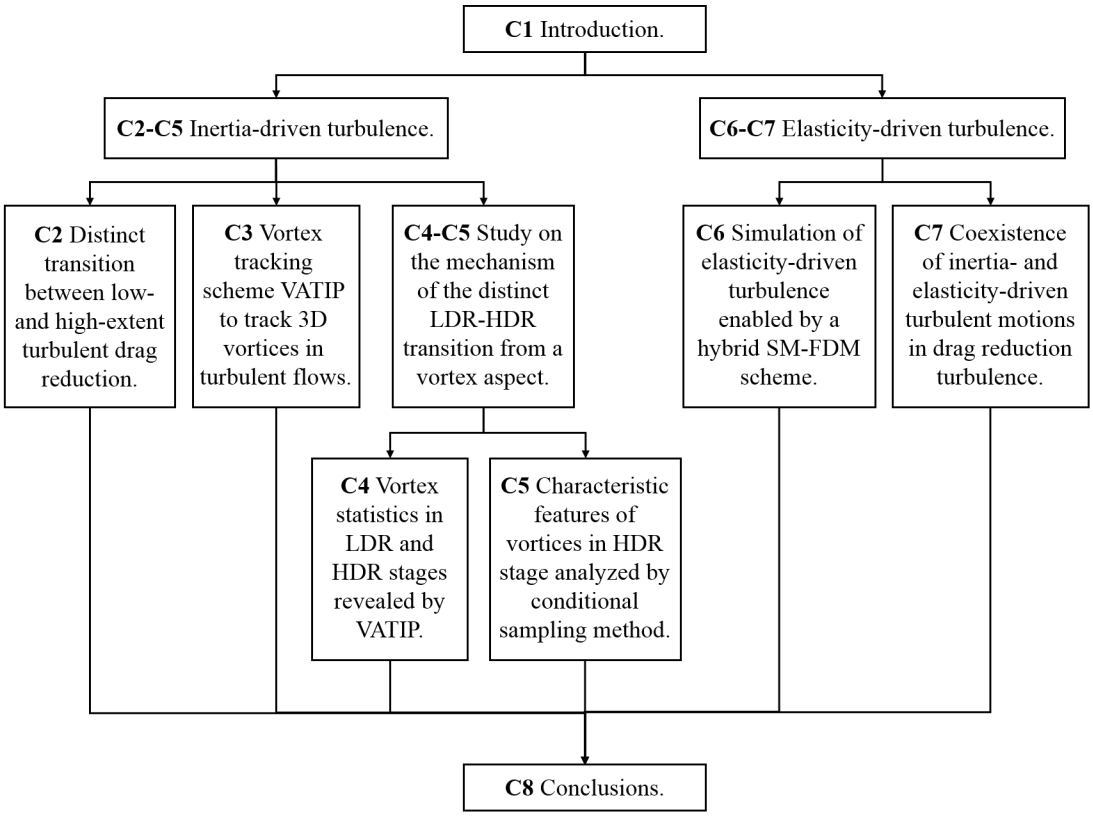

Figure 1.2: Illustration of the dissertation outline.

elasticity-driven turbulence. Simulations on this type of turbulence are enabled by a hybrid pseudo-spectral/finite-difference scheme. Numerical details and validation of this hybrid scheme are presented in Chapter 6. In Chapter 7, we will further discuss the characteristics of the elasticity-driven turbulence and its roles in high elasticity polymeric turbulence.

Bibliography

Adrian, R. J. (2007). Hairpin vortex organization in wall turbulence a. *Phys. Fluids*, **19**(4), 041301.

Adrian, R. J., Meinhart, C. D., and Tomkins, C. D. (2000). Vortex organization in the outer region of the turbulent boundary layer. *J. Fluid Mech.*, **422**, 1–54.

Bernard, P. S., Thomas, J. M., and Handler, R. A. (1993). Vortex dynamics and the production of reynolds stress. *J. Fluid Mech.*, **253**, 385–419.

Bird, R. B., Curtis, C. F., Armstrong, R. C., and Hassager, O. (1987). *Dynamics of polymeric liquids*, volume 2. John Wiley & Sons, New York, 2nd edition.

Brooke, J. W. and Hanratty, T. J. (1993). Origin of turbulence-producing eddies in a channel flow. *Phys. Fluids A-Fluid*, **5**(4), 1011–1022.

Cantwell, B. J. (1981). Organized motion in turbulent flow. *Annu. Rev. Fluid Mech.*, **13**(1), 457–515.

Chakraborty, P., Balachandar, S., and Adrian, R. J. (2005). On the relationships between local vortex identification schemes. *J. Fluid Mech.*, **535**, 189–214.

Chen, Q., Zhong, Q., Qi, M., and Wang, X. (2015). Comparison of vortex identification criteria for planar velocity fields in wall turbulence. *Phys. Fluids*, **27**(8), 085101.

Chong, M. S., Perry, A. E., and Cantwell, B. J. (1990). A general classification of three-dimensional flow fields. *Phys. Fluids A-Fluid*, **2**(5), 765–777.

Corrsin, S. (1943). Investigation of flow in an axially symmetric heated jet of air, naca wartime rept. *NASA Adv. Conf Rep.*

Dallas, V., Vassilicos, J. C., and Hewitt, G. F. (2010). Strong polymer-turbulence interactions in viscoelastic turbulent channel flow. *Phys. Rev. E*, **82**(6), 066303.

Dubief, Y., Terrapon, V. E., White, C. M., Shaqfeh, E. S. G., Moin, P., and Lele, S. K. (2005). New answers on the interaction between polymers and vortices in turbulent flows. *Flow Turbul. Combust.*, **74**, 311–329.

Dubief, Y., Terrapon, V. E., and Soria, J. (2013). On the mechanism of elasto-inertial turbulence. *Phys. Fluids*, **25**, 110817.

Einstein, H. A. and Li, H. (1956). The viscous sublayer along a smooth boundary. *Journal of the Engineering Mechanics Division*, **82**(2), 1–7.

Graham, M. D. (2018). *Microhydrodynamics, Brownian Motion, and Complex Fluids*. Cambridge University Press, Cambridge.

Groisman, A. and Steinberg, V. (2000). Elastic turbulence in a polymer solution flow. *Nature*, **405**, 53–55.

Hamilton, J. M., Kim, J., and Waleffe, F. (1995). Regeneration mechanisms of near-wall turbulence structures. *J. Fluid Mech.*, **287**, 317–348.

Housiadas, K. D. and Beris, A. N. (2003). Polymer-induced drag reduction: effects of variations in elasticity and inertia in turbulent viscoelastic channel flow. *Phys. Fluids*, **15**, 2369–2384.

Housiadas, K. D. and Beris, A. N. (2013). On the skin friction coefficient in viscoelastic wall-bounded flows. *Int. J. Heat Fluid Flow*, **42**, 49–67.

Housiadas, K. D., Beris, A. N., and Handler, R. A. (2005). Viscoelastic effects on higher order statistics and on coherent structures in turbulent channel flow. *Phys. Fluids*, **17**, 035106.

Hunt, J. C. R., , A. A. W., and Moin, P. (1988). Eddies, streams, and convergence zones in turbulent flows. *Studying Turbulence Using Numerical Simulation Databases-I1*, page 193.

Jeong, J. and Hussain, F. (1995). On the identification of a vortex. *J. Fluid Mech.*, **285**, 69–94.

Jeong, J., Hussain, F., Schoppa, W., and Kim, J. (1997). Coherent structures near the wall in a turbulent channel flow. *J. Fluid Mech.*, **332**, 185–214.

Jiménez, J. (2013). Near-wall turbulence. *Phys. Fluids*, **25**(10), 101302.

Jiménez, J. (2018). Coherent structures in wall-bounded turbulence. *Journal of Fluid Mechanics*, **842**, P1.

Kim, H., Kline, S. J., and Reynolds, W. C. (1971). The production of turbulence near a smooth wall in a turbulent boundary layer. *J. Fluid Mech.*, **50**(1), 133–160.

Kim, K., Li, C. F., Sureshkumar, R., Balachandar, S., and Adrian, R. J. (2007). Effects of polymer stresses on eddy structures in drag-reduced turbulent channel flow. *J. Fluid Mech.*, **584**, 281–299.

Kim, K., Adrian, R. J., Balachandar, S., and Sureshkumar, R. (2008). Dynamics of hairpin vortices and polymer-induced turbulent drag reduction. *Phys. Rev. Lett.*, **100**, 134504.

Li, C. F., Sureshkumar, R., and Khomami, B. (2006). Influence of rheological parameters on polymer induced turbulent drag reduction. *J. Non-Newton. Fluid Mech.*, **140**, 23–40.

Li, C. F., Sureshkumar, R., and Khomami, B. (2015). Simple framework for understanding the universality of the maximum drag reduction asymptote in turbulent flow of polymer solutions. *Phys. Rev. E*, **92**(4), 043014.

Li, F. C., Kawaguchi, Y., Segawa, T., and Hishida, K. (2005). Reynolds-number dependence of turbulence structures in a drag-reducing surfactant solution channel flow investigated by particle image velocimetry. *Phys. Fluids*, **17**, 075104.

Li, W. and Graham, M. D. (2007). Polymer induced drag reduction in exact coherent structures of plane Poiseuille flow. *Phys. Fluids*, **19**, 083101.

Marusic, I., McKeon, B. J., Monkewitz, P. A., Nagib, H. M., Smits, A. J., and Sreenivasan, K. R. (2010). Wall-bounded turbulent flows at high reynolds numbers: Recent advances and key issues. *Phys. Fluids*, **22**(6), 065103.

Mathieu, J. and Scott, J. (2000). *An introduction to turbulent flow*. Cambridge University Press.

Morris, S. C., Stolpa, S. R., Slaboch, P. E., and Klewicki, J. C. (2007). Near-surface particle image velocimetry measurements in a transitionally rough-wall atmospheric boundary layer. *J. Fluid Mech.*, **580**, 319–338.

Mullin, T. (2011). Experimental studies of transition to turbulence in a pipe. *Annu. Rev. Fluid Mech.*, **43**, 1–24.

Owolabi, B. E., Dennis, D. J. C., and Poole, R. J. (2017). Turbulent drag reduction by polymer additives in parallel-shear flows. *J. Fluid Mech.*, **453**, 57–108.

Panton, R. L. (2001). Overview of the self-sustaining mechanisms of wall turbulence. *Prog. Aerosp. Sci.*, **37**(4), 341–383.

Pope, S. B. (2000). *Turbulent flows*. Cambridge University Press, Cambridge, United Kingdom.

Procaccia, I., L'vov, V. S., and Benzi, R. (2008). Colloquium: theory of drag reduction by polymers in wall-bounded turbulence. *Rev. Mod. Phys.*, **80**, 225–247.

Robinson, S. K. (1991). Coherent motions in the turbulent boundary layer. *Annu. Rev. Fluid Mech.*, **23**, 601–639.

Robinson, S. K., Kline, S. J., and Spalart, P. R. (1989). A review of quasi-coherent structures in a numerically simulated turbulent boundary layer. Technical report, NASA Ames Research Center.

Samanta, D., Dubief, Y., Holzner, M., Schäfer, C., Morozov, A. N., Wagner, C., and Hof, B. (2013). Elasto-inertial turbulence. *Proc. Natl. Acad. Sci. U. S. A.*, **110**, 10557–100562.

Schlatter, P., Li, Q., Örlü, R., Hussain, F., and Henningson, D. S. (2014). On the near-wall vortical structures at moderate reynolds numbers. *European Journal of Mechanics-B/Fluids*, **48**, 75–93.

Schoppa, W. and Hussain, F. (2002). Coherent structure generation in near-wall turbulence. *J. Fluid Mech.*, **453**, 57–108.

Sid, S., Terrapon, V. E., and Dubief, Y. (2018). Two-dimensional dynamics of elasto-inertial turbulence and its role in polymer drag reduction. *Phys. Rev. Fluids*, **3**, 011301.

Smith, C. R. (1984). A synthesized model of the near-wall behavior in turbulent boundary layers. Technical report, LEHIGH UNIV BETHLEHEM PA DEPT OF MECHANICAL ENGINEERING AND MECHANICS.

Smith, C. R. and Schwartz, S. P. (1983). Observation of streamwise rotation in the near-wall region of a turbulent boundary layer. *Phys. Fluids*, **26**(3), 641–652.

Theodorsen, T. (1952). Mechanism of turbulence. In *Proceedings of the Midwestern Conference on Fluid Mechanics*, pages 1–19, Ohio State University, Columbus, OH.

Toms, B. A. (1948). Some observations on the flow of linear polymer solutions through straight tubes at large Reynolds numbers. In *Proc. 1st Int'l. Congress on Rheology*, volume 2, pages 135–141, Amsterdam.

Virk, P. S. (1975). Drag reduction fundamentals. *AIChE J.*, **21**, 625–656.

Virk, P. S., Merrill, E. W., Mickley, H. S., Smith, K. A., and Mollochr, E. L. (1967). Toms phenomenon - turbulent pipe flow of dilute polymer solutions. *J. Fluid Mech.*, **30**, 305–328.

Wang, S. N., Shekar, A., and Graham, M. D. (2017). Spatiotemporal dynamics of viscoelastic turbulence in transitional channel flow. *J. Non-Newton. Fluid Mech.* submitted.

Warholic, M. D., Massah, H., and Hanratty, T. J. (1999). Influence of drag-reducing polymers on turbulence: effects of Reynolds number, concentration and mixing. *Exp. Fluids*, **27**, 461–472.

White, C. M. and Mungal, M. G. (2008). Mechanics and prediction of turbulent drag reduction with polymer additives. *Annu. Rev. Fluid Mech.*, **40**, 235–256.

Wu, X. and Moin, P. (2009). Forest of hairpins in a low-Reynolds-number zero-pressure-gradient flat-plate boundary layer. *Phys. Fluids*, **21**, 091106.

Xi, L. and Graham, M. D. (2010). Turbulent drag reduction and multistage transitions in viscoelastic minimal flow units. *J. Fluid Mech.*, **647**, 421–452.

Xi, L. and Graham, M. D. (2012a). Dynamics on the laminar-turbulent boundary and the origin of the maximum drag reduction asymptote. *Phys. Rev. Lett.*, **108**, 028301.

Xi, L. and Graham, M. D. (2012b). Intermittent dynamics of turbulence hibernation in Newtonian and viscoelastic minimal channel flows. *J. Fluid Mech.*, **693**, 433–472.

Zhou, J., Adrian, R. J., Balachandar, S., and Kendall, T. M. (1999). Mechanisms

for generating coherent packets of hairpin vortices in channel flow. *J. Fluid Mech.*, **387**, 353–396.

Zhu, L., Schrobsdorff, H., Schneider, T. M., and Xi, L. (2018). Distinct transition in flow statistics and vortex dynamics between low- and high-extent turbulent drag reduction in polymer fluids. *J. Non-Newton. Fluid Mech.*, **262**, 115–130.

Zhu, L., Bai, X., Krushelnycky, E., and Xi, L. (2019). Transient dynamics of turbulence growth and bursting: Effects of drag-reducing polymers. *J. Non-Newton. Fluid Mech.*, **266**, 127–142.

Chapter 2

Distinct transition between low- and high-extent drag reduction

In this chapter, we use direct numerical simulation (DNS) to explore the parameter space of polymer-induced drag reduction (inertia-driven) turbulent flows. In particular, several abrupt changes of the flow statistics and structures are found to accompany the transition from the low-extent to high-extent drag reduction (LDR and HDR). These observations suggest the existence of two different polymer-turbulence interactions in the inertia-driven turbulence. The first starts at the onset of drag reduction where the coil-stretch transition of polymers causes the overall suppression of turbulent fluctuations. The second starts at the LDR–HDR transition which drastically changes flow statistics in the log-law layer and leads to turbulence localization. As the polymer-turbulence interaction during the LDR-HDR transition is not clear, we proposed a hypothesis based on the changing vortex dynamics.

I was responsible for implementing simulations and collecting data. I also post-processed the data with Dr. Li Xi's suggestions. The manuscript was wrote by me

and revised by Dr. Li Xi. The original Newtonian DNS code was developed by Dr. John Gibson. Dr. Li Xi implement the FENE-P model to the Newtonian code. Parallelization of the DNS code was done by Dr. Hecke Schrobsdorff and Dr. Tobias M. Schneider.

This chapter is reprinted with permission from L. Zhu, H. Schrobsdorff, T. M. Schneider and L. Xi. (2018). Distinct transition in flow statistics and vortex dynamics between low-and high-extent turbulent drag reduction in polymer fluids. *J. Non-Newton. Fluid Mech.*, **262**, 115-130 (DOI: 10.1016/j.jnnfm.2018.03.017).

Journal of Non-Newtonian Fluid Mechanics 262 (2018) 115–130

Contents lists available at ScienceDirect

Journal of Non-Newtonian Fluid Mechanics

journal homepage: www.elsevier.com/locate/jnnfm

Distinct transition in flow statistics and vortex dynamics between low- and high-extent turbulent drag reduction in polymer fluids

Lu Zhu[a], Hecke Schrobsdorff[b], Tobias M. Schneider[c,d], Li Xi[*,a,d]

[a] Department of Chemical Engineering, McMaster University, Hamilton, Ontario L8S 4L7, Canada
[b] Max Planck Institute for Dynamics and Self-Organization, Am Fassberg 17, Göttingen 37077, Germany
[c] Emergent Complexity in Physical Systems Laboratory (ECPS), École Polytechnique Fédérale de Lausanne, Switzerland
[d] Kavli Institute for Theoretical Physics (KITP), University of California, Santa Barbara, CA 93106-4030, USA

ARTICLE INFO

Keywords:
Turbulent flows
Viscoelasticity
Coherent structures
Vortex regeneration
Bursting

ABSTRACT

Flexible polymer additives are known to reduce the energy dissipation and friction drag in turbulent flows. As the fluid elasticity increases, the flow undergoes several stages of transitions. Much attention in the area has been focused on the onset of drag reduction (DR) and the eventual convergence to the maximum drag reduction (MDR) asymptote. Between the onset and MDR, recent experimental and numerical observations prompted the need to further distinguish the low- and high-extent drag reduction (LDR and HDR). Fundamental knowledge of this transition will be important for understanding turbulent dynamics in the presence of polymers, as well as for inspiring new flow control strategies for efficient friction reduction. We use direct numerical simulation (DNS) to explore all these transitions in the parameter space and, in particular, demonstrate that the LDR–HDR transition is not merely a quantitative effect of the level of drag reduction, but a qualitative transition into a different stage of turbulence. A number of sharp changes in flow statistics are found to accompany the transition and at HDR, turbulence becomes localized with vortices forming clusters. These observations suggest that polymer-induced drag reduction follows two distinct stages. The first starts at the onset of drag reduction, where the coil-stretch transition of polymers causes an overall suppression of turbulent fluctuations. The second starts at the LDR–HDR transition, where flow statistics become fundamentally changed in the log-law layer and turbulence localization is observed. A mechanism is then proposed for the latter based on the changing vortex regeneration dynamics between LDR and HDR.

1. Introduction

The phenomenon of turbulent drag reduction (DR) caused by polymer additives is widely known and has been studied extensively in the literature [1–3]. As a small quantity of polymers is added to a Newtonian liquid, turbulent structures are modified. The resulting friction drag reduction, measured by

$$\mathrm{DR}\% \equiv \frac{C_{f,s} - C_f}{C_{f,s}} \tag{1}$$

($C_{f,s}$ and C_f are the friction factors of the pure solvent and polymer solution, respectively), can reach up to 80%. As a result, the mean flow rate under the same pressure drop increases which considerably enhances the fluid transportation efficiency. Understanding of this phenomenon has significant practical implications for the development of mechanical flow control schemes and has thus gained significant attention since the 1940s.

In viscoelastic fluids, polymer-induced elasticity is measured by the Weissenberg number $\mathrm{Wi} = \lambda\dot{\gamma}$, which is defined as the product of the polymer relaxation time λ and the shear rate $\dot{\gamma}$ of the flow. Below a critical magnitude of Wi, the mean flow is statistically indistinguishable from that of Newtonian turbulence: in most of the boundary layer, both follow the same Prandtl–von Kármán (PvK) log law [4]

$$U^+ = 2.5y^+ + 5.5 \tag{2}$$

where the superscript " + " indicates quantities in turbulent inner scales: i.e. velocities and lengths are scaled by the friction velocity and viscous length scale or "wall unit" (see definitions in Section 2), respectively. The onset of DR typically occurs at $\mathrm{Wi}_{onset} = O(10)$ [5–8]. Further raising Wi leads to increasing levels of DR (see Fig. 1), which eventually saturate and approach an asymptotic upper bound. Rather surprisingly, this maximum drag reduction (MDR) asymptote is found to be insensitive to the rheological properties of the polymer solution [1].

* Corresponding author at: Department of Chemical Engineering, McMaster University, Hamilton, Ontario L8S 4L7, Canada.
E-mail address: xili@mcmaster.ca (L. Xi).

https://doi.org/10.1016/j.jnnfm.2018.03.017
Received 24 October 2017; Received in revised form 14 February 2018; Accepted 23 March 2018
Available online 27 March 2018

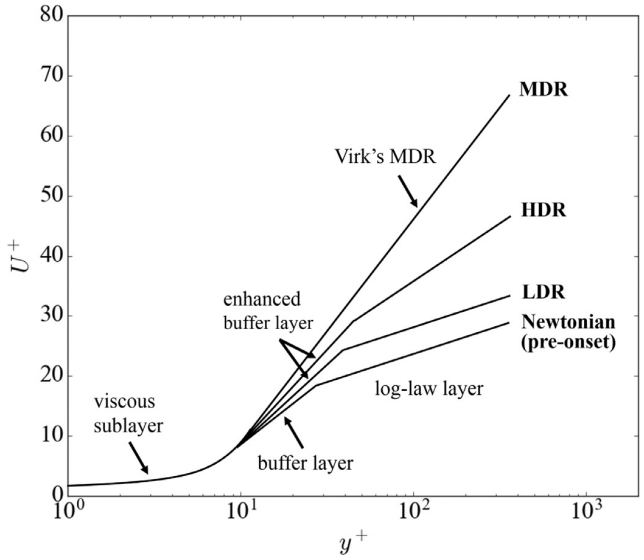

Fig. 1. Schematic of mean velocity profiles (mean streamwise velocity as a function of the distance from the wall) at different stages of DR.

The original theory of Virk [1] postulates that polymer effects concentrate in the buffer layer, corresponding to $5 \lesssim y^+ \lesssim 30$ in Newtonian turbulence (right below the log-law layer) [9]. Increasing Wi leads to a thicker buffer layer, now termed the "elastic sublayer" to reflect the polymer effects, but the log law layer remains unaffected with the same slope and only a larger intercept (Fig. 1). The elastic sublayer keeps on expanding with increasing Wi until MDR is reached where it occupies the whole channel.

Despite the intellectual appeal of its conceptual simplicity, this elastic sublayer theory was later proven oversimplified. Experiments by Warholic et al. [10] revealed that the PvK-like log law is only preserved for low-extent DR (LDR) ($\lesssim$ 35% in that study) and for high-extend DR (HDR), the slope of the mean velocity profile in a linear-log plot is ostensibly higher than the PvK magnitude (Fig. 1). This was further confirmed by a number of experimental and numerical studies [5,7,8,11–13]. Although often associated with the quantitative magnitude of DR% in the literature, emerging evidences have suggested that the LDR–HDR transition is indeed a qualitative change in the turbulent dynamics. A recent analysis by White et al. [14] showed that at HDR U^+ does not even strictly follow a logarithmic dependence. In addition, for minimal flow units (MFUs) and one low Re, Xi and Graham [7] showed that this change in the shape of the $U^+(y^+)$ profile can occur at DR% as low as $\approx$ 15: DR% > 30 is not required for HDR behaviors. Beyond the mean velocity profile, changes between LDR and HDR in other quantities are much less documented. Major observations (in the aforementioned studies) at HDR include significantly reduced Reynolds shear stress and smooth flow field patterns with longer streamwise correlation, although direct connections with the LDR–HDR transition still need to be established.

MDR is arguably the crown jewel of this field, whose curious nature remains puzzling in many respects. However, the hitherto over-shadowed problem of LDR–HDR transition certainly deserves attention in its own right. For one thing, it has significant practical implication in the area of turbulence control. Existing mechanical (non-additive-based) flow control techniques pale in comparison with polymer-induced DR: both the DR% achieved by these techniques and the shape of the $U^+(y^+)$ profile are only comparable to LDR in polymer fluids [15] – understanding the turbulent dynamics of HDR will be pivotal to break this ceiling. Meanwhile, the fundamental significance also should not be overlooked. Despite the ongoing debate between viscous vs elastic mechanisms [16,17], it has been generally accepted that DR is caused by the polymer-turbulence interaction and the resulting suppression of vortical structures [18–21]. This effect kicks in at the coil-stretch transition of the polymers [8] and corresponds to the onset of DR. The additional LDR–HDR transition at Wi distinctly higher than the onset suggests that there is another change in the underlying polymer-turbulence dynamics that we do not as yet understand: i.e. DR with increasing polymer elasticity is a two stage process with a first mechanism being triggered at the onset and a second mechanism at the LDR–HDR transition. The change in the $U^+(y^+)$ profile suggests that the first mechanism mainly acts in the buffer layer whereas the second one extends to the log-law layer.

In the recent framework by Xi and Graham [22], turbulent dynamics in MFUs is classified into two phases: regular strong turbulence that dominates the Newtonian flow is termed active turbulence and weak nearly two-dimensional turbulent state is termed hibernating turbulence. The latter occurs in Newtonian flow as well – which was confirmed in experiments [23] and believed to be intermittent visits towards the laminar-turbulent edge state [24,25] – with very low frequency but become unmasked at high Wi. Its remarkable resemblance to MDR prompts the hypothesis that MDR is an asymptotic state where hibernating turbulence becomes the statistical norm. Taking an ergodic view of turbulence and neglecting the long-range spatial correlation, the temporal intermittency in MFUs (between active and hibernating periods) should reflect the spatial intermittency in extended flow domains. This was investigated recently by Wang et al. [26] who showed that flow-field patches corresponding to active and hibernating regions can be clearly identified in a large domain and the total area of hibernating patches increases as the flow converges to MDR. Interestingly, in MFUs and at least one low Re, the Wi where hibernation frequency starts to ramp up seems to coincide with that of the LDR–HDR transition [27]. If HDR is indeed triggered by the unmasking of hibernating turbulence, that would perfectly explain the change in the shape of the $U^+(y^+)$ profile, as conditional average studies have revealed that hibernating turbulence has a drastically steeper $U^+(y^+)$ profile than active turbulence [26,27]. This link, however, has not been tested in larger domains nor for more than one Re. As we will show later, the correlation between vortex dynamics in different regions turns out to be important for understanding HDR, which was not considered in this MFU framework.

The purpose of this study is first to systematically investigate the differences between LDR and HDR in an extensive flow domain (compared with MFU) by densely sampling the parameter space. In particular, at each Re and in both LDR and HDR regimes, multiple points need to be included to establish the LDR–HDR transition as a qualitative one. A new mechanism will be proposed for the changing vortex dynamics underlying the transition. The paper is organized as follows. After introducing our simulation approach in Section 2, changes in flow statistics at the LDR–HDR transition will first be summarized in Section 3.1. We will then study and quantify the transitions in flow structure (Section 3.2). Our new mechanism for the changing vortex dynamics at HDR is proposed in Section 3.3.

2. Formulation and numerical details

Direct Numerical Simulation (DNS) of the governing equations in a plane Poiseuille geometry is performed following the standard procedure first introduced by Sureshkumar et al. [28]. The geometry of the simulation domain is shown in Fig. 2(a). The flow is driven by a fixed streamwise pressure gradient orientated in the x-direction. The no-slip boundary condition is applied to the walls (y-direction) and the periodic boundary condition is applied to both the streamwise (x-direction) and spanwise (z-direction) boundaries. The periods are denoted by L_x and L_z, respectively. By default, all variables are nondimensionalized by turbulent outer units: i.e., lengths are scaled by the half-channel height l, velocities by the laminar center-line velocity U_c, time by l/U_c, and pressure by ρU_c^2 (ρ is the total density of the fluid). Meanwhile, near-

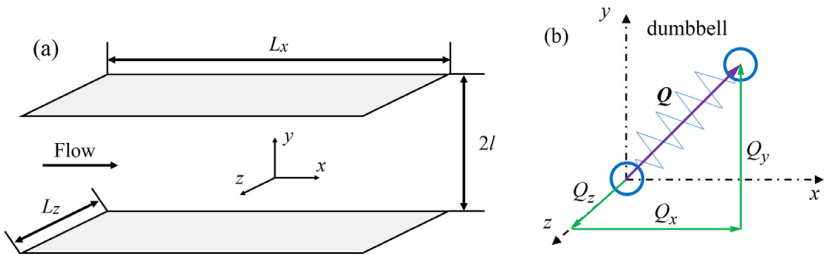

Fig. 2. Schematics of the (a) flow geometry and (b) FENE-P dumbbell.

wall quantities are often represented in inner scales: velocities scaled by the friction velocity $u_\tau \equiv \sqrt{\tau_w/\rho}$ and lengths by the viscous length scale $\delta_v \equiv \eta/\rho u_\tau$, where τ_w is the mean wall shear stress and η is the solution viscosity. Then for $\mathrm{Re} \equiv \rho U_c l/\eta$, the friction Reynolds number $\mathrm{Re}_\tau \equiv \rho u_\tau l/\eta = \sqrt{2\mathrm{Re}}$. The y coordinate in the inner scale y^+ ranges from 0 at the wall to $y^+_{\mathrm{CL}} = \mathrm{Re}_\tau$ at the channel center-line.

The momentum and mass balance equations are

$$\frac{\partial \boldsymbol{v}}{\partial t} + \boldsymbol{v}\cdot\nabla\boldsymbol{v} = -\nabla p + \frac{\beta}{\mathrm{Re}}\nabla^2\boldsymbol{v} + \frac{2(1-\beta)}{\mathrm{ReWi}}(\nabla\cdot\boldsymbol{\tau}_p), \tag{3}$$

$$\nabla\cdot\boldsymbol{v} = 0. \tag{4}$$

where the Weissenberg number Wi is the product of polymer relaxation time λ and the mean wall shear rate, i.e., $\mathrm{Wi} \equiv \lambda U_c/l$, and $\beta \equiv \eta_s/\eta$ is the ratio of the solvent viscosity to the total viscosity. The last term on the right-hand-side of Eq. (3) accounts for the polymer effect, where $\boldsymbol{\tau}_p$ is the polymer stress tensor. It is calculated with the FENE-P constitutive equation [29]

$$\frac{\boldsymbol{\alpha}}{1-\frac{\mathrm{tr}(\boldsymbol{\alpha})}{b}} + \frac{\mathrm{Wi}}{2}\left(\frac{\partial\boldsymbol{\alpha}}{\partial t} + \boldsymbol{v}\cdot\nabla\boldsymbol{\alpha} - \boldsymbol{\alpha}\cdot\nabla\boldsymbol{v} - (\boldsymbol{\alpha}\cdot\nabla\boldsymbol{v})^{\mathrm{T}}\right) = \frac{b\boldsymbol{\delta}}{b+2}, \tag{5}$$

$$\boldsymbol{\tau}_p = \frac{b+5}{b}\left(\frac{\boldsymbol{\alpha}}{1-\frac{\mathrm{tr}(\boldsymbol{\alpha})}{b}} - \left(1-\frac{2}{b+2}\right)\boldsymbol{\delta}\right). \tag{6}$$

The FENE-P model treats polymer molecules as finitely extensible nonlinear elastic (FENE) dumbbells, as shown in Fig. 2(b). The polymer conformation tensor is defined as $\boldsymbol{\alpha} \equiv \langle \boldsymbol{QQ} \rangle$, where $\boldsymbol{Q}$ donates the end-to-end vector of the dumbbell. The length of the dumbbells is constrained by the maximum extensibility parameter b: i.e., $\max(\mathrm{tr}(\boldsymbol{\alpha})) \le b$.

All variables are discretized with a Fourier-Chebyshev-Fourier pseudo-spectral scheme. The grid size in the x direction is $\delta_x^+ = 9.09$ and that in the z direction is $\delta_z^+ = 5.44$; the number of grid points in the y direction is 97, 127, and 195 for $\mathrm{Re}_\tau = 86.15$, 121.84, and 172.31, respectively. For the time integration, we adopt a third-order semi-implicit backward-differentiation/Adams-Bashforth scheme [30], and the time step is chosen to be $\delta_t = 0.01$. Numerical settings used in production runs are listed in Table 1. An artificial diffusion term $1/(\mathrm{ScRe})\nabla^2\boldsymbol{\alpha}$ is added to the right-hand side of Eq. (5) with the Schmidt number $\mathrm{Sc} = 0.5$ for $\mathrm{Re}_\tau = 86.15$ and 0.3 for $\mathrm{Re}_\tau = 121.84$ and 172.31. This term is required for the numerical stability of the pseudo-spectral method

Table 1
Numerical settings for production runs.

Re	Re_τ	δ_t	L_x^+	L_z^+	δ_x^+	δ_z^+
3711	86.15	0.01	4000	800	9.09	5.44
7423	121.84	0.01	4000	800	9.09	5.44
14845	172.31	0.01	4000	800	9.09	5.44
Re	N_y	$\delta^+_{y,\min}$	$\delta^+_{y,\max}$	Sc	1/ScRe	
3711	97	0.046	2.81	0.5	5.39×10^{-4}	
7423	127	0.038	3.03	0.3	4.49×10^{-4}	
14845	195	0.022	2.79	0.3	2.25×10^{-4}	

Table 2
Settings of the validation tests.

No.	Re_τ	Wi	Sc	1/(ScRe)	$L_x^+ \times L_z^+$	$N_x \times N_y \times N_z$
1	86.15	64	0.3	8.98×10^{-4}	4000 × 800	256 × 59 × 87
2	86.15	64	0.5	5.39×10^{-4}	4000 × 800	440 × 97 × 147
3	86.15	64	0.75	3.59×10^{-4}	4000 × 800	640 × 145 × 221

used here and it has been established in the literature that a numerical diffusivity of $O(0.01)$ does not significantly impact the results [8,11,28,31,32]. The magnitudes of diffusivity 1/ScRe used in this study are all at $O(10^{-4})$ (Table 1). According to Sureshkumar et al. [28,31], when the numerical diffusivity decreases (by increasing Sc) linearly with the grid size, the solution converges to that of the original equation. This convergence is validated here for a high-Wi case with proportionally varying resolution and numerical diffusivity as listed in Table 2. As an example, we present the streamwise one-dimensional energy spectra of all three velocity components – defined as

$$E_{ii}(k_x) = \int_{k_z} \hat{v}_i'^{*}\cdot\hat{v}_i' dk_z \tag{7}$$

(where $i = x, y, z$ is the index for velocity components, "′" indicates the fluctuating component of the velocity field, ^ indicates the Fourier transform, and "*" indicates the complex conjugate) – in Fig. 3. For all cases, results from different resolutions and numerical diffusivity magnitudes well collapse onto one another, indicating that our choice of Sc is sufficient.

The numerical code used for this study is a custom MPI-parallelized code developed based on the C++ Channelflow package [33]. A Newtonian version of the code was earlier used for the DNS of Newtonian Poiseuille flow [34]; the code was then extended for viscoelastic simulation by integrating the original algorithm of Xi and Graham [7].

3. Results and discussion

Simulations in this study are all performed in the box size of

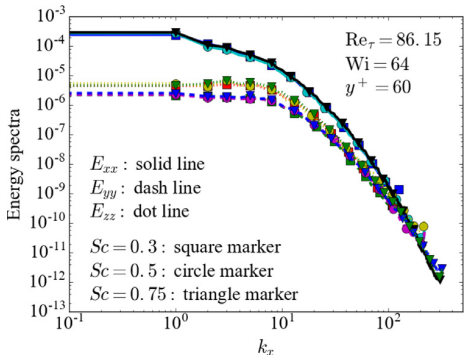

Fig. 3. Three components of the one-dimensional energy spectra against the spanwise wave number at $y^+ = 60$.

$L_x^+ \times L_z^+ = 4000 \times 800$, which is well within the range considered to be an extended domain. A series of Wi at each of three different Re_τ (86.15, 121.84, and 172.31) are reported. These Re_τ values are closer to the critical magnitude $\mathrm{Re}_{\tau,\ \mathrm{crit}} \approx 45$ for the laminar-turbulent transition [35] than several recent high-Re viscoelastic turbulence DNS studies [8,36]. This choice is deliberate. Previous research has clearly shown that all key stages of viscoelastic turbulence are observed in the near-transition regime [1,7]: higher Re is not a necessary condition for the LDR–HDR transition. At lower Re, the turbulent dynamics is more tractable and also different stages of DR are contained in a smaller parameter-space region (see Fig. 5), both bringing mechanistic understanding within reach. On the other hand, unlike most previous studies which focused on the direct comparison between one LDR and one HDR case, our attention is on the parametric dependence of the qualitative behaviours. This requires simulations at a larger number of parameter combinations and keeping the Re at this level reduces the computational cost per run. (Nevertheless, the computation is still substantial: for viscoelastic simulation at the highest $\mathrm{Re}_\tau = 172.31$ and running on 32 processors in parallel, the time-stepper proceeds by ≈ 7 time units per wall-clock hour; each data point, including both equilibration and production runs, requires 3500 time units, which takes more than 20 days on a state-of-the-art computing facility.) For the two lower Re, the full transition path from Newtonian to MDR is captured. For the highest Re, numerical instability starts to show up at Wi = 96. Instead of increasing the artificial diffusivity, we decided to exclude results at higher Wi since Wi = 96 is already well beyond the LDR–HDR transition. The rheological parameters b and β in all cases are fixed to be 5000 and 0.97, respectively. Time average results in this section are all calculated from 20 evenly-spaced snapshots within a total period of 1000 time units, after the DNS solution has reached the statistical steady state.

3.1. Changes in flow statistics

In this section, statistical results are summarized and compared between LDR and HDR. In Fig. 4, DR% as a function of Wi are plotted for three Reynolds numbers Re_τ: 86.15, 121.84 and 172.31. (DR% is defined in Eq. (1) and the friction factor is defined as

$$C_f \equiv \frac{2\tau_w}{\rho U_{\mathrm{avg}}^2} \tag{8}$$

where U_{avg} is the volume average streamwise velocity.) As expected, DR% of all Re increases with Wi. Interestingly, profiles of three Re nearly overlap until they get close to the asymptotic plateau. This suggests that the quantitative dependence of DR% on Wi can be approximated by the same empirical correlation, as also reported by Housiadas et al. [37] and Owolabi et al. [38]. We adopt the same formula used by Housiadas and Beris [37]

$$\frac{\mathrm{DR\%}}{\mathrm{DR\%_{MDR}}} = \begin{cases} 0 & (\mathrm{Wi} < \mathrm{Wi_{onset}}) \\ 1 - \dfrac{2}{1+\exp\left(\frac{\mathrm{Wi}-\mathrm{Wi_{onset}}}{\mathscr{W}}\right)} & (\mathrm{Wi} \geq \mathrm{Wi_{onset}}) \end{cases} \tag{9}$$

which models a smooth monotonic increase from DR% = 0 at $\mathrm{Wi_{onset}}$ to $\mathrm{DR\%} = \mathrm{DR\%_{MDR}}$ as $\mathrm{Wi} \to \infty$; parameter $\mathscr{W}$ adjusts the profile steepness. We set $\mathrm{DR\%_{MDR}} = 51.5\%$ which is the average DR% value of our MDR data points. Eq. (9) is then rearranged to

$$\ln\left(\frac{\mathrm{DR\%_{MDR}} + \mathrm{DR\%}}{\mathrm{DR\%_{MDR}} - \mathrm{DR\%}}\right) = \frac{\mathrm{Wi}}{\mathscr{W}} - \frac{\mathrm{Wi_{onset}}}{\mathscr{W}} \tag{10}$$

from which $\mathscr{W}$ and $\mathrm{Wi_{onset}}$ can be determined with linear regression. The regression line from all our LDR and HDR data points is shown in Fig. 4(b). The data points remain close to the linear line until very high Wi (> 60), indicating that Eq. (9) offers satisfactory correlation except in the regime near MDR (also seen in Fig. 4(a)). Parameters obtained from the regression – $\mathrm{Wi_{onset}} = 5.76$ and $\mathscr{W} = 23.41$ – are very close to the values estimated by Housiadas and Beris [37] ($\mathrm{Wi_{onset}} = 6$ and $\mathscr{W} = 25$). The agreement is expected since Housiadas and Beris's [37] relation was also based on DNS data over a broad range of Re_τ (which covers our Re_τ magnitudes). Note that Eq. (9) is simply a more general form of the Owolabi et al. [38] model: it reduces to the latter when $\mathrm{Wi_{onset}} = 1/2$ and $\mathscr{W} = 1$. Owolabi et al.'s [38] $\mathrm{Wi_{onset}}$ was much lower because there is no one-to-one mapping between the definitions of Wi in experiments and in DNS. Even after this difference is corrected for, fitting of our data to the Owolabi et al.'s [38] form is less successful: the additional steepness parameter $\mathscr{W}$ in Eq. (9) is necessary.

Also noteworthy is that the LDR–HDR transition, which occurs at around DR% = 20% (shown later in Fig. 9), is not reflected as any discernible change of trend in DR%. For the two lower Re_τ where high Wi results are available, DR% eventually saturates to an asymptotic upper limit. In its literal interpretation, MDR is the limit where DR% saturates with polymer elasticity. We will therefore refer to this limit as MDR in this paper. Further increasing the Wi causes the flow to laminarize. Experimentally, MDR should be a self-sustaining turbulent state where laminarization is avoided. However, re-laminarization at Wi is often observed in simulation studies [5,7]. There are several possible causes for this discrepancy, including the lower Re and limited domain size used in simulations. Deterioration of numerical accuracy due to the artificial diffusion may also play a role at this level of Wi [12]. Nevertheless, the LDR–HDR transition studied here occurs at much lower Wi and none of the major conclusions of this study should be affected.

Simulation points reported in this study are summarized in a Re − Wi parameter space in Fig. 5, which is divided into four stages of DR behaviours: pre-onset (P.O.), LDR, HDR, and MDR. In the current domain, $\mathrm{Re}_\tau = 61.28$ is the smallest Re to observe sustained turbulence, where introducing polymers immediately leads to laminarization. At the higher Re, the full transition path from Newtonian turbulence to MDR is observed, resonating with the experimental observation that

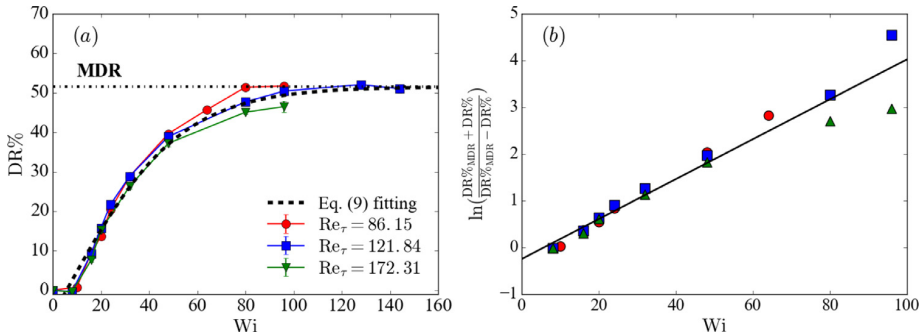

Fig. 4. (a) dependence of the percentage of drag reduction (DR%) on Wi at $\mathrm{Re}_\tau = 86.15$, 121.84 and 172.31 and comparison with the empirical fitting using Eq. (9); (b) linear regression plot using Eq. (10) (data symbols are the same as those in panel (a)).

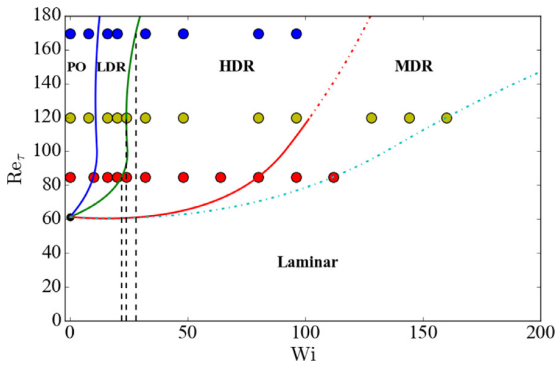

Fig. 5. Multi-stage transitions of DR behaviours in the Re − Wi parameter space. Transition boundaries are drawn according to the B-spline interpolation between the critical Wi of the transitions at different Re$_\tau$. Vertical dashed lines indicate the LDR–HDR transition for each Re$_\tau$.

qualitative transitions in viscoelastic turbulence extend all the way down to the laminar-turbulent transition regime. Critical Wi's for the transitions increases with Re$_\tau$, leading to a wider range of Wi being occupied by each stage. Convergence to MDR occurs at Wi = 80 for Re$_\tau$ = 86.15 and Wi = 128 for Re$_\tau$ = 121.84. Variation in the onset Wi is almost negligible and a Wi$_{\text{onset}} \approx 10$ is observed for all cases. The critical Wi for the LDR–HDR transition is 22, 24, and 28 for Re$_\tau$ = 86.15, 121.84, and 172.31, respectively.

Current results of Re$_\tau$ = 86.15 are compared with the MFU simulation of Xi and Graham [7]. The Re$_\tau$ = 84.85 of that study is very close to the current value and the rheological properties (i.e. β and b) are the same. The only different setting is the size of the simulation domain $L_x^+ \times L_z^+$ which is 4000 × 800 in the current study and in Xi and Graham [7] $L_x^+ = 360$ and $L_z^+ = 140 \sim 260$ depending on the Wi. As a result, the sequence and qualitative behaviours of different stages of DR are the same between the two domain sizes, but the quantitative magnitudes of the critical Wi and DR% for all transitions differ. In MFUs, the LDR–HDR transition occurs at Wi = 20 with DR% ≈ 15 and convergence to MDR is found at Wi = 27 and DR% ≈ 26; whereas in the extended domain, both these transitions are found at higher Wi and DR%. In a way, the restrictive domain of MFU compresses the transitions into a smaller parameter region but still preserves all qualitative aspects.

Fig. 6 shows the mean velocity profiles of the Re$_\tau$ = 86.15 and Re$_\tau$ = 121.84 cases. The Newtonian profile at Re$_\tau$ = 86.15 is parallel to the PvK log law for $y^+ > 30$ but the intercept is slightly higher, because at this lowest Re the log-law layer is not fully developed. At Re$_\tau$ = 121.84, the Newtonian profile is already very close to the PvK log law and at Re$_\tau$ = 172.31 (not shown here) it completely overlaps the latter. Before the onset of DR, viscoelastic profiles are indistinguishable from the Newtonian ones and thus omitted from Fig. 6. At LDR (Wi = 16 for both Re in Fig. 6), the mean velocity profiles rise in the buffer layer region and remain parallel to the Newtonian case in the log-law region. At HDR (i.e. Wi = 32 for Re$_\tau$ = 86.15 and Wi = 48 for Re$_\tau$ = 121.84), the profiles lift up in the log-law layer showing slopes clearly higher than that of the PvK asymptote. For each Re$_\tau$, two profiles are chosen in the MDR stage (i.e. Wi = 80 and 96 for Re$_\tau$ = 86.15 and Wi = 128 and 144 for Re$_\tau$ = 121.84) to show the convergence of the mean velocity. At both Re$_\tau$, the profiles are close to but still slightly below the Virk asymptote. Although it is a common practice in the literature to take the Virk log law as the criterion for identifying MDR, we note that it is only an empirical correlation for experimental data often gathered at higher Re than most computational studies. The appropriateness of the Virk log law is even challenged recently [14]. As stated above, we take a literal interpretation and identify MDR as the asymptotic limit of DR with increasing Wi. The nature and definition of MDR are not the focus of this study.

Fig. 7 shows the distribution of four components ($\langle v_x'^+ v_x'^+ \rangle$, $\langle v_y'^+ v_y'^+ \rangle$, $\langle v_z'^+ v_z'^+ \rangle$ and $-\langle v_x'^+ v_y'^+ \rangle$) of the Reynolds stress across the channel at Re$_\tau$ = 86.15 and 121.84. For both Re and after onset, the streamwise Reynolds stress profiles rise up with increasing Wi while the wall-normal, spanwise, and shear components are all suppressed. All four components converge as MDR is reached. In addition to the commonly discussed change of shape in the mean velocity profile (Fig. 6), the LDR–HDR transition can also be clearly identified with the changing Reynolds stress profiles as well especially of the xy shear component. From the bottom panels of Fig. 7, it is clear that at LDR (Wi = 16 for both Re$_\tau$), the suppression of the $-\langle v_x'^+ v_y'^+ \rangle$ profile is localized in the buffer layer $-5 \lesssim y^+ \lesssim 30$ and at higher y^+ the profile well overlaps with the Newtonian one. By contrast, at higher Wi (after the LDR–HDR transition), the suppression extends across the whole channel. A vertical dashed line is drawn within the log-law layer as an eye guide to show the reduced magnitude there. This transition between local and global suppression is more clearly seen when the deviation of the Reynolds shear stress from the Newtonian case is plotted in Fig. 8.

Note that in our MDR cases, although $-\langle v_x'^+ v_y'^+ \rangle$ is significantly suppressed by polymers, its magnitude remains finite and differs from the Newtonian value by no more than one order of magnitude. Vanishing Reynolds shear stress is often cited in the literature as a key feature of MDR, an argument first made by Warholic et al. [10] based on their experimental observation. Later experimental and numerical observations were not always consistent with this conclusion and non-zero Reynolds shear stress was often seen even when the Virk MDR asymptote is reached [11–13]. Flow statistics at MDR is not our current focus and we do not intend to settle this debate in this paper. However, our observations do indicate that for Reynolds shear stress it is the wall regions of suppression, not the magnitude itself, that determines the

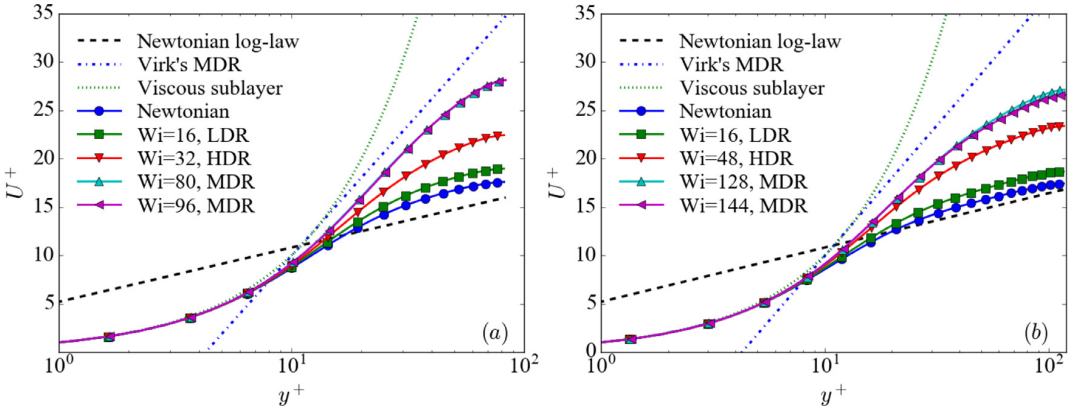

Fig. 6. Mean velocity profiles (U^+ vesus y^+) for (*a*) Re$_\tau$ = 86.15 (*b*) Re$_\tau$ = 121.84.

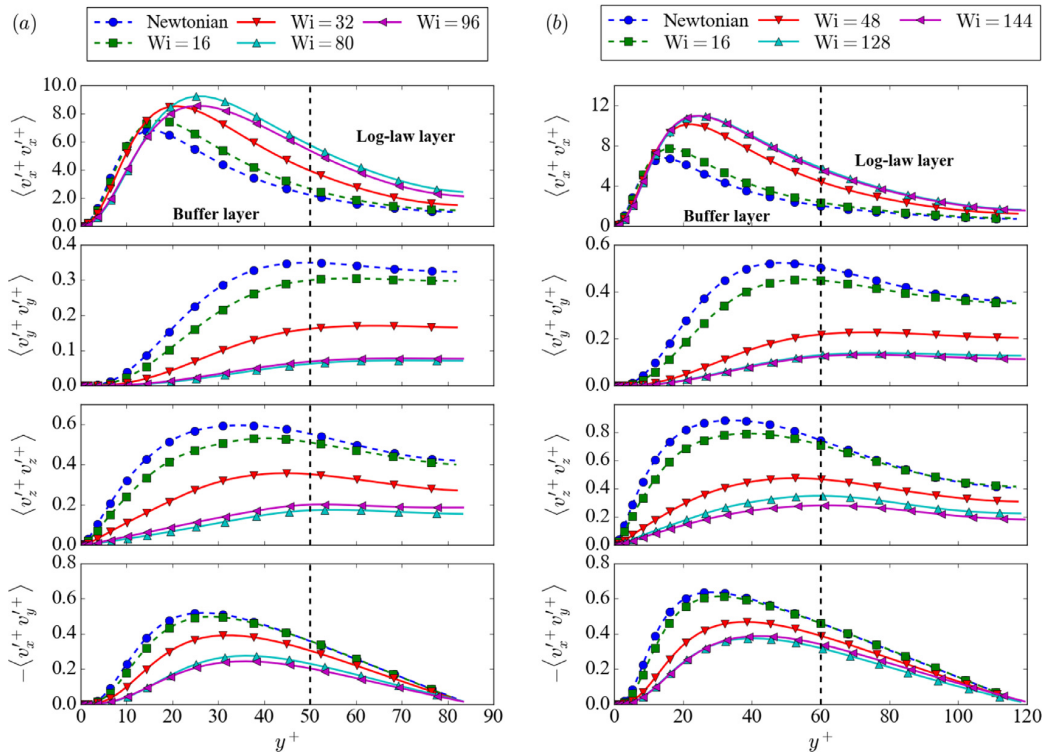

Fig. 7. Reynolds stress profiles for (*a*) Re_τ = 86.15 and (*b*) Re_τ = 121.84.

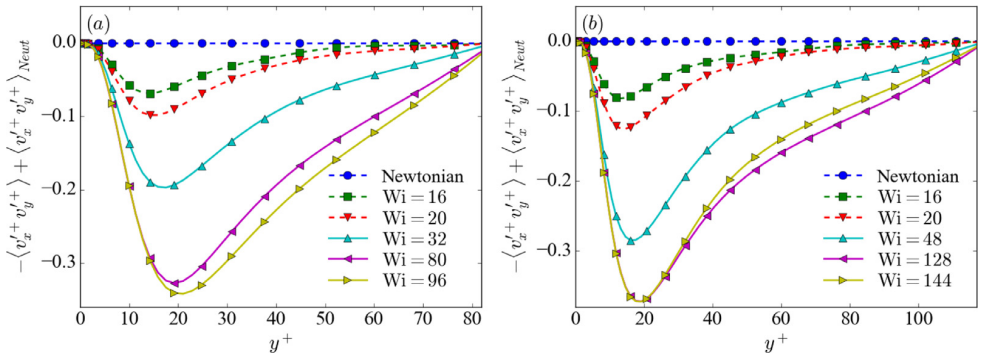

Fig. 8. Deviation of the Reynolds shear stress from the Newtonian case: (*a*) Re_τ = 86.15 and (*b*) Re_τ = 121.84.

onset of HDR.

In other components, changes in the Reynolds stress magnitudes (increase in the streamwise component and decrease in other components) in the log-law layer all become augmented at the LDR–HDR transition. Notably, it even results in a clear change of shape of the wall-normal profile: at LDR, same as the Newtonian limit, the profiles climb up to a maximum near $y^+ = 40$, followed by a steady decline at higher y^+, whereas at HDR, the profiles stay flat in the log-law layer.

Qualitative transitions observed in both Figs. 6 and 7 indicate that fundamental changes have occurred in the turbulent dynamics of the log-law layer. To further tie these transitions to the phenomenological LDR–HDR transition, we compare the trends of quantity changes using multiple data points in both LDR and HDR regimes. Note that the Reynolds shear stress is related to the velocity gradient, which determines the log-law slope of the mean velocity profile, via the shear stress balance

$$\langle \tau_{xy}^+ \rangle = \beta \frac{dU^+}{dy^+} + \langle -v_x'^+ v_y'^+ \rangle + \frac{1-\beta}{\mathrm{Wi}} \langle \tau_{p,xy} \rangle. \tag{11}$$

The three components on the right-hand side of Eq. (11) are the contributions of the mean viscous shear stress, Reynolds shear stress, and polymer shear stress to the total shear stress. Fig. 9(a) and (b) show the quantitative correlation between these terms and DR% in the buffer layer (i.e. $y^+ = 25$) and the log-law layer ($y^+ = 0.6\mathrm{Re}_\tau$), respectively. In the buffer layer (Fig. 9(a)), all three terms vary – increase for the viscous and polymer shear stresses and decrease for the Reynolds shear stress – nearly linearly with DR% between the DR onset and MDR. Comparing different Re, the viscous shear stress decreases and the Reynolds shear stress increases as Re increases, which is consistent with previous observations in Newtonian flows [39,40]. At higher Re (than those reported here), the Re-dependence of these shear stress terms is expected to be weaker according to the previous study of Housiadas and Beris [41]. Interestingly, for these two terms, the slope of the trendlines stays approximately the same with varying Re, suggesting that despite the significant weakening of turbulence, polymer effects remain qualitatively similar in this layer. Meanwhile, the polymer term also shows a Re-dependence but the slope of the trendlines increases. On the other hand, in the log-law region (Fig. 9(b)), clear sharp transitions are found

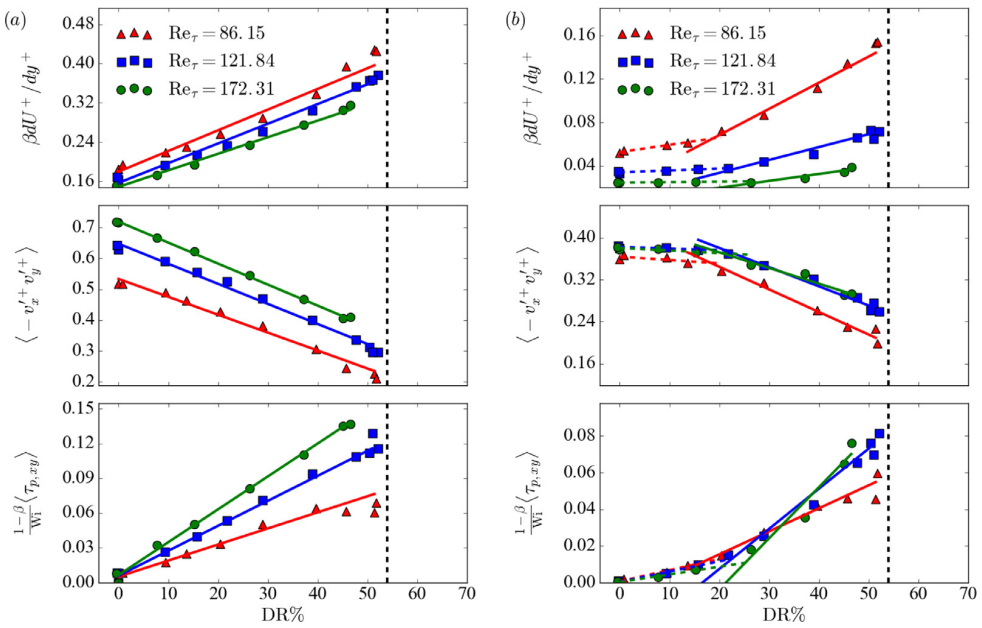

Fig. 9. Correlation between different contributions to the total shear stress (Eq. (11)) with varying DR% at (a) $y^+ = 25$ and (b) $y^+ = 0.6\mathrm{Re}_\tau$. In panel (a), lines represent the linear regression results of all points; in panel (b), dashed lines are for the linear regression results of LDR and solid lines for HDR.

in all three terms between LDR and HDR. Before the LDR–HDR transition, variations in these quantities with increasing DR% are barely existent, but in the HDR regime, a clear trend of either increase or decline is observed. Re-dependence is still observed but becomes less obvious as Re_τ grows higher, especially in the cases of Reynolds and polymer shear stresses. The turning point between these two behaviors puts the LDR–HDR transition at DR% ≈ 20, a value lower than the experimental transition point of DR% ≈ 35 reported by Warholic et al. [10]. This is likely due to our lower Re: note that in Fig. 9(b) the transition point does shift toward higher DR% as Re_τ increases. We stress here again that LDR–HDR is a qualitative transition in the turbulent dynamics that is not tied to a particular quantitative magnitude of DR% for different Re. Observations in Fig. 9 are also consistent with our earlier hypothesis that DR is a two stage process with different mechanisms: the first one is triggered at the DR onset and takes effect in the buffer layer and the second one gives rise to HDR in which the log-law layer dynamics becomes affected.

To further inspect the changing flow statistics in the log-law layer, the energy spectrum of the streamwise velocity E_{xx} (defined in Eq. (7)) is calculated in the log-law layer and plotted in Fig. 10(a). As Wi increases, the profile is raised at smaller k_x and reduced at larger ones. This is consistent with the observation in previous studies that polymer additives suppress small scale fluctuations and strengthen energy-containing large-scale structures [10,42,43]. The effect becomes apparently amplified in HDR, which is more clearly observed when we calculate the proportion of energy contained in the 15 leading modes

$$\tilde{E}_{xx}^{15} = \sum_{k=0}^{15} E_{xx}^{(k)} / \sum_{k=0}^{\infty} E_{xx}^{(k)} \tag{12}$$

and plot it as a function of y^+ in Fig. 10. As Wi increases, the accumulated energy contained in the large scales increases, consistent with the increasing importance of the large-scale turbulent structures. In all cases, the profiles decrease as they approach the center of the channel. For Newtonian and LDR cases, the decline is rather steep: the latter is nearly parallel to the former for the whole channel. Therefore, LDR preserves the same near-wall turbulent dynamics typical of Newtonian flow, where the buffer layer is dominated by recurrent coherent vortical motions and their outward eruptions, the so-called "bursting" events, generate intense small-scale fluctuations at larger y^+ [44]. DR is caused by an across-the-board suppression of turbulent motions extending over the entire channel. By contrast, for the HDR cases, profiles are gradually

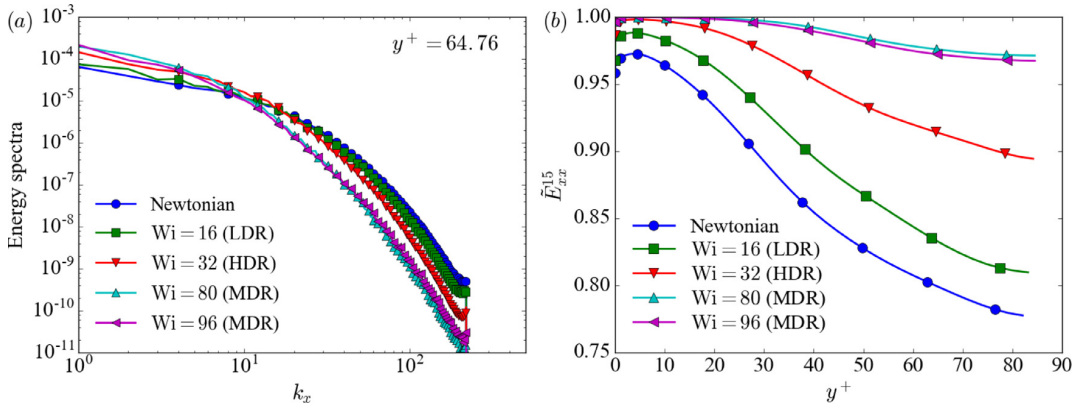

Fig. 10. (a) The energy spectra (x-x component) of different Wi at $y^+ = 64$ and $\mathrm{Re}_\tau = 86.15$ and (b) Proportion of energy contained in the large scales ($k_x \leq 15$).

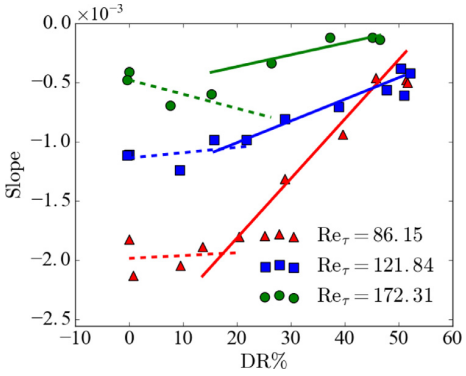

Fig. 11. Characteristic slope of the accumulated energy profile (Fig. 10(b)) in the bulk region of the channel ($|y| \leq 0.5$). The solid and dash lines are obtained with linear regression of the data in the HDR and LDR stages, respectively.

lifting up in the log-law layer and near the center. This suggests that at the HDR and MDR stages, polymers become more effective in suppressing the small-scale fluctuations at high y^+, which supports our hypothesis that a second mechanism is triggered at HDR for DR in the log-law layer. This change of profile shape can be shown to correspond exactly to the LDR–HDR transition when we take the part of each profile in Fig. 10 within the bulk of the channel – defined here as $|y| \leq 0.5$, calculate a profile slope using linear regression, and plot this characteristic slope in Fig. 11 versus DR%. It is clear that at LDR, the characteristic slope is nearly flat with increasing DR% and the slope starts to increase only in HDR. With increasing Re, the characteristic slope increases (becomes less negative) at the Newtonian and LDR end: i.e., the profiles of $\widetilde{E}_{xx}^{15}$ are flatter near the channel center. This is however a trivial observation. It is important to be reminded that the characteristic slope is defined in terms of the wall-normal position in the outer unit – i.e., $|y| \leq 0.5$ – and it does not correspond to the same wall layer in the inner unit. At higher Re, the slope reflects more of the turbulent core than the boundary layer. Likewise, the universal cutoff of $k_x \leq 15$ used in the definition of $\widetilde{E}_{xx}^{15}$ is also arbitrary and affects results from different Re differently. Comparison of the slope in Fig. 11 is only meaningful at the same Re and any interpretation of the Re-dependence can be misleading.

As for the polymer conformation statistics, we show the normalized profiles of the square root of the trace of the polymer conformation tensor $\boldsymbol{\alpha}$ at Re$_\tau$ = 86.15 and 121.84 in Fig. 12. This quantity is essentially proportional to the average end-to-end distance of the polymer chains. As expected, polymer extension increases with Wi, but interestingly the trend does not stop in the MDR stage: i.e., even after the flow statistics have converged, polymer extension continues to increase. There is also a clear qualitative difference between low and high Wi,

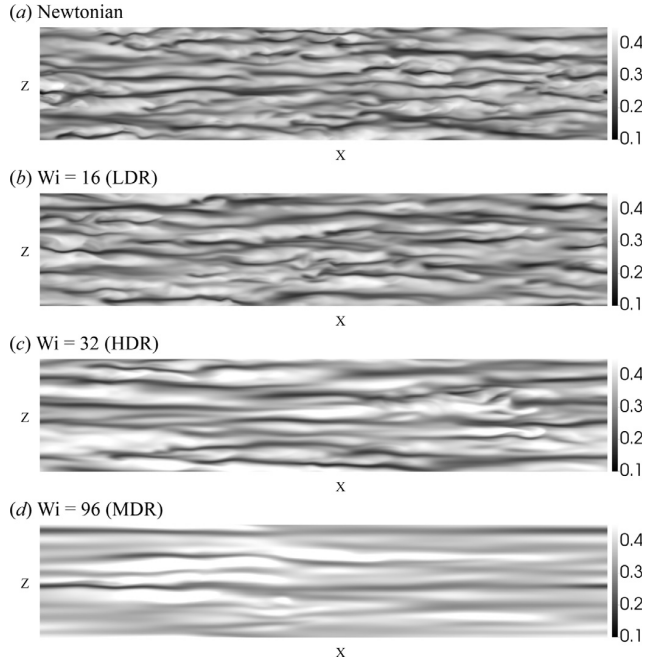

Fig. 13. Instantaneous streamwise velocity in the xz plane at $y^+ = 20$.

which occurs roughly at the LDR–HDR transition. At lower Wi, polymer extension is highest at the wall, where the mean shear rate is highest, and it declines monotonically with y^+. At higher Wi, a maximum is found in the buffer layer between $y^+ = 10$ and 20. A similar change of peak position was also observed in MFUs [7] and it indicates a qualitative shift in the polymer-turbulence interaction.

3.2. Turbulence structures

To unravel the turbulent dynamics behind these changing flow statistics, we first turn to the flow patterns and vortex structures. We will start with velocity distributions which have been widely discussed in the literature. We will then show that the changing velocity patterns are a reflection of a change in the vortex distribution and topology.

3.2.1. Turbulence localization: visualization and quadrat analysis

Fig. 13 shows the streamwise velocity distribution at $y^+ = 20$ for Newtonian, LDR, HDR and MDR stages at Re$_\tau$ = 86.15. The alternating bright and dark stripes correspond to the high- and low-speed streaks, typical of near-wall coherent structures. It is clear that as Wi increases, the length of velocity streaks increases while the curvature of the

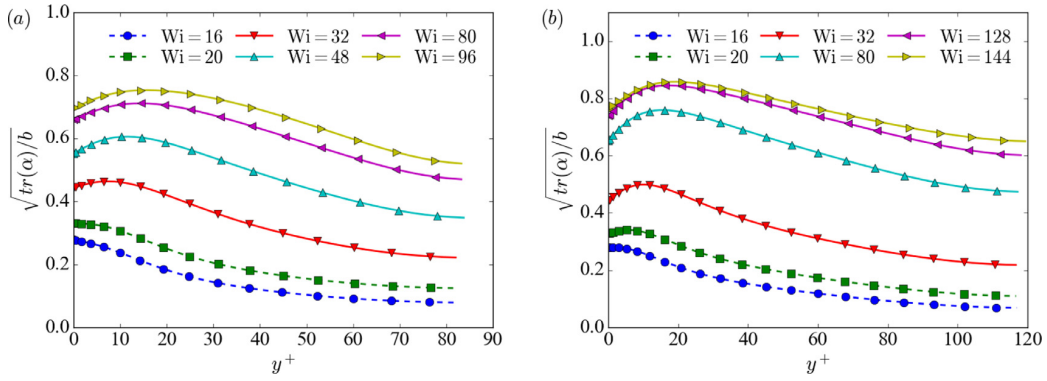

Fig. 12. Normalized profiles of the square root of the trace of the polymer conformation tensor: (*a*) Re$_\tau$ = 86.15 and (*b*) Re$_\tau$ = 121.84.

streaks decreases. For Newtonian and LDR cases, the streaks wiggle around as they extend downstream, whereas in HDR and MDR, the streaks are wide and straight in shape and wrinkles become spotty. These changes are reported in various prior experimental and numerical studies [13,43,45,46].

Vortices in the flow field are identified by the Q criterion [47,48], where

$$Q \equiv \frac{1}{2}(\|\boldsymbol{\Omega}\|^2 - \|\boldsymbol{\Gamma}\|^2) \tag{13}$$

is the difference between the Frobenius norms of the vorticity tensor

$$\boldsymbol{\Omega} \equiv \frac{1}{2}(\boldsymbol{\nabla v} - \boldsymbol{\nabla v}^{\mathrm{T}}) \tag{14}$$

and the rate of strain tensor

$$\boldsymbol{\Gamma} \equiv \frac{1}{2}(\boldsymbol{\nabla v} + \boldsymbol{\nabla v}^{\mathrm{T}}). \tag{15}$$

A pure shear flow has $Q = 0$ and in turbulent flow large positive and negative Q values correspond to regions dominated by rotational and extensional flows, respectively.

Isosurfaces of $Q = 0.7Q_{\mathrm{rms}}$, where Q_{rms} is the root-mean-square of the Q field in that domain, are shown in Fig. 14 for the same four instants of Fig. 13. As Wi increases, not only is the vortex strength weakened – which can be judged from the isosurface level ($\propto Q_{\mathrm{rms}}$) and is expected because polymers are known to suppress turbulence, but the distribution pattern also seems to have changed. In the Newtonian and LDR (Wi = 16) cases, the domain is densely populated by a large number of vortices and the distribution is mostly uniform in space. From the upstream side (left side), the vortices originate from the wall (light color) and lift upwards (darker color) as they extend downstream. Most of them do not exceed ≈ 300 wall units and despite the low Re, the so-called "hairpin" vortices are already observed. A symmetric hairpin is developed when two streamwise vortices lift up at the downstream end and connect via an "arc" in the spanwise direction. More often the hairpin is incomplete or asymmetric where one of the legs is not clearly developed. By contrast, in the case of HDR (Wi = 32) and MDR (Wi = 96), the distribution becomes clearly heterogeneous where vortices tend to agglomerate: i.e., turbulence is more localized and regions between those vortex clusters are nearly laminar. Vortices also become elongated and most remain aligned in streamwise direction. Indeed, the smooth streak patterns observed in Fig. 13 for HDR (and MDR) are simply a reflection of the turbulence localization, where the straightened streaks correspond to the quasi-laminar regions and the spotty wrinkles result from localized vortex clusters.

Vortex structures at $\mathrm{Re}_\tau = 172.31$ are also identified by isosurfaces of $Q = 0.7Q_{\mathrm{rms}}$ and shown in Fig. 15. Same as the lower Re case, distinct aggregation of vortices also occurs at the HDR stage (Wi = 80). Compared with the low Re case, the major difference is the presence of a considerable number of hairpin vortices in Newtonian flow, which is commonly observed in the literature at similar Re levels [49,50]. These hairpin-like vortices are mostly asymmetric with one leg extending much longer than the other. Qualitative changes in the flow structures and patterns between LDR and HDR have been noticed in the literature at even higher Re (e.g., $\mathrm{Re}_\tau = 395$ in Li et al. [13]). Vortex clustering and localization reported here offer an effective explanation for those observations. For example, the emergence of larger quiescent regions results in areas with straight and elongated streaks in velocity contour plots and the localized vortical structure corresponds to isolated wrinkles on those streaks (see Fig. 13 here as well as, e.g., Fig. 4 of Li et al. [13] and Fig. 17 of Housiadas et al. [43]).

In order to quantitatively analyze the level of turbulence localization at high-Wi turbulence, we adopt the so-called quadrat analysis [51]. In this algorithm, the computational domain is divided into an array of rectilinear cells in the xz plane. Within each cell,

$$p \equiv V_{\mathrm{turb}}/V_{\mathrm{cell}} \tag{16}$$

is the fraction of the volume occupied by turbulence V_{turb} over the total

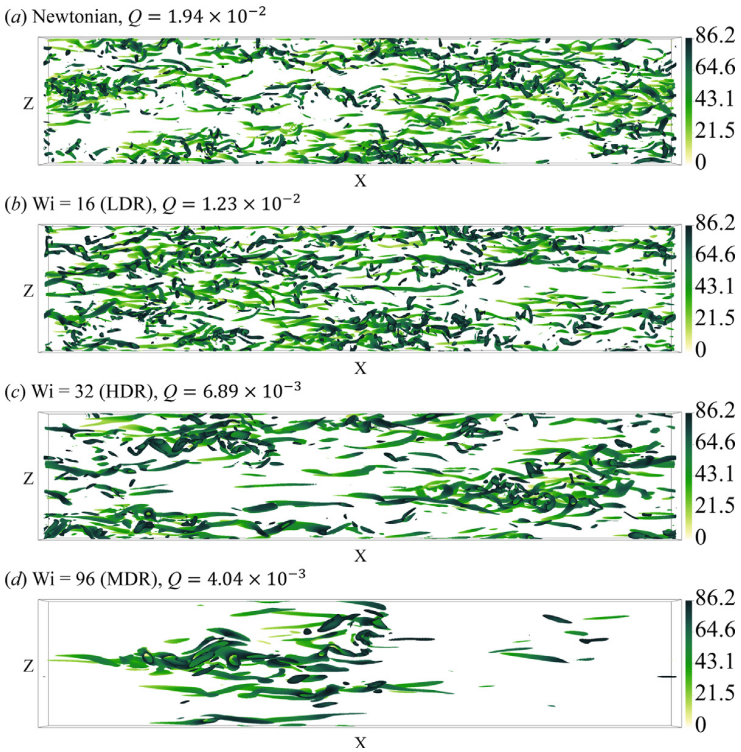

Fig. 14. Typical snapshots of the vortex structures at $\mathrm{Re}_\tau = 86.15$ (top view; only vortices in the bottom half of the channel are shown). Isosurfaces of $Q = 0.7Q_{\mathrm{rms}}$ are chosen to represent the vortex surfaces. The color shade (from light to dark) maps to the wall distance y^+ (from 0 to Re_τ).

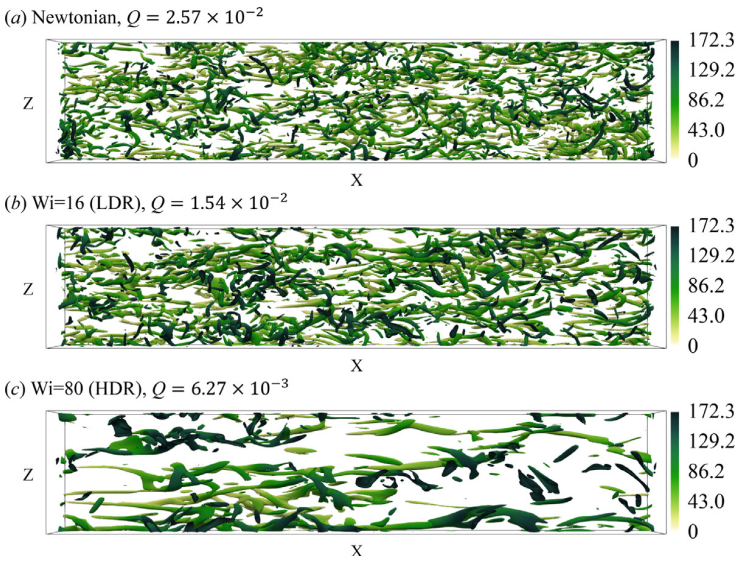

Fig. 15. Typical snapshots of the vortex structures at $\mathrm{Re}_\tau = 172.31$ (top view; only vortices in the bottom half of the channel are shown). Isosurfaces of $Q = 0.7Q_{\mathrm{rms}}$ are chosen to represent the vortex surfaces. The color shade (from light to dark) maps to the wall distance y^+ (from 0 to Re_τ).

cell volume V_{cell}. Here, turbulent regions are identified as those where $Q > 0.7Q_{\mathrm{rms}}$. The extent of localization is quantified by the coefficient of variation

$$\mathrm{CV} = \frac{s_p}{\overline{p}} \tag{17}$$

where s_p and $\overline{p}$ are the standard deviation and the mean of the p values of individual cells. Obviously, when turbulent distribution is more heterogeneous, there will be a larger disparity between the p values of different cells, leading to a larger ratio of its standard deviation to the mean.

Results of this quadrat analysis are presented in Fig. 16. Since the choice of cell size is arbitrary, we tested multiple sizes to make sure that our conclusions do not depend on this artificial parameter; two of the sizes are tested, i.e., $l_x^+ \times l_z^+ = 200 \times 80$ and 50×32, are shown in this figure. It is clear that the cell size only affects the quantitative magnitude of CV without changing the qualitative trend of the profiles. At lower Wi (still above the DR onset), CV remains at the same level as the Newtonian case. After the LDR–HDR transition ($\mathrm{Wi}_{\mathrm{LDR\text{-}HDR}} = 24$), this number steadily increases: i.e., turbulence becomes more localized.

Similar as the case in Fig. 11, differences in CV between the two Re do not lead to any physically meaningful conclusion. Both the cell size and the cutoff threshold of Q are arbitrarily chosen parameters with unknown Re-dependence: comparison is only meaningful at the same Re. We have also tested a two-dimensional variant of the quadrat analysis, where the xz-planar average Q values – at the $y^+ = 25$ (buffer layer) and $y^+ = 0.6\mathrm{Re}_\tau$ (log-law layer) planes – are used in place of Q_{cell} in the identification of turbulent regions. The results are similar to those of the three-dimensional version shown in Fig. 16 (and thus not shown here), which indicates that the clustering of vortices and the turbulence localization are occurring across the domain as the flow enters HDR.

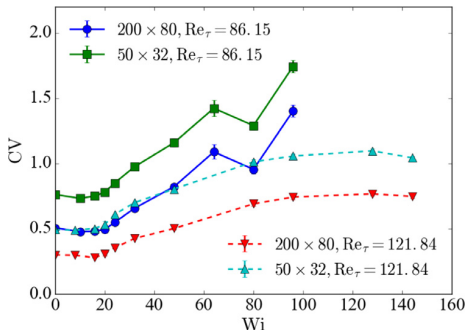

Fig. 16. The three dimensional quadrat analysis at $\mathrm{Re}_\tau = 86.15$ and $\mathrm{Re}_\tau = 121.84$. Two cell sizes are reported: $l_x^+ \times l_z^+ = 200 \times 80$ and 50×32.

3.2.2. Discussion: relationship with flow statistics

The above observations are consistent with our initial hypothesis that DR is a two stage process. At the onset of DR, polymers undergo the coil-stretch transition and start to suppress all vortical motions. This across-the-board vortex suppression occurs throughout all stages of DR after the onset. As shown in Fig. 17, the magnitude of Q steadily decreases with increasing DR% in both LDR and HDR stages. The localization of turbulence, however, only occurs in HDR, which could be the second mechanism for DR and responsible for the qualitative changes in flow statistics.

The observation of turbulence localization at the transition to HDR resonates with the spatio-temporal intermittency between active and hibernating turbulence discussed earlier [22,26,27]. These two concepts are clearly related but the distinction between them should not be overlooked. Of course, the localization and clustering of turbulent vortices open up large regions in the domain with little turbulent activity. This is consistent with the higher fraction of hibernating

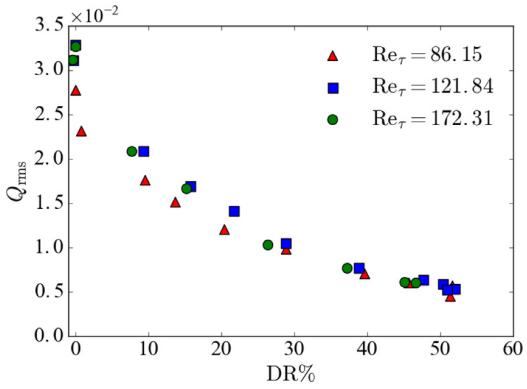

Fig. 17. The root-mean-square of Q with varying DR%.

turbulence at high Wi reported in Xi and Graham [27]. On the other hand, in theory one may as well increase the hibernation fraction without relying on turbulence localization: i.e., by enlarging the hibernating spots evenly across the domain. Indeed, turbulence localization requires the cooperation of coherent structures (shown in Section 3.2.3) over longer length scales not captured in MFUs (from which the active-hibernating framework was first proposed). The nature of this cooperation is the focus of Section 3.3, which is also central to the understanding of HDR.

On the surface, associating HDR with a higher fraction of hibernating regions offers a straightforward explanation for the different flow statistics at HDR. To see this, we need to first make two hypotheses: (1) after the DR onset, polymers suppress buffer-layer structures in active turbulence, which causes DR there but leaves the log-law layer flow statistics largely unaffected and (2) after the LDR–HDR transition, hibernating turbulence becomes statistically significant. Since the mean velocity profile in hibernating turbulence is known to have a much higher slope, not only in the buffer layer but across the channel, its higher fraction will naturally lead to higher log-law layer slope in the time-average profile. To test this, we first divide the domain along the xz plane according to the comparison between the local y-averaged $|Q|$ magnitude

$$\overline{|Q|}_y = \frac{1}{\mathrm{Re}_\tau}\int_0^{\mathrm{Re}_\tau} |Q| dy^+ \tag{18}$$

and a cutoff value Q_{cutoff}: regions with $\overline{|Q|}_y > Q_{\mathrm{cutoff}}$ are considered active and those with $\overline{|Q|}_y \le Q_{\mathrm{cutoff}}$ hibernating. Conditional average mean velocity profiles of these two groups, using two drastically different values of $Q_{\mathrm{cutoff}} = 0.2Q_{\mathrm{rms}}$ and $2Q_{\mathrm{rms}}$, are shown in Fig. 18. Contrary to the first hypothesis above, even for active regions, the mean velocity profile in the log-law layer has clearly risen up, showing much higher slopes than the PvK log law. This result indicates that the binary division into active and hibernating regions while neglecting any correlations between them is too simplified to explain the phenomenology of HDR.

3.2.3. Percolation analysis

A simple extension of the active-hibernating framework from MFU to an extended domain would imply that there is no difference in vortex topology within the active regions between LDR and HDR: at high Wi, polymers only quench the turbulent activity in parts of the domain (hibernating regions) while vortex dynamics in the rest (active regions) are generated from the same instability as in Newtonian turbulence [7,27]. Here, however, using the percolation analysis proposed by Lozano-Durán et al. [52], we discover a fundamental shift in the vortex topology that accompanies the localization of turbulence.

Recall the Q-criterion used in Fig. 14, the choice of the threshold value of Q for vortex identification is largely arbitrary. The resulting vortex configuration clearly depends on this choice: as $Q_{\mathrm{threshold}}$ increases, fewer and fewer regions satisfy the criterion, resulting in fewer and smaller vortices being identified. Vortex configuration with the increasing threshold magnitude, measured by the non-dimensional H parameter defined with

$$Q_{\mathrm{threshold}} \equiv HQ_{\mathrm{rms}}, \tag{19}$$

is shown in Fig. 19. For each H, interconnected vortices are considered to form a vortex cluster and coded with the same color in Fig. 19. (Vortices are determined to be connected when at least two grid points, one from each isosurface, are immediately adjacent to each other.) Identified clusters are then ranked according to their volumes and only larger clusters that accumulatively account for 80% of the total vortex volume in the domain are shown (for the $H = 0.5$ image of the Newtonian case the cutoff is 60%). This is to eliminate the large number of small vortex fragments to clear the view.

In Newtonian turbulence (Fig. 19(a)), at $H = 0.2$, the threshold is lower than even the Q magnitude of the weak rotational motion between vortex cores. These regions form “tunnels” that connect the main vortex bodies, resulting in an interconnected network that percolates the domain. As H increases to 0.4 and 0.5, the “tunnels” quickly break and the percolating network decomposes into separate vortex clusters, marked by different colors. This process is quantified by the ratio of the volume of the largest vortex cluster V_{max} to the total volume of all vortices identified V_{tot} and plotted in Fig. 20. As shown in Fig. 19(a), at the lowest H all vortices belong to the same cluster and therefore $V_{\mathrm{max}}/V_{\mathrm{tot}} = 1$. For the Newtonian case, raising H to around 0.5 triggers a quick collapse of the percolating network into much smaller clusters. Accordingly, $V_{\mathrm{max}}/V_{\mathrm{tot}}$ drops sharply since now even the largest cluster is only a small fraction of the total volume. The ratio stays almost constant as H increases beyond 1, indicating that individual clusters shrink in size proportionally while keeping the volume ratio between themselves. Lozano-Durán et al. [52] suggested that the proper threshold for vortex identification should fall within the transition between percolating and non-percolating behaviors. Our choice of $H = 0.7$ used in Fig. 14 is within this range.

The $V_{\mathrm{max}}/V_{\mathrm{tot}}$ curve for LDR is nearly identical to the Newtonian case. At HDR, the transition period still centers around $H \sim 0.5$ but the decline of $V_{\mathrm{max}}/V_{\mathrm{tot}}$ is smoother and the transition extends over a larger range of H. At the highest Wi shown in Fig. 20 – i.e., 96, the transition starts at H well below 0.1. This indicates that the percolation disintegration evolves into a continuous process. The corresponding vortex configuration is shown in Fig. 19(b). At H as low as 0.2, a clear vortex cluster dominates the domain and no vortical structures are found in the laminar-like (hibernating) regions, reaffirming the true localization of turbulence. As H increases, no sudden disintegration is observed, indicating that the vortices in the cluster are closely connected with strong mutual interaction. The $V_{\mathrm{max}}/V_{\mathrm{tot}}$ ratio only decreases smoothly because the tips of the “tentacles”of the cluster are gradually etched away with higher H. Disintegration of the cluster is not observed until H is close to $O(1)$ and even there the process is progressive with new vortices being shed off with each increment of H. The large H magnitude required to break the cluster and the stepwise nature of its disintegration show that the interaction between vortices in the same cluster is stronger than the “tunnels” between clusters observed in the Newtonian case. All in all, the percolation analysis reveals that the vortex dynamics at HDR becomes qualitatively changed where vortices are generated and sustained in large clusters with strong mutual interactions, whereas at LDR the process appears more stochastic. This difference leads to the apparent turbulence localization.

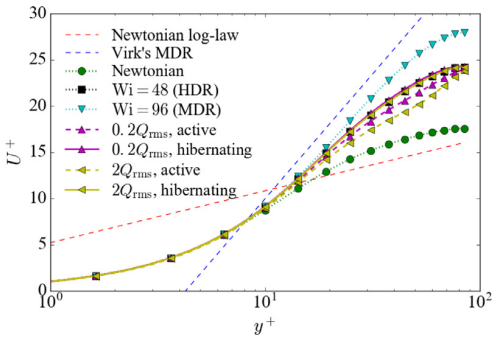

Fig. 18. Conditional average mean velocity profiles of active and hibernating regions at $\mathrm{Re}_\tau = 86.15$ and Wi = 48. Results from two different cutoff magnitudes Q_{cutoff} are shown in comparison with the time-average Newtonian and Wi = 48 profiles.

3.3. Proposed mechanism

We have so far demonstrated that the LDR–HDR transition is not simply a quantitative effect of the level of DR, but a qualitative transition likely involving two different stages of DR mechanisms. The

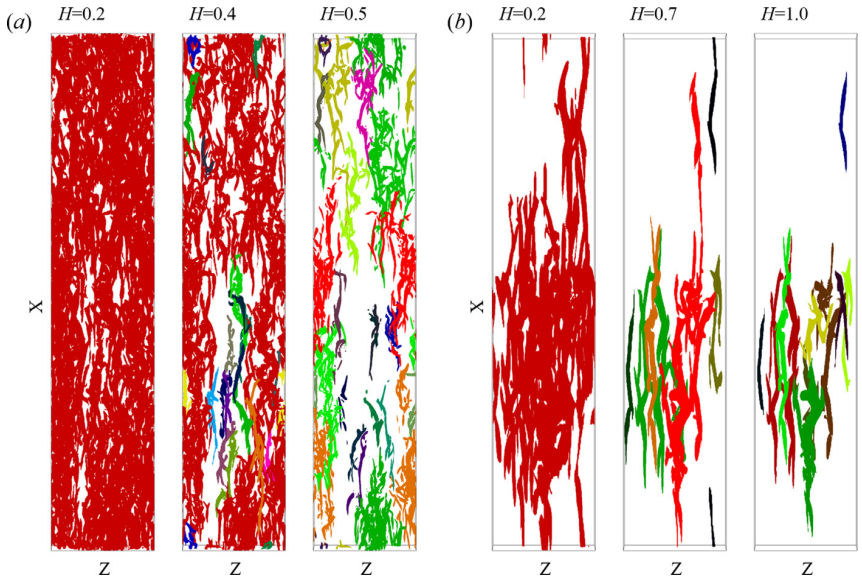

Fig. 19. Vortex decomposition with increasing H (normalized threshold Q value for vortex identification; see Eq. (19)) in the percolation analysis: (*a*) Newtonian, $Re_\tau = 86.15$ and (*b*) Wi = 96, $Re_\tau = 86.15$. Each interconnected vortex cluster is coded with the same color.

transition is associated with a range of qualitative changes in flow statistics, behind which turbulent activities are found to become localized. Although the first mechanism of DR, which sets its onset, is well understood as a generic across-the-board weakening and suppression of turbulent fluctuations [13,19], the nature of the second mechanism, which drives the LDR–HDR transition, is unknown. Here, we make the first attempt at its mechanistic understanding by proposing a possible mechanism that is compatible with currently known observations.

We start our discussion by revisiting the self-sustaining dynamics of Newtonian turbulence. Schoppa and Hussain [53] summarized the vortex regeneration mechanisms proposed in the literature into two major categories (Fig. 21). The first is what we will refer to as the "streak-instability mechanism". Upward ejection of near-wall fluid by streamwise vortices forms low-speed streaks. A strictly x-independent streak is stable but as the streak intensifies (i.e., larger contrast between low- and high-speed streaks), it becomes increasingly susceptible to x-dependent perturbations, which leads to the so-called streak breakdown and the generation of streamwise vortices. This process is not only important for understanding the self-sustaining process of near-wall turbulence [54], streak breakdown is also a central step in the laminar-turbulent transition [55,56]. In the second so-called "parent-offspring mechanism", a "parent" vortex lifts up at its head and instability of the shear layer between the vortex and the wall gives rise to a new "offspring" vortex. In this scenario, the new vortex is generated immediately next to its parent, implying strong correlation and spatial proximity between them. On the other hand, although the streak-instability mechanism does not require any immediate parent vortex, existing vortices still influence the generation of new ones. For example, the bursting of existing vortices generates perturbations that can destabilize streaks elsewhere in the domain. Obviously, this link between existing and new vortices is indirect and not necessarily local, compared with the parent-offspring mechanism. Finally, we note that this binary categorization is simplistic and there are a number of different mechanisms within either category. But it suffices for our discussion on the vortex dynamics leading up to HDR.

Both mechanisms are observed in our DNS. In Fig. 22, we pick and show one typical scenario for each case. Fig. 22(a) shows a typical life cycle of a hairpin vortex following the streak-instability mechanism, which is found in Newtonian turbulence. At $T = 0$, a small tentacle-like vortex lifts up from a packet of streamwise vortices and connects with a neighboring one at $T = 8$ to form a hairpin vortex (Vortex A). As this vortex pair evolves from an initial parallel configuration to a three-dimensional hairpin, the low-speed streak sandwiched between them (not shown) twists with the instability. The hairpin grows from a C-shaped arch ($T = 8$) to a Ω -shaped structure with its head lifting up towards the bulk of the flow ($T = 36$). At $T = 40$, the arch bursts and disappears from the view, with only one leg left behind at $T = 48$. Although difficult to show here in an extended turbulent domain, in our

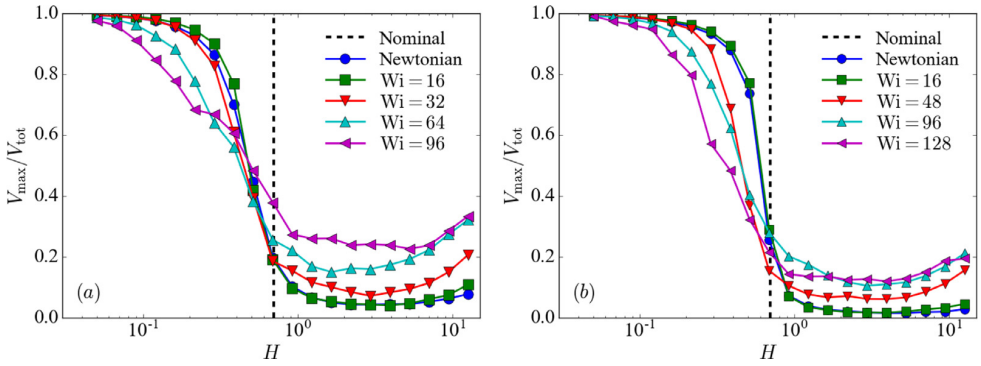

Fig. 20. Percolation diagrams: (*a*) $Re_\tau = 86.15$ (*b*) $Re_\tau = 121.84$. Vertical dashed lines mark the $Q_{threshold} = 0.7Q_{rms}$ used in Fig. 14.

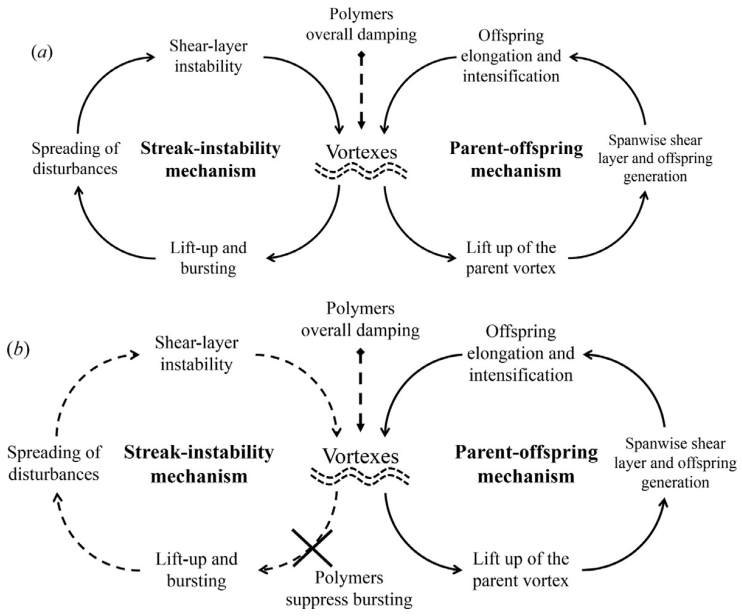

Fig. 21. Vortex regeneration mechanism and polymer effects thereon in (a) LDR and (b) HDR.

recent study [57] where the vortex growth and bursting process were tracked in an MFU, it was observed that the bursting of coherent vortices generates strong small-scale fluctuations that quickly propagate across the MFU. Borrowing that knowledge, we may postulate that the bursting event at $T = 40$ gives rise to small-scale fluctuations that can spread and trigger instabilities in other streaks, thus completing the vortex regeneration cycle.

The self-sustaining process of Newtonian turbulence includes both streak-instability and parent-offspring mechanisms. These two processes offer two parallel pathways whereby the vortex dynamics can be continuously regenerated. Our simulations show that the situation changes at high Wi where the streak-instability process is rare and the parent-offspring pathway becomes exposed. A typical scenario is shown in Fig. 22(b). Compared with the Newtonian case, much fewer hairpin vortices are observed at high Wi, which was also reported by Yarin [58] and was further supported by Kim et al. [59] through their dynamical simulations of counter-rotating pairs of quasistreamwise vortices. These streamwise vortices often align head-to-tail to form a string ($T = 0$), which was also observed by Li et al. [13,60] at higher Re. In the vortex string, new vortices are often generated at the upstream end of their parents (e.g., the births of vortices 4 and 5 at $T = 16$ and 32), effectively extending the string against the oncoming flow. Interestingly, this order of vortex generation – i.e., from downstream to upstream, is opposite to the typical observation reported in Newtonian turbulence, where the offspring is more likely to be generated at the downstream side of the parent [61], although the reversed order was also occasionally observed in the Newtonian case [62]. In addition to suppressing the formation of hairpins, vortex lift-up or eruption and its subsequent bursting are also prevented. Overall, streamwise vortices are stabilized by the high polymer elasticity, allowing them to extend to much longer length scales (see Figs. 13, 14 and also refer to [59,63,64]). Not able to burst, the vortices eventually decay and disappear (vortices 1 & 2 at $T = 64$). This again is consistent with observations made in Bai and Xi [57] that polymers are able to help the flow bypass the bursting of vortices and avoid small-scale fluctuations. Here, instead of bursting, we only observed a mild and temporary swelling and proliferation of vortices at $T = 64$. This regeneration dynamics, that vortices are more often generated as an offspring of a nearby parent, explains perfectly why vortical structures are more localized at high Wi and why vortices within the same clusters are strongly correlated (see Fig. 19). In addition, the suppression of hairpins and their lift-up and eruption at larger y^+ can also explain the suppressed Reynolds shear stress in the log-law layer. And since bursting is bypassed, intense small-scale fluctuations are avoided, which is consistent with the larger proportion of energy

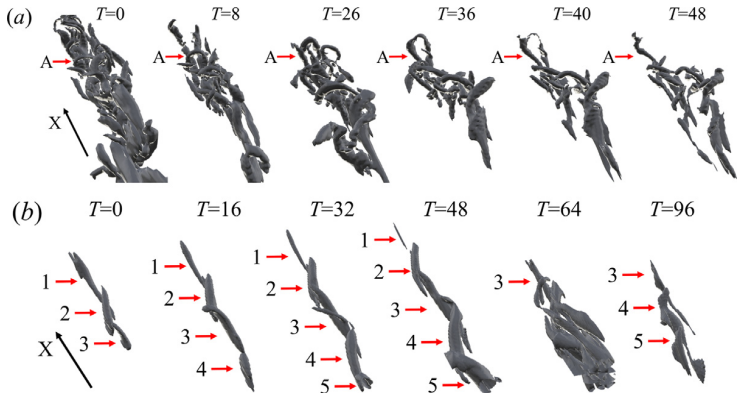

Fig. 22. Typical vortex evolution scenarios observed in our DNS at $Re_\tau = 86.15$: (a) streak-instability mechanism (Newtonian) and (b) parent offspring mechanism (Wi = 96).

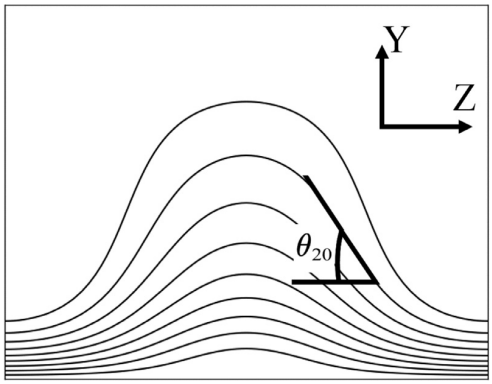

Fig. 23. Schematic of the definition of the streak lift angle measured at $y^+ = 20$: θ_{20}. Solid lines represent the contour of streamwise velocity.

accumulating in large scale structures in the log-law layer (Fig. 10).

After the direct comparison between the vortex regeneration dynamics of a Newtonian and high-Wi cases, we now need to show that the suppression of the streak-instability pathway does indeed correlate with the LDR–HDR transition. According to [53], the relative stability of a streak is determined by its "strength", which is basically described by how much the base flow has been distorted by the upward ejection of the low-speed streak, which creates spanwise variation or contrast in v_x. As sketched in Fig. 23, the strength is quantified locally by the streak lift angle

$$\theta \equiv \arctan\left(\frac{|\omega_y|}{|\omega_z|}\right) \tag{20}$$

where ω_y and ω_z are the wall-normal and spanwise components of the local vorticity. The stability of low-speed streaks is measured by their characteristic lift angle

$$\theta_c \equiv \max(\theta_{20}) \tag{21}$$

at the $y^+ = 20$ plane. Here, regions with $v_x' \leq 0$ are first identified as the low-speed streak regions; local maxima along the x direction that fall into these regions are collected into the sample pool of θ_c.

Fig. 24 shows the probability density functions (PDFs) of the characteristic streak lift angles θ_c collected in each simulation. The solid black line is the average angle. The decrease of the average angle with increasing of Wi shows the weakening of the streak lift-up "strength", which indicates higher streak stability and less probability for vortex generation by streak instability. In addition, the shape of the distribution changes drastically from LDR to HDR. Before the LDR–HDR transition, the distribution is highly skewed with only one sharp peak located in the range of 80 and 90 degrees. As Wi increases, the distribution of θ_c starts to spread towards the side of lower θ_c. At HDR, the distribution becomes nearly even for a wide range of θ_c with no distinct peak at the high θ_c end. The mean and skewness of the distribution are plotted in Fig. 25 against DR% and it is clear that both metrics change sharply at the LDR–HDR transition (DR% ≈ 20%) (The turn of trend in skewness is not as clear only at the lowest Re but it becomes sharp at higher ones). Note that a streak is considered unstable at $\theta_c > 50$ for sinuous streak instability [53]. The sharp change in the distribution at the beginning of HDR indicates a drastic decrease in the number of streaks eligible for instability, which supports the mechanism we propose: HDR is a stage where the streak-instability pathway for vortex regeneration is greatly suppressed, exposing the parent-offspring mechanism as the main pathway (Fig. 21(b)). Since the latter is known to maintain the clustering and close interaction between vortices, this mechanism consistently explains the observed turbulence localization.

4. Conclusions

In this study, DNS simulation of viscoelastic turbulent channel flow is performed for a large number of parameter combinations at a moderate-Re regime not far above Re_{crit}. The landscape of the Re – Wi parameter space is explored (Fig. 5), including the whole range of transitions in DR behaviors. In particular, we focus on the LDR–HDR transition, which occurs between the DR onset and MDR. Literature in the area often attributes the transition to a quantitative effect of the DR %. However, we show that it is indeed a qualitative transition of different turbulent dynamics.

Changes in flow statistics are first investigated and the major features of HDR (compared with LDR) are summarized as follows.

- The mean velocity profile deviates from the PvK log law behavior in the log-law layer (Fig. 6).
- The Reynolds shear stress is suppressed not only in the buffer layer, but across the whole channel (except the viscous sublayer) (Fig. 7).
- As the Reynolds shear stress becomes suppressed in the log-law layer, viscous and polymer shear stresses increases (Fig. 9; in LDR, these changes only occur in the buffer layer).
- The energy spectrum in the log-law layer becomes qualitatively changed in the log-law layer, with a sudden increase in the energy accumulated in large scales (Figs. 10 and 11).

In summary, unlike at LDR where most DR effects are contained in the buffer layer, at HDR these effects extend to the log-law layer. Behind these apparent changes in flow statistics, the turbulent structure has also changed fundamentally. At LDR, turbulent vortices homogeneously spread across the domain, but at HDR they cluster into strongly interacting groups. Turbulence becomes localized, leaving the regions outside these vortex clusters laminar-like. Percolation analysis reveals a fundamentally changed vortex topology at HDR (Fig. 20).

These changes indicate that DR goes through two distinct stages with different mechanisms. The first starts at the onset of DR, where the coil-stretch transition of polymers starts a generic inhibition of all turbulent fluctuations. The second mechanism is triggered at the LDR–HDR transition and its origin is unknown, for which a mechanism is proposed. In Newtonian turbulence, vortex regeneration cycles include two parallel pathways. The streak-instability pathway generates new vortices by perturbing streamwise low-speed streaks and the growth and lift-up of these vortices eventually lead to their bursting, which generates small-scale fluctuates that can destabilize another streak. This process is intrinsically non-local, as the perturbations can spread quickly to other parts of the domain, and the bursting events can feed the turbulence in the log-law layer. The parent-offspring pathway generates new vortices immediately next to an existing one. The vortices are thus clustered and interact strongly with one another. Polymers, for its capability of suppressing bursting and stabilizing streamwise vortices, are able to substantially block the first pathway, leaving the parent-offspring pathway the main mechanism of turbulence self-sustenance at HDR. The proposed mechanism offers a consistent explanation for the changes in flow statistics at the LDR–HDR transition and the localization of turbulence. Quantitative analysis of streak stability shows that after the LDR–HDR transition, much fewer streaks are susceptible to instability, which supports the mechanism.

Admittedly, the binary categorization of vortex regeneration mechanisms is simplistic and, more importantly, there still lacks sufficient direct evidence for the proposed mechanism. The nature of HDR is far from being a solved problem. For future work, we will further test this hypothesis by systematically investigating the polymer effects on the vortex regeneration process. This is difficult to achieve using DNS in statistically steady turbulence (as in this study), where the chaotic dynamics makes any direct comparison of vortex dynamics nearly impossible. Transient processes must be carefully constructed to simulate the vortex generation and growth dynamics. Results from different Wi

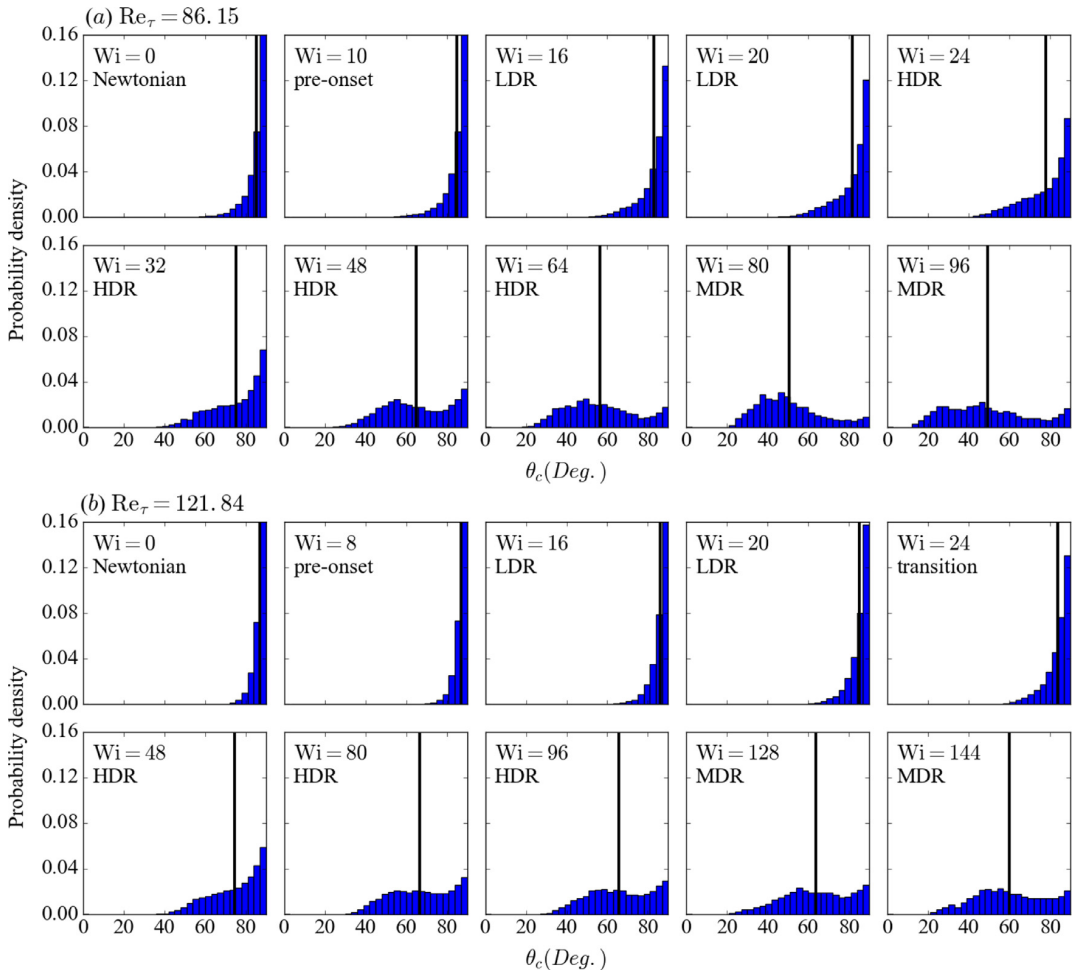

Fig. 24. Probability density functions of the characteristic streak lift angle at (*a*) Re_τ = 86.15 and (*b*) Re_τ = 121.84. Vertical lines mark the mean value of each distribution.

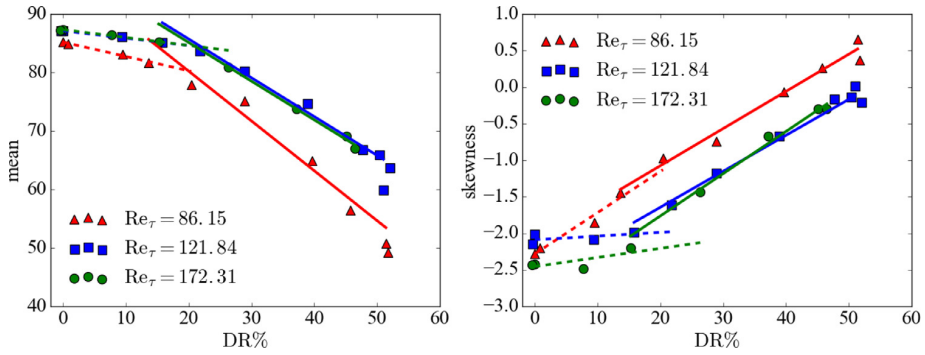

Fig. 25. The mean and skewness of the θ_c distribution for all three Re_τ. The dashed and solid lines are the linear regression outcomes of the LDR and HDR stages, respectively.

can then be systematically compared for complete understanding. In the case of streak breakdown, examples of such transient processes can be borrowed from the existing literature on the Newtonian bypass transition [56]. In particular, recent work by Brandt and de Lange [65] offers a neat example of creating different vortex configurations from controlled collisions between streaks. In addition, conditional sampling also offers a convenient way of generating hairpin vortices [66].

Acknowledgment

The financial support for this work primarily comes from the Natural Sciences and Engineering Research Council of Canada (NSERC) through its Discovery Grants Program (No. RGPIN-2014-04903). All computation was performed on the facilities of the Shared Hierarchical Academic Research Computing Network (SHARCNET: www.sharcnet.ca) under the computing resources allocation awarded by Compute/

Calcul Canada. TMS acknowledges the Swiss National Science Foundation (Grant No. 200021-160088). Both TMS and LX acknowledge the National Science Foundation Grant No. NSF PHY11-25915, which partially supported their stays at the Kavli Institute for Theoretical Physics (KITP) at UC Santa Barbara. The authors thank Tobias Kreilos for his help with our code development.

References

[1] P.S. Virk, Drag reduction fundamentals, AIChE J. 21 (4) (1975) 625–656.
[2] C.M. White, M.G. Mungal, Mechanics and prediction of turbulent drag reduction with polymer additives, Annu. Rev. Fluid Mech. 40 (2008) 235–256.
[3] M.D. Graham, Drag reduction and the dynamics of turbulence in simple and complex fluids, Phys. Fluids 26 (2014) 101301, http://dx.doi.org/10.1063/1.4895780.
[4] J. Kim, P. Moin, R. Moser, Turbulence statistics in fully-developed channel flow at low Reynolds-number, J. Fluid Mech. 177 (1987) 133–166.
[5] K.D. Housiadas, A.N. Beris, Polymer-induced drag reduction: effects of variations in elasticity and inertia in turbulent viscoelastic channel flow, Phys. Fluids 15 (2003) 2369–2384.
[6] W. Li, L. Xi, M.D. Graham, Nonlinear travelling waves as a framework for understanding turbulent drag reduction, J. Fluid Mech. 565 (2006) 353–362.
[7] L. Xi, M.D. Graham, Turbulent drag reduction and multistage transitions in viscoelastic minimal flow units, J. Fluid Mech. 647 (2010) 421–452, http://dx.doi.org/10.1017/S0022112010000066.
[8] C.F. Li, R. Sureshkumar, B. Khomami, Simple framework for understanding the universality of the maximum drag reduction asymptote in turbulent flow of polymer solutions, Phys. Rev. E 92 (2015) 043014, http://dx.doi.org/10.1103/PhysRevE.92.043014.
[9] S.B. Pope, Turbulent Flows, Cambridge University Press, Cambridge, United Kingdom, 2000.
[10] M.D. Warholic, H. Massah, T.J. Hanratty, Influence of drag-reducing polymers on turbulence: effects of reynolds number, concentration and mixing, Exp. Fluids 27 (5) (1999) 461–472.
[11] P.K. Ptasinski, B.J. Boersma, F.T.M. Nieuwstadt, M.A. Hulsen, B.H.A.A.V. den Brule, J.C.R. Hunt, Turbulent channel flow near maximum drag reduction: simulations, experiments and mechanisms, J. Fluid Mech. 490 (2003) 251–291.
[12] T. Min, H. Choi, J.Y. Yoo, Maximum drag reduction in a turbulent channel flow by polymer additives, J. Fluid Mech. 492 (2003) 91–100.
[13] C.F. Li, R. Sureshkumar, B. Khomami, Influence of rheological parameters on polymer induced turbulent drag reduction, J. Non-Newton. Fluid Mech. 140 (1) (2006) 23–40.
[14] C.M. White, Y. Dubief, J. Klewicki, Re-examining the logarithmic dependence of the mean velocity distribution in polymer drag reduced wall-bounded flow, Phys. Fluids 24 (2) (2012) 021701.
[15] B.-Q. Deng, W.-X. Huang, C.-X. Xu, Origin of effectiveness degradation in active drag reduction control of turbulent channel flow at Re_τ = 1000, J. Turbul. 17 (2016) 758–786, http://dx.doi.org/10.1080/14685248.2016.1181266.
[16] J.L. Lumley, Drag reduction by additives, Annu. Rev. Fluid Mech. 1 (1969) 367–384, http://dx.doi.org/10.1146/annurev.fl.01.010169.002055.
[17] P.G. De Gennes, Introduction to Polymer Dynamics, Cambridge University Press, Cambridge, United Kindom, 1990.
[18] E. De Angelis, C.M. Casciola, R. Piva, DNS of wall turbulence: dilute polymers and self-sustaining mechanisms, Comput. Fluids 31 (2002) 495–507.
[19] Y. Dubief, V.E. Terrapon, C.M. White, P.M. E. S. Shaqfeh, S.K. Lele, New answers on the interaction between polymers and vortices in turbulent flows, Flow Turbul. Combust. 74 (4) (2005) 311–329.
[20] W. Li, M.D. Graham, Polymer induced drag reduction in exact coherent structures of plane Poiseuille flow, Phys. Fluids 19 (2007) 083101.
[21] K. Kim, C.F. Li, R. Sureshkumar, S. Balachandar, R.J. Adrian, Effects of polymer stresses on eddy structures in drag-reduced turbulent channel flow, J. Fluid Mech. 584 (2007) 281–299, http://dx.doi.org/10.1017/S0022112007006611.
[22] L. Xi, M.D. Graham, Active and hibernating turbulence in minimal channel flow of Newtonian and polymeric fluids, Phys. Rev. Lett. 104 (2010) 218301, http://dx.doi.org/10.1103/PhysRevLett.104.218301.
[23] R.D. Whalley, J.S. Park, A. Kushwaha, D.J.C. Dennis, M.D. Graham, R.J. Poole, Low-drag events in transitional wall-bounded turbulence, Phys. Rev. Fluids 2 (2017) 034602, http://dx.doi.org/10.1103/PhysRevFluids.2.034602.
[24] L. Xi, M.D. Graham, Dynamics on the laminar-turbulent boundary and the origin of the maximum drag reduction asymptote, Phys. Rev. Lett. 108 (2) (2012) 028301.
[25] L. Xi, X. Bai, Marginal turbulent state of viscoelastic fluids: A polymer drag reduction perspective, Phys. Rev. E 93 (2016), http://dx.doi.org/10.1103/PhysRevE.93.043118.
[26] S.N. Wang, A. Shekarn, M.D. Graham, Spatiotemporal dynamics of viscoelastic turbulence in transitional channel flow, J. Non-Newton. Fluid Mech. (2017).
[27] L. Xi, M.D. Graham, Intermittent dynamics of turbulence hibernation in newtonian and viscoelastic minimal channel flows, J. Fluid Mech. 693 (2012) 433–472.
[28] R. Sureshkumar, A.N. Beris, R.A. Handler, Direct numerical simulation of the turbulent channel flow of a polymer solution, Phys. Fluids 9 (3) (1997) 743–755.
[29] R.B. Bird, O. Hassager, R.C. Armstrong, C.F. Crurtis, Dynamics of Polymeric Liquids. Vol. 2 Kinetic Theory, John Wiley and Sons Inc., New York, NY, 1987.
[30] R. Peyret, Spectral methods for incompressible viscous flow, Springer, New York, 2002.
[31] R. Sureshkumar, A.N. Beris, Effect of artificial stress diffusivity on the stability of numerical calculations and the flow dynamics of time-dependent viscoelastic flows, J. Non-Newton. Fluid Mech. 60 (1995) 53–80, http://dx.doi.org/10.1016/0377-0257(95)01377-8.
[32] C.D. Dimitropoulos, R. Sureshkumar, A.N. Beris, Direct numerical simulation of viscoelastic turbulent channel flow exhibiting drag reduction: effect of the variation of rheological parameters, J. Non-Newton. Fluid Mech. 79 (1998) 433–468.
[33] J.F. Gibson, Channelflow: a spectral navierstokes simulator in c+ +, Tech.Rep. U. New Hampshire, 2014 Channelflow.org.
[34] L.S. Tuckerman, T. Kreilos, H. Schrobsdorff, T.M. Schneider, J.F. Gibson, Turbulent-laminar patterns in plane Poiseuille flow, Phys. Fluids 26 (2014), http://dx.doi.org/10.1063/1.4900874.
[35] M. Nishioka, M. Asai, Some observations of the subcritical transition in plane poiseuille flow, J. Fluid Mech. 150 (1985) 441–450.
[36] G. Samanta, K.D. Housiadas, R.A. Handler, A.N. Beris, Effects of viscoelasticity on the probability density functions in turbulent channel flow, Phys. Fluids 21 (2009) 115106.
[37] K.D. Housiadas, A.N. Beris, On the skin friction coefficient in viscoelastic wall-bounded flows, Int. J. Heat Fluid Flow 42 (2013) 49–67.
[38] B.E. Owolabi, D.J.C. Dennis, R.J. Poole, Turbulent drag reduction by polymer additives in parallel-shear flows, J. Fluid Mech. 453 (2017) 57–108.
[39] T. Wei, W.W. Willmarth, Reynolds-number effects on the structure of a turbulent channel flow, J. Fluid Mech. 204 (1989) 57–95.
[40] H. Kawamura, H. Abe, Y. Matsuo, Dns of turbulent heat transfer in channel flow with respect to Reynolds and Prandtl number effects, Int. J. Heat Fluid Flow 20 (3) (1999) 196–207.
[41] K.D. Housiadas, A.N. Beris, Polymer-induced drag reduction: effects of the variations in elasticity and inertia in turbulent viscoelastic channel flow, Phys. Fluids 15 (8) (2003) 2369–2384.
[42] E. De Angelis, C.M. Casciola, V.S. L'vov, R. Piva, I. Procaccia, Drag reduction by polymers in turbulent channel flows: energy redistribution between invariant empirical modes, Phys. Rev. E 67 (2003) 056312.
[43] K.D. Housiadas, A.N. Beris, R.A. Handler, Viscoelastic effects on higher order statistics and on coherent structures in turbulent channel flow, Phys. Fluids 17 (2005) 035106.
[44] S.K. Robinson, Coherent motions in the turbulent boundary layer, Annu. Rev. Fluid Mech. 23 (1) (1991) 601–639.
[45] M.D. Warholic, D.K. Heist, M. Katcher, T.J. Hanratty, A study with particles image velocimetry of the influence of drag-reducing polymers on the structure of turbulence, Exp. Fluids 31 (2001) 474–483.
[46] C.M. White, V.S.R. Somandepalli, M.G. Mungal, The turbulence structure of drag-reduced boundary layer flow, Exp. Fluids 36 (2004) 62–69.
[47] J. Jeong, F. Hussain, On the identification of a vortex, J. Fluid Mech. 285 (1995) 69–94.
[48] Y. Dubief, F. Delcayre, On coherent-vortex identification in turbulence, J. Turbul. 1 (2000) 1–22.
[49] J. Zhou, R.J. Adrian, S. Balachandar, T.M. Kendall, Mechanisms for generating coherent packets of hairpin vortices in channel flow, J. Fluid Mech. 387 (1999) 353–396.
[50] R.J. Adrian, Hairpin vortex organization in wall turbulence a, Phys. Fluids 19 (4) (2007) 041301.
[51] B.N. Boots, A. Getis, Point Pattern Analysis, 8 Sage Publications, Inc, 1988.
[52] A. Lozano-Durán, O. Flores, J. Jiménez, The three-dimensional structure of momentum transfer in turbulent channels, J. Fluid Mech. 694 (2012) 100–130.
[53] W. Schoppa, F. Hussain, Coherent structure generation in near-wall turbulence, J. Fluid Mech. 453 (2002) 57–108.
[54] J.M. Hamilton, J. Kim, F. Waleffe, Regeneration mechanisms of near-wall turbulence structures, J. Fluid Mech. 287 (1995) 317–348.
[55] L. Brandt, D.S. Henningson, Transition of streamwise streaks in zero-pressure-gradient boundary layers, J. Fluid Mech. 472 (2002) 229–261, http://dx.doi.org/10.1017/S0022112002002331.
[56] P. Schlatter, L. Brandt, H.C. de lange, D.S. Henningson, On streak breakdown in bypass transition, Phys. Fluids 20 (2008) 101505, http://dx.doi.org/10.1063/1.3005836.
[57] X. Bai, E. Krushelnycky, L. Zhu and L. Xi, Effects of drag-reducing polymers on turbulence growth and bursting in a near minimal channel (2018). Submitted for Publication.
[58] A.L. Yarin, On the mechanism of turbulent drag reduction in dilute polymer solutions: dynamics of vortex filaments, J. Non-Newton. Fluid Mech. 69 (2-3) (1997) 137–153.
[59] K. Kim, R.J. Adrian, S. Balachandar, R. Sureshkumar, Dynamics of hairpin vortices and polymer-induced turbulent drag reduction, Phys. Rev. Lett. 100 (13) (2008) 134504.
[60] K. Kim, C.F. Li, R. Sureshkumar, S. Balachandar, R.J. Adrian, Effects of polymer stresses on eddy structures in drag-reduced turbulent channel flow, J. Fluid Mech. 584 (2007) 281–299.
[61] J.W. Brooke, T.J. Hanratty, Origin of turbulence-producing eddies in a channel flow, Phys. Fluids A-Fluid 5 (4) (1993) 1011–1022.
[62] Y. Miyake, R. Ushiro, T. Morikawa, The regeneration of quasi-streamwise vortices in the near-wall region, JSME Int. J. Series B Fluids Thermal Eng. 40 (2) (1997) 257–264.
[63] M.D. Graham, Drag reduction in turbulent flow of polymer solutions, Rheol. Rev. 2 (2) (2004) 143–170.
[64] C.F. Li, R. Sureshkumar, B. Khomami, Simple framework for understanding the universality of the maximum drag reduction asymptote in turbulent flow of polymer solutions, Phys. Rev. E 92 (4) (2015) 043014.
[65] L. Brandt, H.C. de Lange, Streak interactions and breakdown in boundary layer flows, Phys. Fluids 20 (2008) 024107, http://dx.doi.org/10.1063/1.2838594.
[66] K. Kim, R.J. Adrian, S. Balachandar, R. Sureshkumar, Dynamics of hairpin vortices and polymer-induced turbulent drag reduction, Phys. Rev. Lett. 100 (2008) 134504, http://dx.doi.org/10.1103/PhysRevLett.100.134504.

Chapter 3

VATIP: tracking three-dimensional vortices in turbulence

Vortices are essential for the understanding of turbulent dynamics. In polymeric turbulence, vortical structures are significantly modified by polymers, which are strongly related to the qualitative transitions between intermediate flow stages. Studying the modification of vortices is thus important for the understanding of the drag reduction phenomenon. However, most of the available vortex identification criteria in the literature only label spatial regions belonging to vortices, without any information on the identity, topology, and shape of individual vortices. To quantitative analyze those vortical structures in the polymeric turbulence, we developed a new tracking algorithm – VATIP (vortex axis tracking by iterative propagation) – which propagates along the vortex axis lines and iteratively searches for new directions for growth. Based on the new tracking scheme, we also proposed a procedure to classify vortices into commonly observed shapes.

The VATIP algorithm enables the statistical analysis of vortex configurations in

turbulence and offers a pathway to discuss the self-sustaining of turbulence. However, as one early attempt, it is restricted to moderate Re wall-bound turbulence (the focus of this dissertation) that is dominated by vortices with streamwise aligned legs and roughly constant diameter. The improvement of VATIP to adapt to more general vortex configurations, such as reverse hairpin (Wu *et al.*, 2015) and concentrated hairpin packet with random filaments (Wu *et al.*, 2017) that appear in high Re flows, will be discussed in the future.

I was responsible for developing the VATIP scheme and testing it in DNS results. I also collected and post-processed data with Dr. Li Xi's suggestions. The draft was written by me and revised by Dr. Li Xi.

This chapter is reprinted with permission from L. Zhu and L. Xi. (2018). Vortex axis tracking by iterative propagation (VATIP): A method for analysing three-dimensional turbulent structures. *J. Fluid Mech.*, **866**, 169-215 (DOI:10.1017/jfm.2019.75).

J. Fluid Mech. (2019), *vol.* 866, *pp.* 169–215.
doi:10.1017/jfm.2019.75

Vortex axis tracking by iterative propagation (VATIP): a method for analysing three-dimensional turbulent structures

Lu Zhu[1] **and Li Xi**[1,2,†]

[1]Department of Chemical Engineering, McMaster University, Hamilton, Ontario L8S 4L7, Canada

[2]Kavli Institute for Theoretical Physics (KITP), University of California, Santa Barbara, CA 93106-4030, USA

(Received 15 May 2018; revised 23 November 2018; accepted 21 January 2019; first published online 4 March 2019)

Vortex is a central concept in the understanding of turbulent dynamics. Objective algorithms for the detection and extraction of vortex structures can facilitate the physical understanding of turbulence regeneration dynamics by enabling automated and quantitative analyses of these structures. Despite the wide availability of vortex identification criteria, they only label spatial regions belonging to vortices, without any information on the identity, topology and shape of individual vortices. This latter information is stored in the axis lines lining the contours of vortex tubes. In this study, a new tracking algorithm is proposed which propagates along the vortex axis lines and iteratively searches for new directions for growth. The method is validated in flow fields from transient simulations where vortices of different shapes are controllably generated. It is then applied to statistical turbulence for the analysis of vortex configurations and distributions. It is shown to reliably extract axis lines for complex three-dimensional vortices generated from the walls. A new procedure is also proposed that classifies vortices into commonly observed shapes, including quasi-streamwise vortices, hairpins, hooks and branches, based on their axis-line topology. Clustering analysis is performed on the extracted axis lines to reveal vortex organization patterns and their potential connection to large-scale motions in turbulence.

Key words: turbulent boundary layers, turbulence simulation, vortex dynamics

1. Introduction

The dynamics and physics of turbulent flows in wall-bounded geometries have been extensively studied for decades for their fundamental significance and practical implications. The perpetual extraction of fluid kinetic energy from the mean flow to feed turbulent fluctuations (which is eventually lost to viscous dissipation) is a self-sustaining process, in the sense that continuing external disturbance is not required. It is thus natural to ask how turbulence regenerates itself in parallel wall-bounded flows where the laminar state is linearly stable until a Reynolds number

† Email address for correspondence: xili@mcmaster.ca

(Re) much (for the cases of Couette and pipe flows, infinitely) higher than the critical magnitude Re_{crit} for turbulence transition (Mullin 2011). Much progress has been made over the decades but the detailed dynamics remains elusive because of the complexity of turbulent flow fields. The concept of coherent structures, apparently repetitive flow patterns showing strong coherence in space and time frequently observed in the near-wall region of wall turbulence, is now the basis for understanding the physics of turbulence (Cantwell 1981; Robinson 1991; Panton 2001). These structures are believed to play a central role in the self-sustaining dynamics and in the turbulent transport of mass and momentum (Brooke & Hanratty 1993; Schoppa & Hussain 2002; Marusic *et al.* 2010).

The concept of coherent structure was introduced some 80 years ago (Corrsin 1943; Theodorsen 1952; Einstein & Li 1956) and encompasses various types of flow structures. It is often reflected in well-recognizable patterns in turbulent velocity fields, such as the well-known low- and high-speed velocity streaks in near-wall turbulence (Kline *et al.* 1967; Offen & Kline 1975) intricately involved in the turbulence production and regeneration processes (Kim, Kline & Reynolds 1971; Jiménez 2018). Contributions of velocity variations to the shear component of the Reynolds stress (which describes turbulent momentum transport from the mean flow) are usually quantifiable through the quadrant analysis (Wallace, Eckelmann & Brodkey 1972; Willmarth & Lu 1972). This approach was recently generalized by Lozano-Durán, Flores & Jiménez (2012) to analyse three-dimensional flow structures most responsible for the Reynolds shear stress, defined as continuous regions with high $|v_x'v_y'|$ (the apostrophe indicates the fluctuation components of the velocities). Therein, wall-attached structures were found to be self-similar in size and display increasing complexity with wall distance. In addition to this Eulerian perspective, coherent structures are also studied using Lagrangian approaches, in which they are identified as either long-lived events with attracting or repelling material lines or local maxima of finite Lyapunov exponents (Haller 2001). This approach is particularly useful for applications such as mixing and scalar transport. Given the large number of excellent review articles on the topic (Blackwelder & Kaplan 1976; Robinson 1991; Panton 2001; Adrian 2007; Haller 2015; Jiménez 2018), it is not our intention to provide a comprehensive overview of the entire field of coherent structure. Instead, we focus on the vortex structure, which has been particularly instrumental in helping researchers to conceptualize turbulent structures and dynamics. Despite its wide popularity, the concept of a vortex is very difficult to precisely define. Broadly, it describes the general class of revolving flow motions and the axis of fluid rotation is called the vortex axis or centre line: e.g. Robinson (1991) defined vortex as motions with roughly circular or spiral instantaneous streamlines. Although it is conceptually intuitive, the intrinsic flaw in this definition is that the topology of streamlines itself is not Galilean invariant (Haller 2005). More precise criteria for vortex identification and how these impact vortex analysis will be further discussed below.

Understanding how vortices are continuously produced and reproduced is thus the key to the fundamental inquiry into the turbulent self-sustaining dynamics. Many mechanisms for vortex regeneration have been proposed. These known mechanisms can be roughly summarized into two major categories according to Schoppa & Hussain (2002). In the first category, velocity streaks between streamwise vortices are susceptible to three-dimensional disturbances. This instability leads to the so-called ‘breakdown’ of the streaks, which, through nonlinear interactions, further feeds the generation of vortices (Hamilton, Kim & Waleffe 1995). This was the basis for the first self-sustaining model for turbulent dynamics (Waleffe 1997) and has led to the

discovery of various nonlinear travelling-wave solutions featuring the streak-vortex structure (Waleffe 1998; Gibson, Halcrow & Cvitanotić 2009). Streak breakdown is also found to play a pivotal role in the bypass transition to turbulence (Brandt & Henningson 2002; Schlatter *et al.* 2008). In the second category, as an existing vortex (the 'parent') lifts up, its rotational motion leads to a strong spanwise shear layer underneath, from which new vortices ('offspring') can be generated (Bernard, Thomas & Handler 1993; Brooke & Hanratty 1993). Our recent study suggested that when sufficient drag-reducing polymer additives are introduced, the streak-instability mechanism can be greatly suppressed, exposing the parent–offspring mechanism as the primary pathway for vortex regeneration in viscoelastic fluids with high polymer elasticity (Zhu *et al.* 2018).

Vortices in near-wall turbulence appear in distinct shapes. The best-known type is quasi-linear: nearly straight vortex tubes were frequently observed in experiments (Kim *et al.* 1971; Smith & Schwartz 1983) and simulations (Bernard *et al.* 1993). These vortices align mostly along the streamwise direction with their downstream heads sometimes lifting up towards the upper layers. Quasi-streamwise vortices have been studied extensively: they are considered to be the dominant structure in the buffer layer ($5 \lesssim y^+ \lesssim 30$; where superscript $+$ indicates turbulent inner scaling – see § 2.1) (Robinson 1991) and an essential element in both categories of the self-sustaining mechanisms reviewed above (Bernard *et al.* 1993; Hamilton *et al.* 1995; Waleffe 1997; Schoppa & Hussain 2002). On the other hand, vortices with more complex three-dimensional configurations are often observed at larger y^+, from the log-law layer up to the edge of the boundary layer (Robinson 1991). The axis of this type of vortex is often described as Ω- or Λ-shaped: the top of the arc of Ω is a spanwise segment that lifts up from the wall at the downstream end; the two legs extend towards the wall along the streamwise direction at the upstream end. These so-called 'hairpin' or 'horseshoe' vortices were first conjectured in the conceptual model of Theodorsen (1952). Their observations, in both experimental and numerical studies, remained anecdotal for decades (Willmarth & Tu 1967; Head & Bandyopadhyay 1981; Perry & Chong 1982; Smith 1984; Adrian, Meinhart & Tomkins 2000) until model hairpin structures were constructed via the conditional sampling of ejection events in direct numerical simulation (DNS) (Adrian *et al.* 1989; Adrian 1994). Direct evidence for the existence of clearly shaped and well-organized hairpins in unfiltered statistical turbulence was not reported until fairly recently when Wu & Moin (2009) observed a 'forest' of hairpins – arrays of well-aligned near-perfectly Ω-shaped vortex objects – in the DNS of boundary-layer flow. Notably, numerical travelling-wave solutions resembling a hairpin – streamwise vortex pairs coalescing at the lifted-up downstream end – were recently reported (Shekar & Graham 2018). The Wu & Moin (2009) scenario was later challenged by Schlatter *et al.* (2014), who, by analysing a DNS dataset of boundary-layer flow extending to much higher Re, showed that, although the signature of a hairpin forest is clear near the transition to turbulence, hairpin vortices become increasingly insignificant as turbulence further develops. Complete-shaped symmetric hairpin structures conforming to the canonical Ω-shape are never predominant in channel flow. Instead, hairpin-like structures are often highly asymmetric (e.g. one legged) and fragmented, especially at high Re (Morris *et al.* 2007; Dennis & Nickels 2011).

Compared with the relatively well-studied case of quasi-streamwise vortices, the role of hairpin vortices in turbulent dynamics is much less understood and often debated. Because of their stronger presence in the log-law and outer layers, much effort has been invested in unravelling their dynamics and relationship with turbulent

self-sustaining cycles (Smith 1984; Zhou *et al.* 1999; Adrian 2007). The most notable model was by Adrian (2007), which proposed that hairpin regeneration is achieved through their quick reproduction and the formation of 'hairpin packets'. This conceptual model is related to Townsend's (1980) attached eddy model and the alignment and grouping of hairpin vortex objects offer an appealing explanation for the experimentally observed large-scale motions (LSMs) and very-large-scale motions (VLSMs) in high-*Re* flows (Jiménez 1998; Kim & Adrian 1999). However, whether this picture is sufficient to describe the turbulent regeneration cycles in fully developed turbulence is still up for debate (Jiménez 2018). In particular, it remains to be confirmed if hairpins are essential in the generation of turbulence or are they simply consequences of other primary coherent structures (Del Álamo *et al.* 2006; Lozano-Durán & Jiménez 2014). After all, as noted by Schlatter *et al.* (2014), at high *Re*, it is unlikely that such well-defined structures can persist over the extended time period of their lift-up, without being disrupted by other turbulent motions. The challenge of depicting a widely accepted picture of hairpin dynamics is partially attributed to the lack of quantitative information on the evolution and conformation of these structures (Marusic *et al.* 2010). Compared with quasi-streamwise vortices in the buffer layer, hairpin vortices are not only more complex in shape, at higher y^+ they are also submerged in more complex surroundings and their interaction with nearby structures becomes non-trivial. A reliable method that objectively detects and extracts these structures from complex turbulent flow fields is required for their detailed statistical analysis. In addition to the turbulent regeneration mechanism at higher y^+ and higher *Re*, such a method will also be a valuable research tool in other areas. One example is the bypass transition, where different modes of streak instability and streak interaction can lead to various breakdown pathways driven by different types of vortices (Brandt & de Lange 2008; Schlatter *et al.* 2008; Wu *et al.* 2015). Another is turbulent friction drag reduction, where reduced three-dimensional vortices and the dominance of extended quasi-streamwise vortices are strongly associated with high levels of drag reduction (Xi & Graham 2010, 2012).

Objective vortex analysis must go beyond direct visual inspection and rely on quantifiable criteria and properly designed algorithms for vortex auto-detection. Any such approach requires two steps: vortex identification and vortex tracking. The first step goes back to the definition of a vortex and determines the quantitative criterion for identifying vortex regions in a flow field. By instinct, one would most likely be drawn to the concept of vorticity $\boldsymbol{\omega} \equiv \boldsymbol{\nabla} \times \boldsymbol{v}$. However, its fundamental deficiency quickly becomes clear as it does not effectively differentiate between pure shear and real swirling flow motions. Several more rigorous criteria for vortex identification have been proposed, all of which are Galilean invariant and define vortex regions based on the quantitative magnitude of certain scalar quantities calculated from the flow field, or more specifically, the velocity gradient tensor $\boldsymbol{\nabla v}$. The earliest of them is the Q-criterion by Hunt, Wray & Moin (1988), which defines vortex zones as regions where the second invariant of $\boldsymbol{\nabla v}$ is positive. (The original Hunt *et al.* (1988) criterion also requires pressure to reach a minimum within the vortex region, which is, although not identical to the Q-criterion, practically equivalent in most cases (Jeong & Hussain 1995).) The corresponding scalar criterion for vortices in incompressible fluid flow is

$$Q \equiv \tfrac{1}{2}(\|\boldsymbol{\Omega}\|^2 - \|\boldsymbol{S}\|^2) > 0, \tag{1.1}$$

where $\boldsymbol{S} \equiv (\boldsymbol{\nabla v} + \boldsymbol{\nabla v}^{\mathrm{T}})/2$ and $\boldsymbol{\Omega} \equiv (\boldsymbol{\nabla v} - \boldsymbol{\nabla v}^{\mathrm{T}})/2$ are the rate of strain and vorticity tensors and $\|\cdot\|$ denotes the Frobenius tensor norm. Other criteria have been proposed

thenceforth. For example, Chong, Perry & Cantwell (1990) defined vortex zones as regions containing complex eigenvalues of $\nabla \boldsymbol{v}$. For incompressible fluids, the corresponding scalar criterion is

$$\Delta \equiv (R/2)^2 + (Q/3)^2 > 0, \tag{1.2}$$

where Q is given by (1.1) and $R \equiv -\det(\nabla \boldsymbol{v})$ (Chong *et al.* 1990; Chakraborty, Balachandar & Adrian 2005). Another is the λ_2-criterion by Jeong & Hussain (1995) which defines vortex zones as regions where

$$\lambda_2(\boldsymbol{S}^2 + \boldsymbol{\Omega}^2) < 0 \tag{1.3}$$

and $\lambda_2(\cdot)$ denotes the second largest eigenvalue of a tensor. These three criteria are the most widely used in the literature and they all serve the same purpose: turning a velocity field into a scalar field that maps to the strength of vortex motion at different positions in the domain. Taking the Q-criterion for example, $Q > 0$ and $Q < 0$ correspond to regions dominated by rotation and deformation (extension), respectively (Hunt *et al.* 1988) and a small absolute value of Q ($|Q| \ll \|\nabla \boldsymbol{v}\|^2/2$ according to Xi & Bai (2016)) reflects simple shear. Despite their different mathematical origins, for application in real turbulent flows, they are shown to give comparable results with no practically significant differences (Dubief & Delcayre 2000; Chakraborty *et al.* 2005; Chen *et al.* 2015). A number of further attempts were made. For example, Zhou *et al.*'s (1999) swirling-strength criterion extends the Δ-criterion to include information on the local strength in a plane of swirling motions through the imaginary part of the complex eigenvalue of the velocity gradient tensor. Kida & Miura (1998) developed a kinematic swirling condition to be used together with the pressure minimum criterion which avoids the arbitrariness in the choice of the vortex-identification threshold common to all major single scalar identifiers.

Choosing a minimum threshold of Q, Δ or $-\lambda_2$ for a given region to be identified as a vortex structure is non-trivial. The original idea of using 0 as the threshold would connect nearly all vortex regions into an indistinguishable percolating structure that is nearly impossible to decipher – a value larger than 0 is thus required (Blackburn, Mansour & Cantwell 1996; Jeong *et al.* 1997; Chong *et al.* 1998). Obviously, both the size and configuration of the vortex regions identified depend on this threshold (see, e.g. figure 19 of Zhu *et al.* (2018)). Although some arbitrariness is inevitable, Lozano-Durán *et al.* (2012) have demonstrated (for the quadrant quantity $|v_x' v_y'|$ in their case) that there is a well-identifiable threshold range in which individual structures are separated but not yet overly quenched. Their so-called percolation analysis works equally well for vortex identifiers such as Q (Zhu *et al.* 2018). Details of this approach, which is also used in this study, will be discussed in § 4.5. Isosurfaces of the scalar identifier at the threshold value show the volumetric shapes of vortex structures. Jiménez and coworkers have extensively studied the complex three-dimensional vortex structures in high Re turbulence (Moisy & Jiménez 2004; Del Álamo *et al.* 2006). In the case of channel flow, Del Álamo *et al.* (2006) found that using a threshold value (for the Δ-criterion by Chong *et al.* (1990)) that varies with wall distance y^+ can fully reveal the complexity of outer-layer structures which deviate from the classical hairpin shape and are highly branched and often nearly isotropic. These structures are clearly divided into the wall-attached and -detached classes and the former type shows self-similar dimensions with increasing y^+. Lozano-Durán & Jiménez (2014) then proposed an elegant method that, given

sufficiently resolved DNS data, is able to track the temporal evolution of volumetric flow structures and document their lifetime kinetics.

Vortex-identification criteria generate vortex-containing volumes without differentiating their individual identities (e.g. the analysis of Del Álamo *et al.* (2006) was based on vortex 'clusters' – interconnecting vortex regions – instead of individual vortex objects). By carefully adjusting the threshold, individual vortices can be visually spotted by direct inspection. However, this information is not easily passed on to a computer program for automated analysis. A second step of the objective vortex analysis workflow – i.e. vortex tracking – is thus needed. This step turns volumetric vortex structures into line representations reflecting vortex conformation and topology, in which interconnected line segments represent a complete standalone vortex object. (Note that in this study the word 'tracking' refers to the extraction of such line representations from vortex volumes, which is to be differentiated from the temporal tracking of Lozano-Durán & Jiménez (2014).) These vortex lines enable the direct quantitative measurements of the size, position, orientation and conformation of vortices and are instrumental in understanding their roles in turbulent dynamics.

Much less development has been made on this front. The most intuitive approach is to represent vortices with their axis lines – the centre line for the swirling motion of fluid elements in each vortex tube. This is best exemplified by the vortex extraction scheme of Jeong *et al.* (1997) for conditional sampling. The axis line of a vortex tube is considered to cut through each of its cross-sectional planes at its planar maximum. These two-dimensional maximum points are labelled and then connected into the vortex axis line through a so-called 'cone-detective' method (see § 3). The Jeong *et al.* (1997) approach was designed for streamwise vortices only, in which the axis lines are constrained in the streamwise direction. The method was recently adapted for the conditional sampling of streamwise vortices in viscoelastic flows (Zhu & Xi 2018). However, the observations were limited to the changes in the vortex dimension and lifting angle with the addition of drag-reducing polymers. The most important fundamental changes in vortex dynamics, i.e. the suppression of three-dimensional vortices and different vortex regeneration mechanisms, could not be tested because of the restriction of streamwise tracking. A similar approach was used in Kida & Miura (1998) which extracted the axis line of each vortex in isotropic turbulence by connecting the two-dimensional pressure minima (in regions satisfying their swirling condition) within planes that are normal to the direction of vorticity or the third eigenvector of the pressure Hessian matrix. Tracking of three-dimensional vortex structures in inhomogeneous wall turbulence with line representations was only reported very recently by Hack & Moin (2018). They used a 'morphological thinning' method which gradually trims the vortex volume while preserving its topology, until each tube is reduced to a line. Different from the direct axis-line tracking approach of Jeong *et al.* (1997) and Kida & Miura (1998), the Hack & Moin (2018) approach does not always render vortex axis lines. Indeed, it is designed to preserve the connectivity of vortex volumes at the line representation level: vortex tubes that have interconnection in their volumes but no intersection between axis lines – i.e. interacting vortices that are not topologically connected – will result in interconnected representation lines. In another closely related development, Lee *et al.* (2014) proposed and implemented a streak-tracking method – which extracts line representations of velocity streaks by detecting the ridges in a smoothened surface capturing the velocity structure. Distribution of these 'spine' lines reveals the spatio-temporal patterns of LSMs and VLSMs.

In this study, we propose a new algorithm – vortex axis tracking by iterative propagation (VATIP) – for the axis-line tracking and analysis of three-dimensional

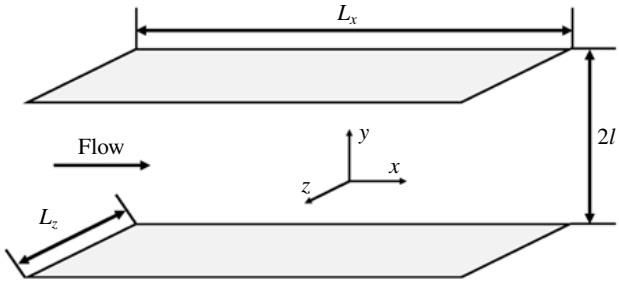

FIGURE 1. Conceptual plot of the plane Poiseuille flow geometry.

vortices in wall turbulence. The method builds on the initial idea of Jeong *et al.* (1997) for tracking vortex axis lines by sequentially connecting axis points (thus the word 'propagation') but extends its target from simple quasi-linear vortex axes to complex three-dimensional configurations representative of generic hairpin-like vortices, including not only the strictly Ω- or Λ-shaped vortices, but also asymmetric, incomplete, distorted and highly branched ones. For this purpose, the algorithm must also 'iteratively' grow the propagating axis line in all three dimensions. We will first test VATIP in transient flow fields in which well-organized hairpin vortices are generated in a controlled manner. It is then applied to flow fields of statistical turbulence at several different Re and the statistics of vortex configuration are analysed. In addition to vortex tracking, we also propose a procedure for vortex categorization based on the axis-line topology. Statistics of vortices of different topologies are thus also analysed. Access to the detailed information about vortex conformation and position, enabled by the new method, allows us to analyse their clustering patterns, which offers direct insight into the organization of vortices and its potential connection with LSMs. After presenting all major results, we will examine the robustness of the method with different parameters and settings. Finally, a major assumption of the method is that vortices can be traced to well-aligned streamwise legs, which applies well to nearly all major vortices in the near-wall layer. However, it no longer holds for complex isotropic structures observed in the outer layer of turbulence at higher Re. This limitation and future development will be discussed at the end.

2. Formulation and numerical details

2.1. *Direct numerical simulation (DNS)*

This study focuses on plane Poiseuille flow. Figure 1 shows the geometry of the simulation domain. A constant streamwise (x-direction) pressure gradient drives the flow between two infinite parallel plates. The periodic boundary condition is applied in the streamwise and spanwise (z-direction) directions with the period dimensions represented by L_x and L_z. A no-slip boundary condition is applied to the walls in the y-direction (wall-normal). By default, non-dimensionalization using turbulent outer scales is applied to all variables: i.e. the half-channel height l is used for the scaling of length, the laminar centre-line velocity U_c for velocity, l/U_c for time and ρU_c^2 for pressure (where ρ denotes the density of fluid). The Reynolds number is thus defined as $Re \equiv \rho U_c l/\eta$, where η is the viscosity of the fluid. Turbulent inner scales are used to report results of near-wall flow statistics and structure, for which the friction velocity $u_\tau \equiv \sqrt{\tau_w/\rho}$ and viscous length (or wall unit) $\delta_v \equiv \eta/\rho u_\tau$ are used. Quantities so scaled are denoted with a superscript '+'. Under these definitions, the friction

Re	Re_τ	δ_t	L_x^+	L_z^+	δ_x^+	δ_z^+	N_y	$\delta_{y,min}^+$	$\delta_{y,max}^+$
3600	84.85	0.01	4000	800	9.09	5.44	97	0.046	2.81
14 400	169.71	0.01	4000	800	9.09	5.44	195	0.022	2.79
80 000	400	0.01	4000	800	9.09	5.44	437	0.011	3.03

TABLE 1. Summary of the numerical settings for the DNS of statistical turbulence.

Reynolds number, $Re_\tau \equiv \rho u_\tau l/\eta$, can be directly related to Re through $Re_\tau = \sqrt{2Re}$. The governing equations of momentum and mass balances are

$$\frac{\partial \boldsymbol{v}}{\partial t} + \boldsymbol{v}\cdot\nabla\boldsymbol{v} = -\nabla p + \frac{1}{Re}\nabla^2\boldsymbol{v}, \tag{2.1}$$

$$\nabla\cdot\boldsymbol{v} = 0. \tag{2.2}$$

A Fourier (x)-Chebyshev (y)-Fourier (z) pseudo-spectral scheme is adopted for spatial discretization while a third-order semi-implicit backward-differentiation Adams–Bashforth scheme (Peyret 2002) is used for time integration. DNSs have been performed at three different Re, i.e. 3600 ($Re_\tau = 84.85$), 14 400 ($Re_\tau = 169.71$) and 80 000 ($Re_\tau = 400$). A summary of the numerical settings for the DNSs of statistical turbulence is provided in table 1. The simulation domain is kept the same in inner units ($L_x^+ \times L_z^+$; and thus in outer units both L_x and L_z scale with $1/Re_\tau$). Likewise, the grid sizes in the transverse directions δ_x^+ and δ_z^+ are also kept constant in inner units. The number of grid points in the y-direction increases with Re to keep the wall-normal resolution approximately the same in inner units. The numerical solver is implemented in a custom code parallelized with MPI based on the open source `ChannelFlow` package (Gibson 2012); the code was first reported in Tuckerman *et al.* (2014).

2.2. *Streak transient growth (STG) simulation*

In statistical turbulence, vortices are often irregular in shape, highly concentrated in space and intricately positioned relative to (sometimes partially connected with) one another. Meanwhile, for the initial test of our vortex-tracking algorithm, a benchmark system that enables controllable generation of well-defined three-dimensional vortex structures is required. We adopt the streak transient growth (STG) approach of Schoppa & Hussain (2002) for this purpose, which controls the vortex configuration by adjusting several parameters of the initial condition. (As another option, one may as well follow the approach of Brandt & de Lange (2008) in which vortices of different configurations are generated from different modes of streak interaction.)

The initial condition for STG is constructed by superposing a base flow with a perturbation velocity. The base flow

$$U_b(y, z) = U_m(y) + U_s(z)g(y), \quad V_b = W_b = 0 \tag{2.3a,b}$$

is quasi-two-dimensional (U_b, V_b and W_b are the x-, y- and z-component, respectively) and itself a superposition of the mean velocity profile of statistical turbulence at the same Re

$$U_m(y) \equiv \int_0^\infty \int_0^{L_x} \int_0^{L_z} v_x(x, y, z, t)\,\mathrm{d}z\,\mathrm{d}x\,\mathrm{d}t, \tag{2.4}$$

Re	Re_τ	δ_t	L_x^+	L_z^+	δ_x^+	δ_z^+	N_y	$\delta_{y,min}^+$	$\delta_{y,max}^+$	η	A_s	β_s	$v_{z,rms}'^+$	A_p	α_p
80 000	400	0.005	400	200	8.33	8.33	291	0.023	4.333	200	4	100	0.4	0.016	400

TABLE 2. Numerical settings and initial condition parameters used for STG simulations.

(where v_x is the instantaneous streamwise velocity component in the statistical turbulence) with a streamwise velocity streak adjustment $U_s(z)g(y)$. The latter is factorized into spanwise and wall-normal dependence terms

$$U_s(z) = A_s \cos(\beta_s(z - z_\beta)) \tag{2.5}$$

and

$$g(y) = y \exp(-\eta y^2). \tag{2.6}$$

Here, A_s adjusts the amplitude of the spanwise undulation, β_s adjusts the spanwise streak spacing, z_β is the spanwise phase parameter which is set so that the low-speed streak is aligned to the middle of the domain and η is set to align the wall-normal maximum at $y^+ = 20$. The perturbation velocity

$$v_x' = v_y' = 0,\ v_z' = A_p \sin(\alpha_p x) g(y) \tag{2.7}$$

(v_x', v_y' and v_z' are the x-, y- and z-component, respectively) adds streamwise dependence to the base flow, without which the instability would not grow (Waleffe 1997). Here, A_p is the perturbation amplitude and α_p is the streamwise wavenumber.

STG parameters used in this study for transient vortex generation, along with the numerical settings of the STG simulations, are listed in table 2. Note that $v_{z,rms}'^+$ is the root mean square (r.m.s.) magnitude of the spanwise perturbation velocity. A small simulation domain close to a minimal flow unit (MFU) (Jiménez & Moin 1991) is used because we only need to focus on a small set of vortex structures for algorithm testing purpose. Vortices are generated by STG only in half of the channel: i.e. both the streak velocity and perturbation velocity are only applied at the $y < 0$ side of the domain while for $y > 0$, $g(y) = 0$ and the initial velocity is simply $U_m(y)$.

3. The algorithm: vortex tracking by VATIP

We first review the original method by Jeong *et al.* (1997) for quasi-streamwise vortex tracking (illustrated in figure 2*a*). In their study, the $-\lambda_2$ isosurfaces are used to identify vortex shells in the three-dimensional flow domain and local maxima of $-\lambda_2$ in yz-planes are considered to be on vortex axes and labelled as vortex axis points (circle markers). The key element of the algorithm is a cone-detective procedure which groups individual vortex axis points into the axis lines for different vortices. Starting from one axis point, a cone is drawn toward the downstream direction. If another axis point at the adjacent downstream yz-plane is found within the cone, i.e. the yz-projection of the vector connecting the two points is shorter than half of the cone diameter d_{max}, the two axis points are grouped to the same vortex (red/solid makers). Because the search is limited to yz-planar maxima and the tracking cone extends in the downstream direction only, the method is only suitable for vortices staying closely aligned with the x-axis. For significantly curved vortices, the tracking stops as soon as the axis line steers towards other directions (hollow marker near the top of figure 2*a*).

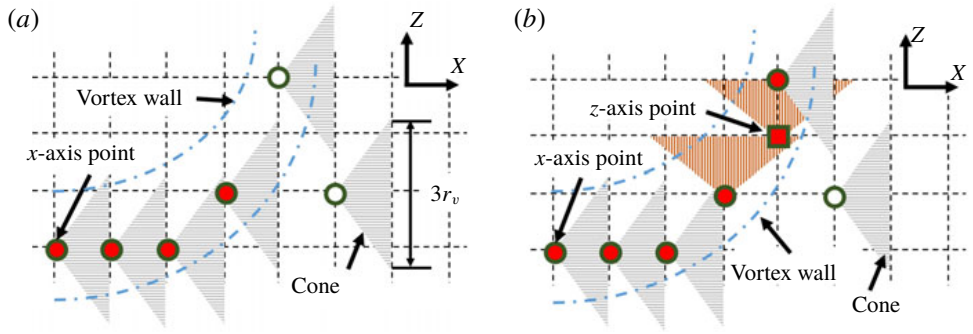

FIGURE 2. (Colour online) Conceptual plots of the vortex-tracking algorithms for (*a*) quasi-streamwise vortices (by Jeong *et al.* 1997) and (*b*) three-dimensional vortices (by VATIP).

Symbol	Description	Symbol	Description
i	Index of planes normal to the search direction	$\mathbb{D}$	Distance set
j	Index of candidate points in plane i	$D_{jj'}$	Distance between points j and j'
j'	Index of candidate points in plane $i+1$	D_{min}	Minimum distance in $\mathbb{D}$
θ	Index of individual vortices	E_θ	Propagation point of vortex θ
$\theta(j)$	Vortex-containing point j	$\mathbb{P}_i$	Set containing all candidate points in plane i

TABLE 3. Nomenclature for VATIP flow charts in figure 3.

Building on the idea of extending an vortex axis line by connecting new points in its direction of propagation, the new VATIP algorithm introduces two major changes to accommodate complex three-dimensional vortices typically observed at larger y^+ and higher Re. First, identification of axis points goes beyond the yz-planar maxima (hereinafter referred to as 'x-axis point' in which 'x' indicates the primary direction of the vortex axis) and also includes two-dimensional maxima in xz- and xy-planes (y- and z-axis points). Second (and more substantially), vortex axis propagation is no longer restricted to the x direction and the search must explore all three dimensions iteratively until all possible directions of axis extension are exhausted. For canonical hairpins, the vortex axis runs from the x (legs), to the y (lift up) and then to the z (the arch) direction. Other complicated (fragmented or highly branched) vortex configures are also observed, which requires the search algorithm to re-examine the x direction after the y and z searches reach their end (figure 2*b*).

The approach of iterative propagation over all three dimensions is thus proposed to allow for more general topologies of vortex axis lines. The resulting algorithm is much more complex than the original Jeong *et al.* (1997) method. Flow charts illustrating all detailed steps in VATIP are presented in figure 3 and the symbols used are explained in table 3. The main algorithm is illustrated in figure 3(*a*) in which two specific subroutines are called: subroutine 1 (figure 3*b*) is used to initiate the vortex axis lines and subroutine 2 (figure 3*c*) is used to extend existing axis lines in a new

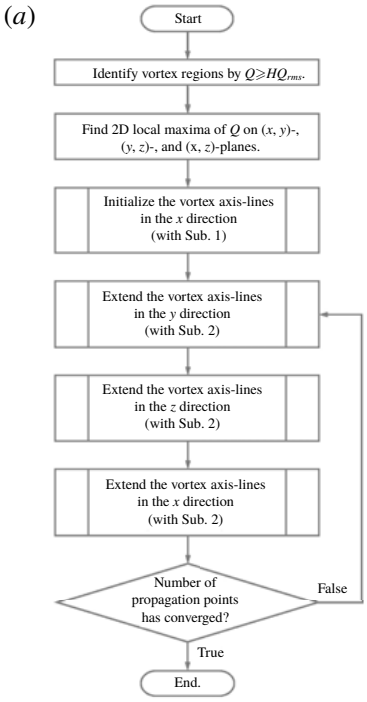

FIGURE 3. For caption see next page.

direction. The latter is repeatedly called in a loop to allow the vortex axis lines to explore different directions of propagation.

A three-dimensional velocity field is first converted to a scalar field of the vortex identifier using one of the criteria reviewed above in § 1. Without loss of generality, the Q-criterion is used here for illustration. (One may adapt the VATIP algorithm to any other vortex-identification criterion as long as the maximum – or minimum – of the scalar identifier marks the vortex axis.) Regions with Q larger than the threshold value of $0.4Q_{rms}$ (Q_{rms} is the r.m.s. value of Q; the threshold choice is discussed in § 4.5) for statistical turbulence or $1.4Q_{rms}$ for STG (a higher threshold is needed because turbulent structures from STG are localized and Q_{rms} is diluted by large non-turbulent regions) are selected, within which local maxima in two-dimensional grid planes of all three dimensions are recorded (figure 3*a*). Maximum points found in the yz-, xz- and xy-planes are labelled as x-, y- and z-axis points, respectively. Regions with lower Q are not considered to avoid the interference from small-magnitude fluctuations in Q.

These scattered axis points are connected to form vortex axis lines through a multistep iterative vortex-tracking process. All axis lines are initialized with subroutine 1 in the x-direction only (figure 3*b*). This choice is based on the conceptual model that vortices generated from the walls initially align along the streamwise direction in the buffer layer. Many of them can then lift up at the downstream end and rise into upper flow layers, forming hairpins, branches or other complex configurations. This model well describes the vortex dynamics in the near-wall boundary layer (Robinson 1991; Zhou *et al.* 1999; Panton 2001) (see figure 8 for example). Consequently, as shown below, VATIP can reliably detect and extract the axis lines for these vortices. However, recent advances in the field revealed that vortex structures can also be generated independently of the walls as long as there is

(*b*)

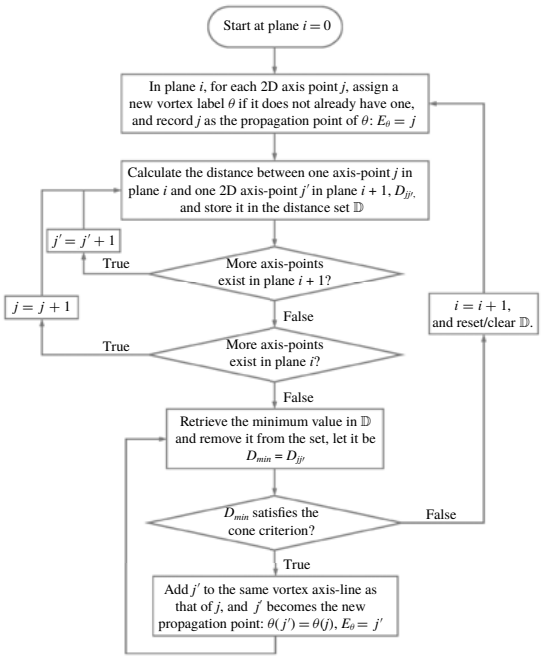

(*c*)

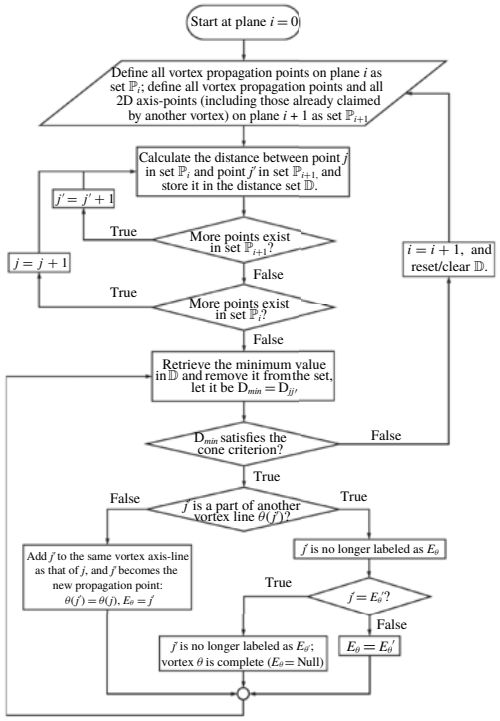

FIGURE 3 (cntd). Flow charts for the VATIP algorithm: (*a*) main routine, (*b*) subroutine 1 for the initial tracking in the x direction, and (*c*) subroutine 2 for the continued tracking by iterative propagation in all directions. For the last, the loop over planes is unidirectional for the x- (downstream) and y- (wall→centre) directions and bidirectional for the z direction – see text.

sufficient mean shear (Del Álamo *et al.* 2006; Jiménez 2013). These 'detached' vortex structures are often more isotropic and complex in shape – it is thus expected that, at higher Re where these structures become more prominent, this bias towards x-lying legs will restrict the applicability of VATIP mainly to near-wall regions. Further discussion about the necessity of this choice and limitations resulting therefrom is deferred to § 4.6.

Starting from the first yz-plane (at $x = 0$ and labelled as plane $i = 0$; as shown in § 4.5, one can choose to start at any other yz-plane, which gives no real difference in the results), all x-axis points on the plane are initially assigned different vortex labels θ. Each growing vortex axis line must have an open connection point – referred to as the propagation point – to which new axis points can be added. The propagation point of the axis line of vortex θ is denoted as E_θ. At the very beginning ($i = 0$), since each axis line only has one point, it is automatically labelled as the propagation point. For every propagation point on plane i, the closest axis point on plane $i + 1$ is found and if the distance between them is shorter than the slant edge of the cone (figure 2), the new axis point is connected to the existing vortex axis line and designated as its new propagation point. If an axis point on plane $i + 1$ is eligible for connection with multiple existing propagation points on plane i, the closest one is chosen. In practice, this is implemented by first calculating all distances between propagation points on plane i and axis points on plane $i + 1$ and storing the results in a set $\mathbb{D}$. Potential connections are processed from the shortest distance in $\mathbb{D}$ up to the cutoff distance (cone slant edge length; see figure 3*b*). After all eligible connections are made, the process is repeated for the next yz-plane. On plane $i + 1$, if an x-axis point is not already designated as the propagation point of an existing vortex (in step i), it is labelled as the propagation point of a new vortex initiating from plane $i + 1$. All these propagation points on plane $i + 1$ are then tested for connection with x-axis points on plane $i + 2$ following the same procedure as the previous step. The iteration continues until all yz-planes are processed. The resulting set of vortex axis lines from this step (subroutine 1) is equivalent to the outcome of the Jeong *et al.* (1997) method.

Extension to three-dimensional vortex tracking requires the continuation of the search in other directions after the initial x-direction tracking stage. As shown in figure 3(*a*), the search continues in the y- and then z-direction. This order is chosen considering the typical configuration of hairpin-like vortices (see, e.g. the $t = 60$ image of figure 5): the legs of the Ω-shaped axis line align in the x-direction and as they extend downstream, the vortex contour lifts up (y-direction axis line) before they merge to form a spanwise arch (z-direction axis line). However, the vortex does not have to conform to this canonical shape: e.g. for a vortex without a clear lift-up (aligned in the y-direction) segment, the search will continue to the z-direction without interruption. The tracking method for axis-line extension (subroutine 2 and figure 3*c*) is very similar to that of axis-line initialization (subroutine 1 and figure 3*b*) with two major modifications. First, it only extends existing vortex axis lines by adding to their propagation points and no new vortex will be initiated from any loose axis point. Limiting vortex initiation to subroutine 1 (which is only called before the iteration of search directions) ensures that vortex segments in different directions are only grouped when they are topologically related: e.g. a y-segment happens to start where an x-segment ends. Planar maximum points of Q that are spatially adjacent but showing no clear topological connection are not included. This is necessary to minimize false connections in complex flow fluids densely populated with vortex structures. Its impact on the generality of the method will be discussed in § 4.6. Second, when the axis point on the next plane (plane $i + 1$) selected for connection is already part of another vortex, these two vortices must be properly merged.

For canonical hairpins, the steps of initial tracking (subroutine 1) in the x-direction followed by continued tracking (subroutine 2) in the y- and then z-direction would suffice. In order to capture more general three-dimensional vortex configurations, especially disfigured, highly branched and partially merged vortices, the loop containing subroutine 2 over all three dimensions must be continued until the number of vortices (measured by the number of propagation points; figure 3*a*) has converged. The specific algorithm of subroutine 2 is nearly identical for different directions with proper adjustment for the directionality: for, e.g. the y- (or z- or x-) direction search, it moves over all xz- (or xy- or yz-) planes and connects y- (or z- or x-) axis points to the propagating axis lines. The only difference is that the vortex axis-line propagation is unidirectional in the x- and y-tracking and bidirectional in the z-tracking. The x-direction propagation proceeds in the flow direction (i.e. plane $i+1$ is immediately downstream of plane i) because of the convective asymmetry: vortex structures are always carried downstream by the flow. The z-direction should be statistically symmetric and thus the propagation must sweep both directions. As shown in § 4.5, the VATIP tracking result is practically unaffected by the choice of start planes in these two dimensions, indicating that these sweeping directions can well account for the translational symmetry in x and z. The y-direction propagation always starts from the walls towards the channel centre (i.e. plane $i+1$ is father away from the wall than plane i). This choice, again, restricts VATIP to wall-generated vortices which generally grow from the buffer layer to higher y^+.

The size of the detection cone is determined based on the average cross-sectional radius of vortex tubes. The average streamwise vortex radius

$$r_v = \sqrt{\frac{A_{v,total}}{\pi N_v}} \tag{3.1}$$

is used as the estimated vortex tube size. Here, regions with $Q > Q_{threshold}$ on all yz-planes are grouped according to spatial adjacency: for a given yz-plane, grid points satisfying the Q-criterion that are immediate neighbours are grouped into the same vortex cross-section. The total area of all vortex regions on these planes $A_{v,total}$ divided by the number of separate vortex cross-sections N_v gives the average cross-sectional area of vortex tubes, from which an average radius is deduced. In this study, the detection core is chosen so that it extends from plane i to plane $i+1$ with a base (on plane $i+1$) radius of $1.5r_v$ (figure 2). The choice of this parameter will again be examined and discussed in § 4.5. In addition, r_v is also used as the minimum separation between identified axis points on each two-dimensional plane. If two or more local Q maxima are separated by less than r_v on the plane, they are considered to belong to the same vortex tube and the one with higher Q value is kept as an axis point.

The computational cost of VATIP is negligible compared with DNS. To analyse a typical DNS flow field image in this study (domain size and resolutions are provided in table 1), the whole algorithm takes ≈100 s, 370 s and 1600 s (running as a serial program on an Intel® E5-2683 v4 2.10 GHz processor) for $Re_\tau = 84.85$, 169.71 and 400, respectively. To imitate the original algorithm of Jeong *et al.* (1997), we turned off the whole iteration loop (see figure 3). The computational time of this streamwise-only search is comparable to that of the full VATIP algorithm. This is because the calculation of the Q field and the finding of its planar maximum points are both computationally intensive within the program. For the search and propagation steps, the first x-search step (subroutine 1) is also more expensive than the following iterative

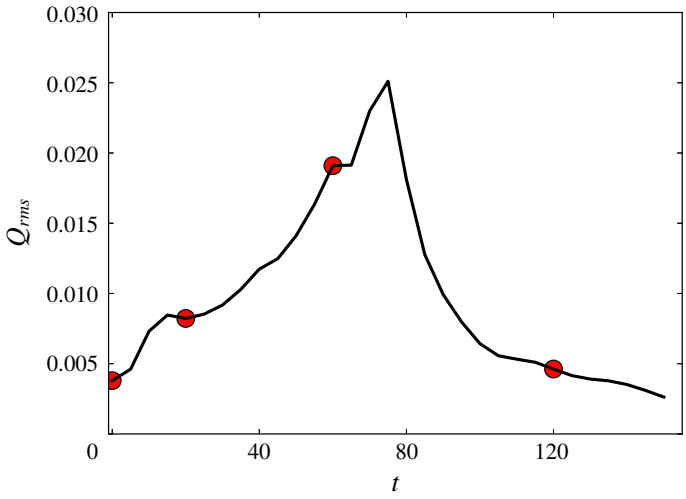

FIGURE 4. (Colour online) Time series of the root mean square of Q in the STG simulation. Moments of the flow fields shown in figure 5 are marked with red circles.

propagation steps (because of its larger number of distance calculations). In all cases, the tracking result converges after 3 iterations or less. The memory requirement of the program is 1.02 GB, 2.25 GB and 5.10 GB (in order of increasing Re).

4. Results and discussion

4.1. *Test of VATIP with STG-generated vortices*

We start by testing the effectiveness of VATIP in STG flow fields, where vortex generation is controllable by the parameters of initial disturbance (Schoppa & Hussain 2002). Figure 4 shows the time series of the root mean square of Q in our STG simulation (numerical settings given in § 2.2) and vortex configurations of selected moments are shown in figure 5. The initial disturbance flow field ($t = 0$) contains strictly streamwise vortices with a spanwise phase shifts between upstream and downstream vortex sets. At the beginning of STG, the Q_{rms} profile starts to grow and reaches the first plateau at around $t = 15$. At this stage, the quasi-streamwise vortices tilt and bend sideways to the spanwise direction but wall-normal lifting up remains small ($t = 20$ in figure 5). After the first plateau, the Q_{rms} profile continuously increases and reaches its peak at $t = 75$. During this period, neighbouring tilted-streamwise vortices lift up and conjoin to form well-defined hairpin vortices ($t = 60$ in figure 5). The value of Q_{rms} gradually decreases after $t = 75$. Vortices in this period have a high lifting tendency despite their lower strength ($t = 120$ in figure 5).

Typical vortex configurations in these moments, including the strictly streamwise ($t = 0$), titled-streamwise ($t = 20$), lifted-up hairpin ($t = 60$) and decaying hairpin ($t = 120$) vortices, are used as our benchmark systems for vortex tracking. The original method of Jeong *et al.* (1997) is recovered when the algorithm of figure 3(*a*) is truncated right after subroutine 1 (i.e. no iterative propagation in other directions). This would be sufficient if the target was limited to streamwise ($t = 0$) or quasi-streamwise vortices (as in the case of Jeong *et al.* (1997)). Its inadequacy starts to surface in titled-streamwise vortices ($t = 20$) where the spanwise segment of the vortex is not fully captured in the axis line obtained (circular markers). For hairpin vortices ($t = 60$ and 120) not only are some of the axis points missing (because they are not

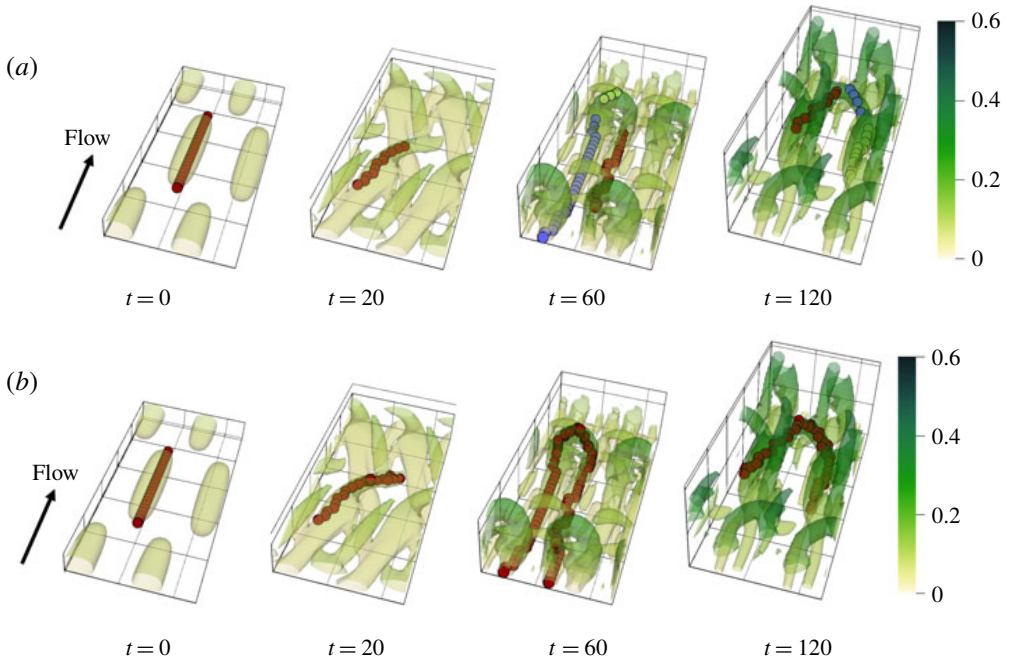

FIGURE 5. (Colour online) Vortex configurations of selected moments in the STG simulation. The isosurfaces are $Q = 0.015$ for $t = 0$, 20 and 60 and $Q = 0.01$ for $t = 120$. The colour scale maps to the distance from the wall in outer units. Vortex axis lines from (*a*) a streamwise-only tracking approach (equivalent to the Jeong *et al.* (1997) method) and (*b*) VATIP are compared (circular marks; different colours are used for different vortices as identified by the method).

yz-plane maxima of Q), the method also breaks the axis line of a well-defined hairpin into separate pieces. The new VATIP algorithm successfully identified the complete axis lines of vortices of all shapes and correctly grouped axis points of the same vortex into one axis line.

4.2. *DNS: flow statistics and visualization*

We now give an overview of the DNS results of statistical turbulence at three different Re ($Re_\tau = 84.85$, 169.71 and 400) in this section. Application of VATIP to these flow fields will be discussed in § 4.3. The mean velocity U^+ as a function of y^+ is plotted in figure 6(*a*). As Re increases, the profile outside the buffer layer ($y^+ \geqslant 30$ (Pope 2000)) gradually approaches the von Kármán log law (Kim, Moin & Moser 1987; Pope 2000)

$$U^+ = 2.5 \ln y^+ + 5.5. \tag{4.1}$$

At the lowest $Re_\tau = 84.85$, the profile is slightly higher than the von Kármán asymptote, indicating that the log-law layer is not fully developed. The agreement is much better at the two higher Re and at the highest $Re_\tau = 400$, it nearly completely collapses onto (4.1) for a wide range of y^+ (until the channel centre).

From a generic logarithmic profile

$$U^+ = A \ln y^+ + B, \tag{4.2}$$

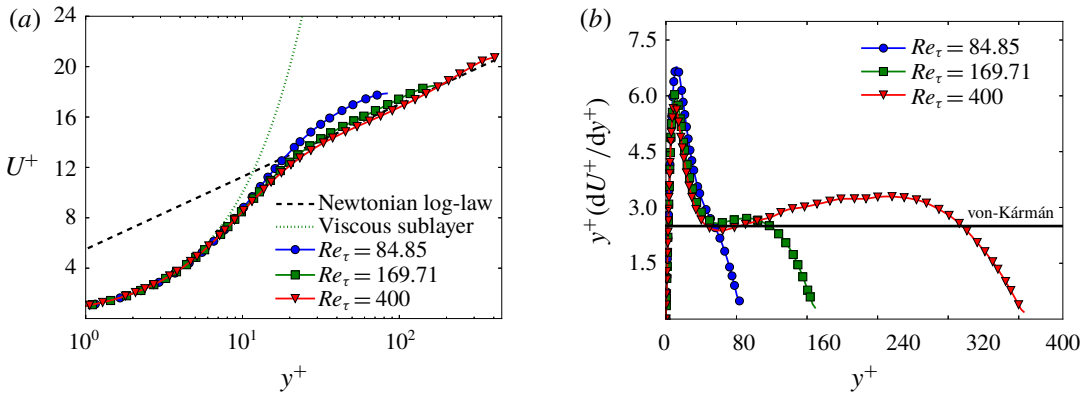

FIGURE 6. (Colour online) (*a*) Mean velocity profiles (U^+ versus y^+) and (*b*) log-law indicator functions ($y^+\mathrm{d}U^+/\mathrm{d}y^+$ versus y^+) of the statistical turbulence at $Re_\tau = 84.85$, 169.71 and 400.

the log-law slope can be expressed as

$$A = y^+ \frac{\mathrm{d}U^+}{\mathrm{d}y^+}. \tag{4.3}$$

When the profile does not strictly follow a logarithmic dependence (4.2), A becomes a function of y^+ – its variation indicates the departure from the log law. This quantity (4.3), which is thus sometimes referred to as the log-law indicator or diagnostic function (Hoyas & Jiménez 2006; Marusic *et al.* 2010), is plotted in figure 6(*b*) for our DNS results. For the lowest $Re_\tau = 84.85$, the function goes nearly straight down with no discernible flat region, indicating the lack of a well-defined log-law layer (despite the fact that the profile is seemingly parallel to the von Kármán asymptote in figure 6*a*). For the two higher Re ($Re_\tau = 169.71$ and 400), an inflection point shows up at $y^+ \approx 50$ with nearly the same value of 2.5, which agrees well with the von Kármán log-law slope reported in Kim *et al.* (1987) and is also consistent with the observations of Moser, Kim & Mansour (1999) and Jiménez & Moser (2007). After the inflection point, the profile is not strictly flat but its variation is small for a distinct range of y^+ ($50 \lesssim y^+ \lesssim 100$ for $Re_\tau = 169.71$ and $50 \lesssim y^+ \lesssim 320$ for $Re_\tau = 400$), indicating that these Re are sufficiently close to and have already shared some common features with fully developed turbulence (Moser *et al.* 1999; Hoyas & Jiménez 2006).

Figure 7 shows the four components of Reynolds stress, $\langle v_x'^+ v_x'^+ \rangle$, $\langle v_y'^+ v_y'^+ \rangle$, $\langle v_z'^+ v_z'^+ \rangle$ and $-\langle v_x'^+ v_y'^+ \rangle$, as functions of y^+. Consistent with the literature (Moser *et al.* 1999; Abe, Kawamura & Matsuo 2001), the profiles of all components rise with Re at y^+ above $\approx$30 while the peak shifts towards the centre of the channel. The Re-dependence is stronger in the transverse components $\langle v_y'^+ v_y'^+ \rangle$ and $\langle v_z'^+ v_z'^+ \rangle$, which reflects increasing energy redistribution (Abe *et al.* 2001), and the dependence in the streamwise component $\langle v_x'^+ v_x'^+ \rangle$ is much weaker.

Figure 8 shows the vortex structures identified by the Q-criterion in typical snapshots at the lowest ($Re_\tau = 84.85$) and the highest ($Re_\tau = 400$) Reynolds numbers. In both cases, the flow fields are filled with tube-like vortices. Quasi-streamwise vortices are more prevalent in the vortex field, but hairpin vortices can still be observed. Examples of these hairpins are shown in the enlarged views. Vortices at the

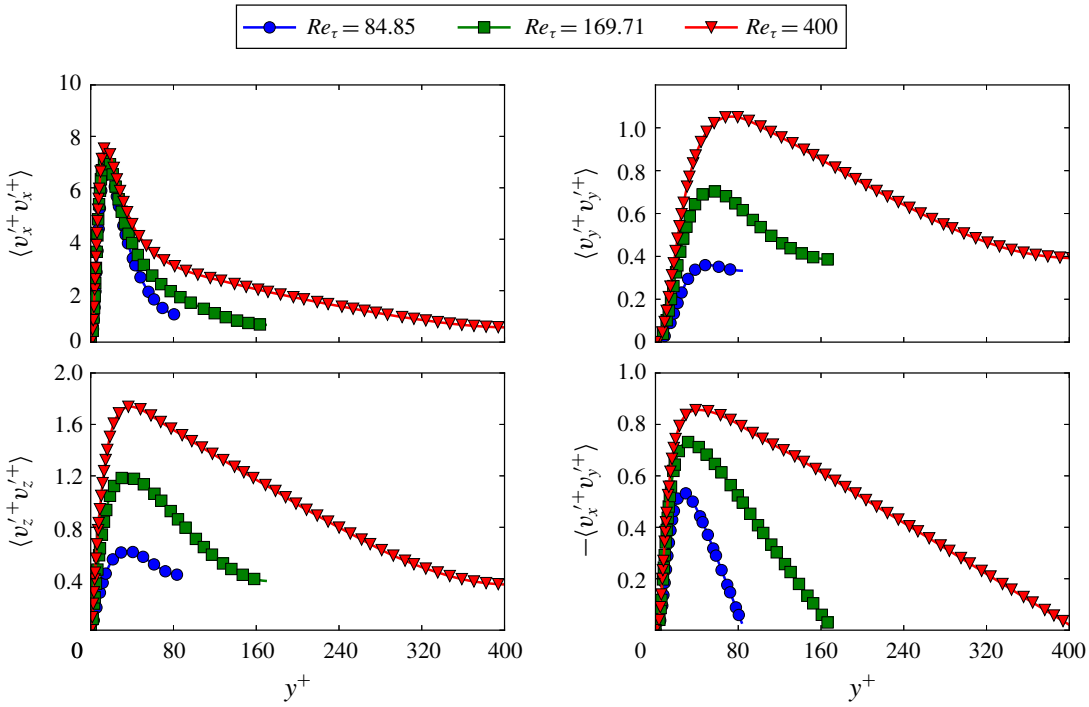

FIGURE 7. (Colour online) Reynolds stress profiles for $Re_\tau = 84.85$, 169.71 and 400.

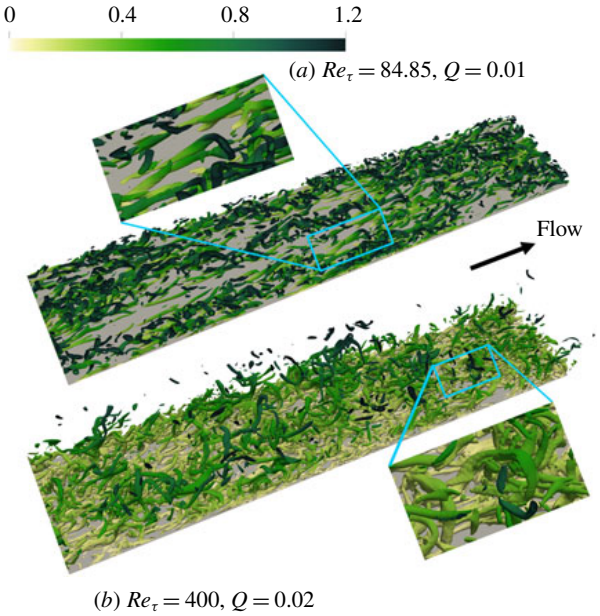

FIGURE 8. (Colour online) Instantaneous vortex structures at (*a*) $Re_\tau = 84.85$ and (*b*) $Re_\tau = 400$. Isosurfaces are identified by the Q-criterion and in the wall-normal direction only the bottom half and 20 % of the top half of the channel are shown (i.e. $0 < y^+ < 1.2Re_\tau$). The colour shade (from light to dark) maps to the distance from the bottom wall in outer units.

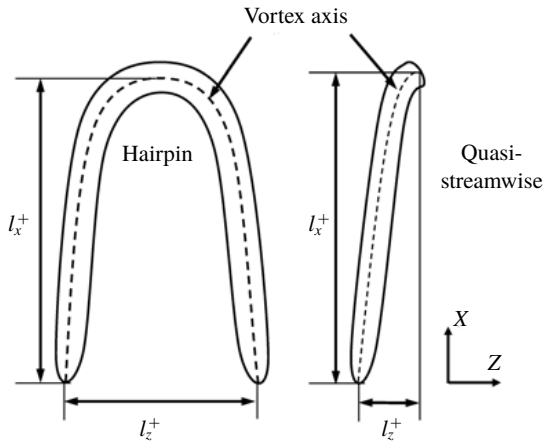

FIGURE 9. Measurements of vortices in x and z dimensions.

higher Re display a high extent of lifting up and many instances of detached vortices are observed. (A vortex becomes detached when its upstream legs leave the wall and become shielded from wall interaction (Perry & Marušić 1995; Marusic *et al.* 2010).) Meanwhile, most of the vortices at the lower Re remain attached to the wall with a comparatively weaker extent of lifting.

4.3. *VATIP application in DNS: vortex classification and conformation*

Visualization based on the Q field can only provide a cursory glance of the instantaneous vortex fields and lacks both quantitative precision and statistical certainty. The new VATIP algorithm automatically detects vortices with a variety of shapes without subjective bias. It thus offers a feasible pathway to the statistical analysis of the population and configurations of vortex structures, facilitating the understanding of their roles in turbulent dynamics. In this section, VATIP is applied to the DNS results of statistical turbulence. Another algorithm is also proposed to classify vortices according to the topology of the vortex axis lines identified thereby. Note that a lower Q threshold of $0.4Q_{rms}$ is used for VATIP as discussed previously in § 3.

To begin with, vortex size is measured according to figure 9: the streamwise and spanwise measurements (l_x^+ and l_z^+) are defined as the maximal separation between axis points in these two dimensions, respectively. The statistical distributions of these measurements are presented in figures 10 and 11. (As discussed below, vortices with $l_x^+ < 50$ are considered fragments and not included in the statistics.) At all Re, the probability density function (PDF) of l_x^+ monotonically decreases with increasing l_x^+. The average l_x^+ is approximately 120 and is nearly independent of Re. This value is comparable with Jeong *et al.*'s (1997) 200 (using their streamwise tracking algorithm) and Panton (2001)'s 100 (from empirical observation). Sensitivity of this measurement to varying $Q_{threshold} \equiv HQ_{rms}$ is rather small: e.g. for $Re_\tau = 84.85$, increasing H from 0.4 to 1.6 (well beyond the percolation level), the average l_x^+ only decreases from 126 to 104. This is consistent with the earlier (§ 3) statement that vortex axis topology is insensitive to the changing H value.

By contrast, Re has a much stronger effect on the spanwise vortex measurement. The distribution of the vortex aspect ratio l_z^+/l_x^+ (figure 11) becomes broader and high l_z^+/l_x^+ values are more frequently sampled with increasing Re. The average aspect

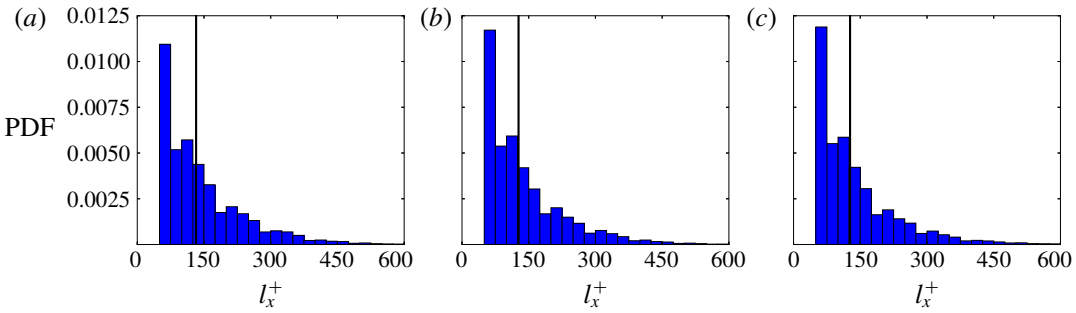

FIGURE 10. (Colour online) Probability density function of the streamwise measurement of vortices: (*a*) $Re_\tau = 84.85$, (*b*) $Re_\tau = 169.71$ and (*c*) $Re_\tau = 400$. The vertical line marks the mean value.

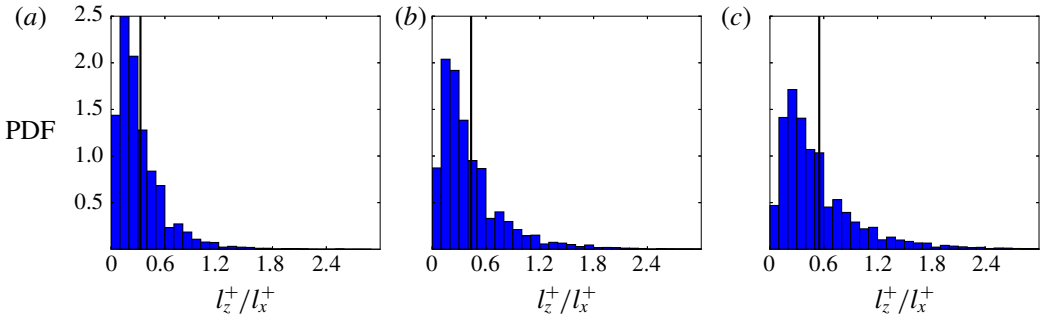

FIGURE 11. (Colour online) Probability density function of the spanwise–streamwise aspect ratio of vortices: (*a*) $Re_\tau = 84.85$, (*b*) $Re_\tau = 169.71$ and (*c*) $Re_\tau = 400$. The vertical line marks the mean value.

ratio also increases with Re. Because l_x^+ is nearly the same, higher l_z^+/l_x^+ is solely due to the increasing spanwise measurement of the vortices. There are two major possible contributions to this increase: (i) streamwise vortices becoming increasingly bent and tilted towards the spanwise direction (see the $t = 20$ panel of figure 5 for an illustration) and (ii) the increasing occurrence of curved and three-dimensional vortices such as hairpins. Quantitative assessment of these changes requires the statistics of vortices of different topologies.

A new procedure is thus proposed to automatically classify the individual vortex axis lines, obtained from VATIP, according to their dimensions, geometry and topology. A flow chart of the procedure is provided in figure 12; the geometric quantities used in the procedure are shown in figure 13 and typical examples of different types in figure 14. The procedure consists of a series of binary decisions. First, all axis lines identified by VATIP are divided into two groups based on their streamwise measurement: those with $l_x^+ \geqslant 50$ are considered as clear-cut vortices and smaller pieces are identified as fragments. This cutoff is smaller than the 150 wall units used in Jeong *et al.* (1997) because VATIP considers vortices with three-dimensional curvatures and the streamwise dimension does not necessarily account for the full vortex axis length. Those identified as vortices are further divided into streamwise versus three-dimensional types based on whether a significant spanwise segment can be found in the axis line. Note that any axis line identified by VATIP is formed

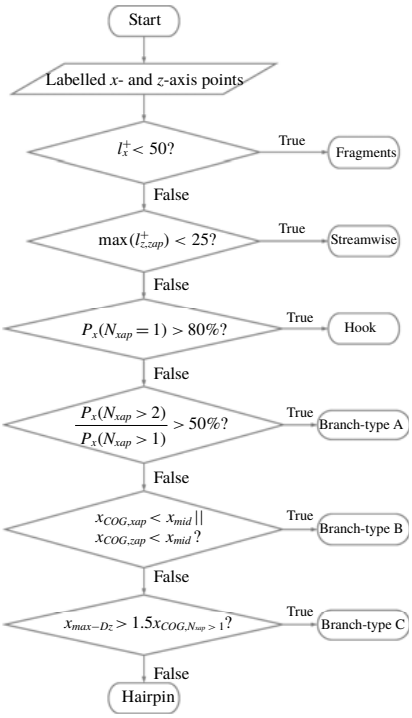

FIGURE 12. Flow chart of the vortex classification procedure.

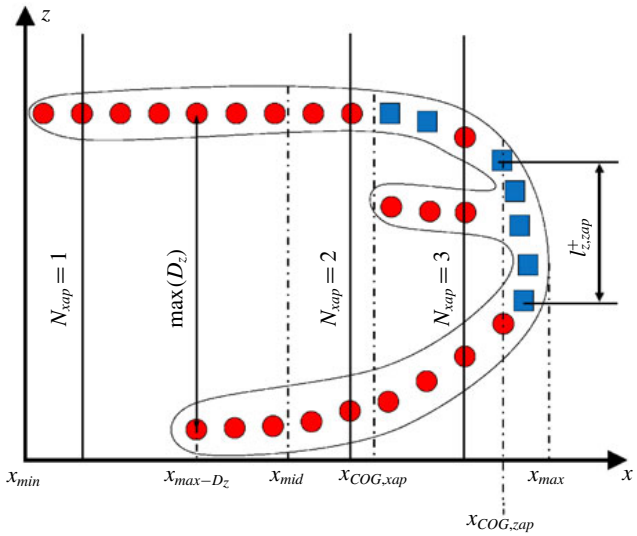

FIGURE 13. (Colour online) Definitions of the geometric quantities used in the vortex classification procedure of figure 12. Circles and squares represent x- and z-axis-points, respectively.

by connecting axis points in any of the three dimensions (figure 13). The spanwise extent of all segments consisting of spanwise axis points only $l_{z,zap}^+$ are measured and if the maximum span $\max(l_{z,zap}^+) \geqslant 25$, it is determined that the vortex can no longer treated as a streamwise one.

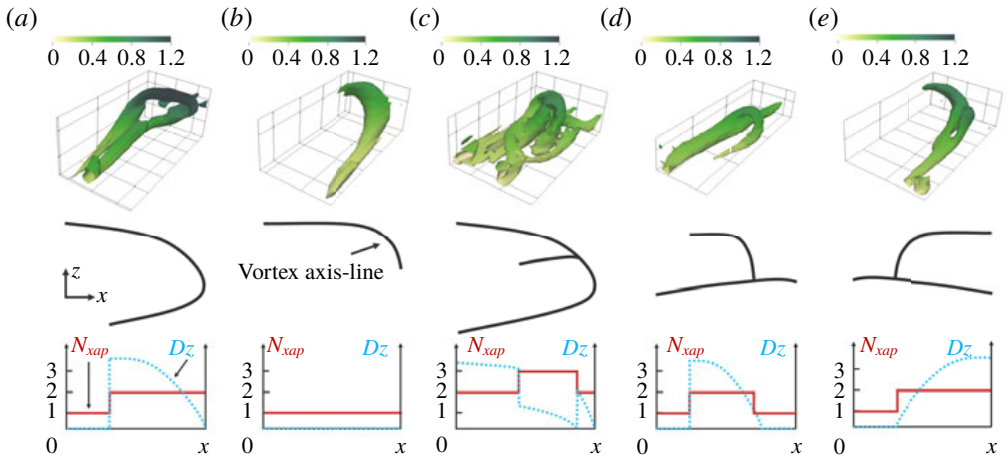

FIGURE 14. (Colour online) Classification of three-dimensional vortices: (*a*) hairpins, (*b*) hooks, (*c*) branch type A, (*d*) branch type B and (*e*) branch type C. Top row – representative examples from DNS; middle row – schematics of the vortex axis line; bottom row – streamwise profiles of the number of x-axis points N_{xap} and spanwise extent D_z.

Non-streamwise (or three-dimensional) vortices are further classified into several types based on the axis topology and geometry. A canonical hairpin is described as a vortex with two largely symmetric streamwise legs conjoining at its downstream head into a spanwise arc (figure 14*a*). Many three-dimensional vortices bear some of the key features of a hairpin but significantly depart from its norm in other aspects. The classification procedure relies on two major geometric metrics of the identified vortex axis line (figure 13) to differentiate these different types: (i) the number of x-axis points at a given x position N_{xap} and (ii) the spanwise separation between legs (again) at a given x position D_z. (For irregular vortices with more than two legs, e.g. column (c) of figure 14, D_z is the spanwise separation between the two closest legs.) Variation of these two metrics with different x positions is sketched for different vortex types in the bottom panels of figure 14. For a canonical hairpin (column (a)), N_{xap} is 2 for the majority of the x range although it may reduce to 1 at the beginning as the legs do not exactly match in length. Its D_z starts high near the leg tips and gradually reduces to 0 as the legs fuse.

For any vortices deemed three-dimensional (versus streamwise) from the previous step, the procedure first checks the percentage of x positions with only one x-axis point $P_x(N_{xap}=1)$ ($P_x(C)$ is the percentage of x positions where a specific condition C is satisfied) – if this quantity is $>80\,\%$, i.e. for over $80\,\%$ of the vortex length it only has one leg, the vortex is a highly asymmetric variant of a hairpin where one of the legs is not clearly developed. This type is termed 'hooks' in our taxonomy. The other vortices have at least two legs, but there are various other branching configurations than the canonical hairpin. For example, in vortex packets where vortices are highly entangled and dynamically coalescing with one another, multi-legged – pitchfork-like – vortices are often observed (figure 14*c*). If a vortex has more regions with three or more legs than those with two, i.e. $P_x(N_{xap}>2)/P_x(N_{xap}>1)>50\,\%$, it is identified as a branch type-A. Even vortices that only branch into two legs may appear significantly different from a canonical hairpin. For instance, the branch type-B (figure 14*d*) looks more like a fusion between a quasi-streamwise vortex with a partial hairpin (or hook).

This type of vortex was also reported in Robinson (1991) and Brooke & Hanratty (1993) and was believed to result from the spanwise shear dragging a side branch of a quasi-streamwise vortex to form an 'arch' on its side (Robinson 1991). The profile of N_{xap} for this type shares some similarity with the hairpins, as both start with two legs which gradually merge. The main difference is that a hairpin ends with the arch where most axis points are counted, whereas in branch type-B the arch is followed by an extended streamwise segment downstream. Here, the x projections of the centre-of-gravity (COG) of all x-axis points $x_{COG,xap}$ and that of all z-axis points $x_{COG,zap}$ are calculated. A canonical hairpin would be much 'heavier' at the downstream end, so if both COGs are at the upstream end, i.e. $x_{COG,xap} < x_{mid}$ and $x_{COG,zap} < x_{mid}$ ($x_{mid} \equiv (x_{max} - x_{min})/2$ being the x coordinate of the middle point of the vortex axis line – see figure 13), the vortex is classified into branch type-B. In a similar scenario, when a side branch from a quasi-streamwise vortex protrudes towards the channel centre, because of the weaker transverse flows and higher mean velocity, the branch extends substantially downstream before any arch is formed. This is labelled as branch type-C in this study (figure 14*e*) and identified by the criterion that $x_{max\text{-}D_z} > 1.5x_{COG,N_{xap}>1}$, where $x_{max\text{-}D_z}$ is the x coordinate of the maximal branch separation D_z and $x_{COG,N_{xap}>1}$ is the x coordinate of the COG of the branched part of the vortex axis line (where $N_{x\text{-}cp} > 1$). Finally, the remaining vortices – i.e. those predominated by two legs and with no substantial quasi-streamwise downstream segments – are classified as hairpins.

The criteria used in this classification procedure are mostly empirical. For starters, there is no physical ansatz supporting the classification of three-dimensional vortices into the five particular types listed in figure 14 – they are chosen solely based on empirical observations in our own and previous studies. Likewise, the dividing criteria and cutoff magnitudes used in the procedure (figure 12) are all chosen based on a combination of physical intuition and practical experience. For example, there is no physical basis as to how long a third leg needs to reach for a vortex to be considered a branch type-A (multi-legged) rather than a slightly modified hairpin. Indeed, the question of whether there is any fundamental difference between various types of branches and the canonical hairpin itself cannot be answered. The lack of objective vortex classification criteria is an inevitable consequence of the current limited knowledge of the complex vortex dynamics in wall turbulence. It is for this reason that an algorithm like VATIP is much needed. Future application of VATIP to a wider range of flow systems is anticipated to bring forth better experience and understanding of the characteristics of turbulent vortices, which will lead to a more standardized approach of vortex classification. Finally, we note that any vagueness in the current classification criteria does not affect the validity of any of the following discussion: e.g. the changes of all three-dimensional vortices show similar Re dependence (figure 17) regardless of the further differentiation between hairpins and different branch types. In addition, from our test, changing the cutoff magnitudes by up to 50 % does not affect the comparison of vortex statistics between different Re.

Figures 15 and 16 show the distributions of vortex axis lines, as identified by VATIP, of different classes for one typical snapshot of the lowest ($Re_\tau = 84.85$) and the highest Re ($Re_\tau = 400$), respectively. Direct visual inspection of these images indicates that the VATIP algorithm together with the vortex classification procedure in figure 12 has successfully identified and extracted all types of vortices and sorted them properly according to their axis topology. This resonates with the earlier tests by STG in figure 8. Comparing different classes of vortices, streamwise ones still dominate at both Re, but the method has no difficulty in finding all types of

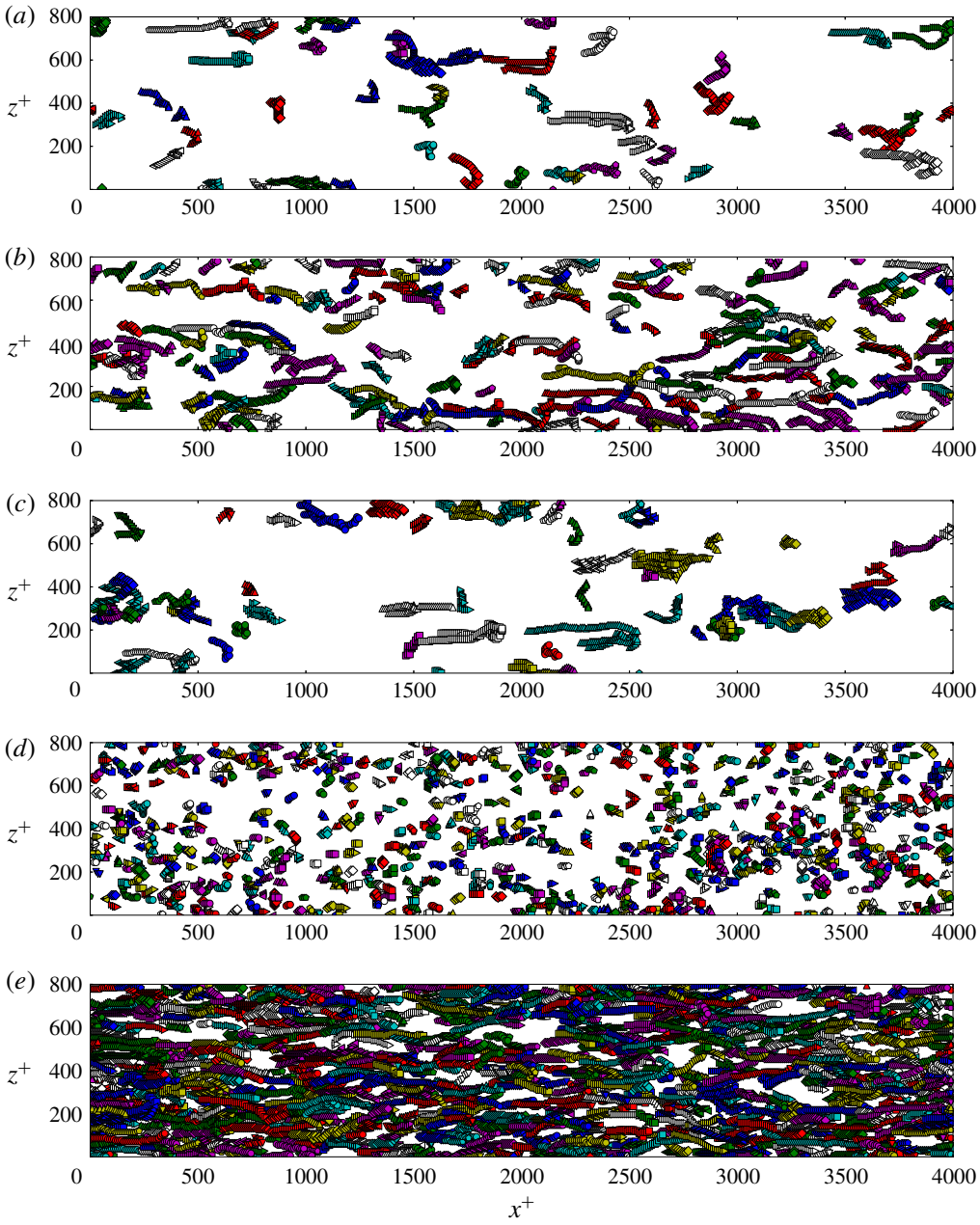

FIGURE 15. (Colour online) Distribution of vortex axis lines of different classes in a typical snapshot at $Re_\tau = 84.85$: (*a*) hairpins, (*b*) hooks, (*c*) branches (all types), (*d*) fragments and (*e*) streamwise vortices. Each marker represents one axis point. Individual vortices are differentiated by colours and marker types.

three-dimensional vortices. Unlike the case of boundary-layer flow where a so-called 'forest' of well-organized hairpins was observed (Wu & Moin 2009), in our DNS results clear-cut hairpins are the minority compared with other three-dimensional configurations. In particular, the asymmetric hook type significantly outnumbers all other three-dimensional vortex types, which validates the earlier empirical notion in the literature about the prevalence of incomplete or one-legged hairpins in plane

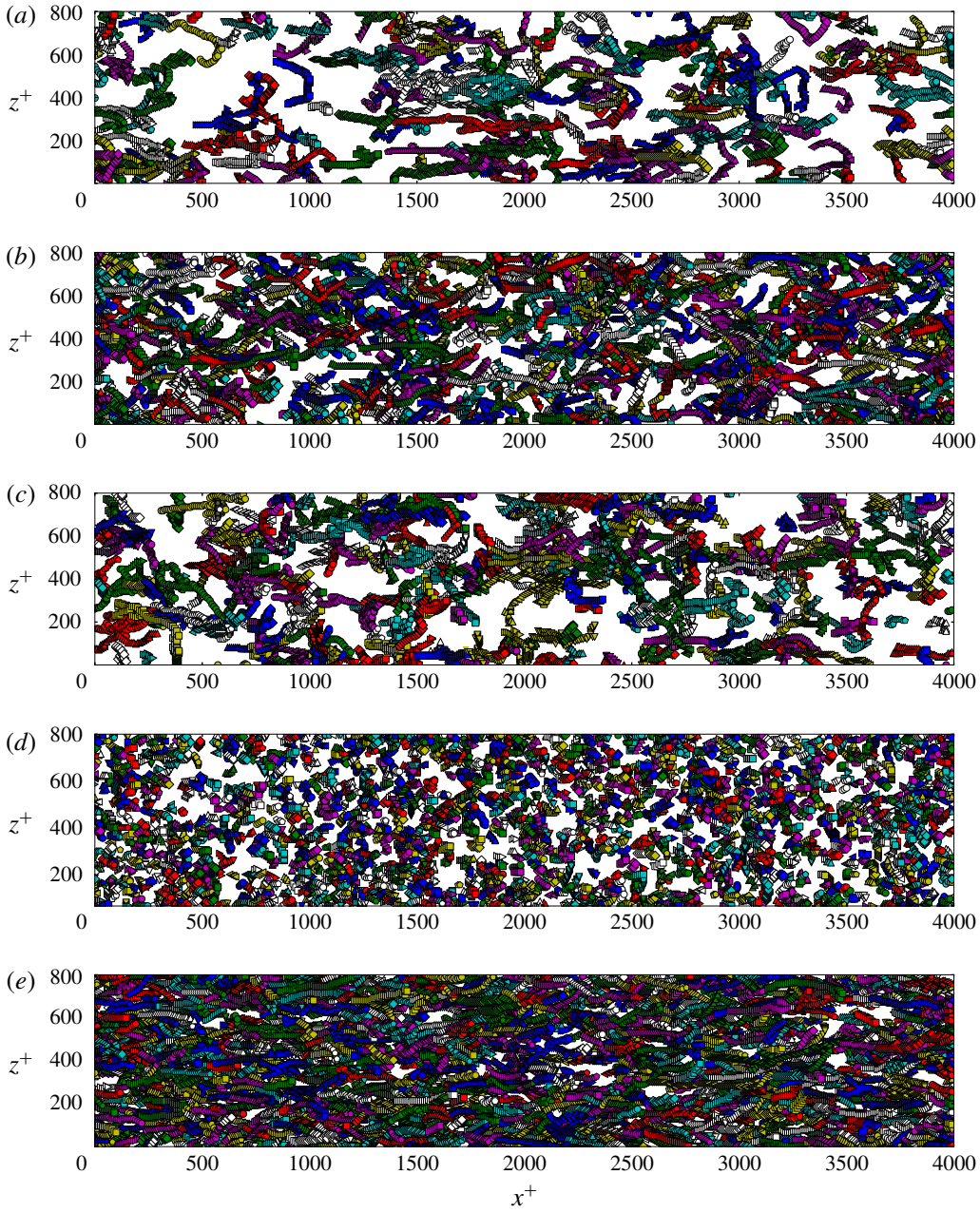

FIGURE 16. (Colour online) Distribution of vortex axis lines of different classes in a typical snapshot at $Re_\tau = 400$: (*a*) hairpins, (*b*) hooks, (*c*) branches (all types), (*d*) fragments and (*e*) streamwise vortices. Each marker represents one axis point. Individual vortices are differentiated by colours and marker types.

Poiseuille flow (Robinson, Kline & Spalart 1989; Robinson 1991). On the other hand, the frequent appearance of various irregular branch types demonstrates the importance of iterative propagation in all three dimensions – a central element of VATIP.

Comparing between the two *Re*, three-dimensional vortices (hairpins, hooks and branches) grow larger in size at higher *Re*. This can be attributed to the increasing thickness of the wall layer (more wall units in the wall-normal direction) which allows

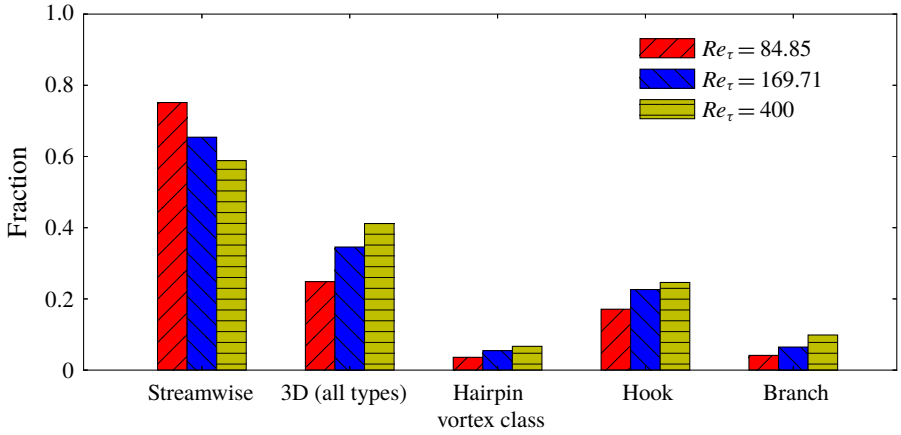

FIGURE 17. (Colour online) Fraction of vortices of different types by vortex numbers. Only vortices with streamwise length $l_x^+ > 50$ are included.

these vortices to further lift up and develop to a higher altitude. They also become more populous at higher Re. Indeed, even after factoring in the across-the-board increase of all vortices, the percentage share taken by three-dimensional vortices still steadily climbs. As shown in figure 17, with increasing Re, quasi-streamwise vortices take up a lower percentage (despite a net increase in their number) and their share is replaced by all types of three-dimensional vortices. From $Re_\tau = 84.85$ to 400, the share of hooks increases by approximately 50 % and those of hairpins and branches more than double. Recall that hooks are often considered as asymmetric or incomplete hairpins, their slower growth (compared with symmetric hairpins and branches) suggests that they are likely the outcome of the insufficient development of hairpins and may become less important at higher Re. Finally, in all Re cases, complete hairpins are significantly outnumbered by their mutants – hooks and branches.

Near-wall vortex growth is often characterized as a lift-up process: the downstream end of the vortex becomes detached from the wall and rises towards the outer layer, where it can further burst and generate new disturbances (Hinze 1975; Zhou *et al.* 1999). Lift-up extent of vortices at different wall layers can now be statistically analysed with the axis lines extracted by VATIP. Figures 18 and 19 show the joint PDF between the wall-normal positions of the heads and tails of all quasi-streamwise and three-dimensional vortices at different Re. The head position y^+_{head} is measured as the highest wall-normal position of all axis points, which is normally found at the downstream end; likewise, the tail position y^+_{tail} is the lowest position normally found at the upstream end. Obviously, the distribution can only sample the upper-left triangle of the domain. Vortices that have not lifted up are represented by the diagonal where the head position is levelled with the tail and regions closer to the ordinate, i.e. $y^+_{head} \gg y^+_{tail}$, and correspond to highly lifted up vortices.

For the lower $Re_\tau = 84.85$ case (figure 18), both the head and tail positions of quasi-streamwise vortices (panel *a*) concentrate at $10 \lesssim y^+ \lesssim 50$: i.e. within or near the buffer layer. Three-dimensional vortices (hairpins, hooks and branches) have a higher altitude and their distribution peaks at (15, 80): i.e. the tail (legs) stretches deep into the buffer layer while the head (arc in the case of hairpins) rises up into the log-law layer. In terms of distribution, the tails are concentrated at $y^+ < 25$ whereas the heads are found in a much broader range extending from $y^+ = 25$ to $y^+ > 80$. These observations can all carry over to the higher $Re_\tau = 400$ (figure 19) where, in

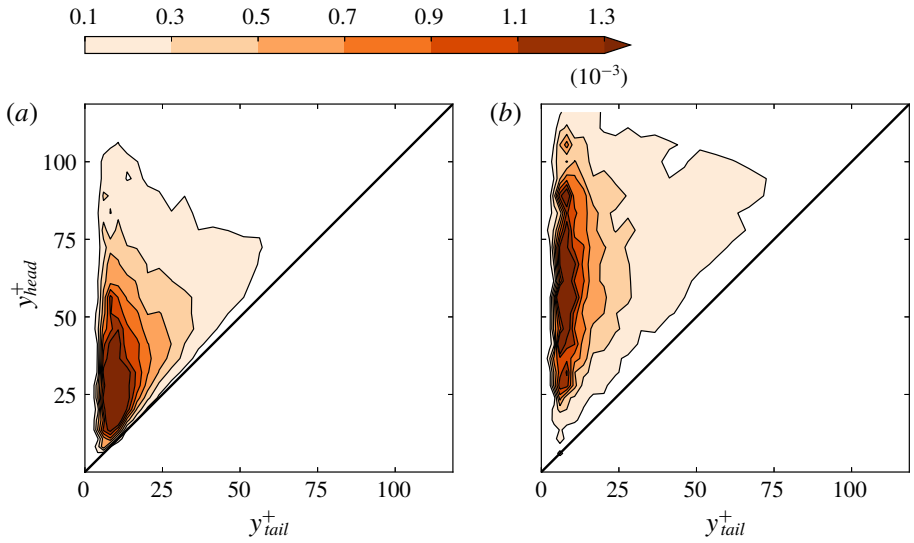

FIGURE 18. (Colour online) Joint probability density function (PDF) between the y^+ positions of the tail and the head of vortices at $Re_\tau = 84.85$: (*a*) quasi-streamwise and (*b*) three-dimensional vortices.

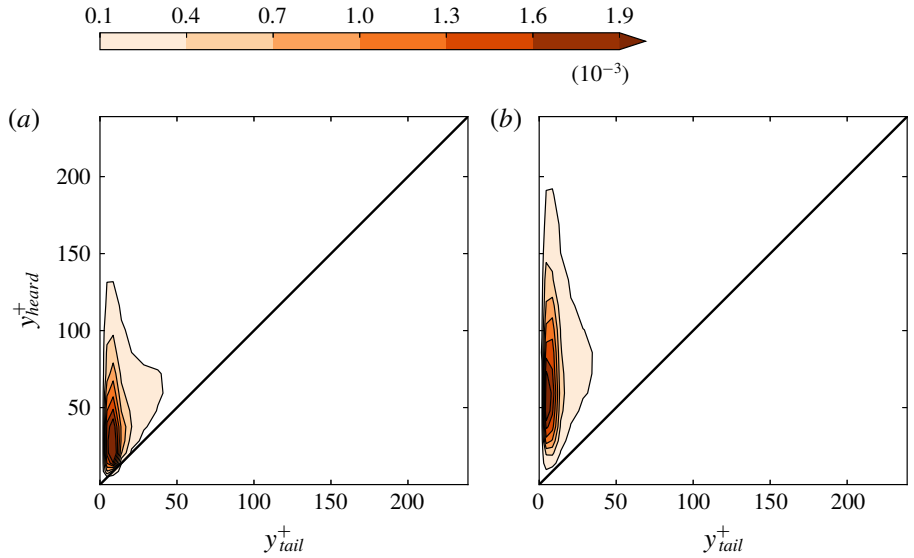

FIGURE 19. (Colour online) Joint probability density function (PDF) between the y^+ positions of the tail and the head of vortices at $Re_\tau = 400$: (*a*) quasi-streamwise and (*b*) three-dimensional vortices.

addition, the larger number of wall units in the y direction allows more room for vortex growth and their lift-up extent is easier to observe. Most quasi-streamwise vortices (figure 19*a*) are lying flat in the buffer layer (concentration peak in the lower-left corner) but two more concentration bands can be spotted: one lies along the ordinate up to $y^+ = 100$, indicating that a small fraction of streamwise vortices can lift up to the log-law layer; the other lies along the diagonal to even higher y^+, indicating the existence of flat-lying vortices at higher altitudes. Both bands are

also clearly visible in the three-dimensional case (figure 19*b*) but the vertical one is stronger over a broader range of y^+, meaning that these vortices are more likely to lift up and their heads can reach various altitudes. Vortex activities at $y^+ > 250$ are much weaker and thus not included in figure 19. (Alternatively, following the example of Lozano-Durán *et al.* (2012), Lozano-Durán & Jiménez (2014), one may apply non-uniform Q threshold values – with lower thresholds for the bulk – for a complete picture.) Observations from this analysis largely confirm the earlier empirical depiction by Robinson (1991) that quasi-streamwise vortices dominate the buffer layer and hairpin-like vortices are more likely to be found in the log-law layer and beyond. Robinson (1991) conceived the log-law layer to be comprised of a mix of streamwise and hairpin vortices, whereas we are able to more clearly show that streamwise vortices are only concentrated in the lower log-law layer ($y^+ < 50$) and three-dimensional vortices can rise up to a variety of altitudes.

4.4. *Vortex organization through clustering analysis*

Previous observations of LSMs and VLSMs ignited an immense interest among researchers in understanding the organization patterns of coherent structures (Jiménez 1998; Kim & Adrian 1999; Lee *et al.* 2014). Given the specific information, available from VATIP, about the location and conformation of axis lines representing individual vortices, we adapt the DBSCAN (density-based spatial clustering of applications with noise) algorithm (Ester *et al.* 1996) – a widely used clustering analysis method in data mining and machine learning – to VATIP results for understanding the clustering patterns of vortices. (Structures classified as fragments according to figure 12 are not considered in this analysis.)

The standard DBSCAN algorithm groups scattered points in space into clusters based on their spatial proximity and mutual relationship. Two points that are close to each other (within a cutoff distance ε) are considered as neighbours. Points inside a cluster are known to have many neighbours. Points with at least $N_{c,min}$ neighbours are thus labelled as 'core points' and all interconnected (in the sense of mutually neighbouring) core points are grouped into one cluster. (Both ε and $N_{c,min}$ are user-specified parameters.) If a point does not qualify as a core point by itself but is neighbour to one or more core points, it is labelled as a 'border point' which resides on the surface of a cluster. Border points are grouped to the same cluster as their nearest neighbouring core point. Points that do not neighbour any core points and are not core points themselves are isolated outliers not belonging to any cluster.

Since the VATIP output contains not simple sizeless points but complex axis lines representing vortex geometry and topology, the simple distance criterion used for neighbour identification needs to be adapted. We consider two vortices to be neighbours if the minimum distance between any two axis points – one on each axis line – does not exceed $\varepsilon = 4r_v$ which is only slightly larger than the detection cone diameter used in VATIP tracking ($2 \times 1.5r_v = 3r_v$). We have tested a wide range of ε and found that for ε as low as $3.5r_v$ nearly all vortices in the domain, from both sides of the channel, are interconnected into the same neighbour network: i.e. for $N_{c,min} = 1$ and any $\varepsilon \geqslant 3.5r_v$, the DBSCAN algorithm will identify one supersized cluster that includes nearly all vortices. The fact that a cutoff distance of the same order as the vortex diameter would connect all vortices is not surprising, considering the level of crowdedness found in their distribution (see figures 15 and 16). Ideally, we would also need to test the ε-dependence at other $N_{c,min}$ levels. However, our priority is to understand the importance of multi-vortex cooperation (instead of inter-vortex

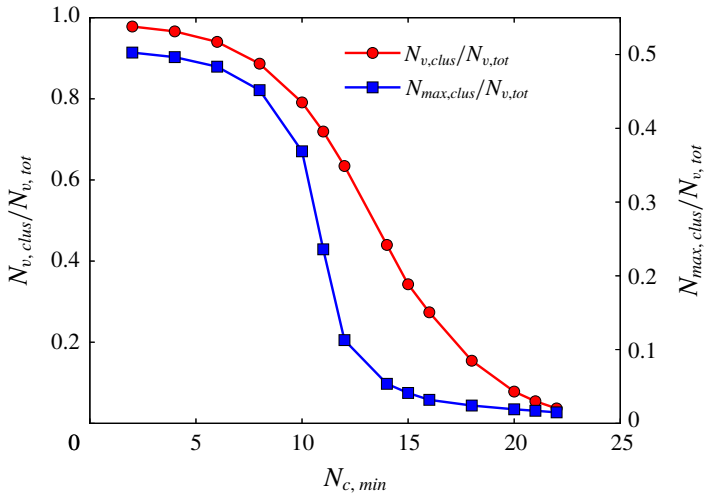

FIGURE 20. (Colour online) Dependence of DBSCAN clustering analysis on $N_{c,min}$ ($Re_\tau = 169.71$): left/red/circle – number fraction of all vortices grouped into clusters; right/blue/square – number fraction of vortices in the largest identified cluster.

distance, which we knew would be close). Therefore, given the limited scope of this investigation, we will focus here on the $N_{c,min}$-dependence of the clustering results at a constant $\varepsilon = 4r_v$.

With increasing $N_{c,min}$, less vortices are qualified as core vortices (counterpart to core points in the standard DBSCAN) and more become isolated outliers. This first leads to the shrinkage of all clusters: for the same total number of vortices $N_{v,tot}$, the number of vortices assigned to clusters $N_{v,clus}$ decreases (figure 20). At $N_{c,min} = 2$ (lowest level shown in figure 20), $N_{v,clus}/N_{v,tot}$ starts at close to 1 (nearly all vortices are grouped into clusters) and steadily drops afterwards towards 0. The number of vortices contained in the largest cluster $N_{max,clus}$ is also calculated. In figure 20, $N_{max,clus}/N_{v,tot}$ starts at $\approx$0.5, because the channel flow geometry has two boundary layers (near each wall) and at the lowest $N_{c,min}$ vortices near each wall are nearly all grouped into one super-cluster. The decline pattern of this profile is very different from that of $N_{v,clus}/N_{v,tot}$ – it drops sharply in a small window of $N_{c,min} = 8 \sim 14$ with the steepest slope found between $N_{c,min} = 10$ and 12. This faster decline cannot be solely accounted for by the overall reduction of qualifying core vortices (otherwise $N_{max,clus}/N_{v,tot}$ would have the same slope as $N_{v,clus}/N_{v,tot}$). Indeed, the steeper descent indicates a sudden disintegration of the dominant clusters into smaller pieces. As $N_{c,min}$ increases beyond $\approx$8, some vortices in the structure, which are not as highly intertwined as most others in the vortex cluster network, are disqualified as core vortices. Removing those 'bridge' vortices dismantles the cluster network into several well-defined and strongly coupled clusters that are much smaller in size. This effect is most clearly seen from the ratio between these two profiles, plotted in figure 21. For all three Re_τ tested, $N_{max,clus}/N_{v,clus}$ is initially flat at low $N_{c,min}$, indicating that, within this regime, drops in both profiles in figure 20 are attributed to the overall reduction of clustered vortices. Disintegration of the dominant clusters starts when the $N_{max,clus}/N_{v,clus}$ profile turns downwards, which for $Re_\tau = 169.71$ occurs at $N_{c,min} \approx 8$. The process finishes as the curve reaches its minimum at $N_{max,clus}/N_{v,clus} = 0.1 \sim 0.15$: the domain is now populated by $O(10)$ well-defined clusters with comparable size (see figure 22*c* for roughly half of the clusters on one side of channel). After the

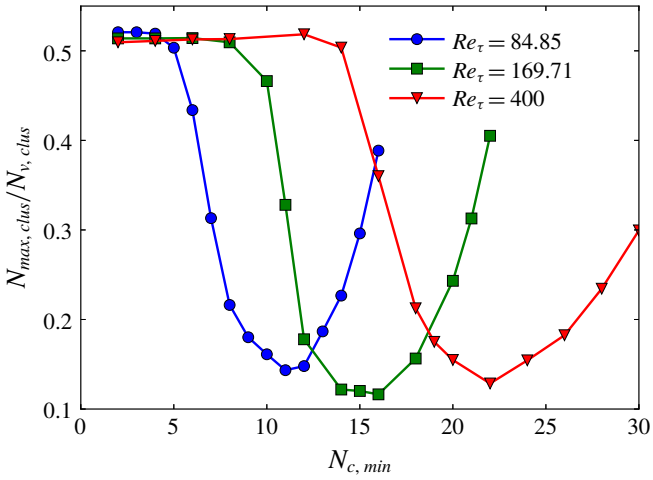

FIGURE 21. (Colour online) Number fraction of vortices included in the largest cluster among vortices in all clusters as a function of $N_{c,min}$.

minimum the profile rises again as a result of smaller clusters gradually being eliminated by the increasingly stringent $N_{c,min}$ cutoff.

The vortex cluster configuration during this disintegration process with increasing $N_{c,min}$ is shown in figure 22 for $Re_\tau = 169.71$. Consistent with our earlier analysis, at $N_{c,min} = 2$ all vortices on one side of the channel are interconnected (by their neighbouring network) into a super-cluster. Disintegration of the network is observed at $N_{c,min} = 12$ (>8 where it starts). At $N_{c,min} = 15$ (figure 22*c*), $N_{max,clus}/N_{v,clus}$ reaches its minimum (figure 21) and the disintegration process has completed with a number of clear vortex clusters remaining unbroken. Much space can be found between the clusters where the turbulent flow field is occupied by unclustered vortices. The Reynolds shear stress, averaged over the wall-normal (y) direction,

$$\bar{\tau}_{xy} = -\int_0^1 v_x'(x, y, z, t) v_y'(x, y, z, t)\, \mathrm{d}y \tag{4.4}$$

is shown with contour lines in the images. Spots with strong $\bar{\tau}_{xy}$ (dense contour lines) are found within or immediately around these vortex clusters, indicating their strong contribution to the Reynold stress generation. Interestingly, the characteristic length (in the x direction) of these clusters seems to be between 500 and 1500 wall units, which is at the same level as the typical streamwise length scales of LSMs reported in the literature (Adrian 2007; Lee *et al.* 2014). The existence of such clusters consisting of a large number ($O(10)$ or higher; see figure 23) of vortices strongly intertwined through multi-body interactions ($>N_{c,min} = 15$ neighbours, in the case of $Re_\tau = 169.71$, with close contacts between their axis lines for the core vortices) is consistent with the hypothesis that LSMs are results of the cooperative dynamics involving many vortices organized as 'packets' (Kim & Adrian 1999). However, these 'packets', as discussed below, are not composed of well-aligned hairpin vortices with their classical shape. In addition, clear evidence for clustering is found in this study for Re_τ all the way down to below 100, suggesting that cooperative dynamics between vortices is a universal feature for wall turbulence not limited to the high-Re regime. Meanwhile, VLSMs are often conjectured to occur at a higher level of organization involving the alignment

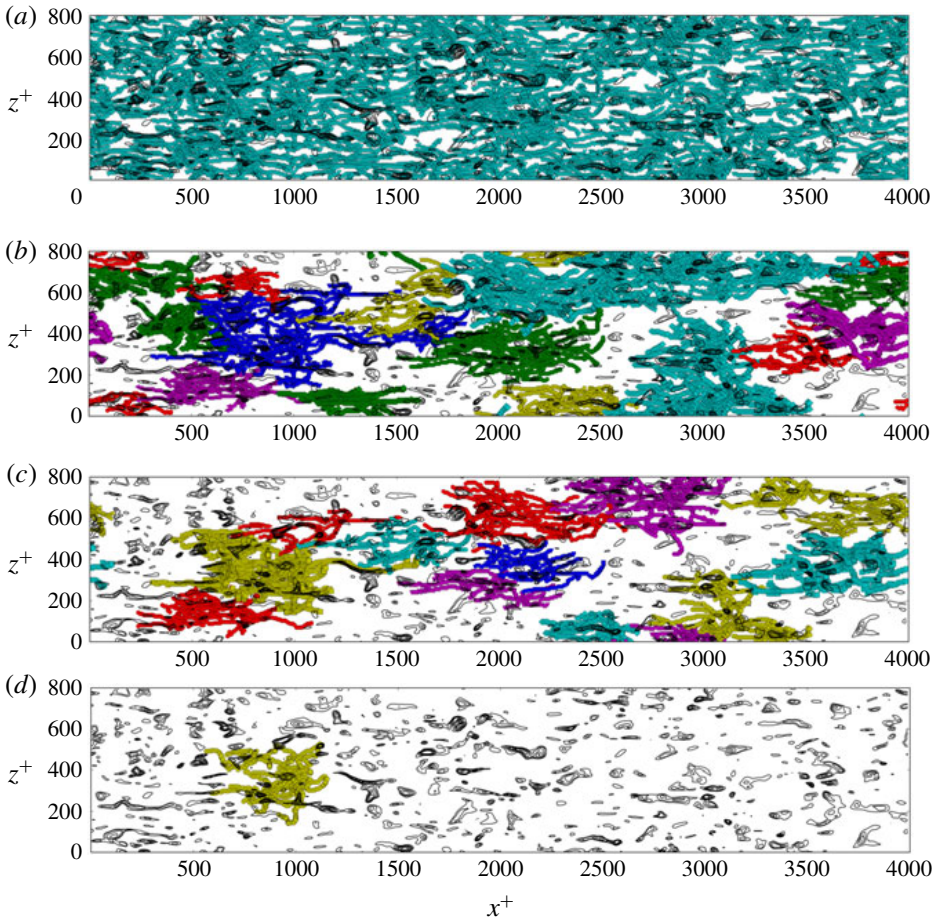

FIGURE 22. (Colour online) Distribution of vortex clusters (on one side of the channel and from a typical instantaneous flow image) at $Re_\tau = 169.71$ identified by DBSCAN with (*a*) $N_{c,min} = 2$, (*b*) $N_{c,min} = 12$, (*c*) $N_{c,min} = 15$ and (*d*) $N_{c,min} = 21$. Individual clusters are differentiated by colour. Black lines show the contours of y-average Reynolds shear stress $\bar{\tau}_{xy}$ (4.4) at 11 equispaced levels from 0.5×10^{-5} to 1.25×10^{-4}; higher contour line density corresponds to higher magnitudes.

of multiple LSMs (Kim & Adrian 1999; Lee *et al.* 2014). This would correspond to the cooperative organization involving multiple vortex clusters in this study. The length scale of VLSMs is comparable to or larger than the current domain size and they were previously studied mostly at much higher Re_τ ($O(10^3)$). For these reasons, they are not discussed here. As $N_{c,min}$ further increases to 21, all clusters are now eliminated except the strongest one, which has shrunken in size but still clearly marks the location of strong Reynolds stress activity.

Note that the term 'cluster' has a different meaning here than that in earlier studies of three-dimensional vortex analysis, such as Del Álamo *et al.* (2006) where clusters referred to the interconnected structures with overlapping vortex volumes identified by the scalar identifier (Δ in that study and Q here), regardless of the individual identities of vortices or their conformation and topology. In our analysis, a cluster is defined as individual vortices grouped together based on the existence of a mutually interacting (neighbouring) network between multiple vortex objects rather than a pure spatial-proximity criterion. There are likely close connections between these

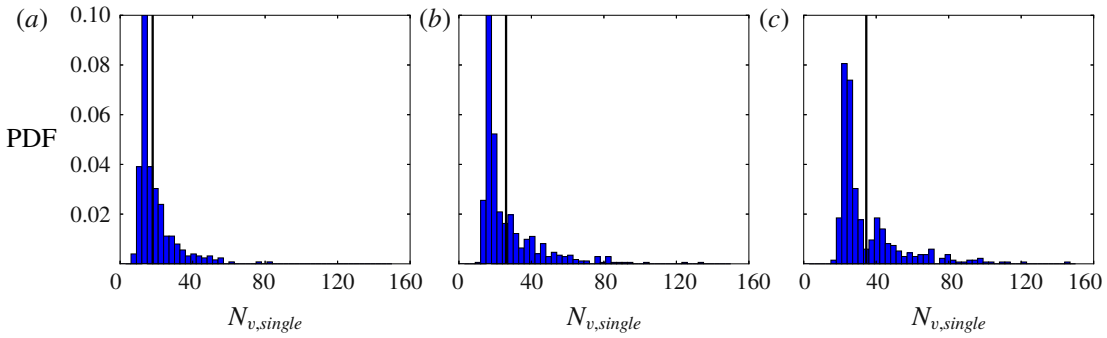

FIGURE 23. (Colour online) Probability density function of the number of vortices in a single cluster at (*a*) $Re_\tau = 84.85$, (*b*) $Re_\tau = 169.71$ and (*c*) $Re_\tau = 400$. The vertical line marks the mean value.

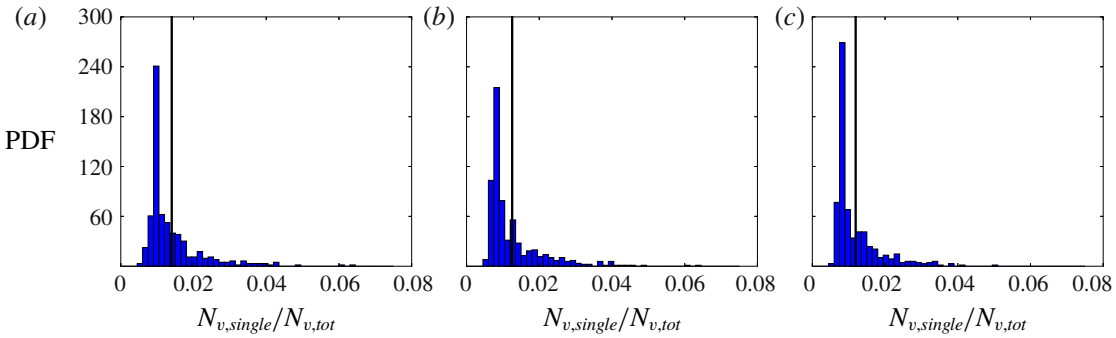

FIGURE 24. (Colour online) Probability density function of the number of vortices in a single cluster normalized by the total number of vortices in the domain at (*a*) $Re_\tau = 84.85$, (*b*) $Re_\tau = 169.71$ and (*c*) $Re_\tau = 400$. The vertical line marks the mean value.

two interpretations, but at this point, a direct comparison is not possible, because, as further discussed in § 4.6, the current VATIP algorithm can only capture a subset of structures analysed in Del Álamo *et al.* (2006) that are directly generated from the lift-up-from-wall process. The strength of the current approach is its access to the information of individual constituting vortices, which we discuss below.

Unless otherwise noted, we pick the $N_{c,min}$ value at the minimum in each $N_{max,clus}/N_{v,clus}$ curve (figure 21) – i.e. $N_{c,min} = 11$, 15 and 22 for $Re_\tau = 84.85$, 169.71 and 400, respectively – for the DBSCAN analysis, which is the point where the percolating super-cluster has been fully disintegrated into unbreakable clusters while most individual clusters are not yet eliminated. (This choice is in the same spirit as the percolation analysis of Lozano-Durán *et al.* (2012) explained in § 4.5.) The PDF of the number of vortices constituting a single cluster $N_{v,single}$, shown in figure 23, is clearly skewed to the right with the most probable value at $O(10)$ but in some extreme cases with $O(100)$ vortices in each cluster. The average $N_{v,single}$ increases with Re and is $\approx$18, 26 and 35, respectively, from the lowest to the highest Re_τ tested. Note, however, that the total number of vortices in the domain $N_{v,tot}$ also increases with Re. Indeed, when $N_{v,single}$ is normalized by $N_{v,tot}$ (figure 24), the distribution profile becomes nearly the same between different Re (mean value at 0.014, 0.013 and 0.012 for $Re_\tau = 84.85$, 169.71 and 400, respectively). Since the domain size of different Re is kept the same in inner units (table 1), this observation, that the

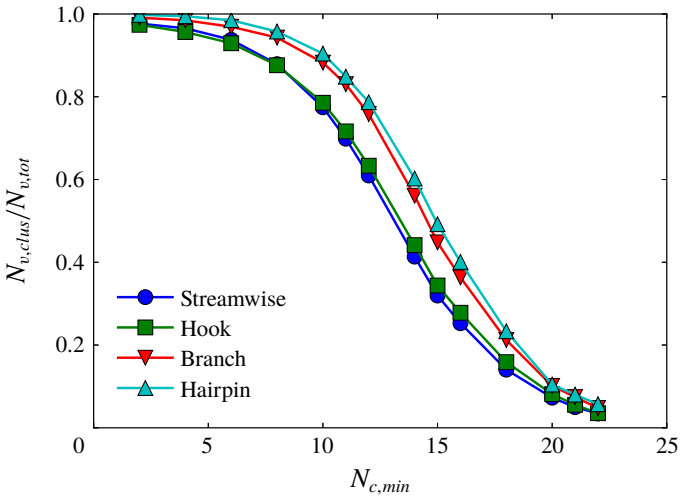

FIGURE 25. (Colour online) Number fraction of vortices of different types grouped into clusters out of the total number of all vortices of the same type in the domain ($Re_\tau = 169.71$).

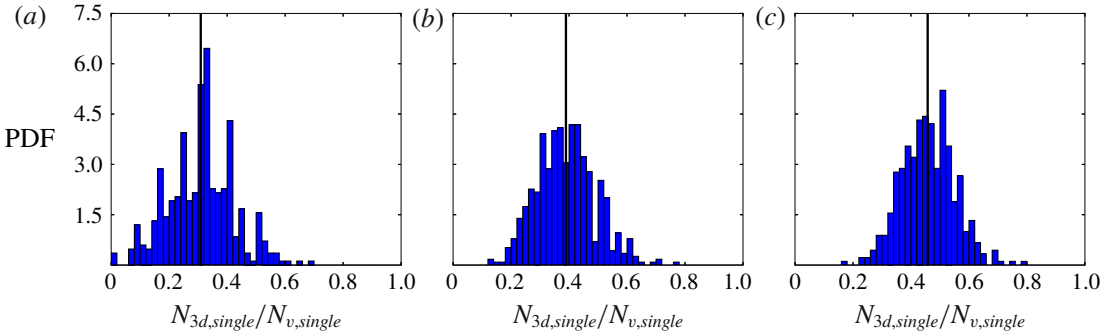

FIGURE 26. (Colour online) Probability density function of the number fraction of three-dimensional vortices in a single cluster at (*a*) $Re_\tau = 84.85$, (*b*) $Re_\tau = 169.71$ and (*c*) $Re_\tau = 400$. The vertical line marks the mean value.

average cluster size in terms of the number fraction of vortices in each cluster (out of all vortices filling the domain), remains roughly constant, suggests that the cluster size is more or less the same in inner units (i.e. streamwise length within $500 \sim 1500$; see figure 22) within the Re range tested (further demonstrated in figure 27).

Comparing vortices of different types (figure 25), hairpins and branches are more likely to be included in a cluster than both streamwise and hook vortices. Since hooks are essentially incomplete or asymmetric hairpins that are also highly lifted up, this indicates that the large dimensions of hairpins and branches are likely the key factor determining their higher clustering tendency. In particular, their wide span in the z direction exposes them to vortices from a wider flow region, which enables them to play a central role in stitching more vortices into a cluster. As seen in figure 26, within a single cluster, a significant fraction of the vortices belong to the three-dimensional classes (hairpins, branches or hooks). This fraction increases with Re and at $Re_\tau = 400$, on average nearly half of the vortices in each cluster are three-dimensional ones. However, note that hooks and branches significantly

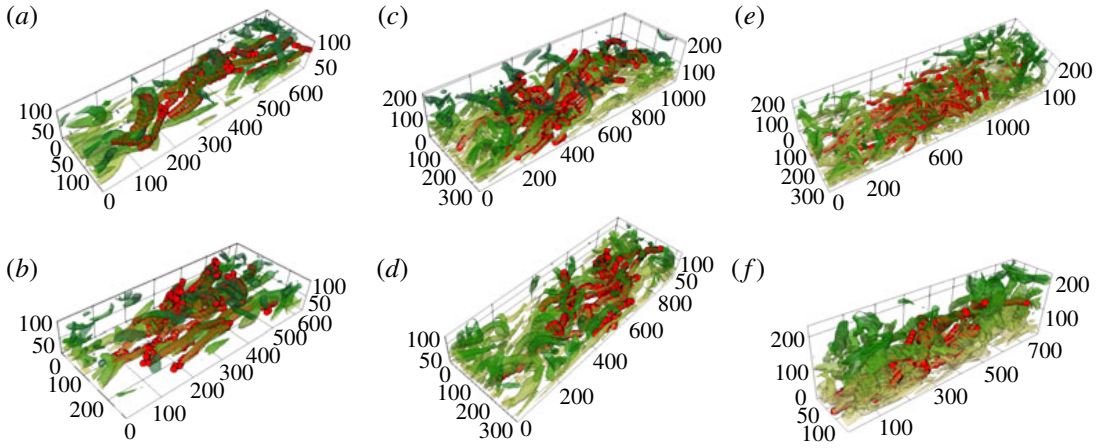

FIGURE 27. (Colour online) Representative images of vortex clusters identified by DBSCAN at (*a*,*b*) $Re_\tau = 84.85$, (*c*,*d*) $Re_\tau = 169.71$ and (*e*,*f*) $Re_\tau = 400$. Isosurfaces show all vortices in the viewable region (colour varies from light to dark with y^+); red dots show the axis lines of vortices in the identified cluster.

outnumber canonical hairpins (figure 17), the hypothesized picture of packets of clean-cut hairpins (Adrian 2007) forming the LSMs is not seen at least at the current Re range.

Direct images of representative vortex clusters are shown in figure 27 where vortices forming the particular cluster are highlighted by explicitly showing their axis lines. Consistent with our earlier observations, these clusters (at different Re) all have a streamwise length in the range of 500–1500 wall units. Two typical organization configurations are observed. In the first (panels *a*,*f*), different vortices forming the cluster have their axis lines braided together along the streamwise direction. These clusters have a shape of twisted doughnuts and they remain slender (narrow in the z direction) while extending downstream for $O(1000)$ wall units. For the second type, which is more frequently observed, other than the downstream twisting, the clusters also expand in the spanwise direction by connecting more vortices through the wider vortex types (hairpins and branches).

Finally, we note that the analysis of vortex clustering and organization in this section is still preliminary and limited in scope. It is intended to provide some first insight into how the axis-line information extracted by VATIP can be used to address some of the most important outstanding questions in turbulent dynamics (Jiménez 2018). Further research is needed to better connect these observations with the existing conceptual models and results from other structure analysis techniques.

4.5. *Determination of parameters and settings in VATIP*

After presenting the main results, we are now ready to assess the robustness of VATIP tracking outcomes and discuss the procedure for choosing its parameters and settings. There are two major adjustable parameters in the method: (i) the threshold magnitude $Q_{threshold}$ for vortex identification with the Q-criterion and (ii) the cutoff cone radius r_{cone} used in the axis-line propagation search (figure 2). In addition, sensitivity to grid sizes and the selection of the search starting plane will also be examined.

The choice of the threshold for Q (or any other vortex identifier) has been widely discussed in the literature for the purpose of vortex visualization. It is a common

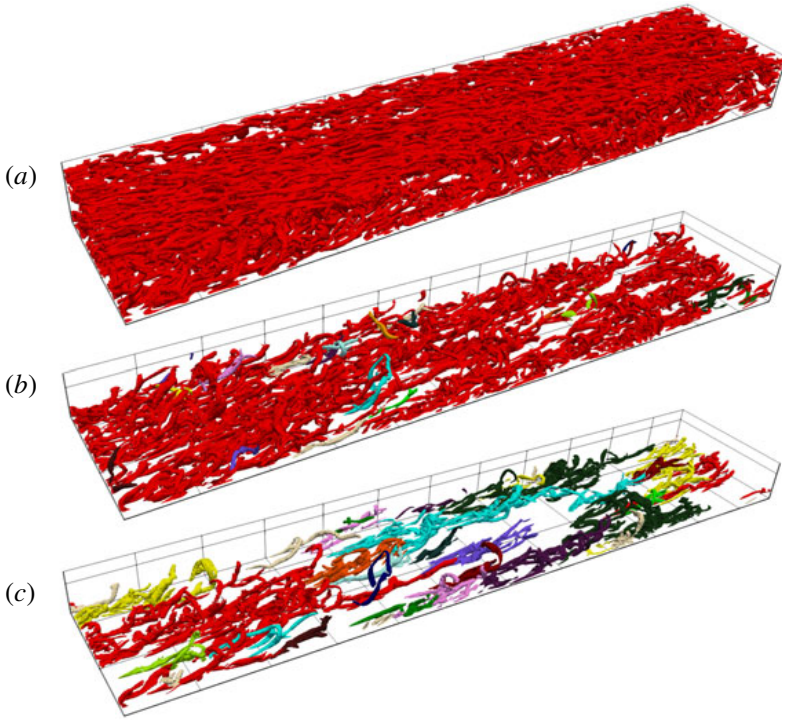

FIGURE 28. (Colour online) Vortex disintegration with increasing $Q_{threshold} = HQ_{rms}$ at $Re_\tau = 169.71$: (*a*) $H = 0.2$, (*b*) $H = 0.4$ and (*c*) $H = 0.7$. Interconnected vortex tube structures are coded with the same colour. For clarity, only the largest vortices that cumulatively account for 80 % (for *a*,*b*) or 60 % (for *c*) of the total vortex volume are shown. For (*b*,*c*), only vortices from the bottom half of the channel are shown.

practice to choose a threshold in proportion to its r.m.s. value in the flow field

$$Q_{threshold} \equiv HQ_{rms}, \tag{4.5}$$

where H in this study is chosen based on the percolation analysis, proposed in Lozano-Durán *et al.* (2012) (from which we also borrowed the notation H). When H is low, the identified vortex regions interconnect with one another and form a percolating network across the domain (figure 28*a*). With increasing H, the 'necks' bridging stronger vortex cores gradually break to reveal individual groups of vortices (figure 28*b*,*c*); meanwhile, a higher threshold also erases many weaker vortices from the view. A percolation diagram (figure 29) plots the ratio of the volume occupied by the largest interconnected structure (V_{max}) to that of all vortex regions (V_{tot}) as a function of H. This value starts at 1 at the low H end where all structures are interconnected into a complete percolating network. Increasing H reduces both V_{max} and V_{tot}, whereas the decrease of their ratio V_{max}/V_{tot} reflects the disintegration of larger interconnected structures into smaller separate pieces. The latter clearly dominates the window of $0.3 \lesssim H \lesssim 0.7$ where the sudden disintegration of the largest structure into multiple objects is reflected in a steep descent in V_{max}/V_{tot}. This window provides the best choices for H, in which individual objects are separate and identifiable whereas the most important vortex structures are not yet erased (as what will happen at higher H) (Lozano-Durán *et al.* 2012).

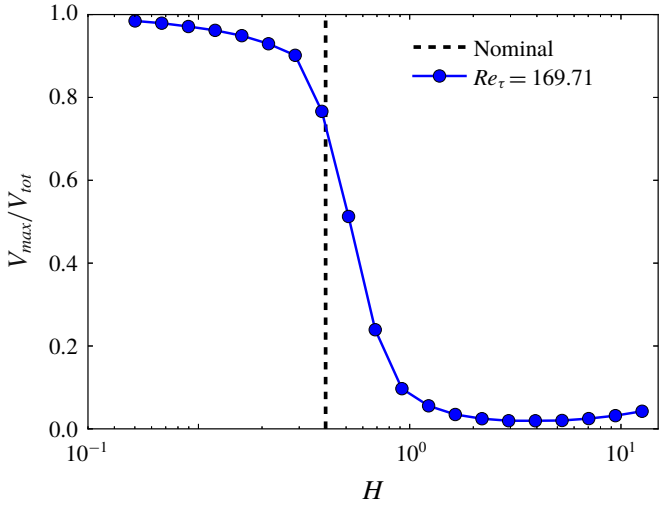

FIGURE 29. (Colour online) Percolation diagram for $Re_\tau = 169.71$. The vertical dashed line marks the $HQ = 0.4Q_{rms}$ used in this study.

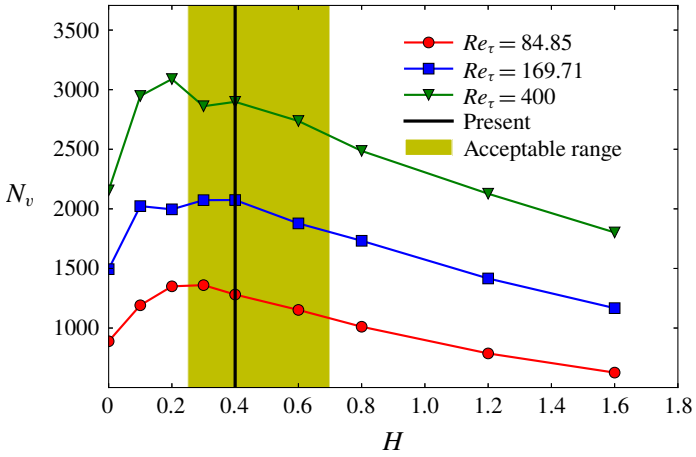

FIGURE 30. (Colour online) Average number of vortices (excluding fragments) detected by VATIP in each instantaneous flow field as a function of H (with $r_{cone} = 1.5r_v$).

Also as a result of the competition between vortex shrinkage and disintegration, the average number of vortices identified by VATIP in each flow domain N_v displays a non-monotonic dependence on H (figure 30). N_v initially increases with H, reflecting the splitting of vortex objects. After reaching a maximum at $H \approx 0.2$, N_v starts to decline because the identified vortices shrink in size with increasing H and are increasingly categorized as fragments. This effect becomes more dominant at higher H after the disintegration of the percolating network. Within the acceptable range of $H = 0.3 \sim 0.7$ – as identified above by the percolation analysis – the drop of N_v is relatively mild ($\lesssim$10 % for the two higher Re_τ). More importantly, as shown later, all major conclusions from the study remain intact within this range of H. It is worth noting that the peak of N_v is found out of this range at a slightly lower H: i.e. the main vortex disintegration events are detected at a slightly lower H using VATIP than the percolation analysis. This is because VATIP is more sensitive to the breakage

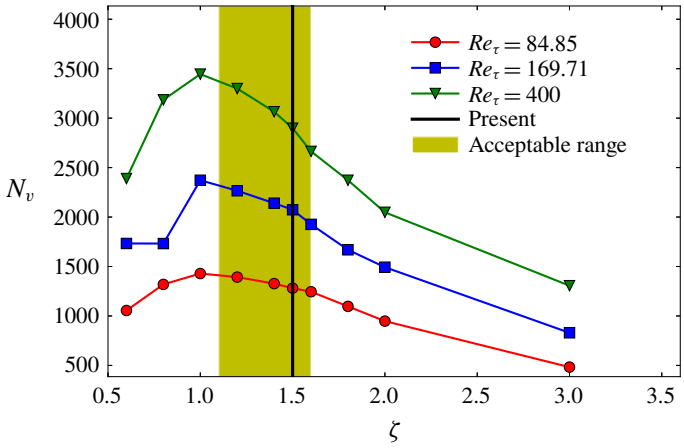

FIGURE 31. (Colour online) Average number of vortices (excluding fragments) detected by VATIP in each instantaneous flow field as a function of ζ (with $Q_{threshold} = 0.4Q_{rms}$).

between vortex structures: neighbouring vortices could well overlap in their shells and be grouped into the same interconnected structure in figure 28 while their axis lines do not have topological connection. This also explains, in part, why N_v does not start from 1 at $H = 0$ in figure 30. (Another reason – further discussed in § 4.6 – is that VATIP is designed with wall-generated vortices in mind and may not fully capture the connections between weaker and more isotropic vortex structures in the bulk region, which are only unveiled at very low H.) Taking this into account, the optimal H pick should be slightly lower than that for the steepest descent in figure 29. Therefore, $H = 0.4$ is chosen in this study for VATIP tracking (in comparison with $H = 0.7$ used in Zhu *et al.* (2018) for vortex visualization). Note that in figure 30, N_v is nearly constant in the range of $H = 0.3 \sim 0.4$.

The cone size is chosen based on the average radius of the vortex tubes (3.1)

$$r_{cone} \equiv \zeta r_v, \tag{4.6}$$

where ζ is expected to be larger than (but of the same order of magnitude as) 1 to account for vortex size variations. The average number of vortices identified by VATIP in each flow domain N_v is also non-monotonic with increasing ζ (figure 31). For $\zeta < 1$, many well-defined vortices are broken into pieces and excluded as fragments. Meanwhile, at $\zeta \gg 1$, false connection between separate vortices becomes more common and N_v decreases with ζ. Interestingly, for all Re_τ tested, N_v reaches its maximum at exactly $\zeta = 1$, indicating that r_v calculated by (3.1) does provide an accurate measurement of the vortex radius. We recommend the range of $\zeta = 1.2 \sim 1.6$ for VATIP where the decline of N_v is modest (compared with higher ζ) and, more importantly, all major physical observations are consistent with changing ζ (shown below). For $\zeta = 1.5$ used in this study, the resulting r^+_{cone} is approximately 15, 16 and 18 wall units for $Re_\tau = 84.85$, 169.71 and 400, respectively. For comparison, Jeong *et al.* (1997) used $r^+_{cone} \approx 10$ for their streamwise-only search at $Re_\tau \approx 180$, which is equivalent to $\zeta \approx 1$. The larger ζ used in VATIP is necessitated by the expansion of the search to all three spatial dimensions. First, dislocation between successive axis points is typically larger around the bends or turns of the axis line, which does not occur in a unidirectional search along nearly straight lines. Second, inclusion of highly lift-up hairpin-like vortices extends the search deep into the log-law layer,

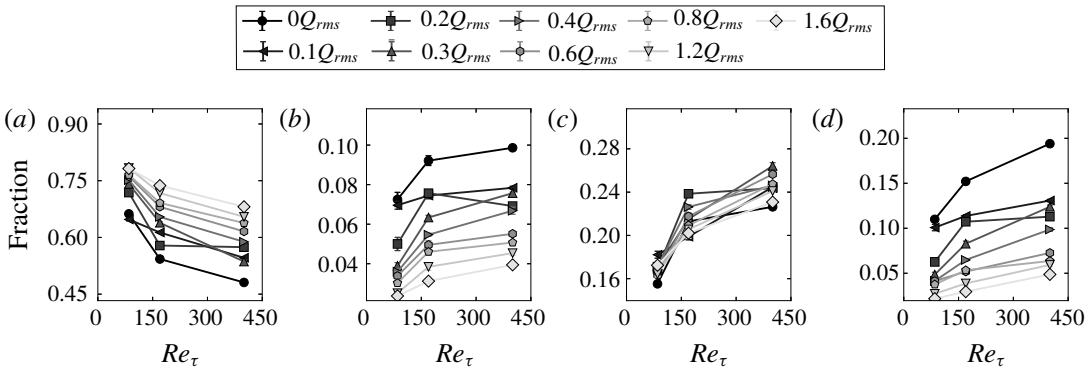

FIGURE 32. Number fraction of different vortex types (excluding fragments) as a function Re identified by VATIP with different H (and a constant $\zeta = 1.5$): (a) streamwise, (b) hairpin, (c) hook and (d) branch.

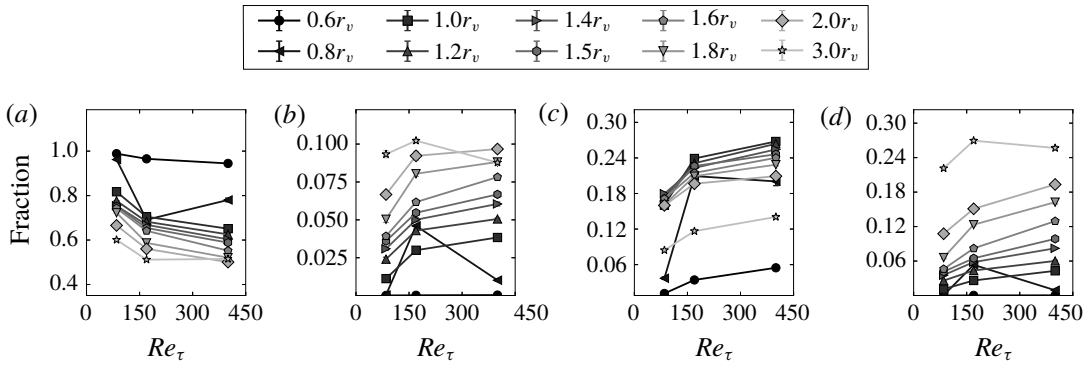

FIGURE 33. Number fraction of different vortex types (excluding fragments) as a function Re identified by VATIP with different ζ (and a constant $H = 0.4$): (a) streamwise, (b) hairpin, (c) hook and (d) branch.

where the vortex diameters are often larger compared with the streamwise vortices in the buffer layer. Lastly, a streamwise search only looks for new axis points in the yz-plane where the numerical grids are typically more refined (than the x direction) in DNS. Searches in other directions need to accommodate axis-point dislocation in the x direction: with the coarser mesh of Jeong *et al.* (1997), $r^+_{cone} = 10$ covers less than one x-grid spacing – $\delta^+_x = 17.7$: i.e. no dislocation in x would be allowed. Our experience also shows that $\zeta = 1$ would break well-defined hairpin vortices (such as in STG) into pieces.

The similarity between N_v profiles of different Re_τ in both figures 30 and 31 suggests the robustness of VATIP at least within the Re range tested. In figures 32 and 33, it is clear that within the recommended ranges of $H = 0.3 \sim 0.7$ and $\zeta = 1.2 \sim 1.6$, changes in vortices of different types with increasing Re follow the same consistent trend with different H and ζ. Clear disruption to the trend is only observed in cases well out of these ranges: most notably $H = 0.2$ in figure 30 and $\zeta = 0.8$ and 3.0 in figure 31. Quantitative magnitudes of the profiles do depend on H and ζ, which is very much expected. As illustrated in figure 34, adjusting these parameters inevitably changes the lengths of vortex branches and legs, to which the classification scheme of figure 12 is very sensitive: missing one axis point at the branch end could result in a vortex being classified as a hook rather than hairpin, or

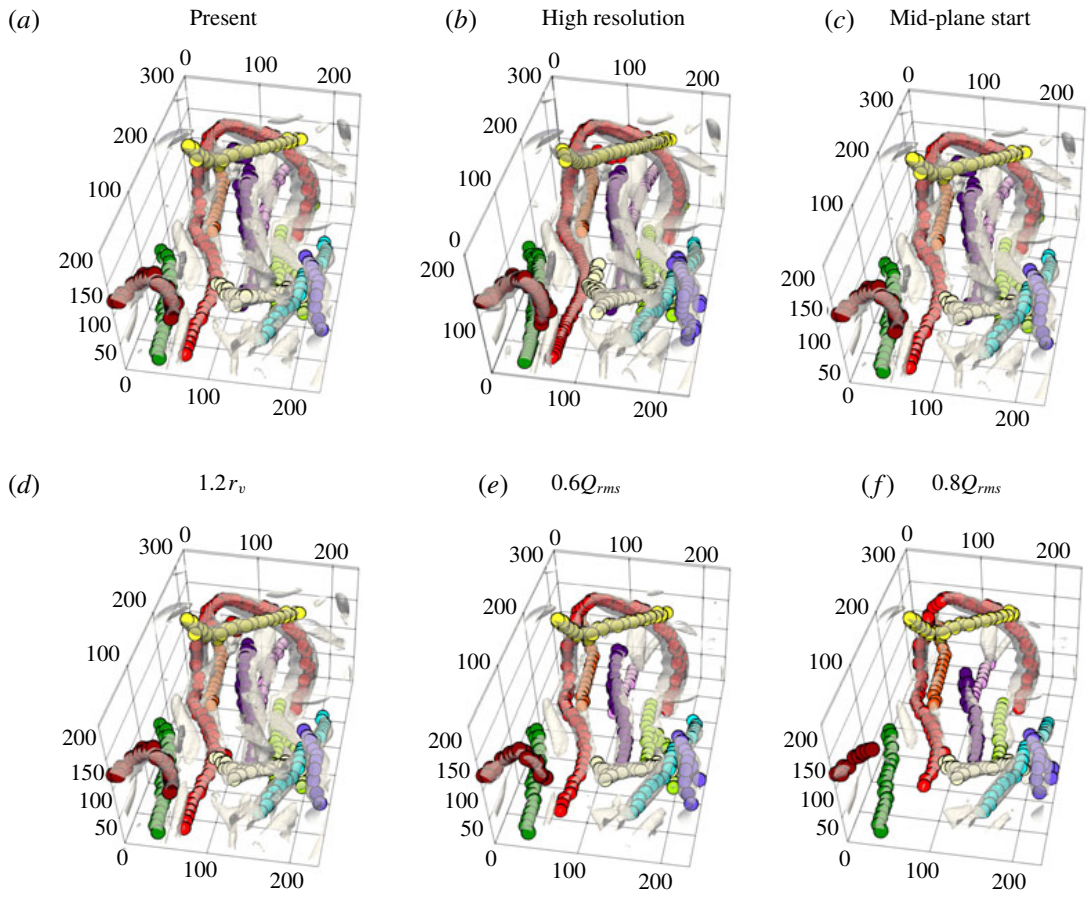

FIGURE 34. (Colour online) Effects of parameters and settings on VATIP tracking results in a representative flow region at $Re_\tau = 169.71$ (note: panel (f) is out of the recommended range of H). Dots represent axis points identified by VATIP (different colours for different vortices) and grey tubes are the isosurfaces of $Q = HQ_{rms}$ (same H used in VATIP). Partial vortices (with parts extending out of the view box) are not included in VATIP tracking.

even a fragment rather than a vortex. Nevertheless, quantitative differences between curves are significantly smaller (mostly contained within a few percentage points) in the ranges of $H = 0.3 \sim 0.7$ and $\zeta = 1.2 \sim 1.6$, compared with those out of these ranges. The physical observation made in figure 17 are completely robust when acceptable H and ζ are used.

The robustness of VATIP is most clearly demonstrated in figure 34 where different parameters and settings are tested and compared for a same flow region with various vortex configurations. Compared with the standard case (panel a) with $H = 0.4$ and $\zeta = 1.5$, changing ζ to 1.2 (panel d) or changing H to 0.6 (panel e) brings little noticeable difference. In panel (f), H is further increased to 0.8 (beyond the recommended range), which only causes the identified vortex tubes to shrink in size, and VATIP still faithfully captures their axis lines. Note that the brown vortex at the lower-left corner has changed from a curved shape to a linear shape at $H = 0.8$ owing to the erosion of one of its legs, which well illustrates how changing parameters affect the number of vortices classified into each category (including fragments). These changes, however, do not reflect the reliability of VATIP itself. We have also doubled the resolutions in the x- and z-dimensions (panel b; the flow

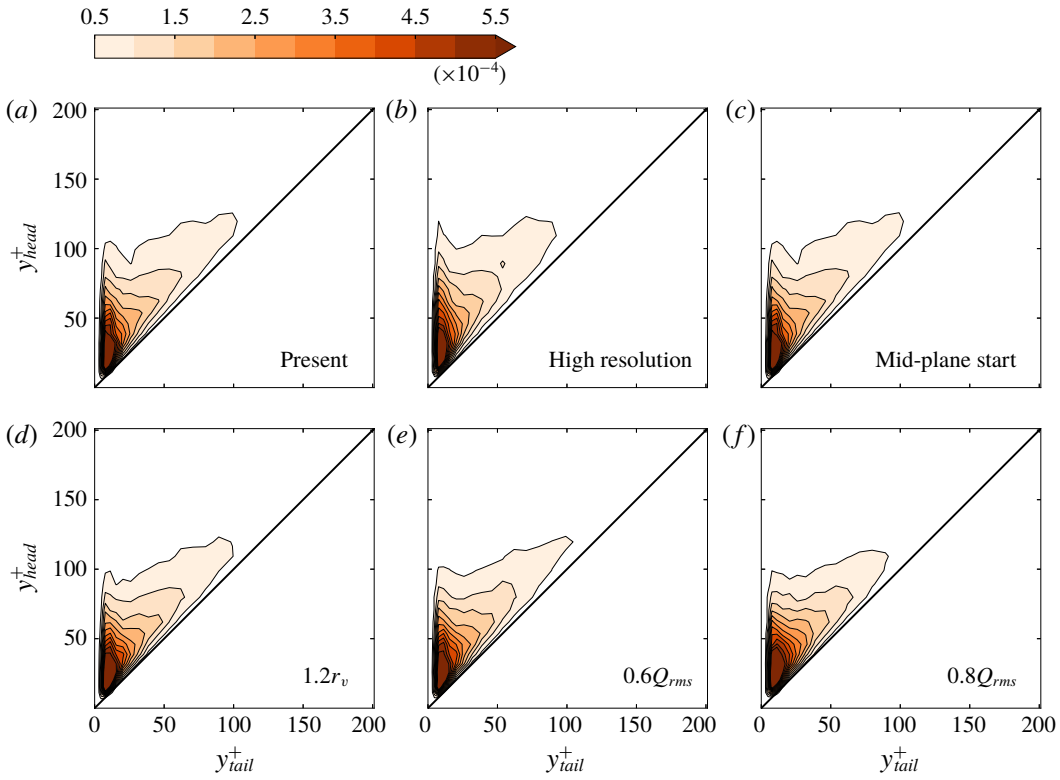

FIGURE 35. (Colour online) Joint PDF between the y^+ positions of the tail and the head of streamwise vortices at $Re_\tau = 169.71$ under different VATIP parameters and settings (note: panel (f) is out of the recommended range of H).

field is interpolated to the finer grid before VATIP analysis) and changed the starting search plane in x and z directions (first steps in subroutines 1 and 2 of figure 3; with no translational symmetry, y-direction searches always start from the walls – also see discussion in § 4.6) from the first planes ($x = 0$ or $z = 0$) to the middle planes ($x = L_x/2$ or $z = L_z/2$). Both do not lead to any discernible difference in the tracking outcome. This observation is general: at $Re_\tau = 169.71$, the average number of vortices in each flow domain (excluding fragments) identified by VATIP $N_v = 2178$, whereas the high resolution case has $N_v = 2193$ and the mid-plane start case has $N_v = 2182$. In both cases, the difference is way less than 1 %.

Finally, echoing the observations in figures 18 and 19, we examine the effects of VATIP parameters and settings on vortex conformation statistics in figures 35 and 36 – this time at $Re_\tau = 169.71$. Despite the small quantitative differences – which, as discussed above, are inevitable as vortices are classified based on quantitative metrics, the qualitative picture is well preserved for all cases shown, including the $H = 0.8$ case which is out of the recommended range. Similar to the earlier observations at other Re_τ, the distribution of streamwise vortices is highly concentrated in the lower-left corner corresponding to the buffer layer. Weaker, but noticeable, concentration bands extend along both the diagonal and the ordinate, reflecting the flat-lying and lifted-up streamwise vortices, respectively. By contrast, three-dimensional vortices are predominantly lifted up, with their concentration peak found well in the log-law layer. Changing resolution or the starting plane shows little effect on these distributions, whereas adjusting H or ζ more directly affects vortex classification and thus causes some subtle changes in the contour shapes, especially at low density levels.

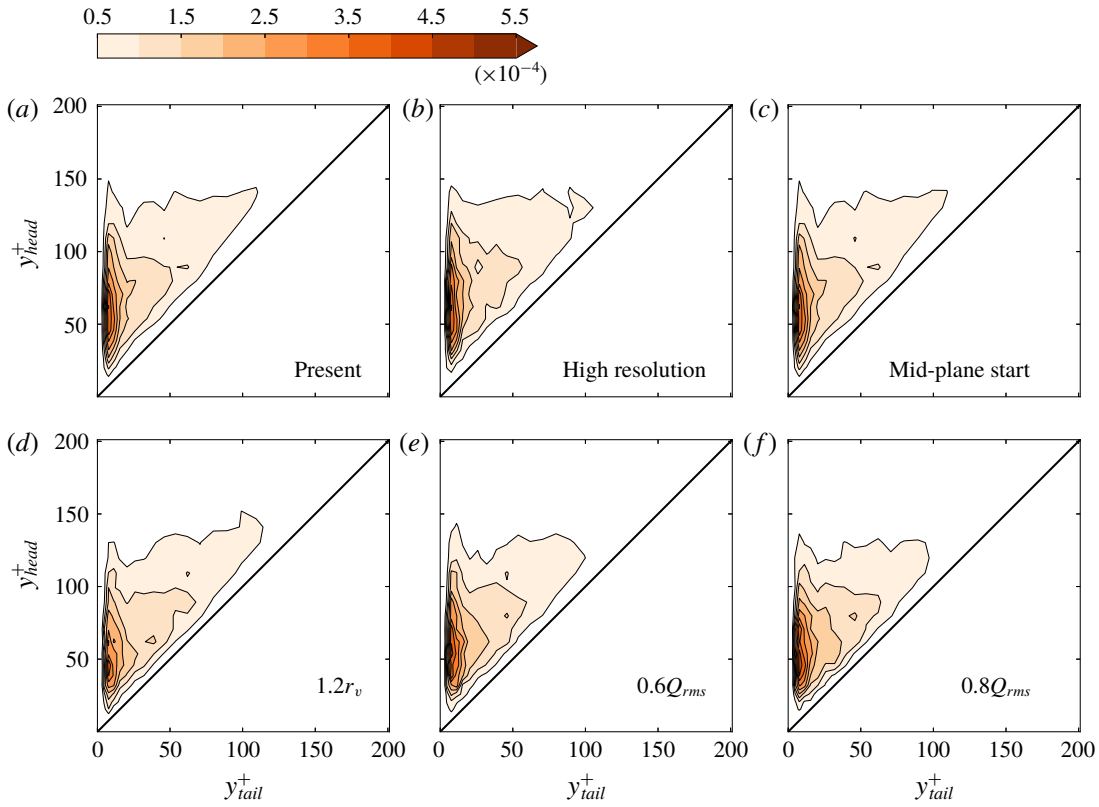

FIGURE 36. (Colour online) Joint PDF between the y^+ positions of the tail and the head of three-dimensional vortices at $Re_\tau = 169.71$ under different VATIP parameters and settings (note: panel (f) is out of the recommended range of H).

4.6. *Discussion: limitations and future development*

Recall from § 3: the algorithm of VATIP is built on the premise that vortices are wall generated, starting with segments or 'legs' that align along the x direction (most often in the buffer layer but the algorithm does not impose this restriction) and can lift up to higher-y^+ layers to bend, curve or branch. VATIP always initiates the propagation points in the x-lying legs and later allows them to move away from the walls (in the y-direction search) and swing sideways (in the z-direction search). For canonical hairpins, the axis lines initiate from both streamwise legs which rise at the downstream end and merge in the middle along the z-direction. Branched vortices are found in a similar manner with one propagation point planted in each streamwise leg and the growing legs (or more appropriately for the branch type – arms) will eventually merge after a limited number of iterations. As demonstrated above (comparing the Q-isosurfaces and VATIP-identified axis lines), this algorithm faithfully captures nearly all vortices identified by the Q-criterion in wall turbulence for $Re_\tau \leqslant 400$ tested in this study.

Recent evidences have indicated that at high Re and large y^+, vortices can be generated in the absence of wall interaction (Del Álamo *et al.* 2006; Jiménez 2013). These vortices can deviate significantly from this premise: they are nearly isotropic (segments are equally likely to align with any direction) and often highly branched (multiple arms with complex connection topology). The current algorithm would not perform as well on those structures. First, the requirement on initialization in

the x-direction search only will undoubtedly bias the resulting axis line to have better sampling of the x-lying segments. For instance, in a strictly y-aligned segment with no connection to any x-segment at the bottom, the current algorithm would still capture a point in the middle that is an yz-planar maximum. It would skip the x-direction propagation (for the lack of other x-axis points) and the next step of y-search would propagate away from the wall only. The end result is missing one part of the segment below the initial point. Second, with only one propagation point in each initial x-segment, the algorithm would struggle with highly branched configurations because the propagation will only pick one of the directions to proceed after each junction. This is not much a problem for wall-generated branched vortices at moderate Re (the focus of this study), because these structures mostly consist of a few conjoining arms, each of which can be traced back to a streamwise leg (i.e. starfish or octopus shaped). The current algorithm has been shown to capture these structures well. However, for detached structures at higher Re_τ and higher y^+ (see, e.g. figure 6 of Del Álamo *et al.* (2006)) with more complex configurations, it will likely miss some of the bridges connecting different arms, if they do not happen to align in the x direction, and falsely break them into pieces.

There seems to be a easy remedy in sight, that as long as we relax these constraints to allow a truly multidirectional tracking – i.e. axis lines are initiated in all three dimensions and propagation is allowed to follow all branches after each junction – we should be able to capture these isotropic and highly branched structures. The problem, however, is its insurmountable side effect: relaxation of the current constraints will inevitably lead to massive false identification and false connection, making the tracking result next to meaningless. There are two major sources of this problem. First, not all planar Q maxima belong to a vortex axis. Consider a simple linear streamwise vortex as an elongated ellipsoid, the true axis line aligns with its major axis and consists of yz-planar Q maxima. However, the minor axes also contain Q maximum points (in xy- and xz-planes), which do not belong to any vortex axis line. This is further compounded by fluctuations in the Q fields, which may create Q maxima unrelated with any actual vortex. The total number of planar maximum points identified in an $L_x^+ \times L_z^+ = 4000 \times 800$ flow domain ranges from $\sim$80 000 to $\sim$350 000 (for the lowest and highest Re_τ tested, respectively). Only 30$\sim$40 % of them are included in the final axis lines (counting both vortices and fragments). Second, in flow fields densely populated by vortices, close encounters between axis lines of separate vortices are common: spatial proximity does not necessarily indicate connectivity. The current algorithm takes advantage of the fact that, despite the overall complexity of vortex configuration and distribution, wall-generated vortices can be traced back to the near-wall region where their legs are regularly aligned (largely in parallel) in the streamwise direction. Regularity in their distribution pattern makes tracking easier and connection is usually unambiguous. This is the rationale behind the choice of axis-line initiation in the x-search. Continued propagation in other (y and z) directions minimizes false inclusion of points and false connection with other vortices by requiring the new segments to be natural extensions from the growing axis line. By contrast, a general multi-initiation and multi-directional algorithm would indiscriminately connect any points in the vicinity of a growing end. Extension of the VATIP algorithm to detached vortex structures with no preference to the x direction and more complex branch configurations calls for new physics-based constraints to be incorporated, which is a focus of our future research.

Another potential challenge of extending the method to higher Re is the determination of parameters. Section 4.5 thoroughly examined the effects of the adjustable

parameters H and ζ and proposed their recommended ranges of use based on the balance between minimizing false connections and minimizing false disintegrations or truncations of vortex axis lines. For higher Re, structures in the bulk regions (higher y^+) become non-trivial. Del Álamo *et al.* (2006) showed that a lower H is required to capture these detached structures because of the overall lower turbulent intensity in those regions. A y^+-dependent H was thus proposed for vortex identification in that study. It is likely that, for VATIP, a similar approach needs to be taken for both H and ζ. Determining the dependence of these parameters on y^+ will require trial and error. Moreover, whether a 'sweet-spot' range still exists for these parameters in the high-Re and high-y^+ regime remains to be seen. Finally, we note that, as a brand new method, its future application and testing in broader parameter regimes and systems will be essential for its continued improvement and generalization. In this sense, the development of VATIP itself is an 'iterative' process that requires the experience and feedback from its application.

5. Conclusions

In this study, a new method has been proposed for the identification and extraction of three-dimensional complex vortices from turbulent flow fields. This method, named VATIP, connects points of vortex axis lines using the cone-detective criterion of Jeong *et al.* (1997) and propagates the growing axis over all three spatial dimensions iteratively in order to accommodate various types of vortex topologies. Transient simulation based on streak instability (STG) is performed to generate flow fields featuring streamwise, titled/curved and hairpin vortices and the method is shown to successfully capture all these types. In addition, a new procedure is proposed to classify the axis lines obtained by VATIP into different topological types commonly observed in wall turbulence, including quasi-linear vortices, hairpins, hooks (asymmetric/incomplete hairpins) and various branched types. Tracking outcome from VATIP is shown to be robust with changing parameters and settings. For both adjustable parameters (H and ζ for the vortex scalar identifier and search cone size, respectively), suitable parameter ranges are identified. The method is the first that directly extracts the individual axis lines of typical three-dimensional vortices found in turbulent near-wall layers. Future work will focus on extending this method for complex isotropic vortex configurations at higher Re and in outer layers, to which the current method is not applicable.

VATIP is applied to analyse the vortex configurations and statistics in statistical turbulence (from DNS) at three different Re, where vortices of all types are successfully identified. The results show that the streamwise vortex length l_x^+ is insensitive to Re with the distribution nearly identical between all three Re tested. The spanwise width l_z^+, however, has higher average values at higher Re as a result of the higher fraction of wide vortices. The number of vortices increases with Re (for the same domain size in inner units). Quasi-streamwise vortices are dominant in the low-to-moderate range of Re (Re_τ from 84.85 to 400) tested, but their number fraction decreases with Re. Complex three-dimensional vortices of all shapes (hairpins, hooks and branches) become more prevalent at higher Re, which accounts for the increasing frequency of large l_z^+ values. The number of symmetric hairpins and branched vortices grows faster than asymmetric vortices (hooks), suggesting that the latter is likely an incomplete version of full hairpins occurring more often at lower Re. Quasi-streamwise vortices populate the buffer layer and the lower log-law layer whereas hairpins and other three-dimensional vortices dominate higher layers

(although the legs of these vortices still stretch down to the buffer layer). The latter are also more likely to be found in a lifted-up state and the head of those vortices can rise to a broad range of distances from the wall.

Clustering analysis is applied to VATIP results for understanding vortex organization patterns. Well-defined vortex clusters consisting of $O(10)$–$O(100)$ individual vortices are consistently identified. These clusters appear at regions with high Reynold shear stress and are reminiscent of the large-scale motions previously observed in the literature. They have a streamwise length scale of 500–1500 wall units, which stays roughly constant (in inner units) for the Re range tested.

The current study focused on the static analysis of vortex conformation and distribution. On the subject of hairpin vortices, which is heatedly debated in the literature, it reveals the definitive evidence for the existence of such structures in the statistically steady turbulence of channel flow. However, it is also shown that canonical hairpin vortices with highly symmetric legs (as reported in the transient boundary-layer flow by Wu & Moin (2009)) remain rarities at least within the range of $Re_\tau \leqslant 400$ tested. They are greatly outnumbered by their asymmetric (hooks) and highly branched mutants. These latter types seem to have the same level of lift-up and may be formed by the incomplete development of hairpins (for hooks) or their coalescence with other structures (for branches). Compared with canonical hairpins, branched vortices seem to be equivalently effective at binding vortices into clusters owing to their similar spanwise dimensions, whereas hooks are more similar to streamwise vortices in this aspect. Important questions on the role of these general hairpin-like vortices in turbulence dynamics, especially, whether they are the cause or consequence of turbulence generation, cannot be answered until a dynamical tracking approach (such as that of Lozano-Durán & Jiménez (2014)) is integrated with VATIP.

The success of VATIP provides access to the detailed statistics on the configuration, topology and distribution of vortices in near-wall turbulence. It thus offers a powerful tool for the study of vortex dynamics and the auto-regeneration mechanism of turbulence, as well as other areas such as vortex development during the bypass transition and the changing vortex dynamics in turbulent drag reduction.

Acknowledgements

The authors acknowledge the financial support from the Natural Sciences and Engineering Research Council of Canada (NSERC; no. RGPIN-2014-04903) and the allocation of computing resources awarded by Compute/Calcul Canada. The computation is made possible by the facilities of the Shared Hierarchical Academic Research Computing Network (SHARCNET: www.sharcnet.ca). We also express our gratitude towards J. F. Gibson, H. Schrobsdorff, T. Kreilos and T. M. Schneider for the DNS code. L.X. acknowledges the National Science Foundation grant no. NSF PHY11-25915, which partially supported his stay at the Kavli Institute for Theoretical Physics (KITP) at UC Santa Barbara. L.Z. acknowledges the European Research Council H2020 program (ERC-2014-ADG 'COTURB') which supported his participation in the Third Madrid Summer School on Turbulence.

REFERENCES

ABE, H., KAWAMURA, H. & MATSUO, Y. 2001 Direct numerical simulation of a fully developed turbulent channel flow with respect to the Reynolds number dependence. *J. Fluid Mech.* **123** (2), 382–393.

ADRIAN, R. J. 1994 Stochastic estimation of conditional structure: a review. *Appl. Sci. Res.* **53** (3–4), 291–303.

ADRIAN, R. J. 2007 Hairpin vortex organization in wall turbulence a. *Phys. Fluids* **19** (4), 041301.

ADRIAN, R. J., JONES, B. G., CHUNG, M. K., HASSAN, Y., NITHIANANDAN, C. K. & TUNG, A. C. 1989 Approximation of turbulent conditional averages by stochastic estimation. *Phys. Fluids* A **1** (6), 992–998.

ADRIAN, R. J., MEINHART, C. D. & TOMKINS, C. D. 2000 Vortex organization in the outer region of the turbulent boundary layer. *J. Fluid Mech.* **422**, 1–54.

BERNARD, P. S., THOMAS, J. M. & HANDLER, R. A. 1993 Vortex dynamics and the production of Reynolds stress. *J. Fluid Mech.* **253**, 385–419.

BLACKBURN, H. M., MANSOUR, N. N. & CANTWELL, B. J. 1996 Topology of fine-scale motions in turbulent channel flow. *J. Fluid Mech.* **310**, 269–292.

BLACKWELDER, R. F. & KAPLAN, R. E. 1976 On the wall structure of the turbulent boundary layer. *J. Fluid Mech.* **76** (1), 89–112.

BRANDT, L. & HENNINGSON, D. S. 2002 Transition of streamwise streaks in zero-pressure-gradient boundary layers. *J. Fluid Mech.* **472**, 229–261.

BRANDT, L. & DE LANGE, H. C. 2008 Streak interactions and breakdown in boundary layer flows. *Phys. Fluids* **20**, 024107.

BROOKE, J. W. & HANRATTY, T. J. 1993 Origin of turbulence-producing eddies in a channel flow. *Phys. Fluids* A **5** (4), 1011–1022.

CANTWELL, B. J. 1981 Organized motion in turbulent flow. *Annu. Rev. Fluid Mech.* **13** (1), 457–515.

CHAKRABORTY, P., BALACHANDAR, S. & ADRIAN, R. J. 2005 On the relationships between local vortex identification schemes. *J. Fluid Mech.* **535**, 189–214.

CHEN, Q., ZHONG, Q., QI, M. & WANG, X. 2015 Comparison of vortex identification criteria for planar velocity fields in wall turbulence. *Phys. Fluids* **27** (8), 085101.

CHONG, M. S., PERRY, A. E. & CANTWELL, B. J. 1990 A general classification of three-dimensional flow fields. *Phys. Fluids* A **2** (5), 765–777.

CHONG, M. S., SORIA, J., PERRY, A. E., CHACIN, J., CANTWELL, B. J. & NA, Y. 1998 Turbulence structures of wall-bounded shear flows found using DNS data. *J. Fluid Mech.* **357**, 225–247.

CORRSIN, S. 1943 Investigation of flow in an axially symmetric heated jet of air, *NASA Adv. Conf Rep.* 3123.

DEL ÁLAMO, J. C., JIMÉNEZ, J., ZANDONADE, P. & MOSER, R. D. 2006 Self-similar vortex clusters in the turbulent logarithmic region. *J. Fluid Mech.* **561**, 329–358.

DENNIS, D. J. C. & NICKELS, T. B. 2011 Experimental measurement of large-scale three-dimensional structures in a turbulent boundary layer. Part 1. Vortex packets. *J. Fluid Mech.* **673**, 180–217.

DUBIEF, Y. & DELCAYRE, F. 2000 On coherent-vortex identification in turbulence. *J. Turbul.* **1**, 1–22.

EINSTEIN, H. A. & LI, H. 1956 The viscous sublayer along a smooth boundary. *J. Engng Mech. Div.* **82** (2), 1–7.

ESTER, M., KRIEGEL, H. P., SANDER, J. & XU, X. 1996 A density-based algorithm for discovering clusters in large spatial databases with noise. In *Kdd*, vol. 96, pp. 226–231. AAAI Press.

GIBSON, J. F. 2012 Channelflow: a spectral Navier–Stokes simulator in c++. New Hampshire.

GIBSON, J. F., HALCROW, J. & CVITANOTIĆ, P. 2009 Equilibrium and travelling-wave solutions of plane Couette flow. *J. Fluid Mech.* **638**, 243–266.

HACK, M. J. P. & MOIN, P. 2018 Coherent instability in wall-bounded shear. *J. Fluid Mech.* **844**, 917–955.

HALLER, G. 2001 Distinguished material surfaces and coherent structures in three-dimensional fluid flows. *Physica* D **149** (4), 248–277.

HALLER, G. 2005 An objective definition of a vortex. *J. Fluid Mech.* **525**, 1–26.

HALLER, G. 2015 Lagrangian coherent structures. *Annu. Rev. Fluid Mech.* **47**, 137–162.

HAMILTON, J. M., KIM, J. & WALEFFE, F. 1995 Regeneration mechanisms of near-wall turbulence structures. *J. Fluid Mech.* **287**, 317–348.

HEAD, M. R. & BANDYOPADHYAY, P. 1981 New aspects of turbulent boundary-layer structure. *J. Fluid Mech.* **107**, 297–338.

HINZE, J. O. 1975 *Turbulence*, 2nd edn. pp. 223–225. McGraw-Gill.

HOYAS, S. & JIMÉNEZ, J. 2006 Scaling of the velocity fluctuations in turbulent channels up to $Re_\tau = 2003$. *Phys. Fluids* **18** (1), 011702.

HUNT, J. C. R., WRAY, A. A. & MOIN, P. 1988 Eddies, streams, and convergence zones in turbulent flows. In *Proceedings of the 1988 Summer Program, Studying Turbulence Using Numerical Simulation Databases, 2*, pp. 193–208. Ames Research Center Stanford University.

JEONG, J. & HUSSAIN, F. 1995 On the identification of a vortex. *J. Fluid Mech.* **285**, 69–94.

JEONG, J., HUSSAIN, F., SCHOPPA, W. & KIM, J. 1997 Coherent structures near the wall in a turbulent channel flow. *J. Fluid Mech.* **332**, 185–214.

JIMÉNEZ, J. 1998 The largest scales of turbulent wall flows. In *CTR Annual Research Briefs*, vol. 137, p. 54. Stanford University.

JIMÉNEZ, J. 2013 Near-wall turbulence. *Phys. Fluids* **25** (10), 101302.

JIMÉNEZ, J. 2018 Coherent structures in wall-bounded turbulence. *J. Fluid Mech.* **842**, P1.

JIMÉNEZ, J. & MOIN, P. 1991 The minimal flow unit in near-wall turbulence. *J. Fluid Mech.* **225**, 213–240.

JIMÉNEZ, J. & MOSER, R. D. 2007 What are we learning from simulating wall turbulence? *Phil. Trans. R. Soc. Lond.* A **365** (1852), 715–732.

KIDA, S. & MIURA, H. 1998 Identification and analysis of vortical structures. *Eur. J Mech. (*B*/Fluids)* **17** (4), 471–488.

KIM, H. T., KLINE, S. J. & REYNOLDS, W. C. 1971 The production of turbulence near a smooth wall in a turbulent boundary layer. *J. Fluid Mech.* **50** (1), 133–160.

KIM, J., MOIN, P. & MOSER, R. 1987 Turbulence statistics in fully-developed channel flow at low Reynolds-number. *J. Fluid Mech.* **177**, 133–166.

KIM, K. C. & ADRIAN, R. J. 1999 Very large-scale motion in the outer layer. *Phys. Fluids* **11** (2), 417–422.

KLINE, S. J., REYNOLDS, W. C., SCHRAUB, F. A. & RUNSTADLER, P. W. 1967 The structure of turbulent boundary layers. *J. Fluid Mech.* **30** (4), 741–773.

LEE, J., LEE, J. H., CHOI, J. & SUNG, H. J. 2014 Spatial organization of large-and very-large-scale motions in a turbulent channel flow. *J. Fluid Mech.* **749**, 818–840.

LOZANO-DURÁN, A., FLORES, O. & JIMÉNEZ, J. 2012 The three-dimensional structure of momentum transfer in turbulent channels. *J. Fluid Mech.* **694**, 100–130.

LOZANO-DURÁN, A. & JIMÉNEZ, J. 2014 Time-resolved evolution of coherent structures in turbulent channels: characterization of eddies and cascades. *J. Fluid Mech.* **759**, 432–471.

MARUSIC, I., MCKEON, B. J., MONKEWITZ, P. A., NAGIB, H. M., SMITS, A. J. & SREENIVASAN, K. R. 2010 Wall-bounded turbulent flows at high Reynolds numbers: recent advances and key issues. *Phys. Fluids* **22** (6), 065103.

MOISY, F. & JIMÉNEZ, J. 2004 Geometry and clustering of intense structures in isotropic turbulence. *J. Fluid Mech.* **513**, 111–133.

MORRIS, S. C., STOLPA, S. R., SLABOCH, P. E. & KLEWICKI, J. C. 2007 Near-surface particle image velocimetry measurements in a transitionally rough-wall atmospheric boundary layer. *J. Fluid Mech.* **580**, 319–338.

MOSER, R. D., KIM, J. & MANSOUR, N. N. 1999 Direct numerical simulation of turbulent channel flow up to $Re_\tau = 590$. *Phys. Fluids* **11** (4), 943–945.

MULLIN, T. 2011 Experimental studies of transition to turbulence in a pipe. *Annu. Rev. Fluid Mech.* **43**, 1–24.

OFFEN, G. R. & KLINE, S. J. 1975 A proposed model of the bursting process in turbulent boundary layers. *J. Fluid Mech.* **70** (2), 209–228.

PANTON, R. L. 2001 Overview of the self-sustaining mechanisms of wall turbulence. *Prog. Aerosp. Sci.* **37** (4), 341–383.

PERRY, A. E. & CHONG, M. S. 1982 On the mechanism of wall turbulence. *J. Fluid Mech.* **119**, 173–217.

PERRY, A. E. & MARUŠIĆ, I. 1995 A wall-wake model for the turbulence structure of boundary layers. Part 1. Extension of the attached eddy hypothesis. *J. Fluid Mech.* **298**, 361–388.

PEYRET, R. 2002 *Spectral Methods for Incompressible Viscous Flow*. Springer.

POPE, S. B. 2000 *Turbulent Flows*. Cambridge University Press.

ROBINSON, S. K. 1991 Coherent motions in the turbulent boundary layer. *Annu. Rev. Fluid Mech.* **23** (1), 601–639.

ROBINSON, S. K., KLINE, S. J. & SPALART, P. R. 1989 A review of quasi-coherent structures in a numerically simulated turbulent boundary layer. *Tech. Rep.* NASA Ames Research Center. NASA-TM-102191.

SCHLATTER, P., BRANDT, L., DE LANGE, H. C. & HENNINGSON, D. S. 2008 On streak breakdown in bypass transition. *Phys. Fluids* **20**, 101505.

SCHLATTER, P., LI, Q., ÖRLÜ, R., HUSSAIN, F. & HENNINGSON, D. S. 2014 On the near-wall vortical structures at moderate Reynolds numbers. *Eur. J. Mech. (*B*/Fluids)* **48**, 75–93.

SCHOPPA, W. & HUSSAIN, F. 2002 Coherent structure generation in near-wall turbulence. *J. Fluid Mech.* **453**, 57–108.

SHEKAR, A. & GRAHAM, M. D. 2018 Exact coherent states with hairpin-like vortex structure in channel flow. *J. Fluid Mech.* **849**, 76–89.

SMITH, C. R. 1984 A synthesized model of the near-wall behavior in turbulent boundary layers. *Tech. Rep.* Lehigh University, Department of Mechanical Engineering and Mechanics. AFOSR-TR-33-1336.

SMITH, C. R. & SCHWARTZ, S. P. 1983 Observation of streamwise rotation in the near-wall region of a turbulent boundary layer. *Phys. Fluids* **26** (3), 641–652.

THEODORSEN, T. 1952 Mechanism of turbulence. In *Proceedings of the Midwestern Conference on Fluid Mechanics*, pp. 1–19. Ohio State University.

TOWNSEND, A. A. R. 1980 *The Structure of Turbulent Shear Flow*. Cambridge University Press.

TUCKERMAN, L. S., KREILOS, T., SCHROBSDORFF, H., SCHNEIDER, T. M. & GIBSON, J. F. 2014 Turbulent-laminar patterns in plane Poiseuille flow. *Phys. Fluids* **26**, 114103.

WALEFFE, F. 1997 On a self-sustaining process in shear flows. *Phys. Fluids* **9**, 883–900.

WALEFFE, F. 1998 Three-dimensional coherent states in plane shear flows. *Phys. Rev. Lett.* **81**, 4140–4143.

WALLACE, J. M., ECKELMANN, H. & BRODKEY, R. S. 1972 The wall region in turbulent shear flow. *J. Fluid Mech.* **54** (1), 39–48.

WILLMARTH, W. W. & LU, S. S. 1972 Structure of the Reynolds stress near the wall. *J. Fluid Mech.* **55** (1), 65–92.

WILLMARTH, W. W. & TU, B. J. 1967 Structure of turbulence in the boundary layer near the wall. *Phys. Fluids* **10** (9), S134–S137.

WU, X. & MOIN, P. 2009 Direct numerical simulation of turbulence in a nominally zero-pressure-gradient flat-plate boundary layer. *J. Fluid Mech.* **630**, 5–41.

WU, X., MOIN, P., ADRIAN, R. J. & BALTZER, J. R. 2015 Osborne Reynolds pipe flow: direct simulation from laminar through gradual transition to fully developed turbulence. *Proc. Natl Acad. Sci. USA* **112**, 7920–7924.

XI, L. & BAI, X. 2016 Marginal turbulent state of viscoelastic fluids: a polymer drag reduction perspective. *Phys. Rev.* E **93**, 043118.

XI, L. & GRAHAM, M. D. 2010 Active and hibernating turbulence in minimal channel flow of Newtonian and polymeric fluids. *Phys. Rev. Lett.* **104**, 218301.

XI, L. & GRAHAM, M. D. 2012 Intermittent dynamics of turbulence hibernation in Newtonian and viscoelastic minimal channel flows. *J. Fluid Mech.* **693**, 433–472.

ZHOU, J., ADRIAN, R. J., BALACHANDAR, S. & KENDALL, T. M. 1999 Mechanisms for generating coherent packets of hairpin vortices in channel flow. *J. Fluid Mech.* **387**, 353–396.

ZHU, L., SCHROBSDORFF, H., SCHNEIDER, T. M. & XI, L. 2018 Distinct transition in flow statistics and vortex dynamics between low- and high-extent turbulent drag reduction in polymer fluids. *J. Non-Newtonian Fluid Mech.* **262**, 115–130.

ZHU, L. & XI, L. 2018 Coherent structure dynamics and identification during the multistage transitions of polymeric turbulent channel flow. *J. Phys.: Conf. Ser.* **1001** (1), 012005.

Bibliography

Wu, X., Moin, P., Adrian, R. J., and Baltzer, J. R. (2015). Osborne Reynolds pipe flow: Direct simulation from laminar through gradual transition to fully developed turbulence. *Proc. Natl. Acad. Sci. U. S. A.*, **112**, 7920–7924.

Wu, X., Moin, P., Wallace, J. M., Skarda, J., Lozano-Durán, A., and Hickey, J. P. (2017). Transitional–turbulent spots and turbulent–turbulent spots in boundary layers. *Proc. Natl. Acad. Sci. U. S. A.*, **114**(27), E5292–E5299.

Chapter 4

Vortex statistics in LDR and HDR revealed by VATIP

Our previous work proposed a hypothesis that the lifting tendency of vortical structures are suppressed by polymers during the low- to high-extend drag reduction (LDR-HDR) transition, which may be responsible for this qualitative transition. In this chapter, this hypothesis is tested through statistically analyzing the vortex configurations using our recently developed vortex tracking algorithm – VATIP (vortex axis tracking by iterative propagation, chapter 3). As indicated by the results, vortices at LDR are across-the-board weaken by polymers. At HDR, the lift-up process of the streamwise vortices is suppressed which prevents their downstream heads from rising into the log-law layer and forming hairpins and other curved vortices. The transfers of momentum and energy of turbulence between the buffer and log-law layers are thus interrupted, which clearly explains the distinct changes of flow statistics during the LDR-HDR transition and supports our hypothesis.

I was responsible for implementing simulations and collecting data. I also post-processed the data with Dr. Li Xi's suggestion. The draft was written by me and revised by Dr. Li Xi.

This chapter has been submitted to *Physics of Fluids*

4.1 Introduction

When a small amount of polymers are added into Newtonian turbulence, their strong interaction with the flow can significantly modify turbulent coherent structures, which results in the drastic reduction of the turbulent friction drag. Polymer-induced turbulent drag reduction (DR) has been a subject of intense interest in the literature (Virk, 1975; White and Mungal, 2008; Graham, 2014) due to its significant practical implications for the development of flow control techniques for enhanced fluid transportation efficiency.

In polymeric turbulent flows, the Weissenberg number $\mathrm{Wi} \equiv \lambda\dot{\gamma}$ (λ and $\dot{\gamma}$ are the polymer relaxation time and the characteristic shear rate of the flow, respectively) measures the level of polymer-induced elasticity. Polymer effects on turbulent flow statistics are not noticeable until Wi exceeds a critical magnitude, often denoted by $\mathrm{Wi}_{\mathrm{onset}}$, which corresponds to the coil-stretch transition of polymer molecules. After the onset, the level of DR increases with Wi but eventually converges to an asymptotic upper bound (Virk, 1975) – the widely known maximum drag reduction (MDR) asymptote. (At low enough Re, laminarization was also observed after the flow passes the Virk asymptote, before another type of instability emerges (Choueiri *et al.*, 2018).) Before MDR, distinction is further made more recently between low-extent (LDR) and high-extent drag reduction (HDR) (Warholic *et al.*, 1999). Starting from the Newtonian limit and with increasing Wi, the flow undergoes a series of transitions between four different stages of behaviors: pre-onset, LDR, HDR, and MDR (Xi and Graham, 2010b).

LDR and HDR were first differentiated because their mean velocity profiles appear different in shape, which is observed in various experimental and numerical studies (Warholic *et al.*, 1999; Ptasinski *et al.*, 2003; Li *et al.*, 2006a; Mohammadtabar *et al.*, 2017). Recall that Newtonian turbulent mean velocity profiles display the Prandtl-von Kármán (PvK) log law

$$U^+ = 2.5 \ln y^+ + 5.5 \tag{4.1}$$

across most of the near-wall layer ($y^+ \gtrsim 30$) (Kim *et al.*, 1987). This log-law layer is connected to the near wall viscous sublayer via a buffer layer at $5 \lesssim y^+ \lesssim 30$ (Pope, 2000). At LDR, the buffer layer velocity profile raises up and its thickness also increases. Meanwhile the log-law layer stays parallel to the PvK log law only with a vertical offset (i.e., same slope but larger intercept compared with eq. (4.1) owing to the DR in the buffer layer). At HDR, however, the slope of the mean velocity profile clearly increases in the log-law layer. This effect was initially attributed to the quantitative magnitude of DR in earlier studies with DR% ≈ 35 (

$$\mathrm{DR}\% \equiv \frac{C_\mathrm{f} - C_\mathrm{f,s}}{C_\mathrm{f}} \times 100\% \tag{4.2}$$

is the percentage drop of the friction factor C_f; subscript "s" indicates the solvent – i.e., Newtonian benchmark fluid) often cited as the cutoff (Warholic *et al.*, 1999). Recent more systematic studies revealed that this transition is accompanied by a series of sharp changes in flow statistics and may occur at much lower DR% at lower Re (Xi and Graham, 2010b; Zhu *et al.*, 2018). Most notably, suppression of Reynolds shear stress (RSS) is mainly contained in the buffer layer at LDR which extends

across the whole boundary layer at HDR. In addition, the mean velocity profile was shown to no longer follow a logarithmic dependence at HDR (White *et al.*, 2012; Elbing *et al.*, 2013). All these evidences indicate that turbulent DR is a two-stage process with distinct mechanisms. The first is a localized weakening of turbulence concentrated in the buffer layer which starts at $\mathrm{Wi}_{\mathrm{onset}}$. The second is a fundamental change in turbulent dynamics in the log-law layer that is only triggered at the LDR-HDR transition. Fundamental understating of the second mechanism (HDR) is very limited which however has important implications in the area of flow control. In particular, existing non-additive based DR techniques mainly results in flow statistics characteristic of LDR (Deng *et al.*, 2016). Knowing how polymers trigger HDR will inspire new approaches that elevate the DR outcome to the next level.

Flow statistics and turbulent dynamics are often conceptualized in the framework of coherent structures such as vortices and streaks (Robinson, 1991; Bernard *et al.*, 1993; Adrian, 2007). These structures are commonly spotted in flow field images (from flow visualization experiments or direct numerical simulations – DNS) and provides a vehicle for describing mechanisms of turbulent self-sustaining processes and momentum transport (Panton, 2001; Jiménez and Moser, 2007; Wallace, 2016). Attempts have also been made to establish the relationship between the mean velocity profile and the underlying coherent structures (Lozano-Durán *et al.*, 2012). For instance, Perry and Marušić (1995) attributed the logarithmic dependence (eq. (4.1)) to the population of highly lifted-up vortices. For viscoelastic turbulence, it is commonly accepted that polymer stresses can cause DR by suppressing the motion of vortices (De Angelis *et al.*, 2002; Dubief *et al.*, 2005; Li *et al.*, 2006b; Kim *et al.*, 2007; Li *et al.*, 2015), which offers a convincing explanation for the onset of DR.

Much less is known about the second stage of DR as the LDR-HDR transition was not considered a qualitative change in turbulent dynamics until very recently (Zhu *et al.*, 2018). Quantitative analysis of vortex distribution revealed that sharp changes in flow statistics coincide with the start of coherent structure localization, with HDR characterized by spotty clusters of vortices separated by laminar-like regions (Zhu *et al.*, 2018), which corroborates the earlier description of the intermittent transitions between active and hibernating turbulence (Xi and Graham, 2010a, 2012b,a; Xi and Bai, 2016). Based on this, Zhu *et al.* (2018) hypothesized that the LDR-HDR transition stems from a fundamental change in the turbulence regeneration mechanism and the two-stage DR process is a reflection of two different modes of polymer effects on turbulent structures. At lower Wi, polymers cause an across-the-board weakening of vortices and thus the onset of DR. At higher Wi they start to suppress vortex lift-up and prevent its subsequent bursting events. Since bursting can lead to the spreading of flow disturbances and trigger streak instability elsewhere in the domain (Hamilton *et al.*, 1995; Schoppa and Hussain, 2002), its suppression effectively blocks this pathway for vortex regeneration and exposes the more localized parent-offspring mechanism – generation of new vortices at the edge of existing ones – as the main process for turbulence sustenance at HDR. Prevention of vortex lift-up also offers an explanation for the breaking of the mean velocity log law at HDR.

Like all studies of turbulent coherent structures, although there is no shortage of anecdotal evidences for this conceptual model, systematical analysis of changes in vortex configuration without subjective bias is a non-trivial challenge. Conditional sampling has been an influential tool in the coherent structure analysis of viscoelastic

turbulence, which averages the flow structures extracted based on events such as velocity ejection (Kim *et al.*, 2007, 2008) and occurrence of streamwise vortices (Sibilla and Beretta, 2005). Its outcome has significantly contributed to the fundamental understanding in this area, especially that of vortex suppression by polymer forces which causes the transition into the first DR stage at $\mathrm{Wi}_{\mathrm{onset}}$ (as reviewed above). However, focusing on the average smears the variation between individual vortex objects and loses the information on the statistical distribution. Reliance on the predetermined detection events also limits its representativeness when studying dynamics involving complex vortex topologies and motions. Proper-orthogonal decomposition (or Karhunen-Loève analysis) was also widely used (De Angelis *et al.*, 2003; Housiadas *et al.*, 2005; Wang *et al.*, 2014; Mohammadtabar *et al.*, 2017), which is most effective for quantifying energy distribution between flow modes of different length scales but information on real individual vortices is still missing. A method that can extract individual realizations of vortex objects and objectively analyze their configurations and topologies can contribute new insight especially to the second stage of DR which, as discussed above, may involve more complex vortex dynamics.

At the conceptual level, this is achieved in a two-step process: (1) vortex identification – determining which regions in the flow field display vortical motions – and (2) tracking – grouping these regions into individual vortex objects. Various vortex identification criteria have been proposed in the literature. The necessity of such criteria may not be obvious at first sight as one would intuitively turn to the vorticity field $\boldsymbol{\omega} \equiv \boldsymbol{\nabla} \times \boldsymbol{v}$ for describing swirling flows. The limitation of vorticity becomes clear when we consider a simple shear flow where, despite the absence of any vortex, still has a vorticity magnitude proportional to the shear rate. Most commonly used

vortex identification criteria are based on scalar identifiers calculated from the velocity gradient tensor $\boldsymbol{\nabla v}$ (Jeong *et al.*, 1997; Chong *et al.*, 1990; Hunt *et al.*, 1988). Here, we take the Q-criterion (Hunt *et al.*, 1988) used in this study as an illustrative example. For incompressible flow, the Q quantity is defined as

$$Q = \frac{1}{2}(\|\boldsymbol{\Omega}\|^2 - \|\boldsymbol{S}\|^2), \tag{4.3}$$

where $\|\cdot\|$ denotes the Frobenius tensor norm: e.g., $\|\boldsymbol{\Omega}\| \equiv \sqrt{\sum_i \sum_j \Omega_{ij}^2}$. The strain-rate tensor, $\boldsymbol{S} \equiv \left(\boldsymbol{\nabla v} + \boldsymbol{\nabla v}^T\right)/2$, and the vorticity tensor, $\boldsymbol{\Omega} \equiv \left(\boldsymbol{\nabla v} - \boldsymbol{\nabla v}^T\right)/2$, are the symmetric and antisymmetric parts of $\boldsymbol{\nabla v}$, respectively. Equation (4.3), on its face, can be interpreted as a comparison between the magnitudes of fluid rotation (measured by $\|\boldsymbol{\Omega}\|^2$) and strain ($\|\boldsymbol{S}\|^2$). The magnitude of Q provides a basis for categorizing flow regions based on their local kinematics. Regions with large positive Q are dominated by strong rotation and thus correspond to vortices. Regions with large negative Q are dominated by strain – i.e., stretching of fluid elements, which indicates extensional flow. For a strict shear flow, it is easily verifiable that $Q = 0$. The reader is referred to Xi and Bai (2016) for a more quantitative discussion on the relationship between Q and local flow type. A similar argument was also adopted by the recent studies of Pereira *et al.* (2017a,b) which divided viscoelastic flow fields into regions with different Q magnitudes. Energy exchanges between these Q regions were analyzed to understand polymer-turbulence dynamics. Other criteria use different definitions for the scalar identifier but the results are practically equivalent in complex turbulent flow fields (Chakraborty *et al.*, 2005). A more detailed introduction of vortex identification was provided in our earlier paper (Zhu and Xi, 2019).

Much less development was seen in vortex tracking. Scalar fields of the identifier, e.g., Q, can be easily visualized by rendering its three-dimensional isosurfaces, although care must be taken in the selection of the threshold level (Chu and Karniadakis, 1993; Lozano-Durán *et al.*, 2012; Lozano-Durán and Jiménez, 2014). This makes vortex objects easy to identify by eyes but not by a computer program for quantitative analysis. A vortex tracking algorithm will enable the identification of individual vortex objects and quantification of their location, size, and topology without the subjectivity of human intervention. A classical example is the method of Jeong *et al.* (1997), which identifies vortex axes – center-lines around which the fluid rotates in a swirling motion – by stitching together local planar maxima of the identifier. The extracted axis-lines can be used in conditional sampling studies to align individual vortex objects for averaging (Jeong *et al.*, 1997; Hussain and Hayakawa, 1987; Zhu and Xi, 2018). This method was however designed only for (quasi-)streamwise vortices whose axis-lines extend in nearly-straight lines aligned with the mean flow. These vortices are important for the self-sustaining process of turbulence at least at lower Re (Waleffe, 1997) and DR in the buffer layer (Li *et al.*, 2006b): the latter, as reviewed above, is responsible for LDR. Vortices of more complex configuration, such as hairpin vortices with Ω-shaped axis-lines, are of broad interest to many outstanding areas of research, including turbulence regeneration at high Re, dynamics in the log-law layer, and bypass transition to turbulence (Adrian, 2007; Wu and Moin, 2009b; Schlatter *et al.*, 2008). In the case of viscoelastic flow concerned here, complex three-dimensional vortices are key to the understanding of HDR. Recall that HDR is marked by qualitative changes in the turbulent statistics of the log-law layer (Zhu *et al.*, 2018) where highly curved vortices are expected to play a more important

role. The mechanism proposed in Zhu *et al.* (2018) for the LDR-HDR transition also requires the understanding of polymer effects on lifted-up vortices, which are again significantly curved away from the streamwise direction.

Motivated by these, Zhu and Xi (2019) have recently developed a new method termed "vortex tracking by iterative propagation" or VATIP. The method borrows the original idea of Jeong *et al.* (1997) of extracting vortex axis-lines by connecting points along their pathways and introduces an iterative search process to connect new points for axis-line propagation in all three spatial dimensions. It has been shown to successfully capture vortices with more general three-dimensional configurations, including those with curved axis-lines, non-streamwise alignment, or complex branched topology. A vortex classification procedure was also proposed in the same study which sorts vortices identified by VATIP into commonly-observed types, such as quasi-streamwise vortices, hooks, hairpins, and irregularly branched ones.

The development of VATIP has enabled for the first time statistical analysis of vortex distribution and conformations. This study will leverage this new tool to investigate polymer effects on vortex dynamics in different stages of viscoelastic turbulence. Although much attention has been dedicated to the vortex-polymer interaction in the literature, this is the first time that the statistical distribution of vortex configuration and topology can be quantitatively analyzed and compared between different Wi in an unbiased manner. Special focus is on the LDR-HDR transition, where knowledge of the dynamics of complex hairpin-like vortices is particularly important, and how the changing vortex dynamics may be responsible for the observed changes in the mean flow. As shown later, our results lead to extensive evidences for the lift-up suppression mechanism hypothesized in Zhu *et al.* (2018) and, perhaps more importantly, the first

complete description of vortex dynamics that accounts for both LDR and HDR. The paper is organized as follows. In section 4.2, we will describe our simulation protocol and provide a brief introduction to the VATIP algorithm. We will then start the results part in section 4.3.1 with flow statistics and highlight their changes between the LDR and HDR stages. This includes the quadrant analysis of velocity fluctuations as an indirect measurement of the changes in coherent structures. Direct visualization of vortex configurations at different stages will be compared in section 4.3.2, where the capability of VATIP in vortex tracking will also be demonstrated. The extracted vortex axis-lines will then be statistically analyzed in sections 4.3.3 and 4.3.4. After polymer effects on different aspects of vortex dynamics are investigated, the paper will conclude with a physical description of the vortex dynamics behind the two DR stages (in section 4.4).

4.2 Formulation and methodology

4.2.1 Direct numerical simulation

DNS in plane Poiseuille flow (the geometry is shown in Figure 4.1) is implemented in this study. The flow is driven by a constant pressure drop and is oriented in the x-direction. The simulation domain size is $L_x \times 2l \times L_z$. Variables in the simulation are nondimensionalized by the turbulent outer units. That is, lengths are normalized by the half-channel height l, velocities by the laminar centerline velocity U_c, pressure by ρU_c^2 (where ρ is the fluid density: i.e., for viscoelastic cases, it is the density of the polymer solution), and time by l/U_c.

Governing equations for the polymeric turbulence are summarized as

$$\frac{\partial \boldsymbol{v}}{\partial t} + \boldsymbol{v} \cdot \boldsymbol{\nabla} \boldsymbol{v} = -\boldsymbol{\nabla} p + \frac{\beta}{\mathrm{Re}} \nabla^2 \boldsymbol{v} + \frac{2\,(1-\beta)}{\mathrm{ReWi}} \left(\boldsymbol{\nabla} \cdot \boldsymbol{\tau}_{\mathrm{p}} \right), \tag{4.4}$$

$$\boldsymbol{\nabla} \cdot \boldsymbol{v} = 0 \tag{4.5}$$

and

$$\frac{\partial \boldsymbol{\alpha}}{\partial t} + \boldsymbol{v} \cdot \boldsymbol{\nabla} \boldsymbol{\alpha} - \boldsymbol{\alpha} \cdot \boldsymbol{\nabla} \boldsymbol{v} - (\boldsymbol{\alpha} \cdot \boldsymbol{\nabla} \boldsymbol{v})^{\mathrm{T}} = \frac{2}{\mathrm{Wi}} (-\frac{\boldsymbol{\alpha}}{1 - \frac{\mathrm{tr}(\boldsymbol{\alpha})}{b}} + \frac{b\boldsymbol{\delta}}{b+2}) + \frac{1}{\mathrm{ScRe}} \nabla^2 \boldsymbol{\alpha}, \tag{4.6}$$

$$\boldsymbol{\tau}_{\mathrm{p}} = \frac{b+5}{b} \left(\frac{\boldsymbol{\alpha}}{1 - \frac{\mathrm{tr}(\boldsymbol{\alpha})}{b}} - \left(1 - \frac{2}{b+2} \right) \boldsymbol{\delta} \right). \tag{4.7}$$

In eq. (4.4), the Reynolds number Re and corresponding friction Reynolds number Re_τ are defined as $\mathrm{Re} \equiv \rho U_c l/\eta$ and $\mathrm{Re}_\tau \equiv \rho u_\tau l/\eta$ (u_τ is the friction velocity), respectively. The two Reynolds numbers can be directly related through $\mathrm{Re}_\tau = \sqrt{2\mathrm{Re}}$. The Weissenberg number measures the level of elasticity and is defined as the product of the polymer relaxation time λ and the mean wall shear rate, i.e., $\mathrm{Wi} \equiv 2\lambda U_c/l$. The viscosity ratio $\beta \equiv \eta_{\mathrm{s}}/(\eta_{\mathrm{s}} + \eta_{\mathrm{p}})$ is the ratio of the solvent viscosity to the total zero-shear-rate viscosity of the polymer solution (subscripts "s" and "p" indicate solvent and polymer contributions to viscosity, respectively). The contribution of polymers to the flow momentum is accounted for by the last term on the right-hand side (RHS) of eq. (4.4), where $\boldsymbol{\tau}_{\mathrm{p}}$ is the polymer stress tensor. The FENE-P constitutive equations (eqs. (4.6) and (4.7)) (Bird *et al.*, 1987), where polymer molecules are treated as finitely extensible nonlinear elastic (FENE) dumbbells, are adopted in this study to calculate $\boldsymbol{\tau}_{\mathrm{p}}$. In FENE-P, $\boldsymbol{\alpha}$ represents the polymer conformation tensor and is defined as $\boldsymbol{\alpha} \equiv \langle \boldsymbol{Q}\boldsymbol{Q} \rangle$, where $\boldsymbol{Q}$ denotes the end-to-end vector of the dumbbell.

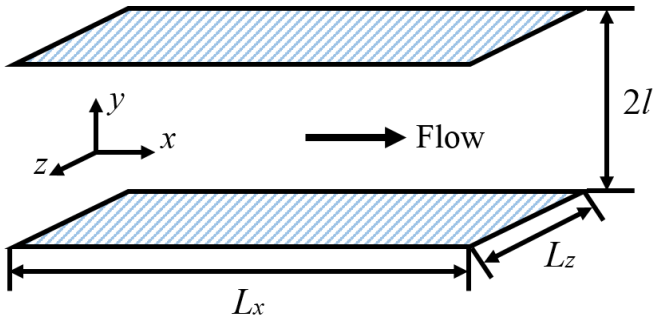

Figure 4.1: Schematic of the flow geometry.

The maximum extensibility parameter b constrains the length of polymer dumbbells through $\max(\mathrm{tr}(\boldsymbol{\alpha})) \leq b$. The last term on the RHS of eq. (4.6) $(1/(\mathrm{ScRe}))\nabla^2\boldsymbol{\alpha}$ (Sc is the Schmidt number) is an artificial diffusion term (not part of the FENE-P model) introduced for the sole purpose of maintaining numerical stability. The use of artificial diffusion is required for the DNS of viscoelastic fluid flows using pseudo-spectral methods (see below). The practice is well studied and established in the literature (Sureshkumar and Beris, 1995).

The Poiseuille flow implies periodic boundary conditions in the x- (streamwise) and z- (spanwise) directions, meaning that all variables are continuous across domain boundaries: e.g., $\boldsymbol{v}(L_x, y, z) = \boldsymbol{v}(0, y, z)$. In the y- (wall-normal) direction, the no-slip boundary condition is applied to the parallel walls for the velocity field: i.e.,

$$\boldsymbol{v} = 0 \quad \text{at } y = \pm l. \tag{4.8}$$

The original FENE-P equation does not require boundary conditions in the y-direction. Adding artificial diffusion introduces second-order partial derivatives and changes the

Re_τ	Wi	β	b	Sc	δ_x^+	δ_z^+	N_y	δ_t	DR%	Stage
172.31	vary	0.97	5000	0.3	9.09	5.44	195	0.01	vary	vary
400	25	0.9	900	0.25	9.09	5.44	473	0.005	16.8	LDR
	50	0.9	3600	0.25					41.2	HDR

Table 4.1: Physical parameters and numerical settings of viscoelastic DNS simulations.

mathematical nature of the equation, for which wall boundary conditions are now required. Boundary values of $\boldsymbol{\alpha}$ are computed at each time step by directly integrating eq. (4.6) in time for grid points at the walls ($y = \pm l$ or ± 1 after nondimensionalization) without the artificial diffusion term. These values then provide boundary conditions for solving the equation, including artificial diffusion, for the rest of the channel.

DNS results of two different Re are analyzed with VATIP in this study. The lower Re case, i.e., Re = 14845 ($\mathrm{Re}_\tau = 172.31$), uses the same dataset previously reported in Zhu *et al.* (2018). At this Re, a clear transition between LDR and HDR is already clearly observable with all features of the transition captured. Also, for Newtonian flow, this Re is sufficient to produce a pronounced PvK log-law layer (Zhu and Xi, 2019). Simulation runs at a wide range of Wi with fixed β and b (see table 4.1) have been performed at this Re, including multiple cases in both LDR and HDR stages. At the higher Re = 80000 ($\mathrm{Re}_\tau = 400$), two viscoelastic cases are simulated. The parameters are so selected that one is at LDR and the other at HDR. Newtonian flow is also simulated for both Re. Parameters for the DNS runs reported in this study are summarized in table 4.1.

A Fourier-Chebyshev-Fourier pseudo-spectral scheme is adopted to discretize all variables in space. The spatial periods are $L_x^+ \times L_z^+ = 4000 \times 800$ for all simulations at

both Re. (The superscript "+" represents quantities nondimensionalized with inner scales – velocities by u_τ and lengths by $\eta/\rho u_\tau$). An $N_x \times N_z = 440 \times 147$ mesh is used for the x and z Fourier transforms and Chebyshev-Gauss-Lobatto points are used for the Chebyshev transform in the y-direction. The number of grid points N_y is adjusted with Re (see table 4.1): for Re = 172.31, the range of y-grid spacing δ_y^+ is 0.022 to 2.79 (minimum at the walls and maximum at the channel center) and for $\mathrm{Re}_\tau = 400$, it is 0.011 to 3.03. The time integration chooses a third-order semi-implicit backward-differentiation/Adams-Bashforth scheme (Peyretr, 2013). Different time step sizes are chosen at the two Re (table 4.1) according to the Courant-Friedrichs-Lewy (CFL) stability condition. The magnitude of the numerical diffusivity 1/(ScRe) (in the artificial diffusion term of eq. (4.6)) is 2.25×10^{-4} for Re = 172.31 and 5×10^{-5} for Re = 400, respectively. This is lower than most studies in the literature in which a numerical diffusivity in the order of $O(0.01)$ is generally found to be safe (Ptasinski *et al.*, 2003; Sureshkumar *et al.*, 1997; Sureshkumar and Beris, 1995; Dimitropoulos *et al.*, 1998). A detailed numerical sensitivity analysis at three different levels of numerical diffusivity and resolution was reported in Zhu *et al.* (2018) and not repeated here. The viscoelastic DNS code used in this study is custom-developed by expanding the open-source package for Newtonian DNS `ChannelFlow`, originally developed by John F. Gibson (Gibson, 2012) and later improved and parallelized by Tobias Schneider, Hecke Degering (Schrobsdorff), and co-workers (Tuckerman *et al.*, 2014).

4.2.2 VATIP for vortex tracking

The purpose of VATIP is to extract the axis-lines of individual vortices around which the fluid rotates. If a vortex is defined as a tube in which the scalar identifier Q

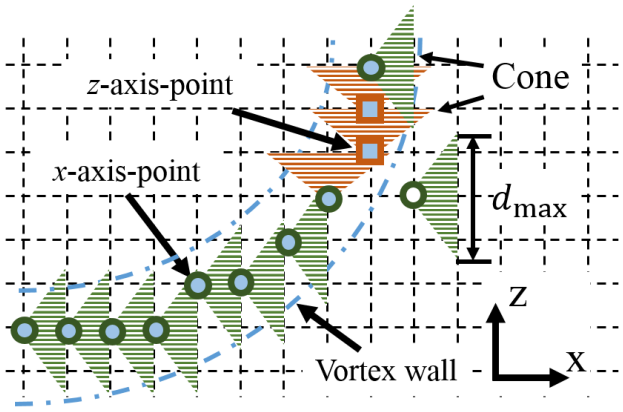

Figure 4.2: The conceptual plot of the VATIP algorithm. A new point is connected to a propagating axis-line if it falls within a detection cone. The x-direction search round looks for local maxima of Q in the yz plane (labeled x-axis-points); the search continues in other directions after no more x-axis-points can be added. For simplicity, the plot only sketches a two-dimensional scenario without explicitly showing the search round in the y-direction. The triangles thus represent the planar projection of the detection cones.

$\mathrm{Re}_\tau = 172.31$	Newt.	Wi = 20	Wi = 80
Q_{rms}	0.0325	0.017	0.0061
$\mathrm{Re}_\tau = 400$	Newt.	LDR	HDR
Q_{rms}	0.0305	0.0125	0.00461

Table 4.2: Values of Q_{rms} in representative Newtonian and viscoelastic DNS flow fields.

exceeds a curtain threshold, the Q magnitude increases from the tube shell inwards and peaks at the axis. The axis-line preserves the position, size, shape, and topology of the vortex and is thus particularly instrumental in vortex analysis. The scalar Q field first needs to be calculated from the velocity data (eq. (4.3)). To determine the threshold value of Q for vortex identification, we follow a systematic procedure based on the so-called "percolation analysis", which has been extensively discussed in previous studies (Zhu *et al.*, 2018; Zhu and Xi, 2019). In short, a very low Q threshold will over-identify vortex regions and render one interconnected (percolating) vortex structure whereas at the other limit (high threshold), vortices will be under-identified with many valid vortices excluded from the result. The percolation analysis identifies Q values at which individual vortex objects are just separated apart but are still mostly preserved. In this study, spatial regions with $Q > 0.4Q_{\mathrm{rms}}$ (Q_{rms} being the root-mean-square – RMS – value of Q over the domain

$$Q_{\mathrm{rms}} \equiv \sqrt{\frac{1}{2lL_xL_z\Delta T}\int_0^{\Delta T}\left(\iiint Q^2 dxdydz\right)dt} \tag{4.9}$$

) are identified as vortex regions. Values of Q_{rms} for several representative cases (in different flow stages) are provided in table 4.2. Notably, Q_{rms} decreases monotonically with increasing DR%, indicating the correlation between vortex weakening and drag reduction. More detailed results and discussion in this regard are found in our earlier study (Zhu *et al.*, 2018).

Each point on the axis-line is the maximum of Q in the corresponding cross-sectional plane of the vortex tube. Depending on the direction of the vortex segment concerned, the axis-point may appear as a local two-dimensional maximum in the yz, xz, or xy plane (for vortex segments aligned in the x, y, or z direction, respectively).

Therefore, all two-dimensional local maxima in planes of all orientations within the identified vortex regions need to be found and recorded as potential axis-points.

Connecting axis-points that belong to the same vortices to form axis-lines is the central task of vortex tracking which is illustrated in fig. 4.2. The process starts with yz planes for x-direction tracking. At each yz grid plane, a new axis-line is initiated from each unassociated potential axis-point. Existing axis-lines attempt to propagate along the x direction by finding eligible axis-points in the next plane for connection. Connection is made if the next axis-point falls within a cone-shaped region projected from the propagating end of the axis-line. The size of the cone is determined from the average radius of a streamwise vortex tube

$$r_{\mathrm{v}} = \sqrt{\frac{\sum_{i=1}^{N_x} A_{\mathrm{v},i}}{\pi \sum_{i=1}^{N_x} N_{\mathrm{v},i}}}, \tag{4.10}$$

(where N_x is the number of x-grid points – i.e., the number of yz-planes, i is the yz-plane index, $A_{\mathrm{v},i}$ is the total area of vortex regions on plane i calculated by adding up all areas that satisfy the vortex identification criterion ($Q > 0.4Q_{\mathrm{rms}}$ in this study) on the plane, and $N_{\mathrm{v},i}$ is the number of separate vortex areas on the plane) and a base diameter of $d_{\max} = 1.4r_{\mathrm{v}}$ is used in this study. This so-called "cone-detective" idea was first proposed by Jeong *et al.* (1997) which however only focused on streamwise vortices and their algorithm stops the search after the x-direction search round. In VATIP, the search continues in the y and then z direction for vortices whose axis-lines are no longer confined in the x-direction. These continued search rounds extend the existing axis-lines in new directions by connecting axis-points in two-dimensional planes of other orientations: e.g., for the search in the z-direction, local Q maxima in xy-planes, which are termed z-axis-points, are added to the growing axis-lines when

they fall into the detection cones (now pointed towards the z direction; see fig. 4.2). Initiation of new axis-lines is not allowed in these continued search rounds to avoid false identification (i.e., all axis-lines are initiated in the first round of x-direction search). However, separate axis-lines are allowed to merge if the detection cone from the propagating end finds another axis-line within its range. Consider a hairpin vortex typically observed in the log-law layer (Robinson, 1991; Adrian, 2007; Wu and Moin, 2009b) with an Ω-shaped axis configuration, its two legs extend towards the wall and along the x-direction and will be captured with the first x-direction search round; at the downstream end, the legs lift up away from the wall (which requires y-direction search) and merge along the z-direction to form an arc (which requires z-direction search and axis-line merging). An x-y-z search cycle would successfully capture such vortices. Many vortices observed in DNS results, however, do not conform to this canonical shape and in order to capture a wider variety of three-dimensional vortices with complex axis-line topology, the VATIP algorithm continues to iteratively loop over searches in all three directions until the number of identified vortices converges.

VATIP was tested with intentionally generated curved vortices such as hooks and hairpins as well as actual DNS flow fields. It was shown to successfully capture vortices of all known shapes and configurations typically observed in near-wall turbulence (Zhu *et al.*, 2018). Note that this section only provides a high-level description of the key elements of VATIP. The readers are referred to Zhu and Xi (2019) for implementation details and further discussions about the method.

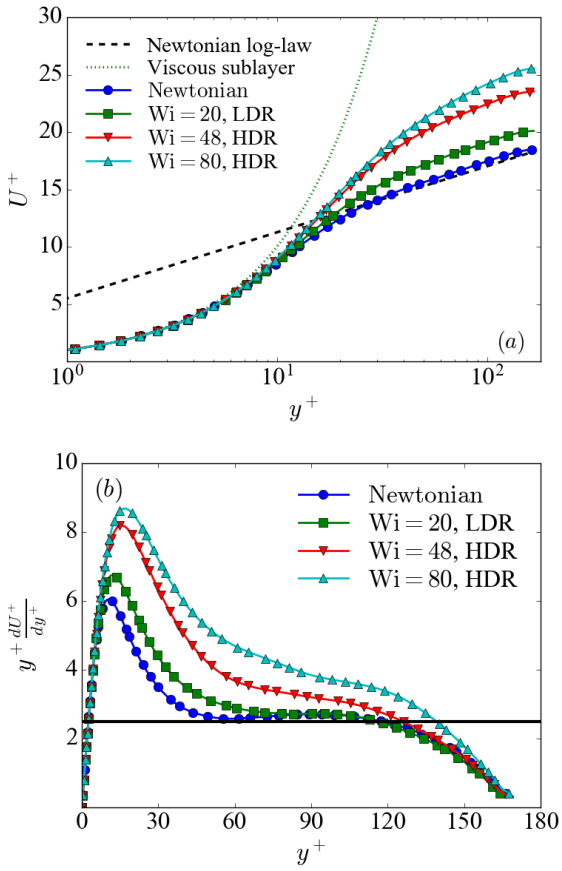

Figure 4.3: (a) Mean velocity profiles (U^+ vesus y^+) and (b) log-law indicator function (y^+dU^+/dy^+ vesus y^+) at $\mathrm{Re}_\tau = 172.31$; horizontal line marks the PvK magnitude of 2.5 (eq. (4.1)).

4.3 Results and Discussion

4.3.1 Flow statistics

By injecting polymers into turbulent flows, properties of the flows are significantly changed which leads to considerable reduction of the friction drag and increase of the mean flow rate. In fig. 4.3(a), we show the mean velocity profiles of the Newtonian and three viscoelastic cases (Wi = 20, 48, and 80) at $\mathrm{Re}_\tau = 172.31$. For the Newtonian

case, the profile closely follows the PvK asymptote (eq. (4.1)) at $y^+ \gtrsim 50$, indicating that the log law layer has been sufficiently developed at this $\mathrm{Re}_\tau = 172.31$. For the $\mathrm{Wi} = 20$ case, the velocity profile lifts up in the buffer layer ($20 \lesssim y^+ \lesssim 50$) but stays parallel to the PvK asymptote at higher y^+. By contrast, the profiles of the $\mathrm{Wi} = 48$ and 80 cases lift up across most of the channel including what used to be the log-law layer. This observation has been the most-discussed difference between LDR and HDR in the literature (Warholic *et al.*, 1999; Ptasinski *et al.*, 2003; Li *et al.*, 2006a; Housiadas and Beris, 2003; Xi and Graham, 2010b; Zhu *et al.*, 2018; Mohammadtabar *et al.*, 2017). In our case, it is clear that $\mathrm{Wi} = 20$ belongs to LDR and $\mathrm{Wi} = 48$ and 80 are well within the HDR regime. The qualitative change in the mean velocity gradient is more clearly seen in the logarithmic law indicator function (fig. 4.3(b)). Note that any $U^+(y^+)$ dependence can be written in the generic form of

$$U^+ = \frac{1}{\kappa} \ln y^+ + B \tag{4.11}$$

where B is a constant and the indicator function

$$\frac{1}{\kappa} = \frac{dU^+}{d \ln y^+} = y^+ \frac{dU^+}{dy^+} \tag{4.12}$$

is a constant only if the profile follows a logarithmic dependence. For Newtonian and LDR ($\mathrm{Wi} = 20$) cases, a clear inflection point with $1/\kappa \approx 2.5$ shows up at $y^+ \approx 50$, which is followed by a nearly flat segment at $50 \lesssim y^+ \lesssim 100$ – a clear log-law layer. For HDR cases ($\mathrm{Wi} = 48$ and 80), the inflection point disappears and the segment at larger y^+ is no longer flat. This indicates the log law is no longer valid at the HDR stage, which is consistent with the finding of White *et al.* (2012).

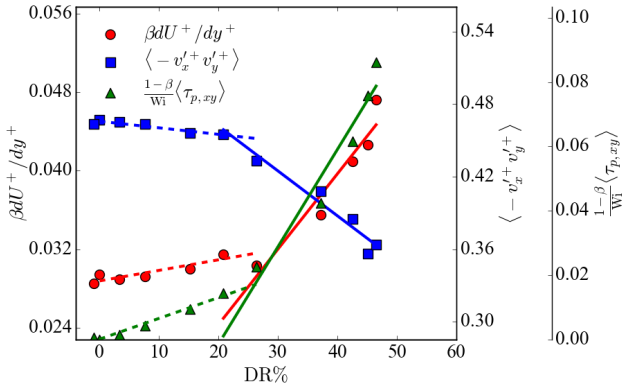

Figure 4.4: Shear stress components at $y^+ = 103.2$ plotted against DR% ($\mathrm{Re}_\tau = 172.31$), including the Newtonian case (DR%) and viscoelastic cases at Wi = 8, 12, 16, 20, 24, 32, 48, 64, 80, and 96 (DR% increases monotonically with Wi with the exception of Wi = 8, which is pre-onset and nearly overlaps with the Newtonian case). The lines are guides to the eyes for the LDR (dashed) and HDR (solid) stages.

The mean velocity gradient (which determines the indicator function – eq. (4.12)) is related with velocity fluctuation and polymer stress through the shear stress balance:

$$\langle \tau_{xy}^+ \rangle = \beta \frac{dU^+}{dy^+} + \langle -v_x'^+ v_y'^+ \rangle + \frac{1-\beta}{\mathrm{Wi}} \langle \tau_{\mathrm{p},xy} \rangle \tag{4.13}$$

where the three terms on the RHS represents contributions from the viscous, Reynolds, and polymer shear stresses, respectively ($\langle \cdot \rangle$ represents averages over x, z, and t axes). Under constant mean pressure gradient, the total shear stress is a constant for given Re and y^+ position –

$$\langle \tau_{xy}^+ \rangle = 1 - \frac{y^+}{\mathrm{Re}_\tau}. \tag{4.14}$$

With increasing DR%, the rise of viscous and polymer shear stresses must be accompanied by the drop of RSS. Recent studies further showed that, similar to the change of $1/\kappa$, the suppression of RSS is contained within and near the buffer layer at LDR

and significant reduction of RSS at larger y^+ is only obvious at HDR (Xi and Graham, 2010b; Zhu *et al.*, 2018). In fig. 4.4, the magnitudes of these shear stress components at $y^+ = 103.2$ (which is well within the log-law layer for the Newtonian case) are plotted against DR% for DNS results at $\mathrm{Re}_\tau = 172.31$, including the Newtonian and viscoelastic cases at ten different Wi (see caption of fig. 4.4). The LDR-HDR transition occurs at DR% $\approx$ 20% and Wi $\approx$ 24, which is marked by a sharp turn in all three components. Variations in these quantities are mild at LDR but for HDR their DR%-dependencies become steep. The rapid decline of RSS, in particular, indicates a new stage of turbulence suppression in the log-law layer which is only initiated at the start of HDR. Note that the transition point of DR% $\approx$ 20% is not universal and at higher Re the critical DR% will be higher. Although earlier studies widely quoted DR% $\approx 30 \sim 35\%$ as the separation between LDR and HDR (Warholic *et al.*, 1999; Li *et al.*, 2006a, 2015), it was recently established that the transition point is a function of Re (Zhu *et al.*, 2018), which again shows that the LDR-HDR transition is more than a quantitative effect of the level of DR% but a shift between two qualitatively different stages of DR.

Velocity fluctuations at $\mathrm{Re}_\tau = 172.31$ are inspected with quadrant analysis which plots the joint probability density function (PDF) between the streamwise and wall-normal velocity fluctuations (figs. 4.5 and 4.6). The distribution is typically skewed towards the second and fourth quadrants (Q2 and Q4) where $v_x'^+$ and $v_y'^+$ have opposite signs and thus contribute positively to the RSS (second term on the RHS of eq. (4.13)). The Q2 events, in which $v_x'^+ < 0$ and $v_y'^+ > 0$, correspond to the upward movement of the slower fluids near the wall to larger y^+ which causes a local reduction in the streamwise velocity and is often termed "ejections". Meanwhile, the opposite

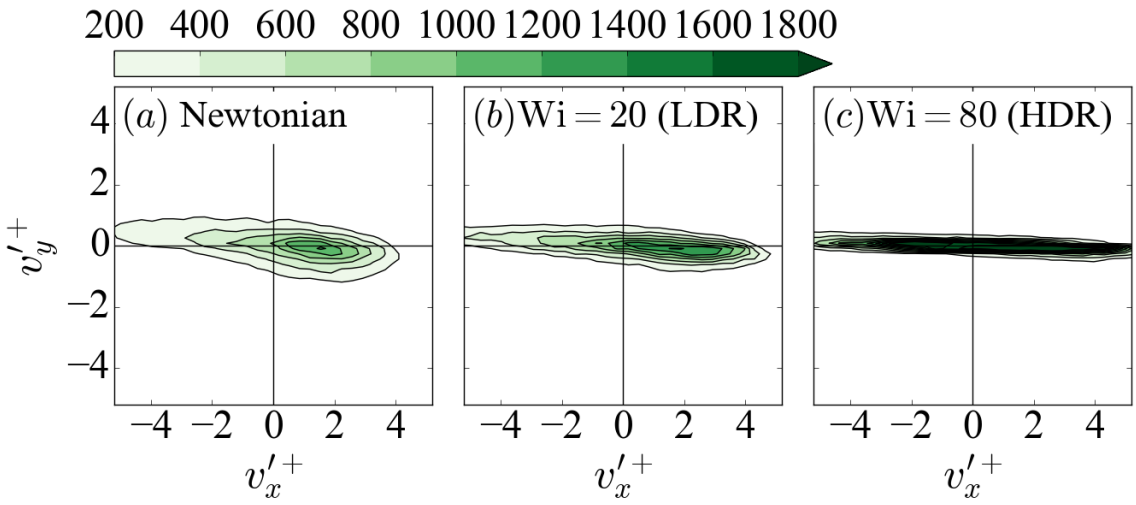

Figure 4.5: Joint PDF of the streamwise and wall-normal velocity fluctuations at $y^+ = 25$ ($\mathrm{Re}_\tau = 172.31$).

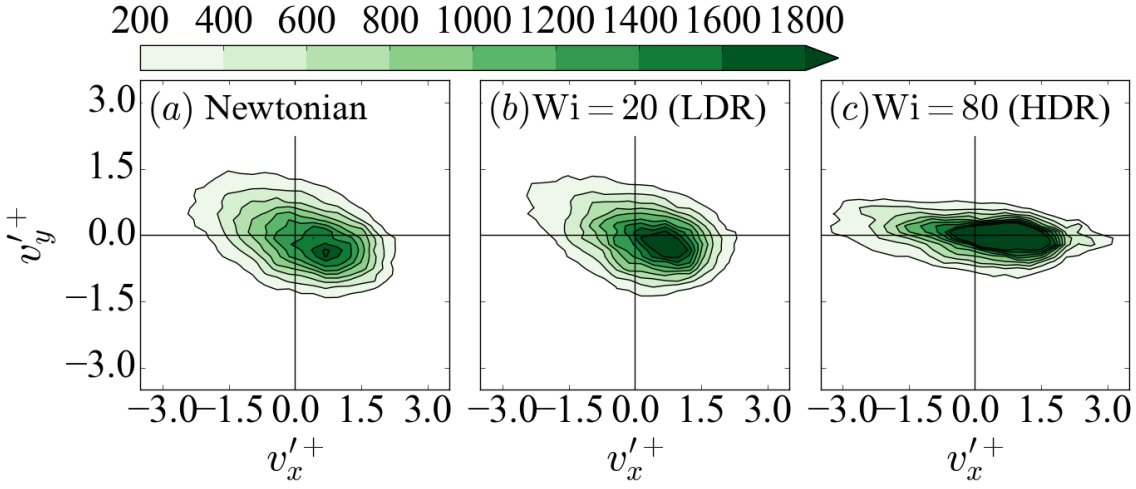

Figure 4.6: Joint PDF of the streamwise and wall-normal velocity fluctuations at $y^+ = 100$ ($\mathrm{Re}_\tau = 172.31$).

Q4 events are called "sweeps" (Lozano-Durán *et al.*, 2012; Wallace, 2016). The buffer layer (Figure 4.5) distribution is flatter owing to its stronger streamwise velocity fluctuations. As Wi increases, the joint PDF contour span shrinks in the y-direction while expands along x-direction, which is consistent with the established observation in the literature that the wall-normal and spanwise velocity fluctuations are suppressed by polymers but the streamwise fluctuations are often enhanced (Sureshkumar *et al.*, 1997; Ptasinski *et al.*, 2003; Min *et al.*, 2003; Li *et al.*, 2006a). Suppression of the ejections and sweeps in the buffer layer reduces the wall-normal momentum fluxes responsible for the high Reynolds stress (Townsend, 1980; Marusic *et al.*, 2010). Note that in the buffer layer, the joint PDF shape is already clearly modified in LDR, which only continues into HDR. By contract, at higher y^+ (fig. 4.6), the transition between LDR and HDR is sharp. The joint PDF patterns are similar between Newtonian and LDR cases whereas at HDR it is clearly flattened, indicating that polymer-induced changes in coherent motions only start at HDR in that wall region. Our quadrant analysis results are remarkably similar to the recent experimental measurement by Mohammadtabar *et al.* (2017) at comparable or lower Re (Re_τ ranges from approximately 200 to 70 from the Newtonian limit to the highest DR%).

Observations in flow statistics suggest that the LDR-HDR transition is underpinned by a sudden shift of the regions or wall layers where polymer interaction with turbulence is substantial. At LDR, polymers mainly suppress turbulence in the buffer layer, causing its enlargement and higher mean velocity gradient, whereas the log-law layer is left largely intact. This is indeed the essence of the elastic sublayer theory of Virk (1975). The theory, however, does not account for the occurrence of the second

stage of DR – HDR – where polymer effects on turbulent dynamics begin to substantially alter the log-law layer. Further evidences for the transitions in flow statistics, as well as the localization in turbulence distribution at HDR, are found in Zhu *et al.* (2018) and not repeated here. The primary focus of this study is to investigate the changes in coherent structure dynamics behind these observations.

4.3.2 Vortex conformation and tracking in instantaneous flow fields

We start with instantaneous images of flow-field vortices and their axis-line conformations identified by VATIP at $\mathrm{Re}_\tau = 172.31$. Vortices are identified with the Q criterion and the isosurfaces of $Q = 0.4Q_{\mathrm{rms}}$ are plotted in fig. 4.7. Although streamwise aligned vortices are seen in all cases especially near the wall, the Newtonian and LDR cases show strong tendency for vortex lift up, in which the vortex legs (in the upstream) are initiated near the wall along the streamwise direction but its head becomes detached from the wall in the downstream. Detached vortex segments become distorted and deviate away from the flow direction. Hairpins are a distinct type of lifted-up vortices with an Ω-shaped contour: a transverse arc at the downstream end with two streamwise legs extending upstream towards the wall. At this Re, they are already populating the flow domain in the Newtonian and LDR cases. The HDR image appear drastically different with significantly reduced instances of vortex lift-up, hairpins, and curved vortices. The vortices are more likely to stick close to the wall and become much more extended in the flow direction than LDR. This observation is consistent with the earlier observations in conditional eddies by Kim *et al.* (2007). This dominance of elongated vortex conformation underlines the

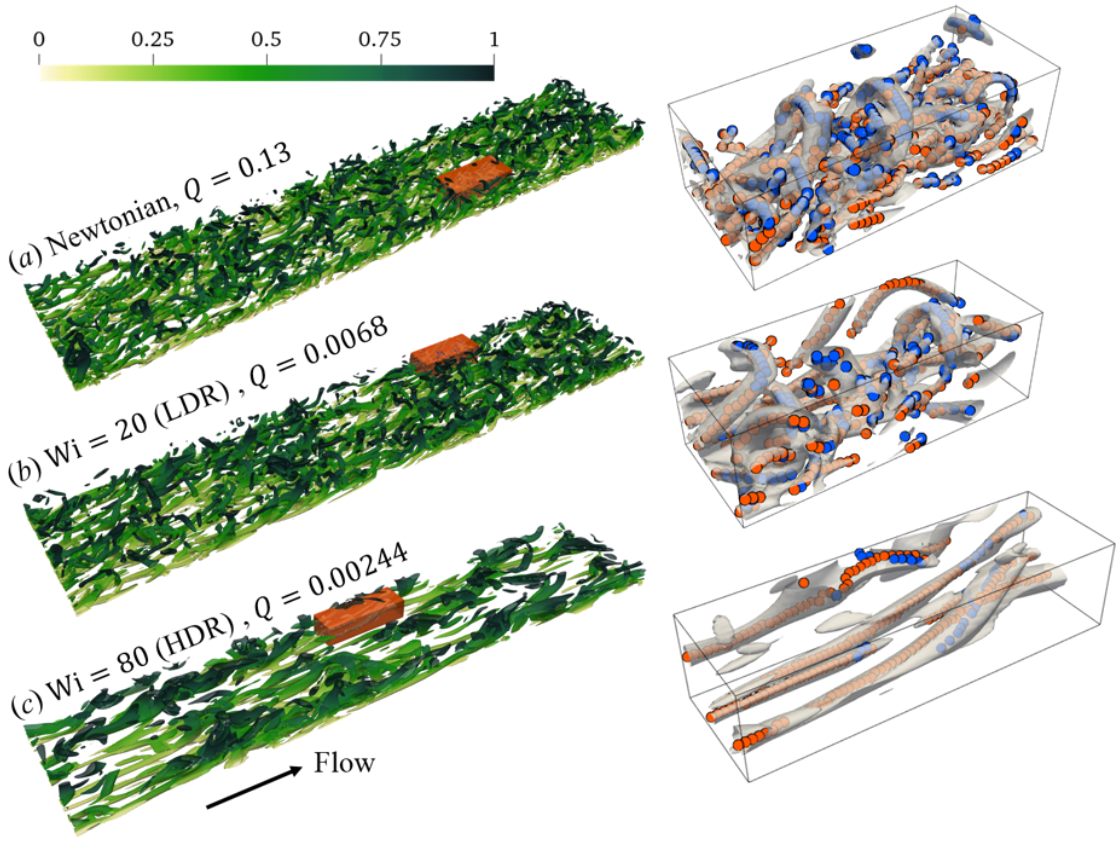

Figure 4.7: Instantaneous vortex structures of (a) Newtonian, (b) Wi = 20 and (c) Wi = 80 cases $\mathrm{Re}_\tau = 172.31$ identified by the Q-criterion (only the bottom half of the channel is shown). The color shade (from light to dark) maps to the distance from the bottom wall in outer units. Part of the domain (orange box) is enlarged and shown on the right. Circular markers are axis-points identified by VATIP: orange (light) for x-axis-points; blue (dark) for y- and z-axis-points.

common observations of much smoother velocity distribution at HDR with extended streak patterns (Warholic *et al.*, 2001; White *et al.*, 2004; Housiadas *et al.*, 2005; Li *et al.*, 2006a).

VATIP allows us to go beyond direct intuitive visual inspection and extract vortex conformations without subjective bias. Vortex axis-points identified by VATIP are shown in fig. 4.7 with circular markers for a smaller region in the domain. It is clear that in all cases, the axis-lines (connecting all axis-points) obtained by VATIP successfully capture all visible vortices and well preserve their size, position, shape, and topology, including both straight (quasi-streamwise) and curved (e.g., hairpins) vortices. Quasi-streamwise vortex axis-lines are mainly composed of x-axis-points (which are local maxima of Q in yz-planes), represented by orange markers. For significantly lifted-up vortices (including hairpins), mostly seen in the Newtonian and LDR cases, y- and z-axis-points (blue markers; local maxima in xz- and xy-planes) must be included. This is a major improvement of VATIP compared with earlier approaches which are limited to streamwise vortices (Jeong *et al.*, 1997; Sibilla and Beretta, 2005). These y- and z- axis-points become less important at HDR where streamwise vortices dominate. Spatial proximity between vortices in the DNS of full steady-state turbulence makes it difficult to clearly visualize individual vortex conformations. More isolated vortices of a variety of shapes can be generated using transient DNS to test the VATIP performance, which was done in Zhu and Xi (2019) and not repeated here.

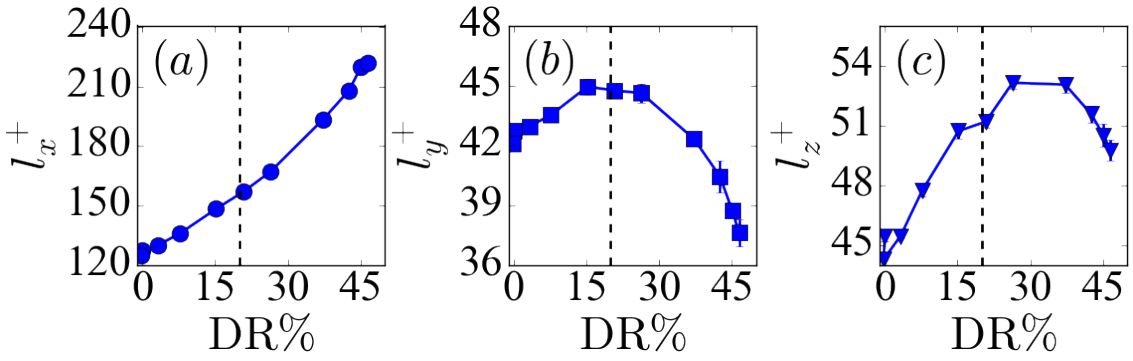

Figure 4.8: Average dimensions of the enclosing cuboid of each vortex at $\mathrm{Re}_\tau = 172.31$: (a) streamwise length l_x^+, (b) wall-normal length l_y^+ and (c) spanwise length l_z^+. Dashed line marks the LDR-HDR transition.

4.3.3 Polymer effects on vortex conformation and lift-up

Axis-lines extracted by VATIP open up the possibility for the statistical analysis of vortex conformations. Figure 4.8 shows the average dimensions of vortices at $\mathrm{Re}_\tau = 172.31$, measured by the edge lengths of a minimal cuboid enclosing each vortex. A dashed line is drawn at DR% = 20%, which was identified earlier as the point of LDR-HDR transition at $\mathrm{Re}_\tau = 172.31$ based on flow statistics (fig. 4.4). This line is provided in all DR%-dependence plots in this study to provide a reference for identifying the correlation, or the lack thereof (if that is the case), between changes in flow statistics and vortex structure measurements. The average streamwise dimension of a vortex l_x^+ (fig. 4.8(a)) increases nearly monotonically with DR%, indicating that vortices become elongated in the streamwise direction with polymer DR effects. This is indeed a well-established observation in the literature (Li *et al.*, 2006a, 2015; Kim *et al.*, 2007, 2008) and consistent with the direct observation in fig. 4.7. The trend continues after the LDR-HDR transition with no notable change in pattern. Streamwise vortex elongation can be interpreted as the result of vortex stabilization (Dubief

et al., 2005; Zhu *et al.*, 2019): when a vortex does not lift up away from the wall or burst into pieces for an extended period of time, it is continuously stretched by the flow. Because vortices are in general not strictly aligned with the x axis, its elongation can also lead to increasing dimensions in the other directions l_y^+ and l_z^+. This effect seems to dominate at LDR where l_y^+ and l_z^+ grow nearly monotonically (fig. 4.8). Due to the increasing stability of vortices, the wall-normal and spanwise length also increase in the LDR stage. However, this trend is turned around after the LDR-HDR transition. In fig. 4.8(b), the wall-normal length l_y^+ immediately drops when the HDR stage is reached, which is consistent with the hypothesis of Zhu *et al.* (2018) that at HDR polymers suppress the lift up of vortices. Lift-up exposes the downstream end, or the "head", of the vortex to transverse flows, which bend the vortex sideways to form spanwise segments of vortex tubes (such as the arc in an Ω-shaped hairpin vortex) and increase its dimension in z direction l_z^+. Suppression of vortex lift-up explains the reduction of curved vortices such as hairpins, as seen in fig. 4.7. The spanwise vortex length l_z^+ (fig. 4.8(c)) does indeed drop substantially at HDR. The turning point is slightly delayed compared with the LDR-HDR transition. This seems to suggest that the start of HDR is more directly linked to lift-up suppression, which blocks the transfer of turbulent motions from the buffer layer to the log-law region, and the reduction of hairpins and spanwise vortex dimension is a secondary effect. Highly lifted vortices will eventually burst into intense fluctuations (Zhu *et al.*, 2019) which may seed new streak stabilities and lead to turbulence proliferation. Confining the stabilized vortices to the streamwise direction leads to their prolonged stretching and a shift in the turbulent regeneration dynamics.

Vortex lift-up can now be quantified by the wall-normal positions of the head

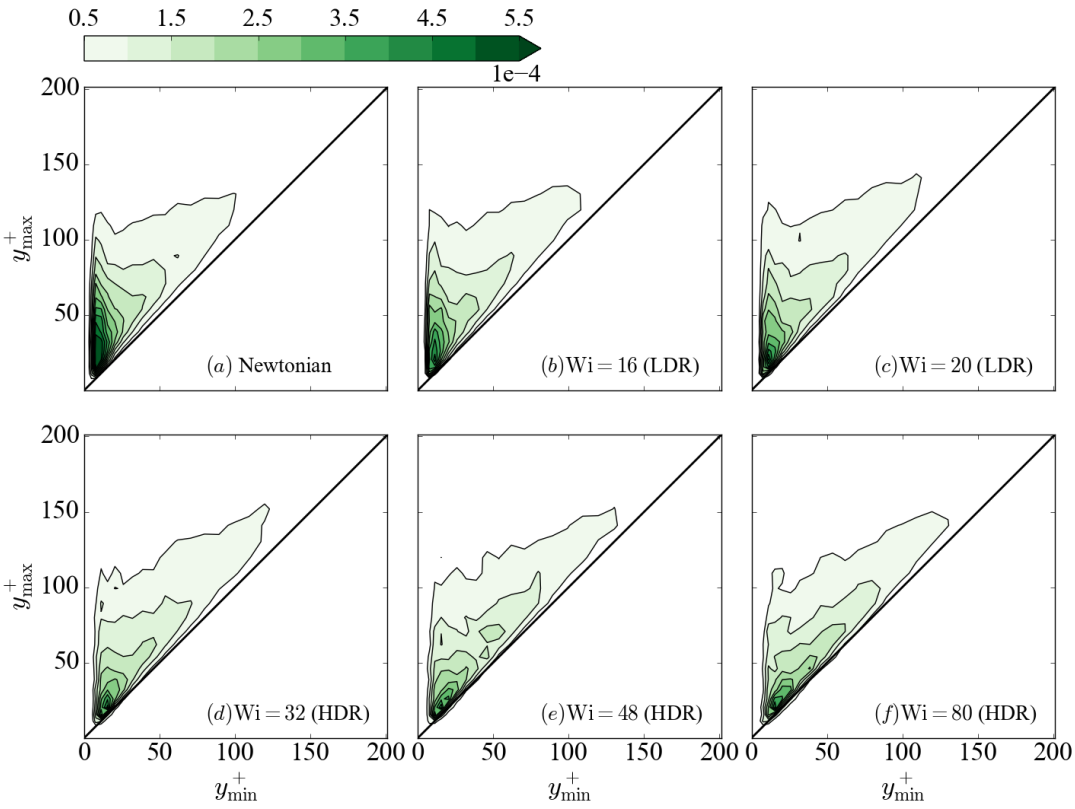

Figure 4.9: Joint PDFs of the wall-normal positions of the head and tail/legs of each vortex, as measured respectively by the maximum and minimum y^+ coordinates of the vortex axis-line, at $\mathrm{Re}_\tau = 172.31$ and different Wi.

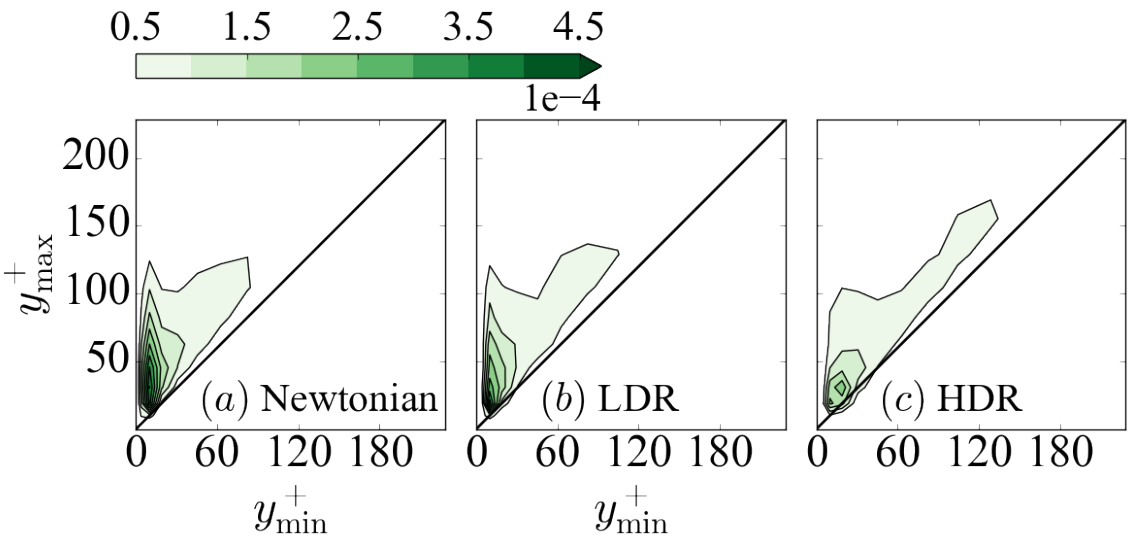

Figure 4.10: Joint PDFs of the wall-normal positions of the head and tail/legs of each vortex, as measured respectively by the maximum and minimum y^+ coordinates of the vortex axis-line, at $\mathrm{Re}_\tau = 400$ and different Wi.

(highest point, typically at the downstream end) and leg(s)/tail (lowest point, typically at the upstream end) of the vortices. These positions can be measured from the axis-lines obtained from VATIP and the joint PDFs between them are shown in fig. 4.9 for the Re = 172.31 case. The distribution at LDR (Wi = 16 and 20 cases) closely resembles that of the Newtonian case and is highly concentrated in the buffer layer ($y^+ < 30$). Two concentration bands extend from the peak distribution there: one along the vertical axis that corresponds to the highly lifted-up vortices (leg/tail $y^+_{\min}$ in the buffer layer but head $y^+_{\max}$ well into the log-law layer) and the other, slightly less populated, along the diagonal that corresponds to flat-lying vortices that align mostly along the streamwise direction. The pattern clearly changes at HDR where the vertical band becomes significantly weakened and the diagonal band is more pronounced and extends to higher y^+. The concentration peak is still found in the buffer layer but it is now more aligned with the diagonal than the ordinate. Distribution

pattern at $\mathrm{Re}_\tau = 400$ (fig. 4.10) is strikingly similar, not only qualitatively (i.e., the pivot towards the diagonal) but also quantitatively. Wall-normal positions and spans of vortices are well comparable, in inner units, between these two distinctly different Re, indicating strong scalability of coherent structures at different DR stages with increasing Re.

From these results, it becomes clear that at LDR, despite an overall weakening of all vortices, vortex distribution has changed little compared with the Newtonian limit, whereas the suppression of vortex lift-up only starts at HDR, which corroborates our earlier notation that the LDR-HDR transition is a reflection of a new stage of DR with a distinct mechanism. Earlier studies have suggested the possibility of lift-up suppression by polymers through direct flow field inspection or conditional sampling of average eddies (Kim *et al.*, 2007; Zhu and Xi, 2018; Zhu *et al.*, 2019). Statistical quantification of vortex lift-up tendency would not have been possible without the specific information on individual vortex axis-lines. More importantly, this is the first time polymer-induced lift-up suppression is associated with the LDR-HDR transition by direct evidence. Vortex lift-up is important in the turbulent momentum transfer between different wall layers and widely believed to be responsible for the PvK log law (eq. (4.1)) (Townsend, 1980; Perry and Marušić, 1995; Lozano-Durán *et al.*, 2012). Its suppression at HDR thus offers a clear pathway to explain the changing mean flow profile in that regime. Meanwhile, extension of the diagonal band indicates the increasing frequency of flat-lying vortices at higher wall layers, which again supports a change in the log-law dynamics.

Townsend (1980) introduced the concepts of "attached" and "detached" vortices. Attached vortices interact closely with the wall and were believed to be responsible for

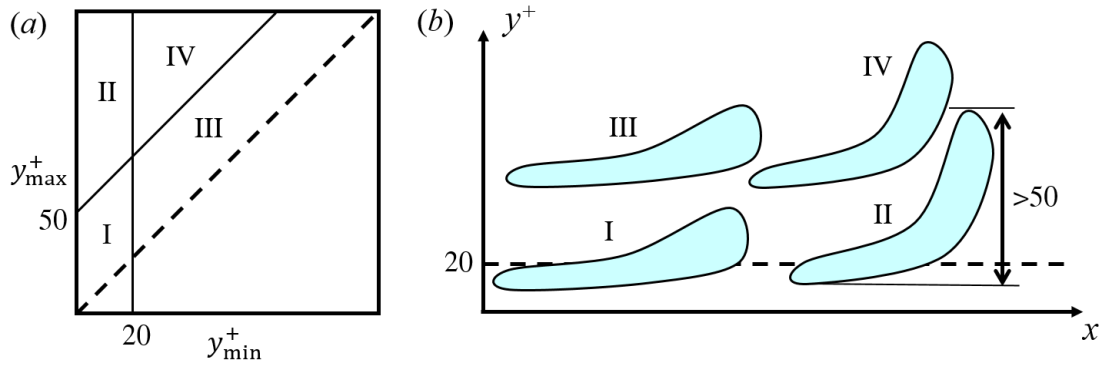

Figure 4.11: Schematics of vortex categorization by wall position and lift-up extent: (I) attached-flat, (II) attached-lifted, (III) detached-flat, and (IV) detached-lifted.

the generation and transport of Reynolds stress and TKE. Detached vortices are found away from the wall and they were conjectured to be associated with the dissipation of turbulent activities (Perry and Marušić, 1995). Lozano-Durán *et al.* (2012) classified coherent structures into attached and detached groups based on their wall positions: structures with their bottom sticking close to the wall (i.e. $y^+_{\text{min}} \leq 20$) were considered to be attached and the others detached. Distinction was further made based on the wall-normal span of the structures by the same authors. In particular, "tall-attached" structures that extend across the channel were believed to be of particular importance in the transport of Reynolds stress. Following the same spirit, we categorize vortices into four types based on these two metrics of vortex wall position and wall-normal span, which are both quantitatively measurable from vortex axis-lines extracted with VATIP. Each type maps to a region in the y^+_{max}-y^+_{min} coordinates (same as fig. 4.9) as illustrated in fig. 4.11. Type I or "attached-flat" vortices are those with $y^+_{\text{min}} \leq 20$ and $l^+_y \equiv y^+_{\text{max}} - y^+_{\text{min}} \leq 50$. Note that the y^+_{min} criterion measures the proximity to the wall and the l^+_y criterion measures the extent of vortex lift-up. This type

thus includes vortices lying flat in regions very close to the wall without strong lift-up. These vortices are the dominant structures in the buffer layer and are most frequently spotted in all cases (fig. 4.9). Type II or "attached-lifted" vortices satisfy $y^+_{\min} \leq 20$ and $l^+_y > 50$. These vortices are generated by wall interaction but their strong lift-up allows them to efficiently transport turbulent activities between the buffer and log-law layers. Type III or "detached-flat" ($y^+_{\min} > 20$ and $l^+_y \leq 50$) and type IV or "detached-lifted" ($y^+_{\min} > 20$ and $l^+_y > 50$) are similarly differentiated by their extent of lift-up and in both cases, the vortices are detached from the wall and thus less influenced by the latter. The cut off magnitudes of $y^+_{\min} = 20$ and $l^+_y = 50$ were arbitrarily chosen based on the observed distribution patterns in fig. 4.9 and our general experience with vortices in channel flow. We have tested that changing the cut off values within a reasonable range ($y^+_{\min} = 20 \sim 40$ and $l^+_y = 35 \sim 50$) would not change the following results in any significant manner.

It is necessary to clarify here that VATIP, in its current form, is an intrinsically static approach. It captures vortex instances from a frozen image of the flow field. Therefore, categorization results according to fig. 4.11 should be interpreted through the lens of ensemble statistics – i.e., for an arbitrarily selected vortex at a random time moment, what is the probability that it is caught in a configuration belonging to one of these four types. The method does not provide direct information on the dynamical lineage of vortices and does not track the time evolution of vortex configuration. The category label does not carry though different times: a vortex may as well evolve into a different type at a future moment. For instance, a classical streamwise vortex in the buffer layer would be categorized as type I, but if it lifts up at a later time, it would become type II.

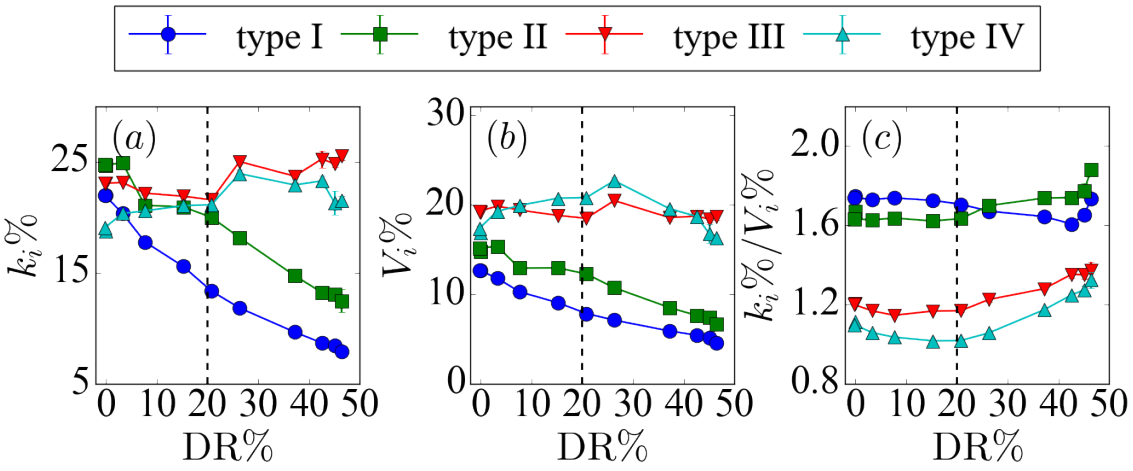

Figure 4.12: Distribution of TKE and volume between vortices of different types at $\mathrm{Re}_\tau = 172.31$: (a) percentage of TKE contained in each type of vortices; (b) percentage of volume occupied by each type of vortex; and (c) normalized TKE density. Percentages are with respect to the flow domain total. Dashed line marks the LDR-HDR transition. Error bars smaller than the symbol size are not shown.

Polymer effects on these vortex types are quantified in fig. 4.12 in terms of the percentage of TKE contained in all vortices of type i

$$k_i\% \equiv \frac{k_i}{k_\mathrm{t}} \tag{4.15}$$

and the percentage of volume occupied by all vortices of type i

$$V_i\% \equiv \frac{V_i}{V_\mathrm{t}} \tag{4.16}$$

where k_t and V_t are the total TKE and total volume of the flow domain, respectively. The ratio between the two

$$\frac{k_i\%}{V_i\%} = \frac{k_i/V_i}{k_\mathrm{t}/V_\mathrm{t}} \tag{4.17}$$

is the volumetric density of TKE in vortex type i normalized by the TKE density of the entire domain. Since VATIP only renders an axis-line, instead of a three-dimensional volume, of each vortex, volumetric statistics of the vortex are calculated within a region around the axie-line. A square with the edge length of $1.5r_{\mathrm{v}}$ is drawn (in the vortex cross-sectional plane) around each axis-point (placed at the center of the square) of the vortex axis-line and regions falling into these confining squares are counted to that vortex. In the Newtonian limit, each type takes up nearly the same share ($\approx 20\%$) of the TKE and volume. (The numbers do not add up to unity because there are regions in the flow domain not allocated to any vortex.) With increasing DR%, type I (attached-flat) vortices are monotonically suppressed with dwindling shares of TKE and volume. Type II (attached-lifted) vortices are also nearly monotonically reduced but there is a clear turning point at the LDR-HDR transition. Reduction of type II vortices at LDR can be attributed to the general weakening of vortices (first mechanism of DR) as well as the smaller numbers of type I available as its feed. For the latter, types I and II can be viewed as different stages of the same category of attached vortices: a type I vortex may develop into a type II as it lifts up later in its lifetime (Perry and Marušić, 1995). At HDR, lift-up suppression becomes important (fig. 4.9 and more evidences below) which leads to the faster decline of shares in type II vortices. Polymer effects on detached (types III and IV) vortices are much subtler. There is a clear increase of TKE shares of both types at the LDR-HDR transition whereas the volume share stays roughly at the same level for all levels of DR. As a result, the normalized TKE density (fig. 4.12(c)) starts to increase after the transition: i.e., as the flow reaches HDR, the relative intensity (compared with other vortex types) of detached vortices increases without them expanding in

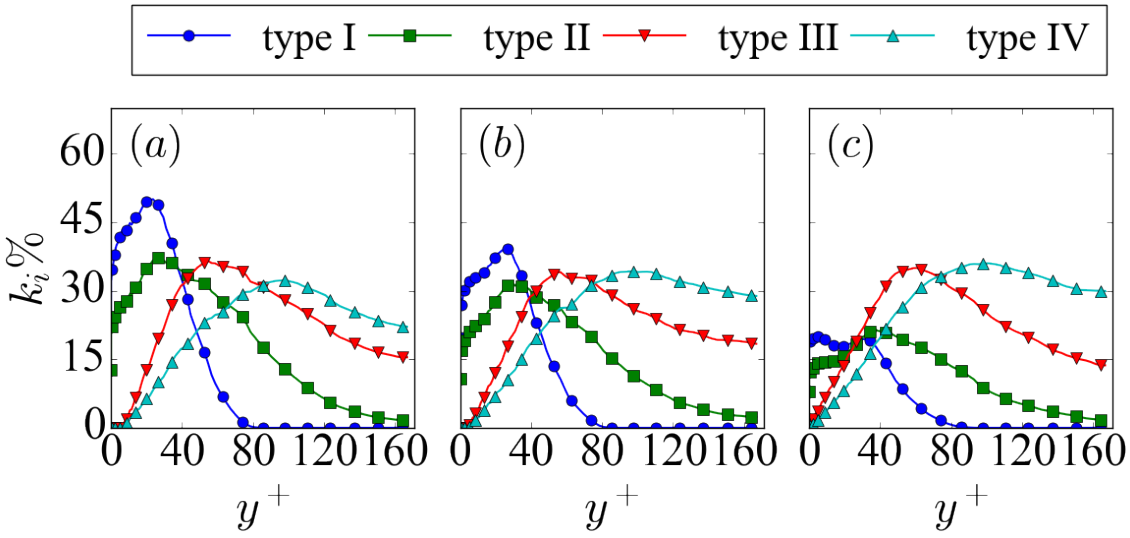

Figure 4.13: Distribution of turbulent kinetic energy contained in each vortex type of (a) Newtonian, (b) Wi = 20 (LDR), and (c) Wi = 80 (HDR) cases at $\mathrm{Re}_\tau = 172.31$.

overall volume. Since the overall turbulent intensity or the average TKE density of the flow domain $k_\mathrm{t}/V_\mathrm{t}$ (denominator in eq. (4.17)) is decreasing with DR%, this simply indicates that detached vortices are much less susceptible to polymer suppression, compared with attached ones, in the HDR regime. Also, attached vortices (types I and II) are much stronger than detached ones with their TKE density more than 50% higher than the latter. At LDR, normalized density of type IV vortices are close to unity (the domain average magnitude), making them nearly not differentiable from the turbulent background. This is consistent with observations in fig. 4.9 that this region (IV in fig. 4.11) is rarely populated by vortices. The role of type IV is thus much less significant than the rest and it is included in our analysis for completeness only.

Figure 4.13 shows the TKE share of each vortex type as a function of y^+ for the Newtonian, LDR (Wi = 20), and HDR (Wi = 80) cases at $\mathrm{Re}_\tau = 172.31$. Type I

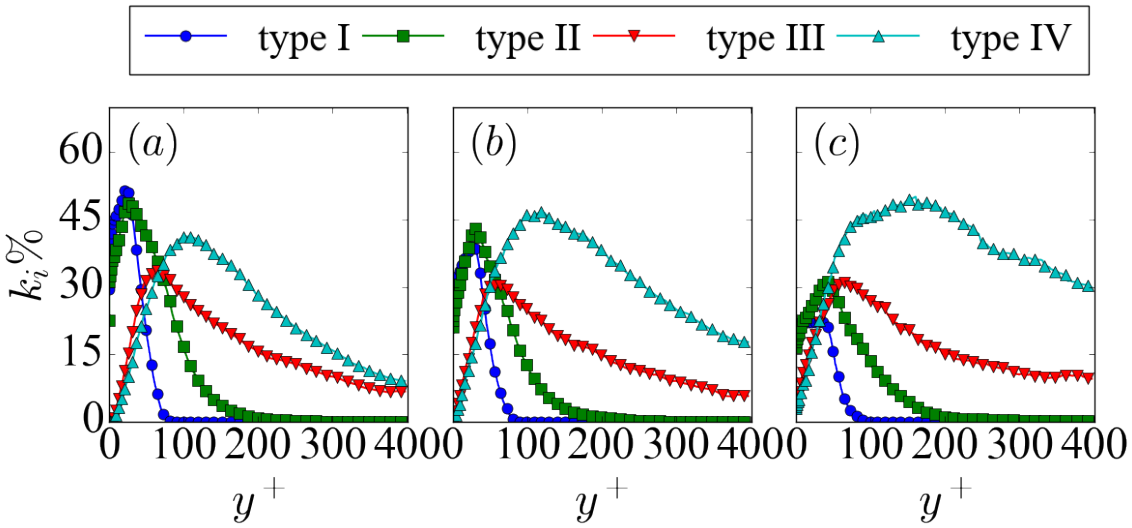

Figure 4.14: Distribution of turbulent kinetic energy contained in each vortex type of (a) Newtonian, (b) LDR, and (b) HDR cases at $\mathrm{Re}_\tau = 400$.

represents the flat-lying attached vortices and they are most predominant in the buffer layer, accounting for 50% of the total TKE in the buffer layer. Detached vortices (types III and IV) only become important in the log-law layer. Type II, meanwhile, carries TKE across the wall layers because they originate from the wall and lift up to upper layers. Compared with the Newtonian case, at LDR vortex type I is significantly suppressed, which corresponds to the first stage of DR effect concentrated mainly in the buffer layer. Changes in other types are much less significant. There is a minor reduction in the type II profile within the buffer layer only, which is consistent with the earlier discussion that at LDR, type II reduction is a combined effect of general vortex weakening and reduced number of type I. Lift-up suppression becomes important only at HDR where reduction of the type II profile in the log-law region becomes significant (as type I share continues to drop). Meanwhile, profiles for detached vortices (types III and IV) are slightly raised.

The same observations are largely preserved at the higher $\mathrm{Re}_\tau = 400$ (fig. 4.14).

Compared with the lower Re case, increasing Re leads to an overall increase of lifted vortices, both attached (type II) and detached (type IV). This is consistent with the previous finding in Newtonian turbulence that lifted-up three-dimensional vortices (e.g., hairpins) become more prevalent at higher Re (Zhu and Xi, 2019). For both Re, attached vortices (types I and II) are contained within roughly the same wall layers in inner units: type I is found at $y^+ \lesssim 100$ and type II shows highest TKE at $y^+ \approx 30$ and its upper end extends close to $y^+ \approx 200$. Meanwhile, detached vortices (types III and IV) are less contained and spread to the highest y^+ available at each Re. The position of peak TKE, however, is still comparable in inner units at different Re. The effect of increasing Wi and comparison between different stages of DR remain the same between these two Re.

In summary, analysis of vortices of different types shows that polymers mainly suppress attached vortices. This effect is confined to the buffer layer at LDR. Polymer effects on TKE distribution in the log-law region becomes important only at HDR because of their suppression of vortex lift-up (evidences in fig. 4.9 and also below), which reduces the turbulent momentum transfer between wall layers and results in the changing flow profiles in the log-law layer.

4.3.4 Vortex shape distribution at different stages of DR

Analysis so far has been focused on the size, wall position, and lift-up status of vortices without considering their topological shape. Determination of the latter by a computer code requires a set of quantitative criteria on the vortex geometry. We will adopt the vortex classification procedure proposed in Zhu and Xi (2019) based on measurements of axis-lines extracted by VATIP. Like before, we will only recapitulate

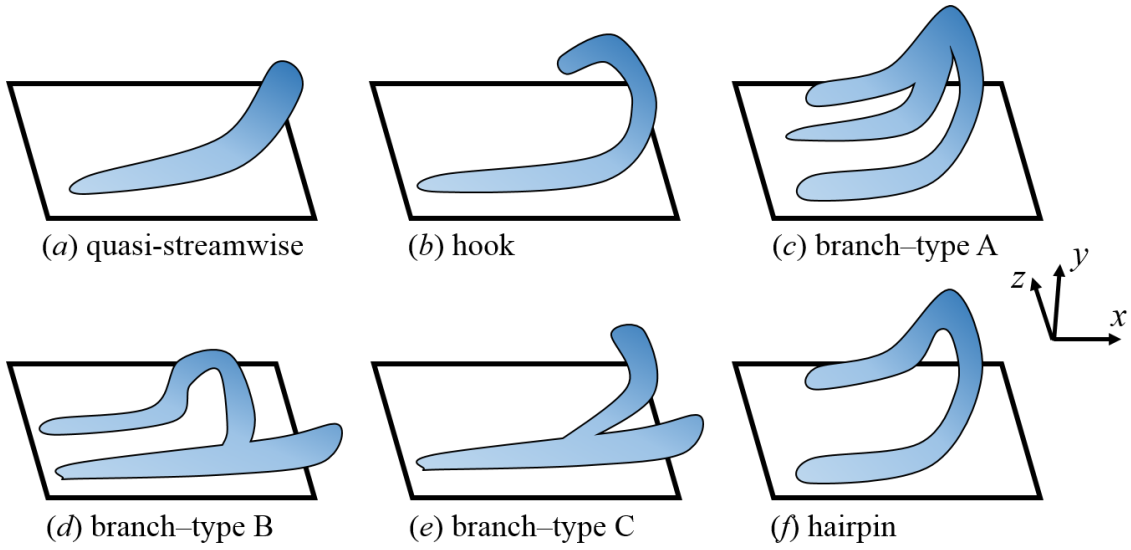

Figure 4.15: Schematic illustrations of major vortex types by shape.

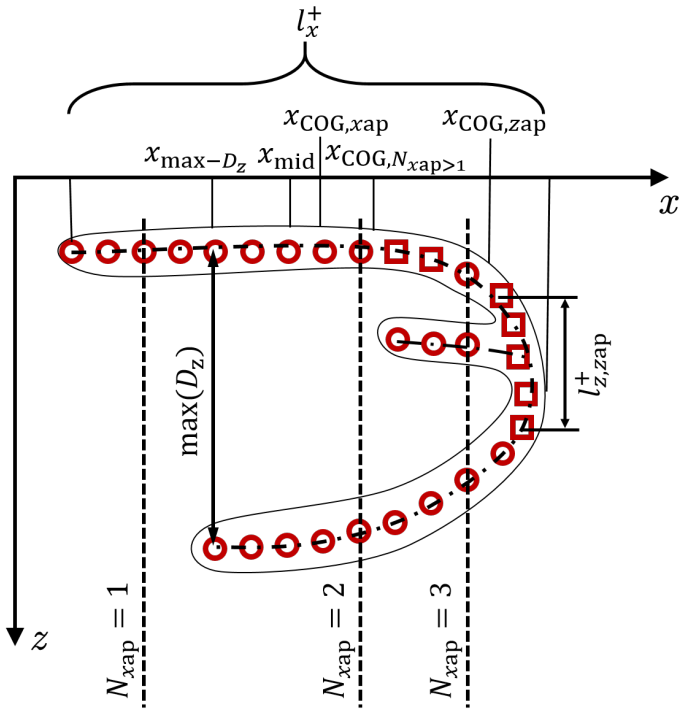

Figure 4.16: Definitions of vortex metrics used in the classification of their shapes (xz-plane projection). Circular and square markers represent x- and z-axis-points, respectively.

Condition	Frag.	Stream.	Hook	Branch			Hairpin
				A	B	C	
$l_x^+ < 50$	T	F	F	F	F	F	F
$\max(l_{z,z\text{ap}}^+) < 25$	-	T	F	F	F	F	F
$P_x(N_{x\text{ap}} = 1) > 80\%$	-	-	T	F	F	F	F
$\frac{P_x(N_{x\text{ap}}>2)}{P_x(N_{x\text{ap}}>1)} > 50\%$	-	-	-	T	F	F	F
$x_{\text{COG},x\text{ap}} < x_{\text{mid}}$ or $x_{\text{COG},z\text{ap}} < x_{\text{mid}}$	-	-	-	-	T	F	F
$x_{\text{max-}D_z} > 1.5x_{\text{COG},N_{x\text{ap}}>1}$	-	-	-	-	-	T	F

Table 4.3: Vortex classification criteria based on geometric metrics of the axis-line.

the approach at the conceptual level here and refer the readers to Zhu and Xi (2019) for implementation details. Vortices are classified into six major types illustrated in fig. 4.15 based on quantitative metrics defined in fig. 4.16. Criteria for differentiating different types are summarized in table 4.3.

The classification is done by a series of binary decisions. First, it differentiates fragments from substantial vortices by requiring the streamwise length l_x^+ to be at least 50 for the latter. Second, it identifies quasi-streamwise vortices by measuring the length of the longest spanwise segment in the axis-line $\max(l_{z,z\text{ap}}^+)$. (Spanwise segments are those consisting of a string of connected z-axis-points.) Those with $\max(l_{z,z\text{ap}}^+) < 25$ are considered to not have a substantial spanwise arm to be considered a hairpin or any other branched type. Note that streamwise vortices that become highly lifted up are still considered in this class because there is no restriction on wall-normal segments. Third, the hook type, which can be viewed as an incomplete hairpin with only one fully developed leg, is identified by counting the number of x-axis-points in each yz-planes $N_{x\text{ap}}$. If more than 80% of the yz-planes spanned by the axis-line has only 1 x-axis-point, it is determined that the vortex is dominated by one streamwise

leg. (In table 4.3, $P_x(N_{x\text{ap}} = 1)$ represents the percentage of yz-planes that satisfy the condition of $N_{x\text{ap}} = 1$). Fourth, the remaining unsorted group are either hairpins or irregularly branched vortices with some features of hairpins but do not conform to their canonical $\Omega-$shape. A commonly-seen type is a branch structure with 3 or more legs. These vortices can be formed when a hairpin is merged with another vortex in highly crowded vortex packets. The third leg is considered to be substantial if the number of yz-planes containing more than 2 x-axis-points (intersected by 3 or more legs) is more than that of those with only 2 (planes intersected by two legs). These vortices are classified as branch type A. Fifth, the branch type B (fig. 4.15) can be formed when a side arm of the streamwise vortex lifts up and is dragged sideways by the spanwise flow to form an arc and, sometimes, another leg. It is similar to a hairpin except that the head or arc of the vortex is not found near the downstream end but somewhere in the middle. The vortex head is considered to be significantly away from the downstream end if the x-coordinate of the center of gravity (COG) of either all x-axis-points $x_{\text{COG},x\text{ap}}$ or all z-axis-points $x_{\text{COG},x\text{ap}}$ is upstream of the middle point of the entire x-span ($x_{\text{mid}} \equiv (x_{\max} + x_{\min})/2$). Sixth, branch type C is formed in a similar manner except that the side arm is stretched by the streamwise flow first before lifting up, creating a branch that opens towards the downstream direction. In this case, the x-coordinate with the maximum spanwise span D_z is found near the downstream end. The quantitative criterion is to compare this coordinate $x_{\text{max-}D_z}$ with that of the COG. of the branched portion (i.e., those where $N_{x\text{ap}} > 1$) $x_{\text{COG},N_{x\text{ap}}>1}$ multiplied by 1.5. Finally, after removing all irregularly branched configurations, the rest are considered to be sufficiently close to the canonical Ω-shape and classified as hairpins.

In summary, after removing the fragments, quasi-streamwise vortices, and hooks from the pool, the algorithm identifies hairpins by removing all other branched types with significant deviation from the canonical Ω-shape. There is obviously some arbitrariness in how the branch types (A, B, and C) are defined and how the cutoffs are chosen (i.e., when is a deviation big enough to disqualify a vortex as a hairpin). Fortunately, at least for this study, this is nothing more than a taxonomic issue. For practical purposes, none of the trends we will discuss below show any difference between hairpins and other branches (types A, B, and C). This is not surprising: within our current limited knowledge of vortex dynamics, all these branches seem to be formed in a similar manner as hairpins. Their existence is merely an inevitability of the irregular nature of turbulent dynamics. For this reason, we will use one umbrella term "hairpin-like" vortices for all these branched structures (including canonical hairpins).

Vortex axis-lines of all these types, at $\mathrm{Re}_\tau = 172.31$, are shown in figs. 4.17 and 4.18 for one typical snapshot at LDR ($\mathrm{Wi} = 20$) and HDR ($\mathrm{Wi} = 80$) each. (The "branch" case includes all three types, A, B, and, C and we make no further attempt to differentiate these groups.) In both cases, near-wall quasi-streamwise vortices are the most prevalent type of vortex structure in the flow field. However, in the LDR case, a considerable number of curved vortices are observed, including many well-defined hairpins (fig. 4.17(a)) and other branches (fig. 4.17(c)). They are however significantly outnumbered by the strongly asymmetric hooks (i.e., one-legged hairpins). Observation in Newtonian flow is similar (Zhu and Xi, 2019). Indeed, it has been long believed that complete well-defined hairpins are not the most likely configuration and incomplete and asymmetric hairpins (hooks) are the norm (Robinson,

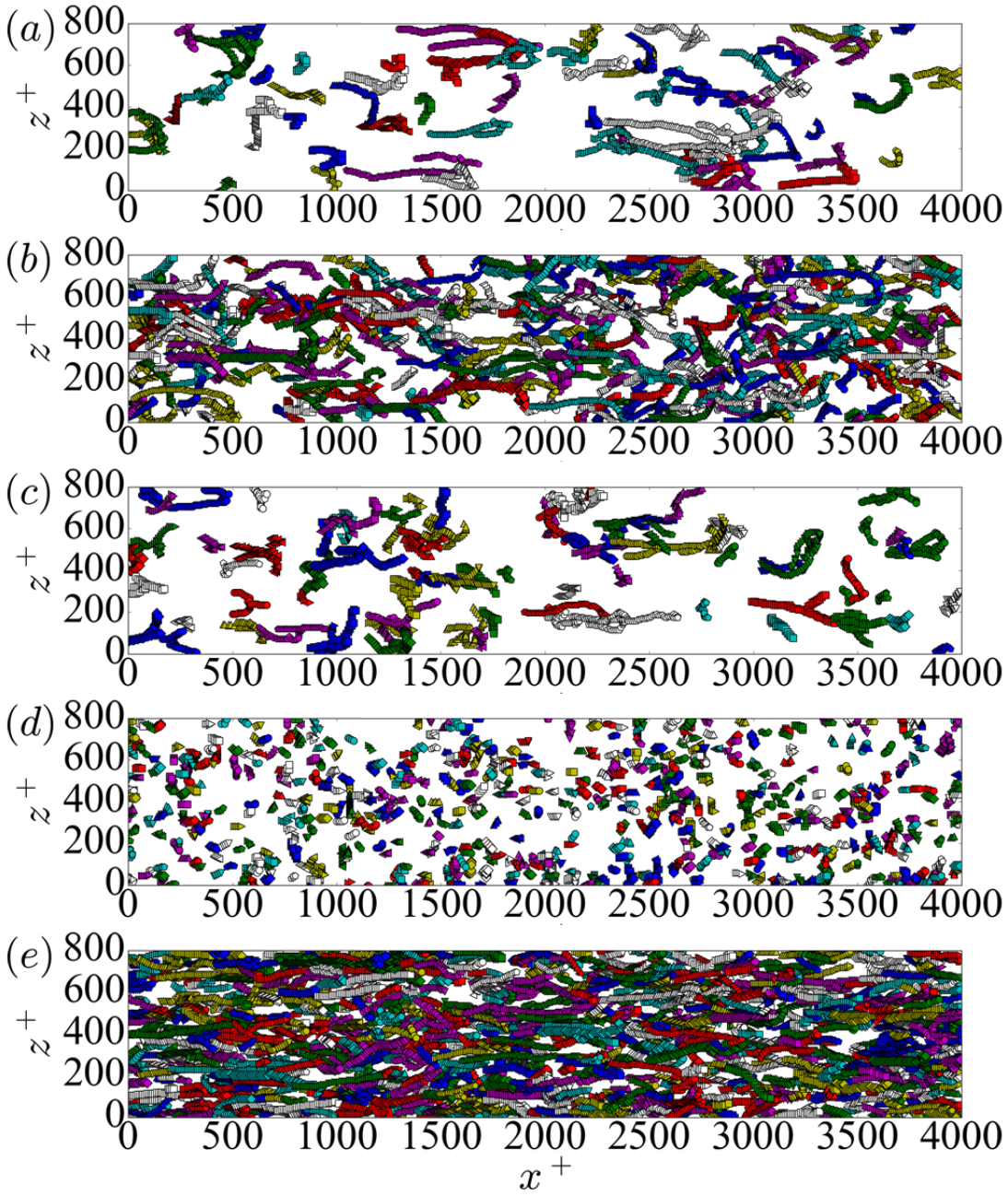

Figure 4.17: Axis-lines of vortices of different shapes extracted by VATIP in a typical snapshot at $\mathrm{Re}_\tau = 172.31$ and $\mathrm{Wi} = 20$ (LDR): (a) hairpin, (b) hook, (c) branch, (d)fragment and (e) quasi-streamwise vortices. Different vortices are represented by different colors and markers. Viewed from above the channel and the projection includes vortices at all y positions.

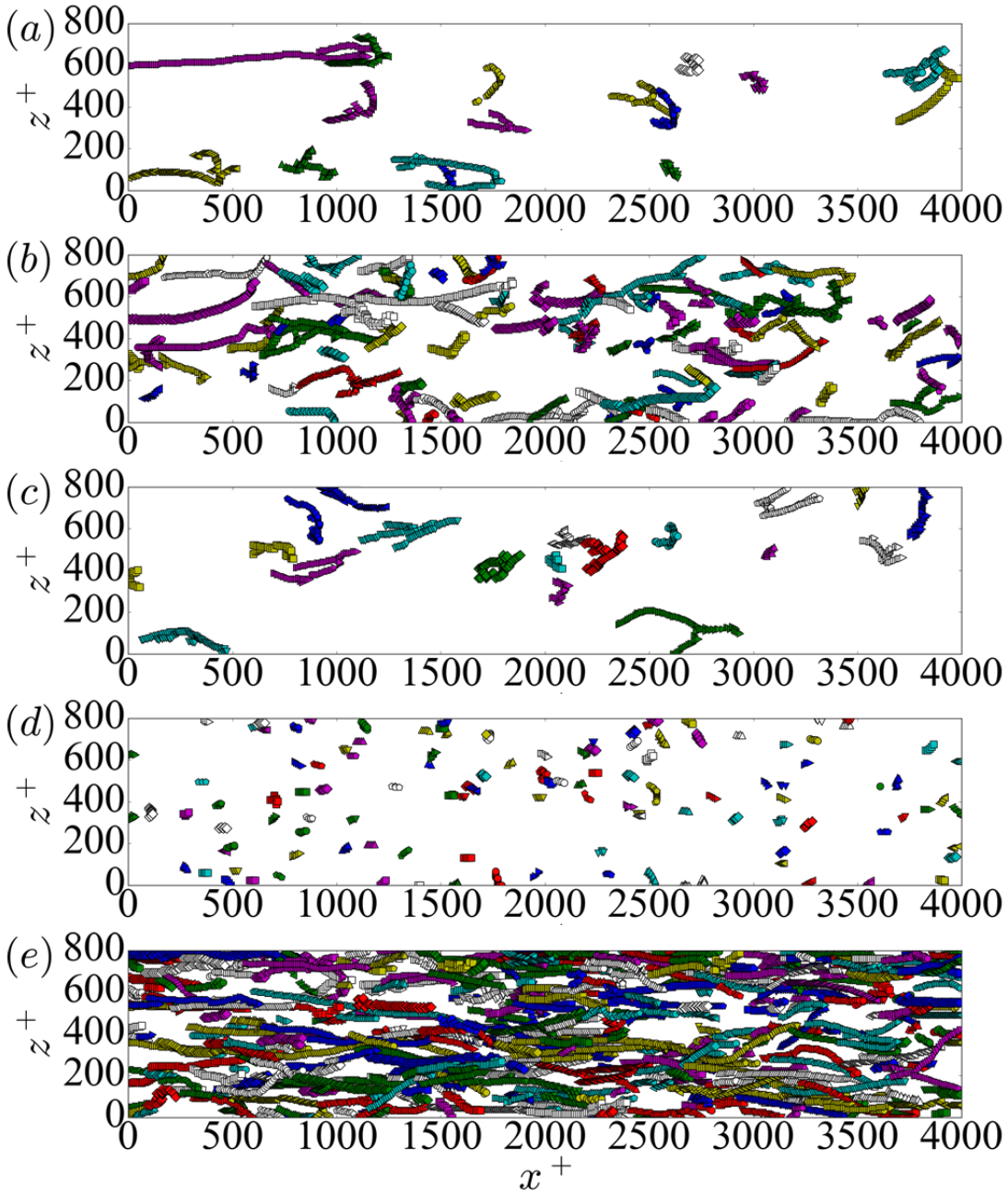

Figure 4.18: Axis-lines of vortices of different shapes extracted by VATIP in a typical snapshot at $\mathrm{Re}_\tau = 172.31$ and $\mathrm{Wi} = 80$ (HDR): (a) hairpin, (b) hook, (c) branch, (d)fragment and (e) quasi-streamwise vortices. Different vortices are represented by different colors and markers. Viewed from above the channel and the projection includes vortices at all y positions.

1991). (A "forest" of nearly symmetric hairpins were observed in the DNS by Wu and Moin (2009a) in boundary layer flow, which is different than the channel flow here.) At HDR, all three-dimensional curved vortices (hairpins, branches, and hooks) are significantly reduced. This again is explained by the suppression of vortex lift-up which is required for their formation. In addition, fragments also become drastically reduced in the HDR case. This is consistent with the proposed mechanism in Zhu *et al.* (2018) that the suppression of vortex lift up prevents its further bursting and generation of small-scale turbulent fluctuations that can trigger instabilities elsewhere in the domain, leading to the dominance of a different vortex regeneration mechanism for HDR.

Percentages of vortices of these shape types at $\mathrm{Re}_\tau = 172.31$ are plotted in fig. 4.19 as functions of DR%. Changes during LDR are relatively small. The fraction of streamwise vortices remains nearly invariant. Some subtle changes are observed in curved vortices in a small region after the onset (DR% $< 5\%$): the shares taken by hairpin-like vortices (panels (b) and (d)) drop slightly, which is compensated by an increase in hooks (panel (c)). This again shows that during this first stage of DR, polymers have an across-the-board vortex weakening effect. It suppresses all types of vortices (Zhu *et al.*, 2018; De Angelis *et al.*, 2002; Dubief *et al.*, 2005; Kim *et al.*, 2007) without tipping the balance between them. Changes between hooks and hairpin-like vortices can be well explained considering that some of the latter type are turned into hooks as their legs are shortened and trimmed by the polymer stress, but they remain distinguishable from quasi-streamwise ones with their spanwise arc and strong lift-up angle. Once HDR starts, all these highly curved vortices (hairpins, branches, hooks) decline sharply as the quasi-streamwise type makes inroads into their shares.

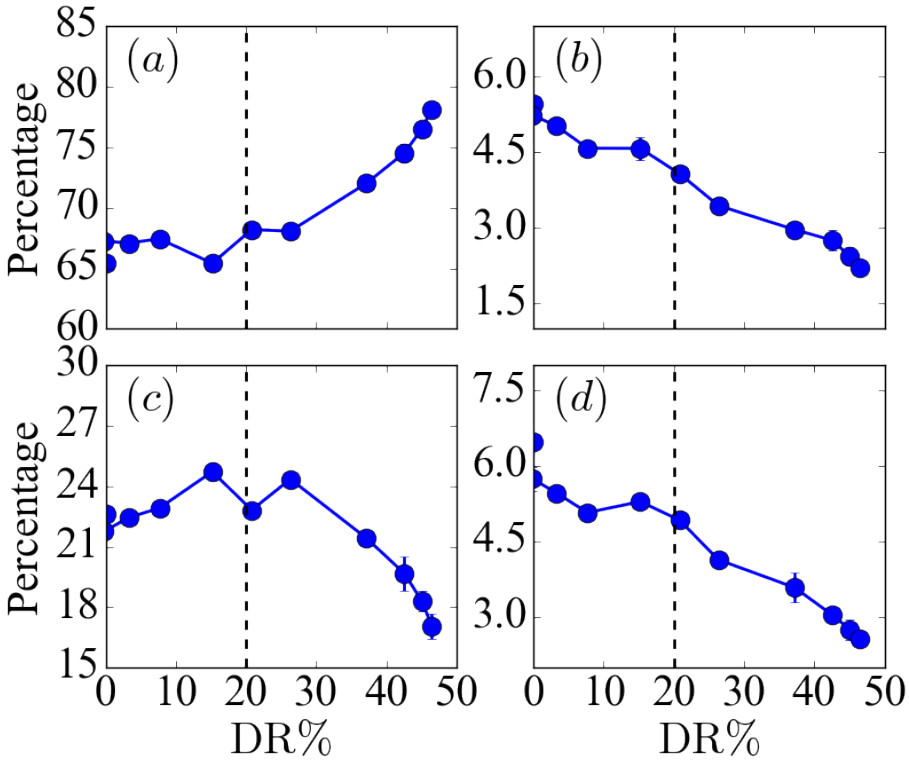

Figure 4.19: Number percentage of vortices of different shapes at $\mathrm{Re}_\tau = 172.31$: (a) quasi-streamwise, (b) hairpin, (c) hook and (d) branch vortices. Dashed line marks the LDR-HDR transition. Error bars smaller than the symbol size are not shown.

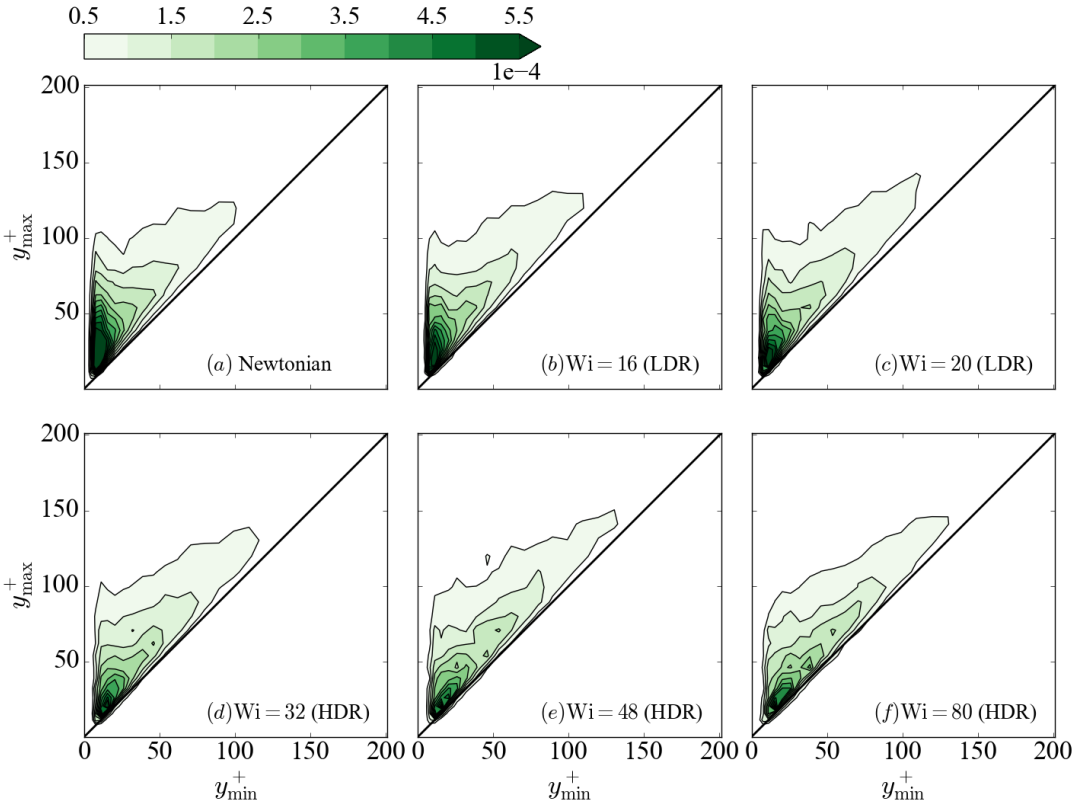

Figure 4.20: Joint PDFs of the wall-normal positions of the head and tail/legs of quasi-streamwise vortices, as measured respectively by the maximum and minimum y^+ coordinates of each vortex axis-line, at different Wi ($\mathrm{Re}_\tau = 172.31$).

This again can be explained by the suppression of vortex lift-up that generates these curved three-dimensional vortices during this second stage of DR. Without lift-up, streamwise vortices is stabilized near the wall and becomes elongated over time as seen in figs. 4.8 and 4.18.

We now revisit the vortex position and lift-up status analysis (see fig. 4.9) but consider vortices of different shapes in separate categories. Figures 4.20 and 4.21 show the joint PDFs of vortex head and tail/legs positions for quasi-streamwise and curved

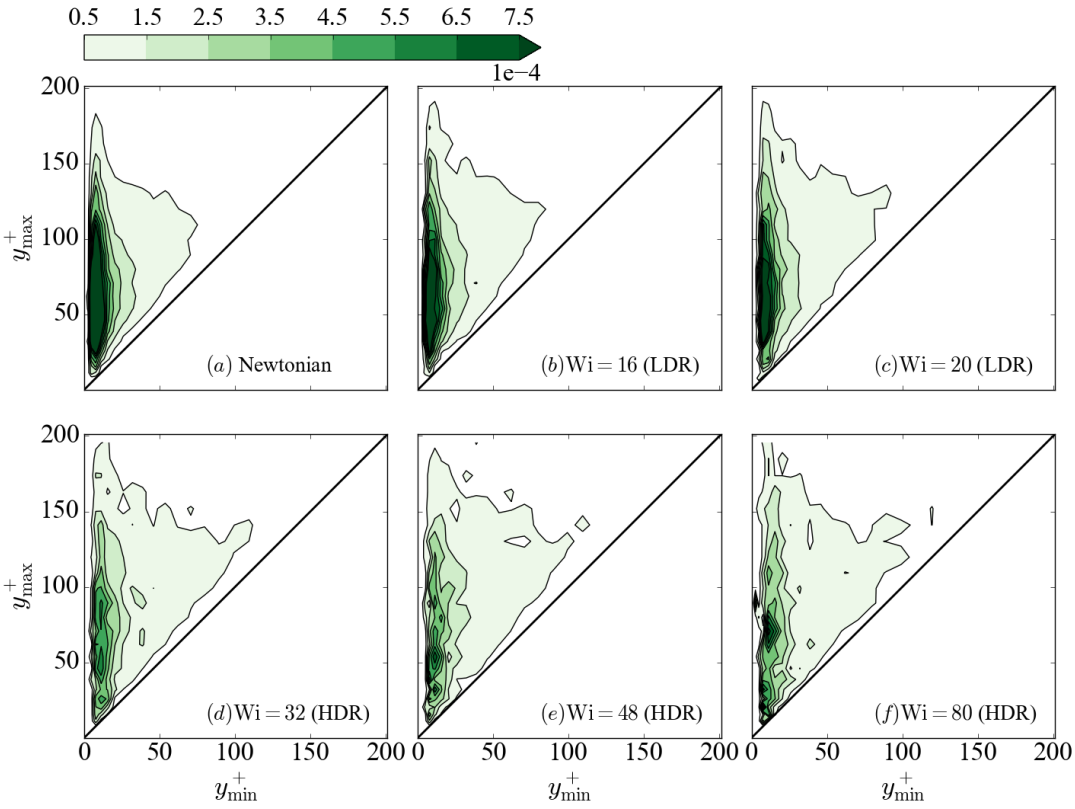

Figure 4.21: Joint PDFs of the wall-normal positions of the head and tail/legs of curved vortices (hairpins, branches, and hooks), as measured respectively by the maximum and minimum y^+ coordinates of each vortex axis-line, at different Wi ($\mathrm{Re}_\tau = 172.31$).

(including hairpins, branches, and hooks) vortices for the lower $\mathrm{Re}_\tau = 172.31$. Distribution patterns are drastically different between these two categories. For Newtonian flow, quasi-streamwise vortices are mostly found in the lower-left corner and belong to the attached-flat class or type I (fig. 4.11). Some of them lift up and form a thin band near the ordinate: i.e. type II attached-lifted vortices. A diagonal band is also noticeable which corresponds to type III detached-flat vortices. By contrast, curved vortices are predominantly type II (attached-lifted) which originate from the wall (legs) but lift high up into the upper layers (the head or arc of the hairpin). At LDR, the contours remain similar to the Newtonian limit for both quasi-streamwise and curved vortices. Earlier observation of the decline of TKE shares contained in types I and II (figs. 4.12 to 4.14) are thus results of the weakening of these vortices rather than any fundamental change in their distribution pattern. This starts to change at HDR. For quasi-streamwise vortices (fig. 4.20), the slim vertical distribution band (type II) disappears as HDR starts, which is accompanied by a distinct shift of the concentration center towards the diagonal. This is a clear indication that polymers start to suppress the lift-up of these vortices and stabilize them in the streamwise direction. Expansion of streamwise vortex distribution to higher y^+ (more detached) positions along the diagonal is comprehensible considering that drag-reducing polymers are known to enlarge the diameter of vortex tubes (Sureshkumar *et al.*, 1997; De Angelis *et al.*, 2003; Li *et al.*, 2006a; Xi and Graham, 2010b), which inevitably raises the positions of their axis-lines. By contrast, curved vortices stay mainly in the type II region for the whole range of DR (fig. 4.21). Entering HDR does not significantly shift their distribution pattern, despite the substantial reduction in their total count. Since curved vortices are products of vortex lift up (generated from lifted

quasi-streamwise vortices), suppression of lift up directly reduces the source for their formation. For those that do come into existence, they maintain their lifted silhouette even at HDR. The distribution density does decline at HDR, which means the distribution must spread to a wider area owing to the conservation of probability. This reflects an enlarged and more homogeneous boundary layer. The same joint PDFs for the higher $\mathrm{Re}_\tau = 400$ case are shown in figs. 4.22 and 4.23. The distribution patterns are again (recall figs. 4.9 and 4.10) strikingly consistent between different Re. Vortices of the same category are again found in the same wall layer, in inner units, at the two Re tested. Reduction in vortex lift up at HDR is consistently observed at both Re. For quasi-streamwise vortices, the suppression of their lift-up tendency was also observed in the inclination angles of conditionally sampled eddies (Sibilla and Beretta, 2005). However, for curved vortices, which are more predominant among lifted vortices, direct evidence was not previously possible before their axis-lines can be statistically extracted by VATIP. Since hairpins are most likely generated from the lift-up of streamwise vortices, as conjectured by Robinson (1991) and directly observed in DNS by Zhu *et al.* (2018), it is the suppression of the lift-up process itself, not that of any particular vortex type, that is important for interrupting the turbulent momentum transfers between the buffer and upper wall layers and the start of the second stage of DR with distinct log-law region flow statistics.

4.4 Summary and conclusive messages

This study focuses on the transition between two distinct stages of DR: LDR and HDR. Distinction between these two regimes has been made in the literature for two decades because of their different mean flow profiles (Warholic *et al.*, 1999). However,

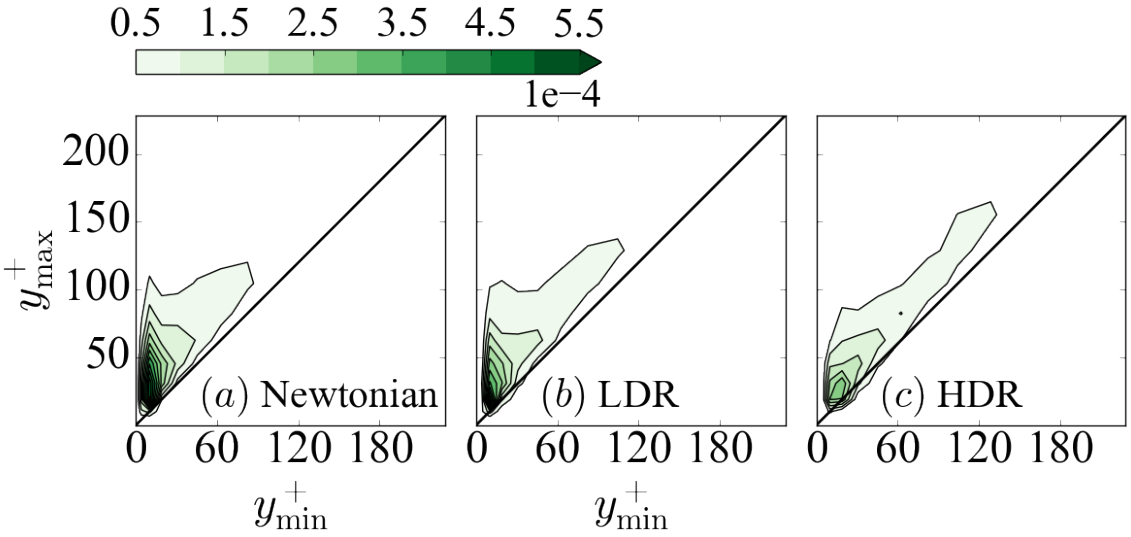

Figure 4.22: Joint PDFs of the wall-normal positions of the head and tail/legs of quasi-streamwise vortices, as measured respectively by the maximum and minimum y^+ coordinates of each vortex axis-line, at different Wi ($\mathrm{Re}_\tau = 400$).

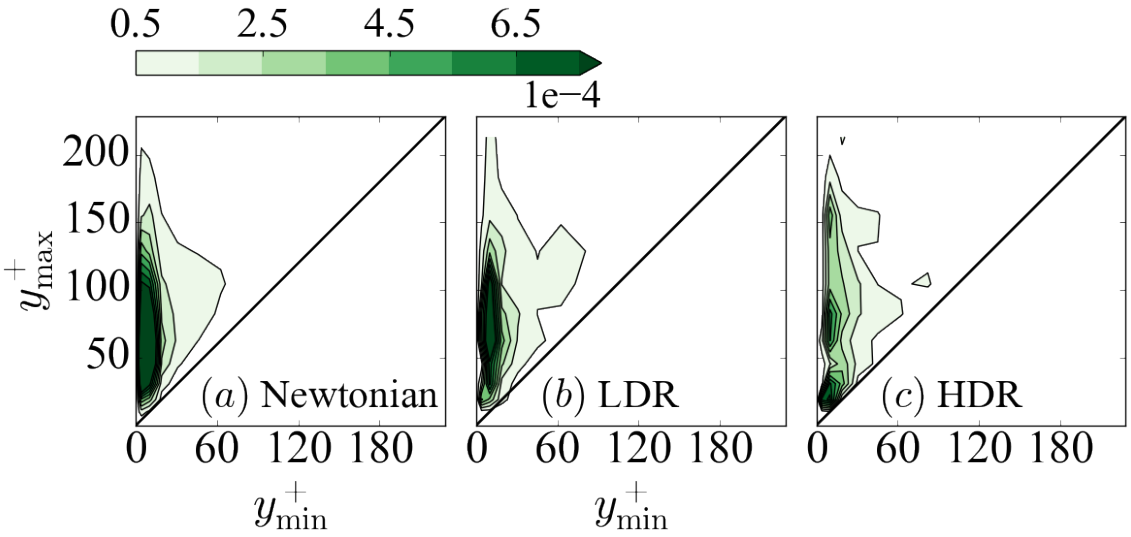

Figure 4.23: Joint PDFs of the wall-normal positions of the head and tail/legs of curved vortices (hairpins, branches, and hooks), as measured respectively by the maximum and minimum y^+ coordinates of each vortex axis-line, at different Wi ($\mathrm{Re}_\tau = 400$).

it was not until recently that evidences have been established to identify them as two qualitatively different stages marked by a sharp transition in flow statistics and vortex configuration (Xi and Graham, 2010b; Zhu *et al.*, 2018). For a given Re and with the introduction of drag-reducing polymers, there are two critical levels of Wi where two separate mechanisms of DR set in. The first is the onset of DR: it marks the start of the LDR stage where DR effects are concentrated in the buffer layer. The second is the LDR-HDR transition where DR effects spread across the log-law layer.

This study leverages the recent development of a new vortex tracking algorithm, VATIP, which enables the automatic detection and extraction of vortex axis-lines without subjective inference (Zhu and Xi, 2019). It allows quantitative and statistical analysis of the size, position, conformation, and shape of vortices in a turbulent flow field. The method is applied to flow fields of a wide range of Wi covering from the Newtonian limit to HDR. Vortices extracted by VATIP are then classified using two sets of criteria. The first is based on the vortex position and lift-up status, which identifies three major groups: (1) type I or attached-flat vortices are closely associated with the wall with little observable lift-up; (2) type II or attached-lifted vortices are generated from the wall but lift up to higher altitudes – often well into the log-law layer; and (3) type III or detached-flat vortices are similar as type I except that they are found at higher positions with less interaction with the wall (type IV, as discussed above, is not as important and omitted here for the simplicity of discussion). The second is based on vortex shape which categorize vortices into fragments, quasi-streamwise vortices, hooks (asymmetric or incomplete hairpins), and hairpin-like vortices (the latter further includes canonical hairpins and irregular branches).

Analysis of our DNS results shows that type I (attached-flat) and type III (detached-flat) vortices are nearly all quasi-streamwise vortices, whereas type II contains some quasi-streamwise vortices plus the majority of the curved – hooks and hairpin-like – vortices. Polymers are found to mainly impact attached vortices. At LDR, this effect is an across-the-board weakening of vortex strength without shifting their distribution pattern. At HDR, polymers start to suppress the lift-up process of vortices and greatly reduces the number of curved vortices including hooks, hairpins, and branches.

A clear conceptual picture thus arises from these observations. In Newtonian flow, the buffer layer is dominated by flat-lying streamwise vortices. These vortices are prone to lift-up and as the downstream vortex head rises into the log-law layers, it is subject to the impact of transverse flow which can swing and stretch the vortex into a curved contour. Existence of these highly lifted vortices facilitates the turbulent momentum transport across the wall layers, which is reflected in the well-known log-law flow statistics (Townsend, 1980; Perry and Marušić, 1995; Lozano-Durán *et al.*, 2012). At LDR, polymers weaken vortex motion and suppress turbulent fluctuations (De Angelis *et al.*, 2002; Dubief *et al.*, 2005; Kim *et al.*, 2007, 2008), without shifting the overall distribution and balance between different classes of vortices. As the flow enters HDR, polymers start to suppress the lift-up of streamwise vortices and interrupt the generation pathway of curved vortices. Reduction in these highly lifted vortices reduces trans-wall-layer turbulent momentum transfer, which offers a clear direction for explaining the changing flow statistics in the log-law layer at HDR. As vortices become stabilized in the streamwise direction, they become elongated and more detached from the wall. The latter makes them less susceptible to polymer

effects.

This is, to our knowledge, the first complete depiction of the vortex dynamics in both stages of LDR and HDR that is based on direct numerical evidences. It substantiates our earlier hypothesis about the suppression of vortex lift-up as the main mechanism for HDR (Zhu *et al.*, 2018) with an extensive analysis of vortex conformation statistics. The second part of the hypothesis regarding the vortex regeneration mechanism at HDR will be a subject for our continuing research.

Bibliography

Adrian, R. J. (2007). Hairpin vortex organization in wall turbulence a. *Phys. Fluids*, **19**(4), 041301.

Bernard, P. S., Thomas, J. M., and Handler, R. A. (1993). Vortex dynamics and the production of reynolds stress. *J. Fluid Mech.*, **253**, 385–419.

Bird, R. B., Hassager, O., Armstrong, R. C., and Crurtis, C. F. (1987). *Dynamics of polymeric liquids. Vol. 2 Kinetic Theory.* John Wiley and Sons Inc., New York, NY.

Chakraborty, P., Balachandar, S., and Adrian, R. J. (2005). On the relationships between local vortex identification schemes. *J. Fluid Mech.*, **535**, 189–214.

Chong, M. S., Perry, A. E., and Cantwell, B. J. (1990). A general classification of three-dimensional flow fields. *Phys. Fluids A-Fluid*, **2**(5), 765–777.

Choueiri, G. H., Lopez, J. M., and Hof, B. (2018). Exceeding the asymptotic limit of polymer drag reduction. *Phys. Rev. Lett.*, **120**, 124501.

Chu, D. C. and Karniadakis, G. E. (1993). A direct numerical simulation of laminar and turbulent flow over riblet-mounted surfaces. *J. Fluid Mech.*, **250**, 1–42.

De Angelis, E., Casciola, C. M., and Piva, R. (2002). DNS of wall turbulence: dilute polymers and self-sustaining mechanisms. *Comput. Fluids*, **31**, 495–507.

De Angelis, E., Casciola, C. M., L'vov, V. S., Piva, R., and Procaccia, I. (2003). Drag reduction by polymers in turbulent channel flows: energy redistribution between invariant empirical modes. *Phys. Rev. E*, **67**, 056312.

Deng, B.-Q., Huang, W.-X., and Xu, C.-X. (2016). Origin of effectiveness degradation in active drag reduction control of turbulent channel flow at $\mathrm{Re}_\tau = 1000$. *J. Turbul.*, **17**, 758–786.

Dimitropoulos, C. D., Sureshkumar, R., and Beris, A. N. (1998). Direct numerical simulation of viscoelastic turbulent channel flow exhibiting drag reduction: effect of the variation of rheological parameters. *J. Non-Newton. Fluid Mech.*, **79**, 433–468.

Dubief, Y., Terrapon, V. E., White, C. M., E. S. Shaqfeh, P. M., and Lele, S. K. (2005). New answers on the interaction between polymers and vortices in turbulent flows. *Flow Turbul. Combust.*, **74**(4), 311–329.

Elbing, B. R., Perlin, M., Dowling, D. R., and Ceccio, S. L. (2013). Modification of the mean near-wall velocity profile of a high-Reynolds number turbulent boundary layer with the injection of drag-reducing polymer solutions. *Phys. Fluids*, **25**, 085103.

Gibson, J. F. (2012). Channelflow: a spectral navier–stokes simulator in c++. *New Hampshire*.

Graham, M. D. (2014). Drag reduction and the dynamics of turbulence in simple and complex fluids. *Phys. Fluids*, **26**, 101301.

Hamilton, J. M., Kim, J., and Waleffe, F. (1995). Regeneration mechanisms of near-wall turbulence structures. *J. Fluid Mech.*, **287**, 317–348.

Housiadas, K. D. and Beris, A. N. (2003). Polymer-induced drag reduction: effects of variations in elasticity and inertia in turbulent viscoelastic channel flow. *Phys. Fluids*, **15**, 2369–2384.

Housiadas, K. D., Beris, A. N., and Handler, R. A. (2005). Viscoelastic effects on higher order statistics and on coherent structures in turbulent channel flow. *Phys. Fluids*, **17**, 035106.

Hunt, J. C. R., , A. A. W., and Moin, P. (1988). Eddies, streams, and convergence zones in turbulent flows. *Studying Turbulence Using Numerical Simulation Databases-I1*, page 193.

Hussain, A. F. and Hayakawa, M. (1987). Eduction of large-scale organized structures in a turbulent plane wake. *J. Fluid Mech.*, **180**, 193–229.

Jeong, J., Hussain, F., Schoppa, W., and Kim, J. (1997). Coherent structures near the wall in a turbulent channel flow. *J. Fluid Mech.*, **332**, 185–214.

Jiménez, J. and Moser, R. D. (2007). What are we learning from simulating wall turbulence? *Philosophical Transactions of the Royal Society of London A: Mathematical, Physical and Engineering Sciences*, **365**(1852), 715–732.

Kim, J., Moin, P., and Moser, R. (1987). Turbulence statistics in fully-developed channel flow at low Reynolds-number. *J. Fluid Mech.*, **177**, 133–166.

Kim, K., Li, C. F., Sureshkumar, R., Balachandar, S., and Adrian, R. J. (2007). Effects of polymer stresses on eddy structures in drag-reduced turbulent channel flow. *J. Fluid Mech.*, **584**, 281–299.

Kim, K., Adrian, R. J., Balachandar, S., and Sureshkumar, R. (2008). Dynamics of hairpin vortices and polymer-induced turbulent drag reduction. *Phys. Rev. Lett.*, **100**(13), 134504.

Li, C. F., Sureshkumar, R., and Khomami, B. (2006a). Influence of rheological parameters on polymer induced turbulent drag reduction. *J. Non-Newton. Fluid Mech.*, **140**(1), 23–40.

Li, C. F., Sureshkumar, R., and Khomami, B. (2015). Simple framework for understanding the universality of the maximum drag reduction asymptote in turbulent flow of polymer solutions. *Phys. Rev. E*, **92**(4), 043014.

Li, W., Xi, L., and Graham, M. D. (2006b). Nonlinear travelling waves as a framework for understanding turbulent drag reduction. *J. Fluid Mech.*, **565**, 353–362.

Lozano-Durán, A. and Jiménez, J. (2014). Time-resolved evolution of coherent structures in turbulent channels: characterization of eddies and cascades. *J. Fluid Mech.*, **759**, 432–471.

Lozano-Durán, A., Flores, O., and Jiménez, J. (2012). The three-dimensional structure of momentum transfer in turbulent channels. *J. Fluid Mech.*, **694**, 100–130.

Marusic, I., McKeon, B. J., Monkewitz, P. A., Nagib, H. M., Smits, A. J., and Sreenivasan, K. R. (2010). Wall-bounded turbulent flows at high reynolds numbers: Recent advances and key issues. *Phys. Fluids*, **22**(6), 065103.

Min, T., Choi, H., and Yoo, J. Y. (2003). Maximum drag reduction in a turbulent channel flow by polymer additives. *J. Fluid Mech.*, **492**, 91–100.

Mohammadtabar, M., Sanders, R. S., and Ghaemi, S. (2017). Turbulent structures of non-newtonian solutions containing rigid polymers. *Phys. Fluids*, **29**(10), 103101.

Panton, R. L. (2001). Overview of the self-sustaining mechanisms of wall turbulence. *Prog. Aerosp. Sci.*, **37**(4), 341–383.

Pereira, A. S., Mompean, G., Thompson, R. L., and Soares, E. J. (2017a). Elliptical, parabolic, and hyperbolic exchanges of energy in drag reducing plane couette flows. *Phys. Fluids*, **29**(11), 115106.

Pereira, A. S., Mompean, G., Thais, L., and Thompson, R. L. (2017b). Statistics and tensor analysis of polymer coil–stretch mechanism in turbulent drag reducing channel flow. *J. Fluid Mech.*, **824**, 135–173.

Perry, A. E. and Marušić, I. (1995). A wall-wake model for the turbulence structure of boundary layers. part 1. extension of the attached eddy hypothesis. *J. Fluid Mech.*, **298**, 361–388.

Peyretr, R. (2013). *Spectral methods for incompressible viscous flow*, volume 148. Springer Science & Business Media.

Pope, S. B. (2000). *Turbulent flows*. Cambridge University Press, Cambridge, United Kingdom.

Ptasinski, P. K., Boersma, B. J., Nieuwstadt, F. T. M., Hulsen, M. A., den Brule, B. H. A. A. V., and Hunt, J. C. R. (2003). Turbulent channel flow near maximum

drag reduction: simulations, experiments and mechanisms. *J. Fluid Mech.*, **490**, 251–291.

Robinson, S. K. (1991). Coherent motions in the turbulent boundary layer. *Annu. Rev. Fluid Mech.*, **23**(1), 601–639.

Schlatter, P., Brandt, L., de lange, H. C., and Henningson, D. S. (2008). On streak breakdown in bypass transition. *Phys. Fluids*, **20**, 101505.

Schoppa, W. and Hussain, F. (2002). Coherent structure generation in near-wall turbulence. *J. Fluid Mech.*, **453**, 57–108.

Sibilla, S. and Beretta, C. P. (2005). Near-wall coherent structures in the turbulent channel flow of a dilute polymer solution. *Fluid Dyn. Res.*, **37**(3), 183–202.

Sureshkumar, R. and Beris, A. N. (1995). Effect of artificial stress diffusivity on the stability of numerical calculations and the flow dynamics of time-dependent viscoelastic flows. *J. Non-Newton. Fluid Mech.*, **60**, 53–80.

Sureshkumar, R., Beris, A. N., and Handler, R. A. (1997). Direct numerical simulation of the turbulent channel flow of a polymer solution. *Physics of Fluids*, **9**(3), 743–755.

Townsend, A. A. R. (1980). *The structure of turbulent shear flow*. Cambridge university press.

Tuckerman, L. S., Kreilos, T., Schrobsdorff, H., Schneider, T. M., and Gibson, J. F. (2014). Turbulent-laminar patterns in plane Poiseuille flow. *Phys. Fluids*, **26**.

Virk, P. S. (1975). Drag reduction fundamentals. *AIChE J.*, **21**, 625–656.

Waleffe, F. (1997). On a self-sustaining process in shear flows. *Phys. Fluids*, **9**, 883–900.

Wallace, J. M. (2016). Quadrant analysis in turbulence research: history and evolution. *Annu. Rev. Fluid Mech.*, **48**, 131–158.

Wang, S. N., Graham, M. D., Hahn, F. J., and Xi, L. (2014). Time-series and extended Karhunen–Loève analysis of turbulent drag reduction in polymer solutions. *AIChE J.*, **60**, 1460–1475.

Warholic, M. D., Massah, H., and Hanratty, T. J. (1999). Influence of drag-reducing polymers on turbulence: effects of reynolds number, concentration and mixing. *Exp. Fluids*, **27**(5), 461–472.

Warholic, M. D., Heist, D. K., Katcher, M., and Hanratty, T. J. (2001). A study with particles image velocimetry of the influence of drag-reducing polymers on the structure of turbulence. *Exp. Fluids*, **31**, 474–483.

White, C. M. and Mungal, M. G. (2008). Mechanics and prediction of turbulent drag reduction with polymer additives. *Annu. Rev. Fluid Mech.*, **40**, 235–256.

White, C. M., Somandepalli, V. S. R., and Mungal, M. G. (2004). The turbulence structure of drag-reduced boundary layer flow. *Exp. Fluids*, **36**, 62–69.

White, C. M., Dubief, Y., and Klewicki, J. (2012). Re-examining the logarithmic dependence of the mean velocity distribution in polymer drag reduced wall-bounded flow. *Phys. Fluids*, **24**(2), 021701.

Wu, X. and Moin, P. (2009a). Direct numerical simulation of turbulence in a nominally zero-pressure-gradient flat-plate boundary layer. *J. Fluid Mech.*, **630**, 5–41.

Wu, X. and Moin, P. (2009b). Forest of hairpins in a low-Reynolds-number zero-pressure-gradient flat-plate boundary layer. *Phys. Fluids*, **21**, 091106.

Xi, L. and Bai, X. (2016). Marginal turbulent state of viscoelastic fluids: A polymer drag reduction perspective. *Phys. Rev. E*, **93**(4).

Xi, L. and Graham, M. D. (2010a). Active and hibernating turbulence in minimal channel flow of Newtonian and polymeric fluids. *Phys. Rev. Lett.*, **104**, 218301.

Xi, L. and Graham, M. D. (2010b). Turbulent drag reduction and multistage transitions in viscoelastic minimal flow units. *J. Fluid Mech.*, **647**, 421–452.

Xi, L. and Graham, M. D. (2012a). Dynamics on the laminar-turbulent boundary and the origin of the maximum drag reduction asymptote. *Phys. Rev. Lett.*, **108**, 028301.

Xi, L. and Graham, M. D. (2012b). Intermittent dynamics of turbulence hibernation in Newtonian and viscoelastic minimal channel flows. *J. Fluid Mech.*, **693**, 433–472.

Zhu, L. and Xi, L. (2018). Coherent structure dynamics and identification during the multistage transitions of polymeric turbulent channel flow. *J. Phys.: Conf. Ser.*, **1001**, 012005.

Zhu, L. and Xi, L. (2019). Vortex axis tracking by iterative propagation (VATIP): a method for analyzing three-dimensional turbulent structures. *J. Fluid Mech.*, **866**, 169–215.

Zhu, L., Schrobsdorff, H., Schneider, T. M., and Xi, L. (2018). Distinct transition in flow statistics and vortex dynamics between low- and high-extent turbulent drag reduction in polymer fluids. *J. Non-Newton. Fluid Mech.*, **262**, 115–130.

Zhu, L., Bai, X., Krushelnycky, E., and Xi, L. (2019). Transient dynamics of turbulence growth and bursting: Effects of drag-reducing polymers. *J. Non-Newton. Fluid Mech.*, **266**, 127–142.

Chapter 5

Vortex characteristics in HDR enabled by conditional sampling method

In chapter 2, we found that the qualitative LDR-HDR transition is associated with the modification of vortex configurations. In this chapter, the characteristic configurations of vortices at different stages of the inertia-driven turbulence are studied using the conditional sampling method (CS). The CS method was frequently adopted to extract the statistical features of turbulent coherent structures. We follow a standard CS process with an improvement in the selection of the reference point for realization alignment. Especially, analysis of the CS eddies supports our previous hypothesis that polymers could suppress the lift-up process of vortices at the HDR stage.

I was responsible for writing the CS code, implementing simulations and collecting data. I also post-processed data with Dr. Li Xi's suggestions. The draft was written by me and revised by Dr. Li Xi.

IOP Conf. Series: Journal of Physics: Conf. Series **1001** (2018) 012005 doi:10.1088/1742-6596/1001/1/012005

Coherent structure dynamics and identification during the multistage transitions of polymeric turbulent channel flow

Lu Zhu and Li Xi

Dept. Chemical Eng., McMaster U., 1280 Main St. W., Hamilton, ON L8S 4L7, Canada

E-mail: zhul13@mcmaster.ca

Abstract. Drag reduction induced by polymer additives in wall-bounded turbulence has been studied for decades. A small dosage of polymer additives can drastically reduce the energy dissipation in turbulent flows and alter the flow structures at the same time. As the polymer-induced fluid elasticity increases, drag reduction goes through several stages of transition with drastically different flow statistics. While much attention in the area of polymer-turbulence interactions has been focused on the onset and the asymptotic stage of maximum drag reduction, the transition between the two intermediate stages – low-extent drag reduction (LDR) and high-extent drag reduction (HDR) – likely reflects a qualitative change in the underlying vortex dynamics according to our recent study [1]. In particular, we proposed that polymers start to suppress the lift-up and bursting of vortices at HDR, leading to the localization of turbulent structures. To test our hypothesis, a statistically robust conditional sampling algorithm, based on Jenong and Hussain [2]'s work, was adopted in this study. The comparison of conditional eddies between the Newtonian and the highly elastic turbulence shows that (i) the lifting "strength" of vortices is suppressed by polymers as reflected by the decreasing lifting angle of the conditional eddy and (ii) the curvature of vortices is also eliminated as the orientation of the head of the conditional eddy changes. In summary, the results of conditional sampling support our hypothesis of polymer-turbulence interactions during the LDR-HDR transition.

1. Introduction

It is widely known that adding a small amount of polymers into Newtonian turbulence will significantly modify the flow statistics and structures. As a result, the friction factor of the flow is considerably reduced by polymers [3, 4]. In certain flow setups, such as the flow in a straight channel, polymer-induced drag reduction can reach up to 80%. This phenomenology is highly valuable in the development of new flow control strategies for enhancing the transportation efficiency of fluids. One example of the application of polymer additive drag reduction is the Trans-Alaska Pipeline system which saves the pump power by injecting polymers in to the pipe [5]. However, although the polymer additives drag reduction has been intensively studied in the past 60 years, the complex mechanisms behind them are still not fully understood.

In polymeric turbulence, several flow stages occur sequentially as the elasticity increases: the onset of drag reduction (ODR), low-extent drag reduction (LDR), high-extent drag reduction (HDR) and maximum drag reduction (MDR). Before ODR, the effect of polymers on the flows is indiscernible and the mean flow is statistically indistinguishable from those of Newtonian turbulence. Further raising the elasticity leads to the enhancement of drag reduction which

eventually converges to an universal upper bound, i.e. MDR. Between the ODR and MDR, recent experimental and numerical studies suggest the existent of two intermediate stages: LDR and HDR [4, 6, 7]. Out recent study indicated that these two stages are distinguished by the regions where flow statistics are affected by polymers: at the LDR stage polymer effects are constrained to the buffer layer while they extend to the whole wall layer at the HDR stage [1].

Same as many other drag reduction strategies, polymer additives drag reduction is the result of the disruption of the turbulence generation cycle. A widely accepted explanation of the polymer-turbulence interaction is that polymers can damp the intensity of the near-wall streamwise vortices in turbulent flows [3]. Dubief et.al. [8] found that the polymer forces applied to the near vortices tend to damp the ejection and sweeping process. Meanwhile, Ptasinski et.al. [9] suggested that polymers could absorb and redistribute the turbulence kinetic energy since the polymer work in the shear stress balance is negative. The mechanism of polymer damping vortices is in good agreement with observations from DNS simulations and experiments [3] and is sufficient to explain the occurrence of drag reduction at ODR. However, this mechanism is not sufficient to explain the drastic changes of flow statistics and coherent structures at the LDR-HDR transition.

The qualitatively different behaviors between these two intermediate stages suggest the existent of another mode of polymer-turbulence interaction that starts during the LDR-HDR transition. In addition to the indiscriminate suppression of vortex intensity, several recent studies observed additional effects of polymers on the coherent structures. Yarin et.al. [10] studied the thin vortex filaments and found that the generation of horseshoe and hairpin vortexes in the near-wall region is prevented by polymers in the high elasticity regime. Moreover, Biancofiore et.al. [11] observes that the critical amplitude of perturbation to trigger a sustained turbulence increases with elasticity at the high elasticity regime, but is constant at the low elasticity regime. This phenomenon is related to the considerable suppression of the lifting strength of near-wall streaks in high elasticity regime. In addition, our recent study [12] on the laminar-turbulence transition of polymeric flows found that polymers can stabilize the primary streak-vortex structures and suppress the bursting of vortexes. These studies all relate the polymer-turbulence interaction at the HDR stage to the lifting process of coherent structures and its following bursting event.

In our recent study [1], a systematic study on the statistical and dynamic changes of turbulence during the LDR-HDR transition was done and a new mechanism which links the LDR-HDR transition to the modification of coherent structures was proposed. In our hypothesis, the lifting and breakdown of vortices and streaks are suppressed by polymers after the LDR-HDR transition. As a result, the bursting process is weakened which prevents the transportation of energy from the buffer layer to the log-law layer and leads to the decreasing of turbulent intensity in the log-law layer. This mechanism is consistent with all known observations of the HDR stage, e.g. turbulence localization and the changing flow statistics in the log-law layer. However, direct evidences are still needed. The conditional sampling approach allows us to understand the statistical properties of vortices and offer an accessible way to study the polymer-turbulence interaction.

The conditional sampling method was initially used in experimental studies of turbulence to obtain quantitative information of a turbulent flow; the readers are referred to Antonia's comprehensive review [13] for more details. In essence, the conditional sampling method is used to obtain the best estimation of certain targeted events. In early experimental studies, the quadrant (based on Q2 and Q4 events) [14] and the Variable Interval Time Average (VITA; based on the large variances of the streamwise velocity) [15] schemes gained considerable attention. But these methods are originally not appropriate to reveal the spatial details of the flow field [16]. Later, the development of numerical simulation allows researchers to have fully 3D representation of turbulence and then spatial conditional sampling techniques were proposed. In most of these

spatial conditional sampling techniques, three steps are involved: (i) applying a predetermined event identification criterion to the flow field of turbulence, (ii) extract individual coherent structures from the target field, and (iii) determining the reference points for alignment and implementing zone average.

For step (i), the velocity-gradient-tensor-based algorithms are one of the most widely adopted local criteria (i.e. applied to individual points) in the area of vortex identification [17]. The simplest criterion in this category is vorticity. However, the vorticity is not able to distinguish the difference between the pure shear and the real swirling motion [2, 17]. Then, Hunt et.al.[18] introduced the Q quantity

$$Q \equiv 1/2(\|\mathbf{\Omega}\| - \|\mathbf{S}\|), \tag{1}$$

to describe the swirling motion, i.e. the so-called Q-criterion. The strain-rate tensor $\mathbf{S}$ and the vorticity tensor $\mathbf{\Omega}$ in equation (1) are the symmetric and antisymmetric parts of the velocity-gradient tensor $\nabla \boldsymbol{v}$, respectively. In the current study, The Q-criterion is adopted to identify the vortex structures in polymeric turbulence.

Step (ii) is of particular importance to obtain representative structures in the flows. For this step, a common approach in the literature takes advantage of the spatial/temporal separation of structures. For instance, applications based on the VITA and quadrant schemes [19, 20] employ the spatial continuity to recognize individual coherent structures. For those algorithms, a careful selection of a cutoff threshold is needed to decrease the potential influence of structure percolation. On the other hand, Hussain et.al. [21] chose the local extrema of vorticity as the sampling events. In their approach, the local extrema are picked without predefining the cutoff threshold which could effectively avoid the percolation issue. Interestingly, Jeong et.al. [2] extended Hussain et.al. [21]'s 2D local extreme conditional sampling to the 3D spatial fields by computing the local extrema of the λ_2 eigenvalue at each streamwise plane. This method is designed to capture the centre line of streamwise vortices and is robust to the cutoff threshold.

As for Step (iii), the geometry center is normally adopted as the reference point for alignment [2, 19, 21, 22]. However, a smearing problem may raise due to the shape variation of vortex structures. To deal with the smearing issue, a filter is usually set up to discard structures that differ greatly from the target events [16, 19]. Furthermore, Jeong et.al. [2] shifted the reference point according to cross-correlation between realizations.

In polymeric turbulence, the near-wall vortices are elongated and weakened by polymers [3], meanwhile, the long streamwise vortices dominate the near-wall flow field [23]. Therefore, we adopt the Jeong et.al. [2]'s method which is highly efficient in capturing the streamwise vortices. In this study, the original Jeong et al.'s method is adapted to the polymeric case and conditional vortex structures therein are sampled. Comparison is then made with the Newtonian turbulence. The results offer new insight into the coherent structure modification by polymers during the LDR-HDR transition.

2. Methodology

2.1. Direct numerical simulation

In this study, Direct Numerical Simulation (DNS) is adopted to simulate the polymeric turbulence in a plane Poiseuille geometry with a fixed pressure drop. The flow geometry is shown in figure 1, where x, y and z denote the streamwise, wall-normal and spanwise directions, respectively. The periodic boundary condition is applied to x- and z-directions while the no-slip boundary condition is used in the y-direction. The governing equations are

$$\frac{\partial \boldsymbol{v}}{\partial t} + \boldsymbol{v} \cdot \nabla \boldsymbol{v} = -\nabla p + \frac{1}{\mathrm{Re}} \nabla^2 \boldsymbol{v} + \frac{2\,(1-\beta)}{\mathrm{ReWi}} \left(\nabla \cdot \boldsymbol{\tau}_p\right), \tag{2}$$

$$\nabla \cdot \boldsymbol{v} = 0, \tag{3}$$

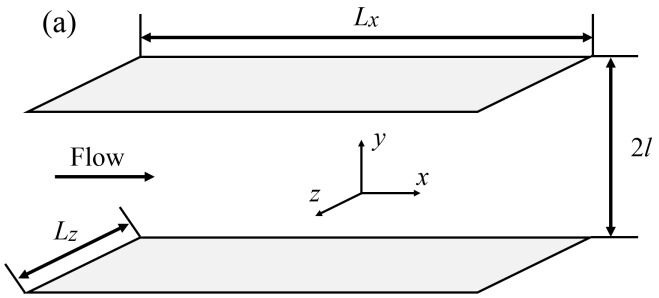

Figure 1. The conceptual plot of the flow geometry

$$\frac{\boldsymbol{\alpha}}{1-\frac{tr(\boldsymbol{\alpha})}{b}}+\frac{\mathrm{Wi}}{2}\left(\frac{\partial\boldsymbol{\alpha}}{\partial t}+\boldsymbol{v}\cdot\nabla\boldsymbol{\alpha}-\boldsymbol{\alpha}\cdot\nabla\boldsymbol{v}-(\boldsymbol{\alpha}\cdot\nabla\boldsymbol{v})^{T}\right)=\frac{b\boldsymbol{\delta}}{b+2}, \tag{4}$$

$$\boldsymbol{\tau}_p=\frac{b+5}{b}\left(\frac{\boldsymbol{\alpha}}{1-\frac{tr(\boldsymbol{\alpha})}{b}}-\left(1-\frac{2}{b+2}\right)\boldsymbol{\delta}\right). \tag{5}$$

In the above equations, the Reynolds number is defined as $\mathrm{Re}\equiv\rho U_{\mathrm{CL}}l/\eta$ where ρ, U_{CL}, l, and η are the fluid density, laminar center-line velocity, half-channel height, and fluid viscosity, respectively; under this definition, the friction Reynolds number $\mathrm{Re}_\tau=\sqrt{2\mathrm{Re}}$. The Weissenberg Wi number, defined as $\mathrm{Wi}\equiv 2\lambda U/l$ (λ is the polymer relaxation time), measures the level of elasticity. $\beta\equiv\eta_s/\eta$ is the ratio between the solvent and solution viscosities. The FENE-P constitutive equations (4)-(5) [24] is adopted to determine the polymer stress tensor $\boldsymbol{\tau}_p$ in equation (2), where $\boldsymbol{\alpha}$ is the polymer conformation tensor and the maximum extensibility parameter b constrains the square length of the polymer chains $\mathrm{tr}(\alpha)$.

A series of Wi under $\mathrm{Re}=3711$ (i.e., $\mathrm{Re}_\tau=84.85$) is investigated. The rheological parameters β and b are fixed to 0.97 and 5000, respectively. The streamwise and spanwise periods are $L_x^+\times L_z^+=4000\times 800$, where the superscript "+" indicates quantities in turbulent inner scales. A Fourier-Chebyshev-Fourier pseudo-spectral scheme is applied for spatial discretization. Meanwhile, a third-order semi-implicit backward-differentiation-Adams-Bashforth scheme[25] is used to integrate equations in time. In addition, an artificial diffusion term $1/(\mathrm{ScRe})\nabla^2\boldsymbol{\alpha}$ with the Schmidt number $\mathrm{Sc}=0.5$ is introduced in equation (4) to achieve better numerical stability.

2.2. Conditional sampling

In this study, vortexes are identified by adopting the Q-criterion (equation (1)) [17]. $Q=0$ indicates a pure shear flow while a large negative and positive Q correspond to regions dominated by extensional and rotational flows, respectively. The vortex structures are chosen by satisfying $Q>0.7Q_{rms}$ (where Q_{rms} is the root-mean-square of Q).

The conditional sampling algorithm based on Jeong et.al.[16]'s method involves several steps: (1) detect vortex region which satisfies $Q>0.7Q_{rms}$ in the 3D instantaneous flow field; (2) calculate the local maxima of the accepted regions at each y-z plane – the local maxima are regarded as the x-centrepoints of streamwise vortices; (3) group the local maxima to individual vortices by adopting a cone detection method, connecting these points form the centrelines of vortices; (4) categorize vortices into two categories according to the senses of rotation (clockwise/anticlockwise), the sense is determined by the sign of streamwise vorticity at the vortex axis; (5) realizations are discarded if they do not satisfy: (a) the vortex streamwise length $l_x^+\geq 50$, and (b) the average height of the vortex axis $h_y^+\leq 50$; (6) the x-centrepoint

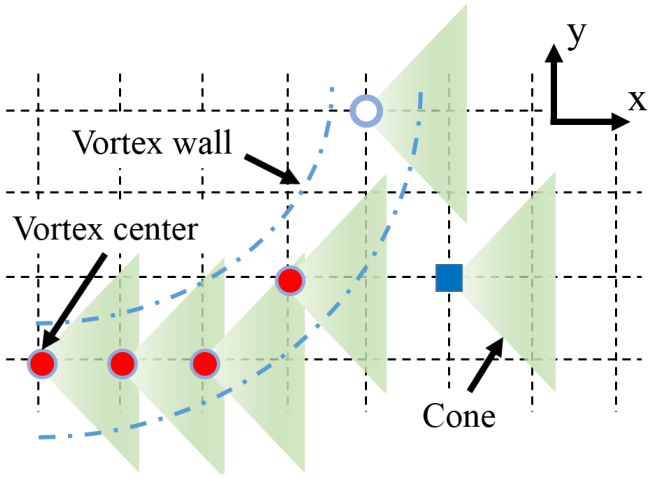

Figure 2. Schematic diagram of the cone algorithm method

located at $y^+ = 50$ is chosen as the reference point for alignment and realizations with the same sense of rotation are aligned and averaged to obtain the conditional eddy.

In order to extract individual vortices, the cone detective method is involved. In this method, two x-centrepoints are considered to belong to the same vortex when they satisfy: (a) the two points locate at two adjacent y-z planes; (b) the downstream point is the closest local maximum on its plane to the upstream point; and (c) the distance between the downstream point and the projection of the upstream point is smaller than a threshold, i.e., the downstream point locates within a confining cone extending from the upstream point. A schematic plot of the cone detective method is shown in figure 2. Dots in this figure are the x-centrepoints while the dot dash lines indicate the wall of a vortex. Centrepoints are grouped by the detective method if they fall into the cone (the triangles in figure 2). However, note that this method is inefficient to detect vortices with a high deviation of vortex line from the streamwise direction, e.g. vortex with a strong lifting tendency as shown in the figure.

In Jeong et.al.'s original method [16], the geometry center of vortex axis is chosen to be the reference point for realization alignment. However, since the lengths of streamwise vortexes are different, fixing the reference point to the geometry center will lead to the misalignment of heads and tails of vortices, as shown in figure 3a, and cause the smearing problem. This is worse for high Wi cases where the vortices have a broader range of size and shapes. Instead, we move the reference point for realization alignment to the x-centrepoint at $y^+ = 50$. The new reference point ensures the precise alignment of the heads of vortices (figure 3b). Benefiting from this modification, some important dynamics of vortices, such as the lifting process, can be accurately captured. In addition, the choice of the reference point relaxes the strict constraint of vortex length in step (5) of the conditional sampling algorithm, as the variation of vortex length now has less effects on the conditional eddies (especially in the head region) compared with the original method.

3. Results and discussion

The presence of multiple stages in the polymeric turbulence suggests the existence of multiple types of polymer-turbulence interactions at different stages. In this study, we focus on the change of interaction involved in the LDR-HDR transition. As has been discussed in the literature[3, 4], the statistical quantities of turbulence in LDR and HDR stages exhibit qualitatively different

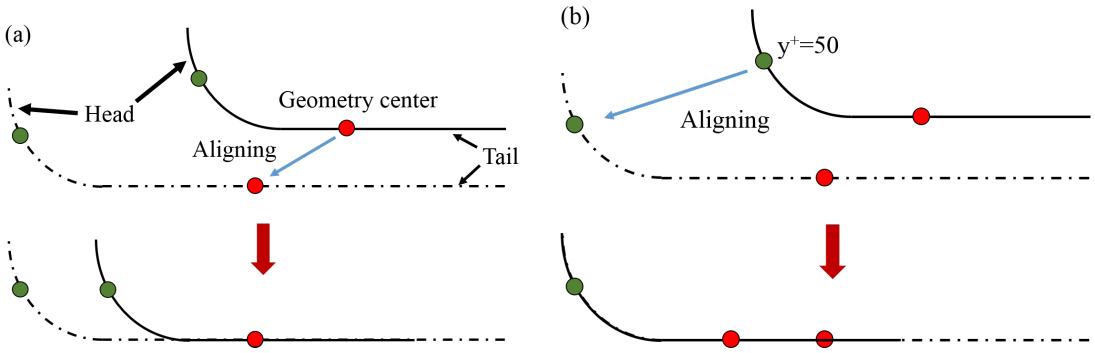

Figure 3. Selection of the reference point at (a) the geometry center and (b) the head

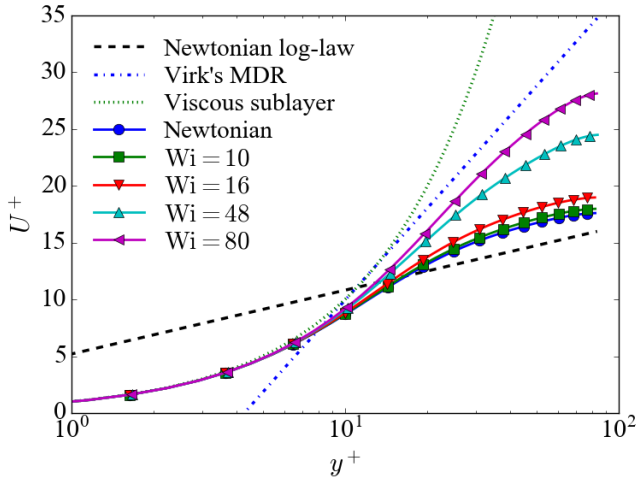

Figure 4. Mean velocity profiles at $\mathrm{Re}_\tau = 86.15$

behaviors. Figure 4 shows the mean velocity profiles of Newtonian, LDR (Wi = 16), HDR (Wi = 48) and MDR (Wi = 80) at $\mathrm{Re}_\tau = 86.15$. Starting at the ODR (Wi $\leq$ 10), the velocity profiles lift up as Wi increases and reach an upper bound at the MDR stage. The identification between LDR and HDR depends on the influenced zones of polymers. For the LDR case (Wi = 16), the effect of polymers is constrained in the buffer layer ($y^+ \approx 5 \sim 30$): the velocity profile rises in buffer layer but stays parallel to the Newtonian profile outside the buffer layer region ($y^+ > 30$). By contrast, the slopes of the mean velocity profiles at HDR and MDR stages differ from the Newtonian profile in the whole channel.

The systematic analysis of the statistical and dynamic changes during the LDR-HDR transition is the focus of a separate study of ours [1]. Therein, we hypothesized that at the LDR-HDR transition polymers start to suppress the bursting of turbulence by preventing vortices from lifting up. The typical vortex structures extracted from the instantaneous flow field before and after the LDR-HDR transition are presented in figure 5. Before the LDR-HDR transition, vortexes tend to aggregate into vortex packets. A hairpin vortex is observed at the downstream end of this vortex packet. As the head of the hairpin vortex lifts up, the vortex eventually breaks

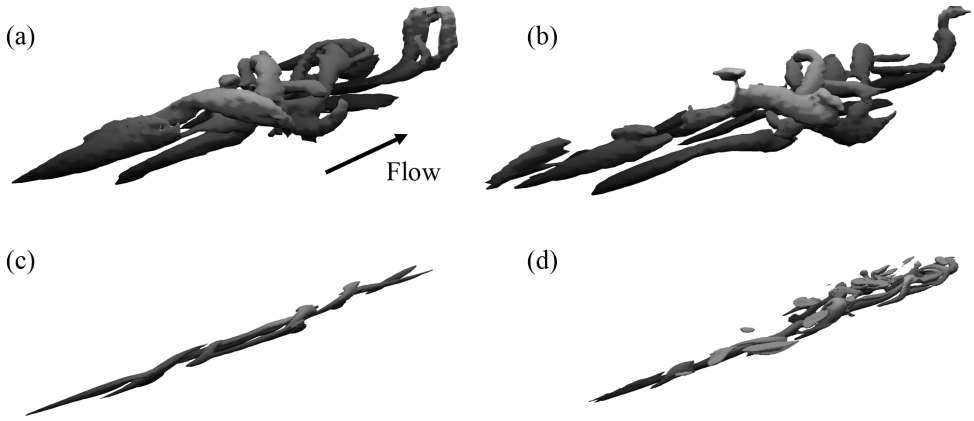

Figure 5. Typical instantaneous vortex structures in cases before and after the LDR-HDR transition: (a) and (b) – before, time interval $\Delta t = 8$; (c) and (d) – after, time interval $\Delta t = 32$

down after a period of time. In addition to the hairpin, other type of vortices (e.g. the pseudo-streamwise vortices) also have a high tendency of lifting. In fact, the lift-up and bursting of vortices play an important role in the instability-based vortex regeneration cycle [26, 27]. However, in the high elasticity turbulence (HDR and MDR), the lift-up strength of vortexes is weakened and the hairpin vortices are eliminated by polymers, as shown in figure 5c. Instead, longer and smoother streamwise vortices with weaker lifting strength dominate the near-wall coherent structures. Note that these streamwise vortices usually organize to a ultra-long (the streamwise length $l_x^+ \geq 400$) streamwise vortex string in which the head of a upstream vortex overlaps the tail of an adjacent downstream vortex. The vortex string is similar to those vortices generated by the parent-offspring vortex regeneration cycle[28]. Eventually, as the strength of vortices exceeds a certain threshold, the vortex string suddenly bursts and forms a group of vortices in the adjacent region (figure 5d).

The modification of the vortex organization pattern is due to the change of vortex regeneration mechanism. In our hypothesis, since the instability-based mechanism is interrupted by polymers in HDR and MDR stage due to the prevention of lifting and bursting of vortices, the other mechanism – the parent-offspring vortex mechanism, becomes exposed.

To understand the statistical characteristics of vortices at different stages, the aforementioned conditional sampling algorithm, improved based on ref. [16], is implemented. Figure 6 shows the probability density functions (PDF) of streamwise lengths of vortices at different y^+. The PDF distribution of the polymeric flow (Wi = 96) covers a wider range from 0 to over 800 wall units while the Newtonian turbulence only expands to 500 wall units. Also, the peak of the PDF distribution adheres to the wall ($y^+ = 30$) in the Newtonian case while it approaches the center of the channel ($y^+ = 50$) in the polymeric case. To alleviate the potential smearing problem (figure 3), a minimum streamwise length cutoff of vortexes is set to filter vortices with a short streamwise length. In Jeong et al's conditional sampling of the Newtonian flow, the cutoff ($l_x^+ = 200$) is larger than the average length of vortices. As a consequence, the relatively large cutoff biases the sample by eliminating many qualified structures, which limits the representativeness of the conditional eddies. Despite the long cutoff, the issue of uneven vortex length still apparently caused smearing in their conditional eddy. The new criterion for selecting the reference point (the x-centrepoint located at $y^+ = 50$) in our improved algorithm significantly alleviates the smearing issue with a much smaller cutoff ($l_x^+ = 50$). As a consequence, more realizations are included in constructing the conditional eddy which improves the representativeness of the

conditional eddy.

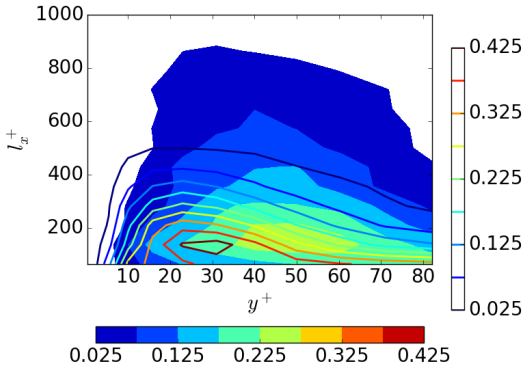

Figure 6. Probability density functions of vortex streamwise lengths: the color flood is for the Wi=96 case and lines are for the Newtonian case.

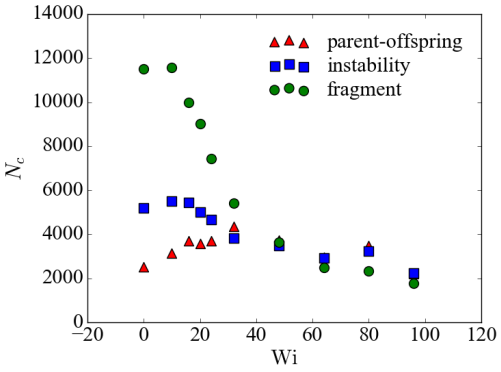

Figure 7. The average number of centre points in each vortex class increasing Wi.

Based on their streamwise length, vortices can be grouped into two categories: major vortices ($l_x \geq l_{\text{cutoff}}$) and fragments ($l_x \leq l_{\text{cutoff}}$). On the other hand (as reviewed above), the vortex regeneration mechanisms in wall-bounded flow can be categorized into two types [29]: the parent-offspring and instability-based mechanisms. Noting that the parent-offspring mechanism depends on the direct contact between the parent and the offspring vortices while the steak instability does not, major vortices may thus be categorized according to their generation mechanisms based on their spatial proximity to other vortices. Pseudo-streamwise vortices overlapping with another vortex with the opposite sense of rotation are categorised to the parent-offspring vortex class and other vortices are categorised to the instability vortex class. By employing this classification, we are able to investigate the changing vortex regeneration mechanism at different stages. The average number of vortex centrepoints N_c of these two classes for different Wi is plotted in figure 7. Since the threshold to determine fragments is arbitrary, a number of thresholds are tested and the trend of the profiles is robust to the threshold. In figure 7, the cutoff threshold is 150.

The critical Wi of the PO-LDR, LDR-HDR and HDR-MDR transitions in figure 7 are 10, 24 and 80, respectively. The number of centrepoints in the instability class starts to decrease at Wi = 20 which is close to the LDR-HDR transition, suggesting a strong relation between the LDR-HDR transition and the suppression of the instability mechanism. The parent-offspring vortices, however, does not decrease until well after Wi = 32. In other words, the parent-offspring mechanism is more persistent to the strong polymer effect at HDR. On the other hand, fragments continuously decrease after the onset of drag reduction as polymers suppress the overall intensity of vortices. These observations are in good agreement with our proposed polymer-turbulence interaction during the LDR-HDR transition. However, readers should note that figure 7 is an imprecise estimation of vortex number at different classes. For example, the poor capability of current vortex tracking method in tracking curved vortexes will overestimate the number of vortices in the fragment class. To overcome this issue, the detective algorithm needs to be improved to accommodate higher vortex curvatures, which will be the focus of our future work.

The conditional eddies are obtained in cases before (Newtonian) and after (Wi = 96) the LDR-HDR transition and are presented in figure 8. As a reminder, vortex realizations are

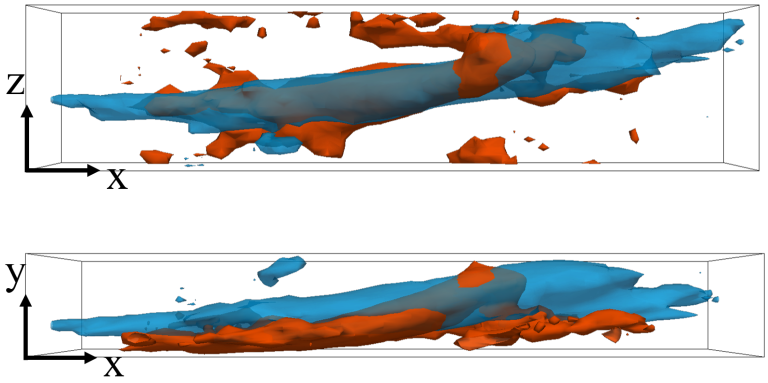

Figure 8. (a) The top and (b) side views of the conditional eddies of the Newtonian (red) and Wi = 96 (blue) turbulence.

separated into two classes according to the sign of streamwise vorticity before zone averaging. In figure 8, only the counter-clockwise conditional eddy are shown since the clockwise conditional eddy is its mirror image.

Figure 8(a) shows the top view of the conditional eddies. In general, the length of the conditional eddy at Wi = 96 is longer than that of the Newtonian case, which is consistent with observations in instantaneous flow field images. Comparing the two cases, the tilting angles are similar, but the head of the Newtonian eddy bends further to the positive z direction, which is attributed to the prevalence of highly curved vortexes, e.g. hairpins. In figure 8(b), the lifting angle of the conditional eddy before the transition (Newtonian) is larger than that after the transition (Wi = 96), which agrees with our previous discussion of polymers suppressing the lifting process of vortices. Also, in both cases, an additional iso-surface with opposite streamwise vorticity appears under the head of the main body. Its existence indicates a high probability of another vortex with the opposite sense of rotation showing up under the head of the upstream vortex. Note that in the Newtonian case, the additional structure appears irregular; only in the high-Wi case does the additional eddy become more coherent. This change is possibly a reflection of the increasing importance of the parent-offspring mechanism.

4. Conclusions

Despite recent efforts in the literature, a complete picture of the polymer-turbulence interaction is still missing. Especially, the interaction responsible for the LDR-HDR transition remains a puzzle. A hypothesis was put forward in our recent study on the LDR-HDR transition[1], in which polymers suppress vortex regeneration through streak instability by preventing the lift-up and bursting of vortices. In this study, a conditional sampling algorithm improved from that of ref. [16] is employed to compare the vortex dynamics before and after the LDR-HDR transition.

Observations of the conditional eddies obtained support our hypothesis. The lifting angle of the Newtonian eddy is considerably larger than that of the Wi = 96 case. Also, the different shapes of the vortex head suggest that highly curved vortices (e.g., hairpins) existing in the Newtonian and LDR cases are suppressed by polymers at the HDR and MDR stages.

The near-wall vortices are also divided into three classes: one is fragments and the other two are major vortices generated by the streak-instability and parent-offspring mechanisms. The number/size of vortices generated by the streak-instability mechanism drops during the LDR-HDR transition ($Wi = 20$) while those in the parent-offspring class remain frequent until well

beyond $Wi = 32$. This result also agrees well with our hypothesis of the modification of vortex regeneration mechanism.

Acknowledgments
Financial support from the Natural Sciences and Engineering Research Council of Canada (NSERC) through its Discovery Grants Program (No. RGPIN-2014-04903) is acknowledged. The computation is made possible by the facilities of the Shared Hierarchical Academic Research Computing Network (SHARCNET: `www.sharcnet.ca`) and through the computing resources allocation awarded by Compute/Calcul Canada. The authors thank Javier Jiménez and Miguel P. Encinar for fruitful discussions. This work was also funded in part by the Coturb program of the European Research Council.

References

[1] L. Zhu, H. Schrobsdorff, T. M. Schneider and L. Xi 2017 submitted.
[2] Jeong J and Hussain F 1995 *J. Fluid Mech.* **285** 69–94
[3] White C M and Mungal M G 2008 *Annu. Rev. Fluid Mech.* **40** 235–256.
[4] Xi L and Graham M D 2010 *J. Fluid Mech.*, **647** 421–452.
[5] Burger E D, Chorn L G and Perkins T K 1980 *J. Rheol.*, **24** 603–626.
[6] Li W. and Graham M. D. 2007 *Phys. Fluids* **19** 083101.
[7] K. D. Housiadas, A. N. Beris and R. A. Handler, 2005 *Phys. Fluids* **17** 035106.
[8] Dubief Y, Terrapon V E , White C M, Shaqfeh E S, Moin P and Lele S K 2005 *Flow Turbul. Combust.* **74** 311–329.
[9] Ptasinski P K, Boersma B J, Nieuwstadt F T M, Hulsen M A, Van den Brule B H A A and Hunt J C R 2003 *J. Fluid Mech.* **490** 251–291.
[10] Yarin A L 1997 *J. Non-Newtonian Fluid* **69** 137–153.
[11] Biancofiore L Brandt L and Zaki T A 2017 *Phys. Rev. Flu.* **2** 043304.
[12] Bai X. and Xi L. 2017 submitted.
[13] Antonia R A 1981 *Ann. Rev. Fluid Mech.* **13** 131–156.
[14] Willmarth W W and Lu S S 1972 *J. Fluid Mech.* **55** 65–92.
[15] Blackwelder R F and Kaplan R E 1976 *J.Fluid Mech.* **76** 89–112.
[16] Jeong J, Hussain F, Schoppa W and Kim J 1997 *J. Fluid Mech.* **332** 185–214.
[17] Kol V 2007 *Int. J. Heat Fluid Fl.* **28** 638–652.
[18] Hunt J C R, Wray A A and Moin P 1988 *Proc. Center Turbul. Res. Summer School* 193–208 (Stanford U.).
[19] Lozano-Durn A, Flores O and Jiménez J 2012 *J. Fluid Mech.* **694** 100-130.
[20] Chu D C and Karniadakis G E 1993 *J. Fluid Mech.* **250** 1–42.
[21] Hussain A K M F and Hayakawa M 1987 *J. Fluid Mech.* **180** 193–229.
[22] Kim J and Moin P 1986 *J. Fluid Mech.* **162** 339–363.
[23] Graham M D 2004 *Rheology reviews* **2** 143-170.
[24] Bird R B, Armstrong R C and Hassager O 1987 *Dynamics of polymeric liquids. Vol. 2: Kinetic Theory* (New York: John Wiley).
[25] Peyret R 2013 *Spectral methods for incompressible viscous flow* (New York: Springer).
[26] Robinson S K 1991 *Ann. Rev. Fluid Mech.* **23** 601–639.
[27] Hamilton J M , Kim J and Waleffe F 1995 *J. Fluid Mech.* **287** 317–348.
[28] Brooke J W and Hanratty T J 1993 *Phys. Fluids A* **5** 1011–1022.
[29] Schoppa W and Hussain F 2002 *J. Fluid Mech.* **453** 57–108.

Chapter 6

A hybrid SM-FDM method for simulation of elasticity-driven turbulence

At a high elasticity, the polymeric turbulence can be driven by the elastic force and express completely different behaviors comparing with the inertia-driven turbulence. However, this new type of turbulence was not captured in DNS studies that adopted the pseudo-spectral method (SM), as a global artificial diffusion term is added to the polymer constitutive equations to stabilize the simulation. This chapter focuses on developing a hybrid pseudo-spectral/finite-difference method (HM), in which a finite-difference total variational diminishing (TVD) scheme is adopted for the spatial discretization of the convective term of the FENE-P equations while the other spatial derivatives are discretized by SM. The HM scheme largely benefits from the accuracy and efficiency of SM while maintaining stability without GAD. It also has good portability to be embedded into the pseudo-spectral method that are widely

adopted by the existing DNS codes for canonical geometries.

I was responsible for developing and testing the numerical scheme. I also collected the data, post-processed it and wrote the draft with Dr. Li Xi's suggestions.

This chapter is under preparation for future publication.

6.1 Introduction

Research on the friction drag reduction in the turbulent system always occupies one crucial seat in the area of fluid mechanics due to its wide applications in industry. A well-known technique to reduce the friction drag in the oil delivery system (e.g. the pipeline) is the so-called polymer additives drag reduction (DR). In the 1940s, Toms (1948) found that adding a small amount of flexible polymers into the turbulent flows can significantly change the flow structures and result in up to 80% of friction reduction in the pipeline system (Virk, 1975; Myska and Stern, 1998). Such extraordinary performance to reduce friction drag has attracted great attention since then (Nesyn *et al.*, 2018).

Significant progress has been achieved to uncover the mask of this drag reduction phenomenon using both experimental and numerical tools (Virk, 1975; Warholic *et al.*, 2001; Xi and Graham, 2010a; Wang *et al.*, 2017). The DR turbulence is usually regarded as Newtonian-like, i.e., the flow is driven by inertial force and exhibits behaviors similar to the Newtonian turbulence (Xi and Graham, 2010a; Li *et al.*, 2005a; Housiadas *et al.*, 2005). Polymers in this inertia-driven turbulence(IDT) are mainly responsible for suppressing turbulence which leads to the DR phenomenon. On the other hand, recent study by Dallas *et al.* (2010) found that polymers can also feed energy to the turbulent flow at high elasticity regime. In this type of turbulence, sheet-like polymer structures and spanwise vortices are found which are entirely different from those dominated streamwise vortices in IDT (Sid *et al.*, 2018). In this so-called "elasticity-driven" turbulence (EDT, or "elasto-inertial" turbulence (EIT) (Samanta *et al.*, 2013; Dubief *et al.*, 2013; Shekar *et al.*, 2019)), polymers are responsible for both the generation of elastic structures and the suppression of

Newtonian structures. As a result, the IDT flow can be largely erased while the EDT flow becomes dominant.

One widely adopted tool to study the polymeric turbulence is the direct numerical simulation (DNS). This tool was originally developed to study Newtonian turbulence (Moin and Kim, 1982; Kim *et al.*, 1987). Extension to polymeric turbulence requires coupling the Newtonian system with the polymer constitutive equations which describe the behaviors of polymers in the flows. Following Sureshkumar *et al.* (1997)'s work, we adopt the FENE-P (finite extension nonlinear elastic model with Peterlin closure approximation) model (Bird *et al.*, 1987a) (details will be presented in section 6.2.1) to govern the polymer conformation tensor $\boldsymbol{\alpha}$ (which defines the average extension length and orientation of polymers). In DNS of Newtonian turbulence, the pseudo-spectral method (SM) has been proved to be one powerful algorithm with high efficiency and accuracy (Gottlieb and Orszag, 1977; Canuto *et al.*, 1988; Rogallo and Moin, 1984). This algorithm has also been involved in many studies (Sureshkumar and Beris, 1995; Li *et al.*, 2005b; Xi and Graham, 2010b) to solve the polymeric turbulent system. However, the hyperbolic nature (due to the lack of diffusion term) of the polymer constitutive equations could cause strong numerical oscillations and break down the simulation when adopting SM. A common practice to resolve the oscillation issue is to introduce an global artificial diffusion (GAD) term $1/(\mathrm{ScRe})\nabla^2\boldsymbol{\alpha}$ (Sc is the Schmidt number to control the magnitude of GAD; and Re is the Reynolds number) to the constitutive equations (Sureshkumar and Beris, 1995). With an appropriate GAD, the numerical oscillations can be largely eliminated. Nevertheless, introducing this term would also alter the nature of the equations which may accidentally lose some physical insight of the flows (Yu and Kawaguchi, 2004; Dubief *et al.*, 2004).

Thus the magnitude of the GAD, 1/(ScRe), must be strictly restricted (Sureshkumar and Beris, 1995; Xi and Graham, 2010b).

Pseudo-spectral method coupling with GAD could give a reasonable prediction in the DR turbulence (Sureshkumar and Beris, 1995). However, recent study by Sid *et al.* (2018) doubted the capability of this method in the high elasticity regime of polymeric flows. Especially, they argued that the involved GAD can significantly damp the small scale polymer structures and prevent the growth of EDT (Dubief *et al.*, 2005, 2013; Samanta *et al.*, 2013). Alternatively, finite-difference method (FDM) may offer a better solution for the polymeric turbulent system. With an elaborate treatment of the convection term (which is the source of the numerical oscillations (Sureshkumar and Beris, 1995; Sid *et al.*, 2018)) of the polymer constitutive equations, the FDM DNS either completely (Vaithianathan *et al.*, 2006; Yu and Kawaguchi, 2004; Dallas *et al.*, 2010) or mostly (Min *et al.*, 2001; Dubief *et al.*, 2005) avoids adding the artificial diffusion and is thus closer to the exact solution.

The initial attempt to solve polymeric turbulence with FDM was done by Min *et al.* (2001, 2003) who adopted a third-order compact upwind scheme to deal with the convection term of the constitutive equations. Dubief *et al.* (2004) improved this method by involving a special treatment to restrict the maximum extension of polymers. An alternative way to treat the convection term was done by Lee and Zaki (2017) who involved a third-order weighted essentially non-oscillating (WENO) scheme (Shu, 1998, 2009) in their DNS. These algorithms are benefited from their relative high order of accuracy but with the sacrifice of computational speed. Also, a local artificial diffusion (LAD, the artificial diffusion is only added to local grid points) is still required by these methods to stabilize local oscillations that occasionally occur

in the flows. One faster second-order FDM was developed by Yu and Kawaguchi (2004). They introduced the second-order upwind total variation diminish (TVD) scheme (Harten, 1983; Sweby, 1984; LeVeque, 1996) – a classical and widely adopted approach to solve the convection-dominated problems – to discretize convection terms in DR turbulence. The excellent stability of the TVD scheme allows them to get rid of the artificial diffusion completely. Moreover, a second-order central difference scheme was involved in the polymeric turbulent system by Vaithianathan *et al.* (2006) to maintain the strictly provable positive-definiteness of the polymer conformation tensor at all grid points.

Note that the FDM schemes may encounter numerical diffusion (Douglas and Russell, 1982; Sod, 1978) due to the limited order of accuracy. Therefore, numerical schemes with a high-order of accuracy (comparing with those 2nd-order schemes) are always necessary for an accurate solution in DNS of Newtonian and viscoelastic turbulence (Dallas *et al.*, 2010; Laizet and Lamballais, 2009). However, even for those high-order schemes, e.g., the fourth-order scheme reported by Sid *et al.* (2018), the order of accuracy is still much lower than SM whose accuracy order is infinite. Besides, the high-order FDM will inevitably increase the computational cost. On the other hand, SM benefits from its high order of accuracy and excellent computational efficiency. But it requires additional GAD to stabilize the system which may violate the nature of the system. In this study, we propose a hybrid pseudo-spectral/finite-difference method (HM) to solve the polymeric turbulent system. The HM scheme uses the standard SM to solve all of the spatial derivative terms in the system except for the convection term of the polymer constitutive equation which will be discretized by a conservative upwind TVD scheme. As will be discussed later,

this special treatment could efficiently eliminate numerical oscillations without any artificial diffusion. Also, it maximizes the benefits of SM, i.e., the high order accuracy and computational efficiency, and is potable to be embedded into the widely used pure SM architecture. In this study, we will first describe the hybrid method and numerical details in section 6.2. A steak transient growth (STG) simulation is then implemented in section 6.3.1 to validate the correctness of the method and the code. Next, we also implement the steady-state simulation of both inertia-driven turbulence and elasticity-driven turbulence (EDT) in a relative smaller simulation geometry by using the HM and SM (with artificial diffusion) schemes in section 6.3.2. The performance of the two schemes and the effects of AD are also discussed in a large geometry (section 6.4). At the end (section 6.4.1), we will discuss the mesh resolution sensitivity of the new scheme.

6.2 Methodology

6.2.1 Computational domain and governing equations

In this study, simulation of the plane Poiseuille polymeric flows are implemented. The geometry of the computational domain is illustrated in fig. 6.1. The incompressible polymeric flow is driven by a constant pressure drop and oriented in x-direction (streamwise). Two parallel walls are located in y-direction (wall-normal) with a distance of $2l$. The periodic boundary condition is applied to x- and z-directions (spanwise) with the periods of L_x and L_z, respectively. The no-slip boundary condition is applied to the walls. The half-channel height l, the Newtonian laminar centerline velocity U are employed to nondimentionalize the length and velocity scales. The

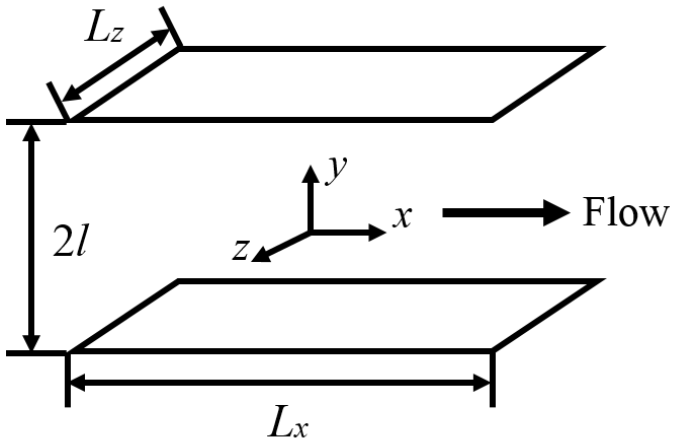

Figure 6.1: Schematic of the flow geometry.

pressure p and time t are then scaled by ρU^2 (ρ is the total density of the solution) and l/U, respectively. Direct numerical simulation of the polymeric flow solves the equation system coupling the momentum balance (eq. (6.1)) and continuity equations (eq. (6.2)) with the FENE-P constitutive equations (eqs. (6.3) and (6.4)) as given by

$$\frac{\partial \boldsymbol{v}}{\partial t} + \boldsymbol{v} \cdot \boldsymbol{\nabla} \boldsymbol{v} = -\boldsymbol{\nabla} p + \frac{\beta}{\mathrm{Re}} \nabla^2 \boldsymbol{v} + \frac{2\,(1-\beta)}{\mathrm{ReWi}} \left(\boldsymbol{\nabla} \cdot \boldsymbol{\tau}_p \right), \tag{6.1}$$

$$\boldsymbol{\nabla} \cdot \boldsymbol{v} = 0. \tag{6.2}$$

$$\frac{\partial \boldsymbol{\alpha}}{\partial t} + \boldsymbol{v} \cdot \boldsymbol{\nabla} \boldsymbol{\alpha} - \boldsymbol{\alpha} \cdot \boldsymbol{\nabla} \boldsymbol{v} - (\boldsymbol{\alpha} \cdot \boldsymbol{\nabla} \boldsymbol{v})^{\mathrm{T}} = \frac{2}{\mathrm{Wi}} (-\frac{\boldsymbol{\alpha}}{1 - \frac{\mathrm{tr}(\boldsymbol{\alpha})}{b}} + \frac{b\boldsymbol{\delta}}{b+2}), \tag{6.3}$$

$$\boldsymbol{\tau}_p = \frac{b+5}{b} \left(\frac{\boldsymbol{\alpha}}{1 - \frac{\mathrm{tr}(\boldsymbol{\alpha})}{b}} - \left(1 - \frac{2}{b+2} \right) \boldsymbol{\delta} \right). \tag{6.4}$$

The Reynolds number in eq. (6.1) is defined as $\mathrm{Re} \equiv \rho U l/\eta$ (where η is the total zero-shear rate viscosity) which is directly related to the friction Reynolds number $\mathrm{Re}_\tau \equiv \rho u_\tau l/\eta$ ($u_\tau \equiv \sqrt{\tau_w/\rho}$ is the friction velocity, where τ_w is the wall shear stress)

through $\mathrm{Re} = \mathrm{Re}_\tau^2/2$. The Weissenberg number, defined as $\mathrm{Wi} \equiv 2\lambda U/l$, is the product of the polymer relaxation time λ and the characteristic shear rate, β is the ratio of the solvent viscosity η_s and the total viscosity η, i.e., $\beta \equiv \eta_s/\eta$. The effect of polymers on the flow is accounted for by the last term on the right-hand side of the momentum balance equation (eq. (6.1)). Here, $\boldsymbol{\tau}_p$ is called polymer stress tensor and is modeled by the FENE-P constitutive equations (Bird *et al.*, 1987b) which describe a polymer as a finitely extensible nonlinear elastic (FENE) dumbbell. In eq. (6.3), the polymer conformation tensor $\boldsymbol{\alpha}$, defined as $\boldsymbol{\alpha} \equiv \langle \boldsymbol{QQ} \rangle$ (where $\boldsymbol{Q}$ indicates the end-to-end vector of dumbbells), is solved and used to compute the polymer stress tensor $\boldsymbol{\tau}_p$ through eq. (6.4). The extension of polymers in the FENE-P model is constrained by the maximum extensible parameter b through $\max(\mathrm{tr}(\boldsymbol{\alpha})) \leq b$.

6.2.2 Numerical procedures

Time discretization of the equation system adopts a third-order semi-implicit backward-differentiation/Adams-Bashforth scheme (BDAB3) (Peyret, 2002a). BDAB3 updates the linear terms with the implicit third-order backward differentiation method while nonlinear terms with the explicit third-order Adams–Bashforth method.

As for spatial discretization, we developed a hybrid pseudo-spectral/finite-difference method, in order to maximize the high order accuracy and efficiency of SM while stabilize the simulation without additional GAD. Except for the convection term $\boldsymbol{v} \cdot \boldsymbol{\nabla \alpha}$ of the FENE-P equations (eq. (6.3)), all other spatial derivative terms in the equation system (eqs. (6.1) to (6.4)) are discretized by a Fourier–Chebyshev–Fourier pseudo-spectral projection. The $\boldsymbol{v} \cdot \boldsymbol{\nabla \alpha}$ term is crucial for the generation of small elastic scales (Sid *et al.*, 2018) and is also the source of the numerical instability. In the

new algorithm, we choose to discretize this term using a conservative second-order upwind TVD (total variation diminishing) scheme which has been well established for hyperbolic problems (Zhang *et al.*, 2015) and has been implemented in the polymeric turbulence DNS (Yu and Kawaguchi, 2004). Details of implementation of this hybrid algorithm will be further presented in section 6.2.2.

Time advancement

As mentioned in section 6.2.2, the equation system (eqs. (6.1) to (6.4)) is advanced in time using the BDAB3 (Peyret, 2002b). The velocity field is solved following a classical pseudo-spectral method as discussed by Xi (2009). The velocity and pressure fields are firstly decomposed to the base and perturbation fields

$$\boldsymbol{v} = U\boldsymbol{e}_x + \boldsymbol{v}^\dagger, \text{ and } \boldsymbol{p} = \Pi\boldsymbol{e}_x + \boldsymbol{p}^\dagger, \tag{6.5}$$

where $\boldsymbol{v}^\dagger$ and $\boldsymbol{p}^\dagger$ indicate the perturbation component of the velocity and pressure. U is the mean velocity profile of the laminar plane Poiseuille flow, Π is the mean pressure gradient which is fixed to $-2\mathrm{Re}$ in this study, and $\boldsymbol{e}_x$ is the unit vector in the x-direction. The decomposed velocity and pressure fields are substituted into the momentum balance equation which is then reorganized as,

$$\frac{\partial \boldsymbol{v}^\dagger}{\partial t} = -\boldsymbol{N} - \boldsymbol{\nabla} p^\dagger + \boldsymbol{L} + \boldsymbol{C} + \boldsymbol{S}_p \tag{6.6}$$

ς	a_0	a_1	a_2	b_0	b_1	b_2
11/6	-3	3/2	$-1/3$	3	-3	1

Table 6.1: Numerical coefficients for the third-order Adams-Bashforth/backward-differentiation discretization method (Peyret, 2002b)

where $\boldsymbol{N}$ and $\boldsymbol{S}_p$ stand for the inertia and polymer nonlinear terms, $\boldsymbol{C}$ is the constant term and $\boldsymbol{L}$ indicates the linear term. They are defined as

$$\boldsymbol{N} \equiv \boldsymbol{v} \cdot \boldsymbol{\nabla} \boldsymbol{v}, \tag{6.7}$$

$$\boldsymbol{S}_p \equiv \frac{2(1-\beta)}{\mathrm{ReWi}} \boldsymbol{\nabla} \cdot \boldsymbol{\tau}_p, \tag{6.8}$$

$$\boldsymbol{C} \equiv (\frac{\beta}{\mathrm{Re}} \frac{\partial^2 U}{\partial y^2} - \Pi) \boldsymbol{e}_x, \tag{6.9}$$

$$\boldsymbol{L} \equiv \frac{\beta}{\mathrm{Re}} \nabla^2 \boldsymbol{v}^{\dagger}. \tag{6.10}$$

After taking Fourier transform in x- and z-directions and discretizing in time with BDAB3 scheme, eq. (6.6) is rewritten as

$$\frac{\varsigma}{\Delta t} \tilde{\boldsymbol{v}}^{\dagger, n+1} - \tilde{\boldsymbol{L}}^{n+1} + \tilde{\boldsymbol{\nabla}} \tilde{p}^{\dagger, n+1} = \sum_{j=0}^{2} (-\frac{a_j}{\Delta t} \tilde{\boldsymbol{v}}^{\dagger, n-j} + b_j (\tilde{\boldsymbol{N}}^{n-j} - \tilde{\boldsymbol{S}}_p^{n-j})) + \tilde{\boldsymbol{C}}. \tag{6.11}$$

In above equation, n and $n+1$ are the index of the current and next steps. ς, a_j and b_j are the numerical coefficients of the BDAB3 scheme and are listed in table 6.1. "$\sim$" indicates variables in the Fourier-Physical-Fourier space(in $x-y-z$ dimensions).

The continuity equation (eq. (6.2)) is coupled with the momentum balance equation (eq. (6.1)) using the influence matrix method (Canuto *et al.*, 1988). The inertia term in eq. (6.1) is computed by an alternating form, i.e., the convection form $\boldsymbol{v} \cdot \boldsymbol{\nabla} \boldsymbol{v}$

and the divergence form $\boldsymbol{\nabla}\cdot(\boldsymbol{vv})$ are switched at each time step. More details regarding the numerical procedure to solve eqs. (6.1) and (6.2) are referred to Xi (2009).

The conformation tensor is also advanced based on the BDAB3 scheme with two major differences compared with the classical BDAB3 scheme used in SM (Xi and Graham, 2010b): (*i*) time advance is implemented in physical space, and (*ii*) an implicit time-stepping modification suggested by Vaithianathan *et al.* (2006) and Dubief *et al.* (2005), is introduced to enforce the upper-boundness of the polymer conformation tensor. The discretized formula of the FENE-P equations is written as,

$$\frac{\varsigma}{\Delta t}\boldsymbol{\alpha}^{n+1} = \sum_{j=0}^{2}(-\frac{a_j}{\Delta t}\boldsymbol{\alpha}^{n-j} + b_j\boldsymbol{N}_p^{n-j}) + \boldsymbol{C}_p - \frac{2}{\mathrm{Wi}}\frac{\boldsymbol{\alpha}^{n+1}}{1-\mathrm{tr}\boldsymbol{\alpha}^{n+1}/b}. \tag{6.12}$$

where $\boldsymbol{N}_p$ and $\boldsymbol{C}_p$ are the nonlinear and constant terms defined by,

$$\boldsymbol{N}_p \equiv -\boldsymbol{v}\cdot\boldsymbol{\nabla}\boldsymbol{\alpha} + \boldsymbol{\alpha}\cdot\boldsymbol{\nabla}\boldsymbol{v} + (\boldsymbol{\alpha}\cdot\boldsymbol{\nabla}\boldsymbol{v})^{\mathrm{T}} + \kappa\Delta^2\nabla^2\boldsymbol{\alpha}, \tag{6.13}$$

$$\boldsymbol{C}_p \equiv \frac{2}{\mathrm{Wi}}\frac{b\boldsymbol{\delta}}{b+2}. \tag{6.14}$$

Note that the last term in eq. (6.13) is a local artificial diffusion term adopted by Min *et al.* (2003); Dubief *et al.* (2005) to stabilize the simulation. However, the coefficient κ is set to 0 in all simulations included in the current study, as the extraordinary stability of the hybrid algorithm. We show this term in eq. (6.13) only for the convenience of comparison. Δ is the grid spacing.

In the FENE-P model, as polymers approach their maximum extension b, the relaxation term (i.e., the last term on the left-hand side of eq. (6.12)) becomes extremely high, which prevents the further stretching of the polymers. Therefore, the FENE-P model can automatically restrict polymer extension to its upper bound b.

However, due to the accumulated numerical errors, polymer extension may occasionally jump out of the range $[0, b]$ which would cause numerical instability. To resolve this problem, Vaithianathan *et al.* (2006); Dubief *et al.* (2005) proposed an elegant procedure where the relaxation term is treated implicitly. In this procedure, the constitutive equation of diagonal components of the conformation tensor $\boldsymbol{\alpha}$ are summed and reorganized as,

$$(\Phi^{n+1})^2 - (-\frac{\Delta t}{\eta b}\mathrm{tr}(\boldsymbol{R}_p^n) - \frac{2\Delta t}{\eta \mathrm{Wi}} + 1)\Phi^{n+1} + \frac{2\Delta t}{\eta \mathrm{Wi}} = 0, \tag{6.15}$$

where

$$\Phi^{n+1} = 1 - \mathrm{tr}(\boldsymbol{\alpha})^{n+1}/b, \tag{6.16}$$

$$\boldsymbol{R}_p^n \equiv \sum_{j=0}^{2}(-\frac{a_j}{\Delta t}\boldsymbol{\alpha}^{n-j} + b_j \boldsymbol{N}_p^{n-j}) + \boldsymbol{C}_p. \tag{6.17}$$

Equation (6.15) is a second order polynomial for Φ containing one positive root,

$$\Phi^{n+1} = \frac{B + \sqrt{B^2 + 4C}}{2} \tag{6.18}$$

where,

$$B = -\frac{\Delta t}{\eta b}\mathrm{tr}(\boldsymbol{R}_p^n) - \frac{2\Delta t}{\eta \mathrm{Wi}} + 1, \tag{6.19}$$

$$C = \frac{2\Delta t}{\eta \mathrm{Wi}}. \tag{6.20}$$

The positive root Φ^{n+1} is solved through eq. (6.18) and is substituted into eq. (6.12). Note that the extra operations to solve eq. (6.18) may slightly increase the computational cost, however, it is negligible comparing with the entire DNS procedure. Then the polymer conformation tensor $\boldsymbol{\alpha}^{n+1}$ can be advanced once the non-linear

term $\boldsymbol{N}_p$ in eq. (6.12) is computed. The procedure to obtain $\boldsymbol{N}_p$ will be discussed in section 6.2.2.

Spacial discretization of the polymer nonlinear term

Solving the nonlinear term $\boldsymbol{N}_p$(eq. (6.13)) in the FENE-P equation is crucial for the stability and accuracy of the simulation. There are three terms in $\boldsymbol{N}_p$: (i) the convection term $-\boldsymbol{v}\cdot\boldsymbol{\nabla\alpha}$, (ii) the stretching term $\boldsymbol{\alpha}\cdot\boldsymbol{\nabla v}+(\boldsymbol{\alpha}\cdot\boldsymbol{\nabla v})^{\mathrm{T}}$, and (iii) the LAD term $\kappa\Delta^2\nabla^2\boldsymbol{\alpha}$. They are treated separately and added together to obtain $\boldsymbol{N}_p$. Here, the treatment of these terms will be discussed.

For the stretching term, the velocity gradient $\boldsymbol{\nabla v}$ is computed prior in Fourier-Chebyshev-Fourier spectral space. Reverse transform is then implemented to get $\boldsymbol{\nabla v}$ in physical space which is then multiplied by $\boldsymbol{\alpha}$ to obtain the stretching term. For the LAD term, the second derivative of the conformation tensor, $\nabla^2\boldsymbol{\alpha}$, is discretized using a classical fourth-order centre difference scheme.

The treatment of the convection term requires more attention. In essence, there are a plethora of differentiation schemes that are elaborately designed for the pure convection problem. After testing the performance of several schemes in a benchmark problem (discussed in section 6.2.3), we choose a conservative second-order upwind TVD scheme considering the balance of efficiency and accuracy. In the TVD scheme, the convection term of each component of the conformation tensor α_{ij} can be written as,

$$\boldsymbol{v}\cdot\boldsymbol{\nabla}\alpha_{ij}=\boldsymbol{\nabla}\cdot(\boldsymbol{v}\alpha_{ij})=\sum_{k=0}^{3}\frac{\partial v_k\alpha_{ij}}{\partial x_k}. \tag{6.21}$$

Adopting the conservative form and let $F\equiv v_k\alpha_{ij}$ to be the numerical flux in direction

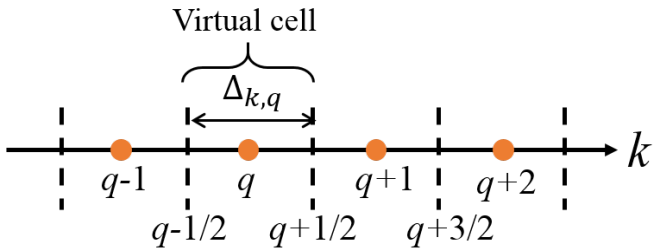

Figure 6.2: Schematic of grids and cells.

k, the convection term at the grid point q can be discretized as,

$$\frac{\partial v_k \alpha_{ij}}{\partial x_k}|_q = \frac{\partial F}{\partial x_k}|_q = \frac{F_{q+1/2} - F_{q-1/2}}{\Delta_{k,q}}. \tag{6.22}$$

where $[q-1/2, q+1/2]$ indicates a virtual cell that contains the grid point q at the center. Therefore, $F_{q+1/2}$ and $F_{q-1/2}$ are the numerical flux across the boundary of the cell. $\Delta_{k,q}$ is the size of the virtual cell q in k-direction. Figure 6.2 shows the 1D schematic of grids and cells. The convection term can be evaluated once the boundary numerical fluxes are obtained. Before adopting the TVD scheme to approach the boundary numerical fluxes, the Lax-Friedrichs flux splitting (LFFS) (Shu, 1998) should be applied to all of the grids and boundary numerical fluxes in order to achieve the upwinding feature of the algorithm. The LFFS splits a numerical flux $F_p = v_p \alpha_p$ at the position p (here, p can be any grids or cell boundaries, v_p and α_p are the velocity and conformation tensor at position p) into a positive flux F_p^+ (flux direction orients to the axis direction) and a negative flux F_p^- (flux direction is opposite to the axis direction), i.e.,

$$F_p = F_p^+ + F_p^-. \tag{6.23}$$

Here,

$$F_p^{\pm} = \frac{1}{2}(F_p \pm |v_{k,\max}|\alpha_p), \tag{6.24}$$

where $v_{k,\max}$ is the velocity with the maximal value. It is important to notice that $v_{k,\max}$ in eq. (6.24) will have different meanings along different axes. In x- and z-directions, the periodic feature of the flow is suitable for a global LFFS, i.e., $v_{k,\max}$ is the velocity with maximal value over all grid points in direction k. However, in the y-direction, the periodic feature is no longer satisfied. As the velocity changes greatly from the wall to the center, adopting the global LFFS in the y-direction could cause $|v_{k,\max}|\alpha_p \gg F_p$, which can introduce a strong numerical dissipation in the near-wall region (Delis *et al.*, 2000). To overcome this issue, a local LFFS procedure is implemented in y-direction. Here, $v_{k,\max}$ becomes the maximal velocity of all grid points in the stencil of a numerical scheme to approach the targeted boundary flux. For example, the stencil of the TVD scheme to approximate numerical flux at the cell boundary $q + 1/2$ is $[q-1, q, q+1, q+2]$, as shown in fig. 6.2. The definition of $v_{k,\max}$ guarantees $|v_{k,\max}| \geq v_p$, therefore, the direction of F_p^+ is positive while F_p^- is negative.

Positive and negative fluxes at boundaries of each virtual cell will be treated separately by using the MINMOD scheme (Roe, 1981; Zhang *et al.*, 2015) – one classical TVD scheme that has been proved to be a robust and stable scheme in DNS of polymeric turbulence (Yu and Kawaguchi, 2004) – and then summed to obtain the boundary flux. Here, we will take the $q + 1/2$ boundary for illustration, other boundary fluxes can be obtained likewise. For uniform grids, F^+ and F^- at $q + 1/2$

are approached by,

$$\begin{cases} F^+_{q+1/2} = F^+_q + \frac{1}{2}\phi(r^+_{q+1/2})(F^+_q - F^+_{q-1}), \\ F^-_{q+1/2} = F^-_{q+1} + \frac{1}{2}\phi(r^-_{q+1/2})(F^-_{q+1} - F^-_{q+2}). \end{cases} \tag{6.25}$$

In eq. (6.25), $F^+_{q+1/2}$ adopts a left bias local stencil $[q-1, q, q+1]$, whereas $F^-_{q+1/2}$ adopts a right bias local stencil $[q, q+1, q+2]$. The flux limiter function ϕ can have several forms, examples can be found in Sweby (1984); Waterson and Deconinck (2007); Zhang *et al.* (2015). The MINMOD scheme (Roe, 1981) defines the flux limiter function as

$$\phi(r) \equiv \max[0, \min(1, r)], \tag{6.26}$$

where r is the successive gradient ratio which estimates the smoothness of solution at current cell boundary. For $F^+_{q+1/2}$ and $F^-_{q+1/2}$,

$$r^+_{q+1/2} = \frac{F^+_{q+1} - F^+_q}{F^+_q - F^+_{q-1}} \quad \text{and} \quad r^-_{q+1/2} = \frac{F^-_q - F^-_{q+1}}{F^-_{q+1} - F^-_{q+2}}. \tag{6.27}$$

The definition of the flux limiter function ensures that $\phi(r)$ is in the range of $(0, 1)$. When the solution is smooth, $\phi(r)$ approaches 1, the numerical fluxes in eq. (6.25) will be evaluated by a 2nd-order upwind scheme, whereas at the discontinuity, $\phi(r)$ is close to 0 and eq. (6.25) reduces to a 1st-order upwind scheme.

For non-uniform mesh, e.g., the mesh in the y-direction, eqs. (6.25) and (6.27) are

modified accordingly to adapt to the changing grid spacing in flux interpolation,

$$\begin{cases} F^+_{q+1/2} = F^+_q + \frac{\Delta_{y,q}}{2}\phi(r^+_{q+1/2})\frac{F^+_q - F^+_{q-1}}{y_q - y_{q-1}} \\ F^-_{q+1/2} = F^-_{q+1} - \frac{\Delta_{y,q+1}}{2}\phi(r^-_{q+1/2})\frac{F^-_{q+1} - F^-_{q+2}}{y_{q+1} - y_{q+2}} \\ r^+_{q+1/2} = (\frac{F^+_{q+1} - F^+_q}{y_{q+1} - y_q})/(\frac{F^+_q - F^+_{q-1}}{y_q - y_{q-1}}) \\ r^-_{q+1/2} = (\frac{F^-_q - F^-_{q+1}}{y_q - y_{q+1}})/(\frac{F^-_{q+1} - F^-_{q+2}}{y_{q+1} - y_{q+2}}) \end{cases} \tag{6.28}$$

In eq. (6.28), y_q is the location of the grid point q. Note that the cell size $\Delta_{y,q}$ needs to be determined prior to the discretization. In this study, the non-uniform Chebyshev grids are adopted in y-direction as required by the pseudo-spectral discretization used for all other terms. To ensure that each grid point is located at the virtual cell's center, the size of each cell must satisfy

$$\Delta_{y,q} + \Delta_{y,q-1} = 2(y_q - y_{q-1}). \tag{6.29}$$

The sizes of the cells are determined once the first cell $\Delta_{y,0}$ (i.e., the cell that attaches to the top wall of the channel) is determined. We eventually decide to set $\Delta_{y,0}$ to 0 due to the characteristic of the Chebyshev grids. Under this definition, the wall grid point and the cell boundary of the points next to the wall are merged, i.e., $y_0 = y_{1/2}$, as shown in fig. 6.3. This implementation can significantly simplify the treatment of boundary conditions at the walls. More importantly, it gives a smoothly increasing cell size from the wall to the center of the channel which could be beneficial for the stability and convergence of simulations.

The overall procedure of HM is as follows. At the beginning of the time step n, the velocity gradient $\boldsymbol{\nabla v}$ is computed in the Fourier-Chebyshev-Fourier (spectral) space. Inverse Fourier and Chebyshev transforms are then implemented to transform the

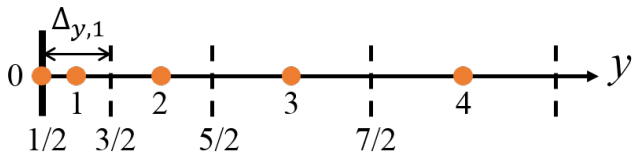

Figure 6.3: Schematic of grids and cells near the wall in y-direction.

velocity $\boldsymbol{v}$ and the velocity gradient $\boldsymbol{\nabla v}$ to physical space. Here, the convection term $\boldsymbol{N}$ of the momentum balance equation is directly computed at each grid point. For the FENE-P equations, the three components of the nonlinear term $\boldsymbol{N}_p$ (including $\boldsymbol{\alpha} \cdot \boldsymbol{\nabla v}$, $\boldsymbol{\nabla} \cdot (\boldsymbol{\alpha v})$, and $\nabla^2 \boldsymbol{\alpha}$) are respectively computed by following the procedures described above and then added together to obtain $\boldsymbol{N}_p$. Thus, the FENE-P equations are advanced in time (section 6.2.2) to update the polymer conformation tensor $\boldsymbol{\alpha}$. In the meantime, the polymer stress term $\boldsymbol{\tau}_p$ is also computed which is then transformed to spectral space to compute the polymer force term $\boldsymbol{\nabla} \cdot \boldsymbol{\tau}_p$. After that, the nonlinear terms ($\boldsymbol{\nabla} \cdot \boldsymbol{\tau}_p$ and $\boldsymbol{v} \cdot \boldsymbol{\nabla v}$) of the momentum balance equation (eq. (6.1)) are transferred to intermediate (Fourier-Physical-Fourier) space and then added together. The time advancement procedure to update the velocity field $\boldsymbol{\nabla v}$ starts by following Xi (2009).

The HM scheme is embedded into a custom MPI-parallelized DNS code (Channelflow 2.0) that was developed by Gibson *et al.* (2019); Gibson (2014) and extended for polymeric flows by Xi and Graham (2010b); Xi (2009) with the pure pseudo-spectral scheme. To validate the correctness and the performance of the current code, we apply it to the steady-state (SS) simulations and the streak transient growth (STG) (Schoppa and Hussain, 2002; Zhu and Xi, 2019) simulations and compare its performance with the pure pseudo-spectral scheme (Xi and Graham, 2012b). Note that to stabilize the simulations, we have to add a GAD to the SM cases of the steady-state simulations. The magnitude of GAD, $1/(\mathrm{ScRe})$, is set to 5.5×10^{-4} which is

smaller than the accepted magnitude of $O(10^{-2})$ for the IDT flow, as established by previous studies from various groups (Xi and Graham, 2010b; Sureshkumar *et al.*, 1997; Ptasinski *et al.*, 2003; Housiadas *et al.*, 2005; Li *et al.*, 2006). The Reynolds number performed in this study is $\mathrm{Re} = 3600$ and thus $\mathrm{Re}_\tau = 84.85$. The polymeric parameters b and β are fixed to 5000 and 0.97, respectively. Wi is varied in the range of $[1, 64]$ in order to access to different stages of the polymeric flow.

Table 6.2 summarizes the geometry and resolution of the 3D runs performed in this study. Here, "+" indicates quantities scaled by the friction velocity and viscous length scale, i.e., the inner unit. δ_x^+ and δ_z^+ are the constant grid sizes in x- and z-directions, whereas $\delta_{y,\mathrm{min}}^+$ and $\delta_{y,\mathrm{max}}^+$ are the minimum and maximum grids in the y-direction. N_x, N_y, and N_z are the number of the grids in x-, y-, and z-directions, respectively. Note the resolution adopted in the current steady-state simulations is significantly higher than those DNS in the literature (Zhu *et al.*, 2018; Xi and Graham, 2010a; Li *et al.*, 2005a). Such high resolution is required to resolve the EDT flows (Sid *et al.*, 2018). We also implement the 2D and 3D steady-state DNS to test the dependence of the mesh resolution in the IDT and EDT flows (section 6.4.1). The information of the 3D tested mesh is also summarized in table 6.2. Note that the 2D nature of EDT allows it to sustain in the 2D simulation (Sid *et al.*, 2018). Therefore, 2D DNS is also performed when testing the mesh dependence of the EDT flow, in order to reduce the computational cost. The geometry and resolution information of the 2D runs is summarized in Table 6.3.

	$L_x^+ \times L_z^+ \times L_y^+$	$N_x \times N_z \times N_y$	$\delta_x^+ \times \delta_z^+ \times \delta_{y,\min}^+/\delta_{y,\max}^+$
STG	$360 \times 250 \times 169.71$	$80 \times 95 \times 145$	$4.5 \times 2.66 \times 0.02/1.85$
SS(standard)	$360 \times 250 \times 169.71$	$128 \times 126 \times 131$	$2.81 \times 1.98 \times 0.025/2.05$
IDT resolution	$360 \times 250 \times 169.71$	$40 \times 46 \times 73$	$9.0 \times 5.43 \times 0.081/3.70$
		$64 \times 62 \times 109$	$5.63 \times 4.03 \times 0.036/2.47$
		$80 \times 94 \times 145$	$4.5 \times 2.66 \times 0.020/1.85$
		$128 \times 126 \times 217$	$2.81 \times 1.98 \times 0.0090/1.23$
EDT resolution	$720 \times 250 \times 169.71$	$128 \times 70 \times 97$	$5.63 \times 3.29 \times 0.045/2.78$
		$256 \times 70 \times 131$	$2.81 \times 3.29 \times 0.025/2.05$
		$512 \times 142 \times 185$	$1.41 \times 1.62 \times 0.012/1.45$

Table 6.2: Summary of geometry and mesh information for 3D DNS runs.

	$L_x^+ \times L_y^+$	$N_x \times N_y$	$\delta_x^+ \times \delta_{y,\min}^+/\delta_{y,\max}^+$
EDT resolution	360×169.71	288×97	$2.50 \times 0.045/2.78$
		288×369	$2.50 \times 0.0031/0.72$
		512×185	$1.41 \times 0.012/1.45$
		512×369	$1.41 \times 0.0031/0.72$
		512×731	$1.41 \times 0.00079/0.37$
		1280×369	$0.56 \times 0.0031/0.72$

Table 6.3: Summary of geometry and mesh information for 2D DNS runs.

6.2.3 Scheme performance for pure-convection problem

In this section, the performances of several schemes to deal with the convection term of the hyperbolic problem are discussed by involving them in a 1D pure-convection benchmark problem. The governing equation of the benchmark problem is,

$$\frac{\partial c}{\partial t} + \frac{\partial (vc)}{\partial x} = 0. \tag{6.30}$$

Equation (6.30) describes the time evolution of a concentration profile $c(x,t)$ with the convective velocity $v(x)$ (v is independent of time). The initial condition of c,

$$c(x,0) = \begin{cases} 1 & 0.1L < x \leq 0.3L \\ 0 & \text{else} \end{cases}, \tag{6.31}$$

is a square wave in the control domain with the length of $L = 2$. The roaming speed of the concentration profile is governed by the convective velocity,

$$v(x) = \begin{cases} 0.2 + 4(x - 0.5L)(0.9L - x) & 0.5L < x \leq 0.9L \\ 0.2 & \text{else} \end{cases}. \tag{6.32}$$

The varying velocity profile is used to mimic the real velocity field in the DNS which can never be a constant. In addition, both the concentration and velocity profiles satisfy the periodic condition as a prerequisite of SM. Figure 6.4 shows the initial concentration profile $c(x,0)$ and the convective velocity $v(x)$ of the benchmark problem. The positive convective velocity ensures that the concentration profile will gradually moves rightward. The periodic boundary condition is applied to domain boundaries (i.e. $x = 0$ and $x = L$). The time advancement of eq. (6.30) still uses the BDAB3

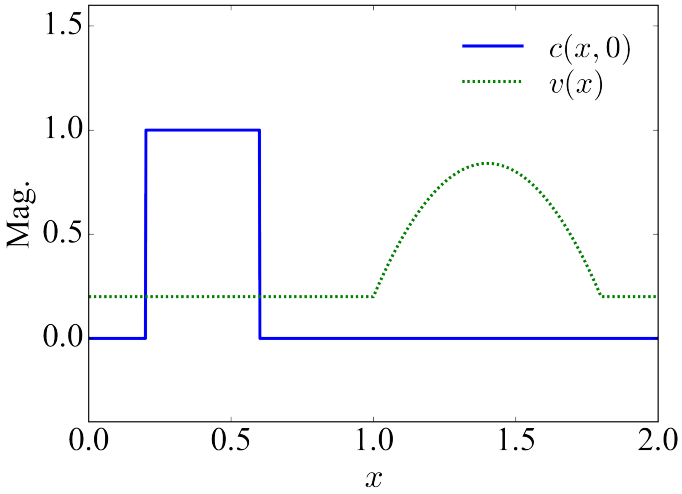

Figure 6.4: The initial concentration profile $c(x,0)$ and convective velocity $v(x)$ of the benchmark problem

scheme to be consistent with the DNS in this study, eq. (6.30) is thus rewritten as

$$\frac{\varsigma}{\Delta t}c^{n+1} = \sum_{j=0}^{k-1}(-\frac{a_j}{\Delta t}c^{n-j} + b_j(\frac{\partial(vc)}{\partial x})^{n-j}). \tag{6.33}$$

Five differentiate schemes are adopted to discretize the convection term $\partial(vc)/\partial x$: (I) a 2nd-order MINMOD TVD scheme (Sweby, 1984; Zhang *et al.*, 2015) (TVD), (II) a pseudo-spectral scheme (Sureshkumar *et al.*, 1997; Xi, 2009) (SM), (III) a 5th-order WENO scheme (Shu, 1998, 2009) (WENO), (IV) a 3rd-order compact upwind scheme (Min *et al.*, 2001; Dubief *et al.*, 2005) (CUD3), and (V) a 2nd-order upwind scheme (Zhang *et al.*, 2015) (UD2). A brief description of each scheme is summarized as follows, reader can also refer to (Sweby, 1984; Zhang *et al.*, 2015; Sureshkumar *et al.*, 1997; Xi, 2009; Shu, 1998, 2009; Min *et al.*, 2001; Dubief *et al.*, 2005) for more details and discussion of each scheme.

The TVD scheme implemented in the benchmark problem is consistent with that

described in section 6.2.2. The virtual cells are generated and the LLFS is applied. An uniform mesh is adopted in the benchmark case. The convection term at a grid point q is

$$\frac{\partial(vc)}{\partial x}|_q = \frac{F_{q+1/2} - F_{q-1/2}}{\Delta_q} = \frac{(F^+_{q+1/2} + F^-_{q+1/2}) - (F^+_{q-1/2} + F^-_{q-1/2})}{\Delta_q}. \tag{6.34}$$

Where $F^+_{q+1/2}$, $F^-_{q+1/2}$, $F^+_{q-1/2}$, and $F^-_{q-1/2}$ are the positive/negative numerical fluxes at the two boundaries of the virtual cell q according to eqs. (6.22) to (6.24), Δ_q is the size of grids. Numerical fluxes in eq. (6.34) are approached according to eqs. (6.25) to (6.27).

Same as the TVD scheme, the WENO and UD2 schemes also adopt the LLFS to guarantee the upwind feature. Differences between these schemes are the way they approach the numerical flux. The UD2 scheme utilizes a similar formula as eq. (6.25) except that the flux limiter function $\phi = 1$. Still, we will take the cell boundary $q + 1/2$ for illustration. The positive and negative fluxes at the $q + 1/2$ in the UD2 scheme are approximated by,

$$\begin{cases} F^+_{q+1/2} = F^+_q + \frac{1}{2}(F^+_q - F^+_{q-1}), \\ F^-_{q+1/2} = F^-_{q+1} + \frac{1}{2}(F^-_{q+1} - F^-_{q+2}). \end{cases} \tag{6.35}$$

For the WENO scheme, the positive/negative numerical fluxes are approached by the weighted sum of the three polynomials. Here, we only take the positive flux at $q + 1/2$ boundary for example,

$$F^+_{q+1/2} = w_1 F^{+,(1)}_{q+1/2} + w_2 F^{+,(2)}_{q+1/2} + w_3 F^{+,(3)}_{q+1/2} \tag{6.36}$$

where $F^{+,(1)}_{q+1/2}$, $F^{+,(2)}_{q+1/2}$, and $F^{+,(3)}_{q+1/2}$ are the 3rd-order polynomials to approximate $F^{+}_{q+1/2}$ using the grids in the local stencils $[q-2, q-1, q]$, $[q-1, q, q+1]$, and $[q, q+1, q+2]$, respectively. They are formulated as

$$\begin{cases} F^{+,(1)}_{q+1/2} = \frac{1}{3}F^{+}_{q-2} - \frac{7}{6}F^{+}_{q-1} + \frac{11}{6}F^{+}_{q}, \\ F^{+,(2)}_{q+1/2} = -\frac{1}{6}F^{+}_{q-1} + \frac{5}{6}F^{+}_{q} + \frac{1}{3}F^{+}_{q+1}, \\ F^{+,(3)}_{q+1/2} = \frac{1}{3}F^{+}_{q} + \frac{5}{6}F^{+}_{q+1} - \frac{1}{6}F^{+}_{q+2}. \end{cases} \tag{6.37}$$

In eq. (6.36), w_1, w_2, and w_3 are the weight of each polynomial and are determined by the smoothness analysis (Shu, 1998, 2009). The smoothness analysis measures the relative smoothness of the concentration profile in the local stencil of each polynomial. Essentially, a smoother concentration profile in the local stencil will give a larger weight. The polynomial is thus more influential in eq. (6.36) to approach $F^{+}_{q+1/2}$. The entire stencil adopted in the WENO scheme to compute $F^{+}_{q+1/2}$ (i.e., $[q-1, q, q+1, q+2]$) is left bias to reflect the upwind feature. For the negative flux $F^{-}_{q+1/2}$, a right-biased stencil is selected.

The CUD3 and SM schemes solve the FENE-P equations in a non-conservative form. Here, we also take the non-conservative form of eq. (6.30),

$$\frac{\partial c}{\partial t} + v\frac{\partial c}{\partial x} + c\frac{\partial v}{\partial x} = 0. \tag{6.38}$$

As the convective velocity (eq. (6.32)) is independent of time, the analytical solution of $\partial v/\partial x$ is fixed which is substituted into eq. (6.38) prior to the simulation. The $v\partial c/\partial x$ term is going to be solved by CUD3 and SM. In CUD3, $\partial c/\partial x$ is obtained by solving

$$(2-3s_q)(\frac{\partial c}{\partial x})_{q+1}+8(\frac{\partial c}{\partial x})_q+(2+3s_q)(\frac{\partial c}{\partial x})_{q-1}=\frac{6}{\Delta_x}((1-s_q)c_{q+1}+2s_qc_q+(1+s_q)c_{q-1}). \tag{6.39}$$

where s_q is the sign of velocity at the grid point q: $s_q = 1$ when $v_q \geq 0$, $s_q = -1$ when $v_q < 0$.

As for the SM scheme, $\partial c/\partial x$ is computed in Fourier space and is then inverse transformed to physical space and multiplied by v, hence,

$$\frac{\partial c}{\partial x} = \mathrm{FFT}^{-1}(2\pi i\xi\tilde{c}), \tag{6.40}$$

where FFT^{-1} stands for the inverse Fourier transform, i is the imaginary unit, and ξ is the wavenumber. Note that the artificial diffusion is not added to the SM scheme which is different from the real DNS.

The benchmark case adopts an uniform mesh with $\Delta_x = 1.95 \times 10^{-3}$. The time step is chosen to be $\Delta t = 1.95 \times 10^{-4}$ in order to satisfy the CFL condition. Figure 6.5 shows the concentration profiles at $t = 7$ obtained by different schemes. Note that the exact solution of the benchmark problem should preserve the shape of the initial condition, i.e., a square wave. In general, all methods are accurate for most of the domain except near the discontinuities. At the discontinuities, the UD2 scheme triggers a strong numerical oscillations. Therefore, it is essentially not suitable for the pure convection problem with sharp gradients. When using the SM scheme, high frequency oscillations are also triggered. Note that these oscillations could eventually lead to the breakdown of the real DNS. Despite the oscillations, the concentration profile approached by SM (without any AD) has a much sharper cliff edge comparing

Scheme	TVD	SM	UD2	WENO	CUD3
CPU time (s)	2.18	1.92	2.04	16.80	15.64

Table 6.4: CPU time required by each scheme to run a 10^4 time units benchmark simulation.

all these tested FDM schemes, reflecting its high-order accuracy. In fact, SM is still more accurate than those FDM schemes but is not stable without AD, whereas adding AD will change the governing equation. The TVD, CUD3, and WENO schemes all give an oscillation-free prediction but the resulting profiles are more tapered at the points of discontinuity. Compared with the TVD and the WENO schemes, CUD3 produces a profile that has a small bulge near the cliff edge. This numerical bulge may also threaten the stability of DNS and thus require an additional local artificial diffusion to stabilize simulations (Min *et al.*, 2001; Dubief *et al.*, 2005). Surprisingly, the 2nd-order TVD scheme performs as good as the 5th-order WENO scheme, as the gradient of TVD is only slightly lower. As regards the computation cost, the TVD scheme is much lower than that of WENO and CUD3, and is comparable to the efficient SM scheme. Table 6.4 lists the CPU time required by each scheme to run a 10^4 time units benchmark simulation. The TVD, SM, and UD2 schemes have a similar CPU time ($\sim 2s$) while the WENO and CUD3 schemes ($\sim 16s$) are about 8 times slower than the previous three schemes. In this study, we develop the HM scheme which applies the TVD scheme to deal with the convection term of the FENE-P equations, whereas other terms adopt the SM scheme. The HM scheme is intended to achieve a better compromise between accuracy, stability, and efficiency.

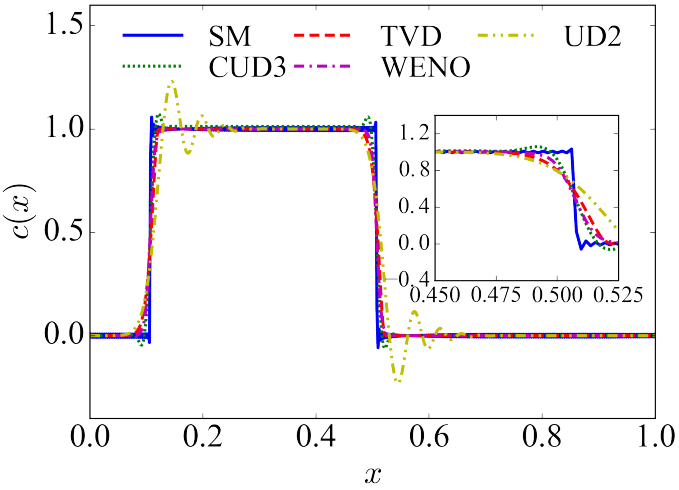

Figure 6.5: Comparison of the solutions to the benchmark problem at $t = 7$ using different spatial discretization schemes. Only the left half of domain, i.e. $(0, 1)$, are shown.

6.3 Results and Discussion

6.3.1 Scheme validation with STG simulation

The correctness of implementation of the hybrid SM-FDM scheme is tested by comparing a peseudo-spectral method (Xi and Graham, 2010b; Zhu *et al.*, 2018) without AD in a low elasticity STG simulation. The STG simulation is usually involved to study the transient evolution of turbulence. It enables a controllable way to generate well-defined flow structures, e.g. vortex, and is thus desirable for the direct comparison of different schemes. Details about the STG simulation can be found in Zhu and Xi (2019). The initial condition of the STG simulation for polymeric turbulence requires a velocity field and a polymer conformation tensor field. For the initial polymer conformation tensor, we set each diagonal component to 1/3 whereas the other components to 0 everywhere in the domain. For the initial velocity, we follow

the STG approach described by Zhu and Xi (2019): the velocity field consists of a perturbation and a base flow. The perturbation velocity is

$$v'_x = v'_y = 0, v'_z = A_p \sin(\alpha_p x) g(y), \tag{6.41}$$

where v'_x, v'_y and v'_z are the x-, y-, and z-components of the perturbation velocity, respectively. A_p is the perturbation amplitude and α_p is the streamwise wave number. $g(y)$ adds the wall-normal dependence to the perturbation

$$g(y) = y \exp\left(-\beta_g y^2\right), \tag{6.42}$$

where β_g is adjusted to obtain the maximum magnitude at $y^+ = 20$. The base flow formulates the mean flow of a turbulent boundary layer with the low- and high-speed streamwise streaks locating near the bottom wall of the channel, it has the definition of

$$U_b(y, z) = U_m(y) + U_s(z) g(y), V_b = W_b = 0, \tag{6.43}$$

where U_b, V_b, and W_b are the x-, y-, and z-components of the base flow. $U_m(y)$ is the mean velocity profile of a SS DNS at the same parameter settings. $U_s(z)g(y)$ defines a streamwise-invariant streaks which would not trigger turbulence by itself (Waleffe, 1997). The streaks are located at the bottom side of the channel and

$$U_s(z) = A_s \cos\left(\beta_s \left(z - z_\beta\right)\right). \tag{6.44}$$

β_g	A_s	β_s	A_p	α_p
9.0	3.0	125	0.071	360

Table 6.5: Parameters of the initial condition for STG simulations.

Here, A_s controls the magnitude of the spanwise undulation, β_s is the spanwise streak spacing, z_β is a spanwise phase parameter to adjust the spanwise location of the streaks. A summary of parameters to construct the initial velocity field is presented in table 6.5.

In order to ensure faithful solution from SM as a benchmark for comparison, we focus on low Wi = 1 that is below the onset of DR. At this Wi, a relatively stable solution and faithful can be obtained by the pseudo-spectral scheme without GAD. Note that setting GAD to 0 requires to have an infinite Sc which is numerically difficult by using the current SM architecture. Instead, we decide to choose a negligible GAD by setting the Schmidt number Sc = 10^5. For the hybrid scheme, neither the GAD nor the LAD is required.

In fig. 6.6, the time series of the root-mean-square (r.m.s) value of the Q quantity and the trace of the polymer conformation tensor tr($\boldsymbol{\alpha}$) in the STG simulations of HM and SM are compared. The Q quantity, initially proposed by Hunt *et al.* (1988), is a scalar criterion used to identify vortex structures in turbulent flows (Jeong and Hussain, 1995; Kolář, 2007). In the Q-criterion, vortices in incompressible fluid flow can be identified as regions where

$$Q \equiv \frac{1}{2}(\|\boldsymbol{\Omega}\|^2 - \|\boldsymbol{S}\|^2) > 0, \tag{6.45}$$

where $\boldsymbol{\Omega} \equiv \left(\boldsymbol{\nabla v} - \boldsymbol{\nabla v}^T\right)/2$ and $\boldsymbol{S} \equiv \left(\boldsymbol{\nabla v} + \boldsymbol{\nabla v}^T\right)/2$ are the vorticity and the rate-of-strain tensors, and $\|\cdot\|$ denotes the Frobenius tensor norm. In figs. 6.7 and 6.8, we also show the iso-surfaces of $Q = Q_{\text{rms}}$ and $\text{tr}(\boldsymbol{\alpha}) = \text{tr}(\boldsymbol{\alpha})_{\text{rms}}$ at the four moments that are marked by the square markers in fig. 6.6. Starting from the initial condition, the Q_{rms} profiles of the SM and HM cases gradually increase and reach the first peak at $t = 60$. In this period, the quasi-streamwise vortices sweep in the spanwise direction (fig. 6.7(a)). Their heads bend sideways to build spanwise bridges which eventually lift up and form the head of asymmetric hairpins (fig. 6.7(b)). After the peak, the Q_{rms} profiles of the two cases decrease until reaching a basin at $t = 100$ where the spanwise head of the asymmetric hairpins sheds their legs and starts to decay (fig. 6.7(c)). The profiles then rise up and reach a plateau. In this period, the legs of the original hairpins (i.e. quasi-streamwise vortices) grow stronger while their heads continuously decay. Eventually, the quasi-streamawise vortices become dominant in the flow domain (fig. 6.7(d)). As for $\text{tr}(\boldsymbol{\alpha})$, the profiles of the SM and HM cases quickly increase to a plateau starting from the initial condition, after which they barely change due to the low Wi chosen in the STG simulations.

Comparing the HM case with the SM case, the time trajectories of both Q_{rms} and $\text{tr}(\boldsymbol{\alpha})$ (fig. 6.6) are nearly the same without distinguishable differences. The vortex fields (identified by the Q-criterion in fig. 6.7) at the four picked time moments are also consistent between the two methods. The $\text{tr}(\boldsymbol{\alpha})$ fields (fig. 6.8) still look similar at $t = 30$ and 60. Accompanied with the well-organized streamwise and hairpin vortices, wave-like polymer structures are generated and sequentially align along the streamwise direction. At $t = 100$ and 160, in the narrow region between two nearby opposite-rotating vortices, polymers are drastically stretched by the vortices, which

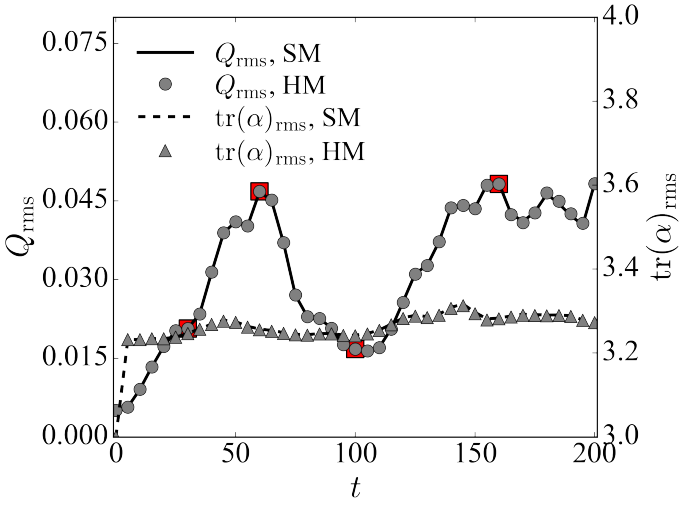

Figure 6.6: Time series of r.m.s of Q and $\mathrm{tr}(\boldsymbol{\alpha})$ in STG simulations. Data points corresponding to the snapshots shown in figs. 6.7 and 6.8 with red squares.

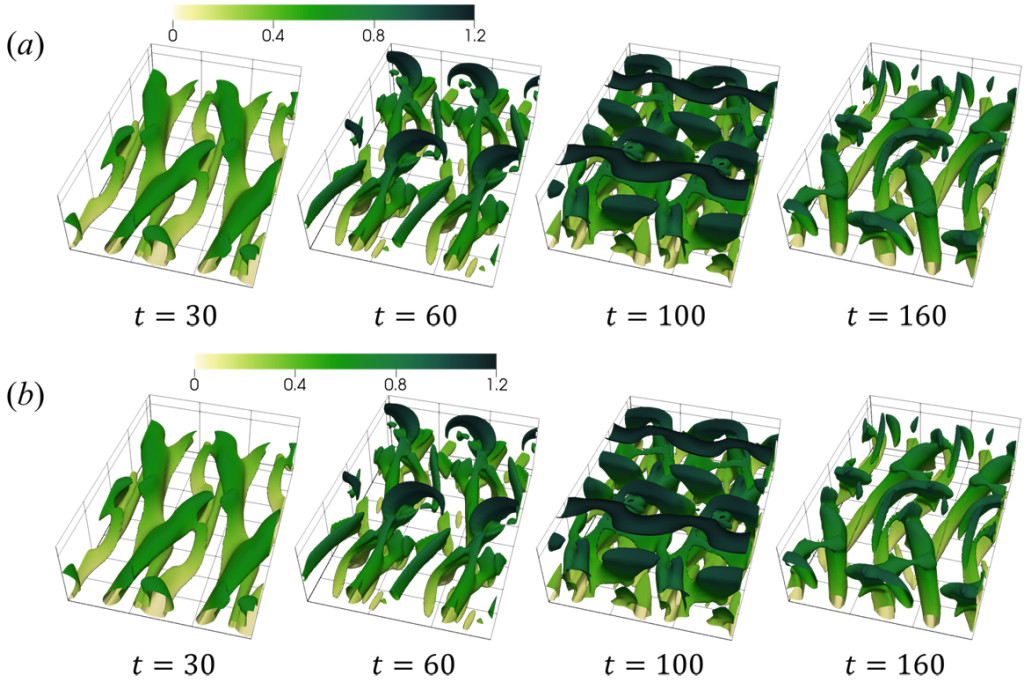

Figure 6.7: Vortex configuration identified by $Q = Q_{\rm rms}$ in STG simulations. Color varies from light to dark with the distance from the bottom wall.

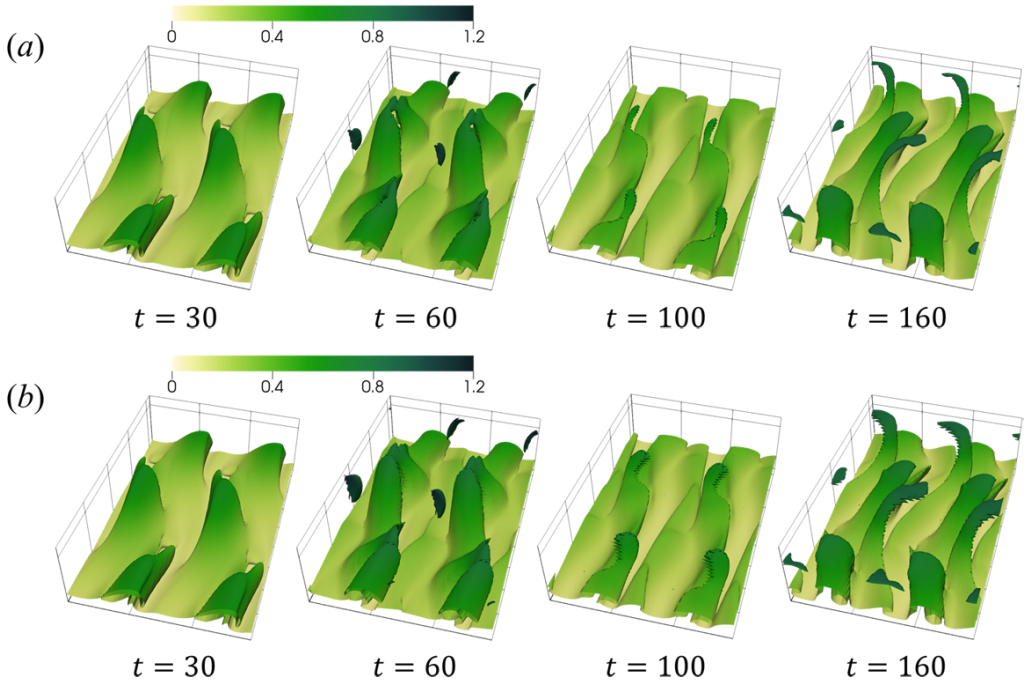

Figure 6.8: Iso-surfaces of polymer conformation identified by $\mathrm{tr}(\boldsymbol{\alpha}) = \mathrm{tr}(\boldsymbol{\alpha})_{\mathrm{rms}}$ in STG simulation. Color varies from light to dark with the distance from the bottom wall.

result in a sharp finger at the head of each wave-like structure. The finger-like structures indicate a sharp gradient of the polymer conformation tensor in these regions. It is thicker with jagged edges in the SM case (fig. 6.8(b)) in comparison with the smoother and thinner fingers obtained by HM (fig. 6.8(a)). These differences suggest the different performances of the pseudo-spectral and hybrid methods when encountering drastically changed $\boldsymbol{\alpha}$. It is well known that SM is generally not suitable for hyperbolic problems with a sharp gradient and will easily cause oscillations without special treatments (e.g. GAD). These oscillations could significantly affect the accuracy of the simulation. Even worse, it may break down the simulation as the accumulated errors become out of bounds. On the other hand, the hybrid method applies a stable FDM to deal with the convection term in the FENE-P equation (section 6.2.2) which performs better compared with the pseudo-spectral method. Despite the small differences in fig. 6.8, the strong similarity of results obtained by the HM and the SM schemes supports the correctness and suitability of the new scheme for polymeric turbulence.

6.3.2 Scheme validation with steady-state simulation

The steady-state simulation is also performed in this study. The hybrid scheme is compared with the pseudo-spectral scheme at two Wi which exhibit two qualitatively different turbulent flows: (i) an inertia-driven turbulence (IDT) at Wi = 23 and (ii) an elasticity-driven turbulence (EDT) at Wi = 64. IDT, in which inertia is mainly responsible for the generation and evolution of turbulence, is observed in polymeric flows with relatively low Wi and in Newtonian turbulence. The dynamics and statistics of polymeric flows at this stage share many common features with that

of Newtonian turbulence. For example, they are all dominated by streamwise vortices and streaks. Polymers in IDT are primarily responsible for suppressing turbulent intensity which leads to a reduction of turbulent friction drag. As Wi continuously increases, the IDT cannot solely sustain and will decay. In the meantime, instability caused by the elastic force starts to grow and eventually dominates the flow, leading to the elasticity-driven turbulence. Flow structures and statistics in EDT are significantly different from IDT. The flow field is dominated by spanwise vortices and sheet-like polymer structures. Note that the EDT flow mentioned here is conceptually similar to the EIT flow described by Samanta *et al.* (2013); Sid *et al.* (2018) who also claimed the pure elastic nature of the turbulent flows. EDT can sustain itself, e.g., in the 2D DNS (Sid *et al.*, 2018) or at a very low Re (far below the critical Re of laminar-turbulence transition). In addition, it can also coexist with IDT in the dilute polymeric flow. In this sense, turbulence is governed by both inertial and elastic forces.

The concept of EDT is relatively fresh comparing with the long-known IDT. One of the reasons is the introduction of GAD in the widely adopted SM which could smear polymer field and break near-wall EDT structures. Note that EDT is a strict 2D solution which is independent of the spanwise direction (Sid *et al.*, 2018). Therefore, it can sustain in the 2D geometry. However, to simplify the comparison with IDT, all of the simulations in this chapter are run in the 3D domain. Both HM and SM are applied to the steady-state simulation and can obtain a sustained IDT at Wi = 23. However, only HM can capture EDT at Wi = 64 while the SM cases directly relaminarize.

In fig. 6.9, the mean streamwise velocity profile (U^+ versus y^+) and the time-averaged log-law indicator function,

$$A^+ \equiv y^+ \frac{\partial U^+}{\partial y^+}, \tag{6.46}$$

are plotted. Note that the indicator function is obtained by taking the differentials of the log-law relationship of the mean velocity profile. It would have a flat region if the mean velocity profile has a log-law slope. As shown in fig. 6.9(a), the mean velocity profiles of the two IDT cases are consistent, which suggests a limited influence of GAD on the statistics of IDT. In the log-law layer ($y^+ > 30$), the two profiles are slight higher than the PvK log law due to the effect of polymers. Note that the IDT profiles are also consistent with the results reported by Xi and Graham (2010b) at a similar flow condition. In fig. 6.9(b), the log-law slopes of the two IDT cases are largely persevered as a flat region shows up. For the EDT case, the mean velocity profile is distinctly higher than the Virk's MDR. The indicator function does not show any prominent regions with log-law dependence, as demonstrated in fig. 6.9(b). The missing log-law relationship at high elasticity flows had been discussed by White *et al.* (2012), and was also observed at the HDR stage of IDT (Zhu *et al.*, 2018).

The normalized trace of the polymer conformation tensor is also presented in fig. 6.10. The two IDT profiles are largely similar, which suggests a reasonable prediction by SM at a low Wi. After the initial plateau near the wall ($y^+ < 10$), the IDT profiles quickly drop until reaching $y^+ = 30$ after which the decreasing speed drastically slows down. The profile of EDT is significantly higher than the IDT profiles in most of the channel. As it leaves the wall, a local maximum is firstly reached at $y^+ = 10$. After the peak, the profile continuously drops until it approaches 0 at the

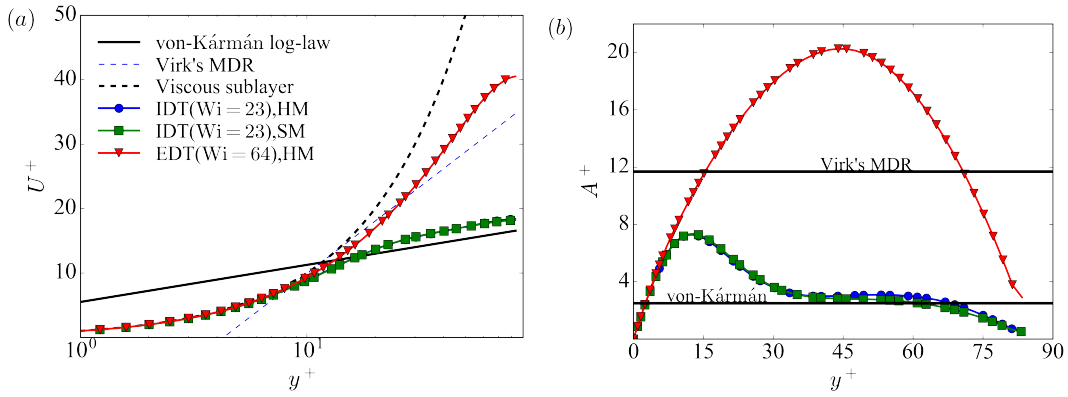

Figure 6.9: (a) Mean streamwise velocity (U^+) and (b) log-law indicator function (A^+) as functions of the wall distance y^+

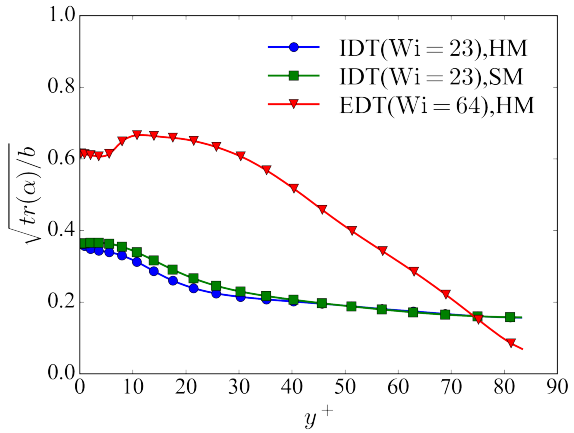

Figure 6.10: The square root of the normalized trace of polymer conformation tensor

center of the channel. The highly decreasing speed of the EDT profile suggests that EDT is intensive near the wall while weak in the center. Also note that the shape of the EDT profile is similar to the 2D EDT profile observed by Sid *et al.* (2018).

To understand the dynamics of IDT and EDT, we plot the time series of several selected quantities in figs. 6.11 to 6.13. The quantities monitored are: (a) instantaneous

log-law indicator function in the layer $20 \leq y^* \leq 30$, defined by

$$A^*_{20-30} \equiv \frac{1}{10}\int_{20}^{30} y^* \frac{\partial U^*}{\partial y^*} dy^* \tag{6.47}$$

(where "$*$" indicates quantities scaled by the instantaneous friction velocity and the instantaneous viscous length scale), (b) bulk-average Reynolds shear stress, $-(v_x'^* v_y'^*)_b$, (c) area-average wall shear rate, $\langle \partial v_x/\partial y \rangle_w$, (d) normalized trace of polymer conformation tensor, $\mathrm{tr}(\boldsymbol{\alpha})/b$, and (e) wall spatial-temporal shear rate patterns along $x^+ = 0$ (Xi and Graham, 2012b,a). Results on the bottom side of the channel are included. The choice is arbitrary but does not affect our discussions due to the symmetric geometry.

Comparing figs. 6.11 and 6.12, the time series of the two IDT cases share many common features. Variations of these quantities are strongly correlated and alternation between active and hibernating phases are clearly identifiable. In the active phase (e.g., $t = 1900$ in fig. 6.11 marked by the dash line), turbulence is highly intensive, the Reynolds shear stress ($-(v_x'^* v_y'^*)_b$) and the wall shear rate ($\langle \partial v_x/\partial y \rangle_w$) are thus high. Influenced by the strong turbulence, a lower magnitude of slope of the mean velocity profile (identified by A^*_{20-30}) is observed, reflecting the lower flow rate. In the meantime, polymers in active stage are significantly stretched ($\mathrm{tr}(\boldsymbol{\alpha})/b$ is thus high), indicating strong polymer activity in this stage. Note that in IDT, polymers is mainly responsible for the suppression of turbulence. Due to the strong effect of polymers, the intensity of turbulence starts to drop and the flow transfers to the hibernation state (e.g., $t = 1650$ in fig. 6.11 marked by the solid line). Comparing with the active phase, $-(v_x'^* v_y'^*)_b$, $\langle \partial v_x/\partial y \rangle_w$, and $\mathrm{tr}(\boldsymbol{\alpha})/b$ in the hibernation phase are lower, whereas A^*_{20-30} is higher.

In fig. 6.11(e) and fig. 6.12(e), the wall shear rate $\partial v_x/\partial y$ along one spanwise line $x = 0$ (z-axis) on the bottom wall is also plotted against time (t-axis). As the streak moves forward by convection in the periodic box, the sensor at $x = 0$ will be detecting different parts of the streak and the resulting signal varies periodically even though the streak is not changing in time. In both IDT cases, lighter and darker quasi-streamwise bands are found lying alternatively in the z-direction, which corresponds to the high- and low-speed streaks, respectively. In the t-direction, there are also alternative lighter-darker intervals occur on each high-speed streak, which corresponds to the alternative occurrence of the active/hibernation stages. The blurry areas (such as the one near $t = 6000$) are the hibernation turbulence, as the variation between low- and high-speed streaks has less contrast. As for the active turbulence, the contrast becomes higher.

The EDT time series (Wi = 64, fig. 6.13) are significantly different from IDT. The mean velocity slope A^*_{20-30} is mostly higher than the Virk's MDR. The Reynolds shear stress $-(v'^*_x v'^*_y)_b$ is one-order smaller than IDT. The wall shear stress $\langle \partial v_x/\partial y \rangle_w$ has a similar value comparing with IDT but the variation is small (unlike the strong variation between the active and hibernation stages in IDT). Note that other measured EDT quantities also have small variation, but they are at least one order of magnitude smaller than the IDT cases. Important differences can be seen in the spatial-temporal shear rate pattern. The EDT case does not have a clear streamwise streak (note that the range of the color bar in fig. 6.13 is narrower comparing with figs. 6.11 and 6.12). Also, the pattern is highly oscillated along the t axis, reflecting the fast variation of the flow structures.

The instantaneous flow structures in IDT obtained by the HM and SM schemes

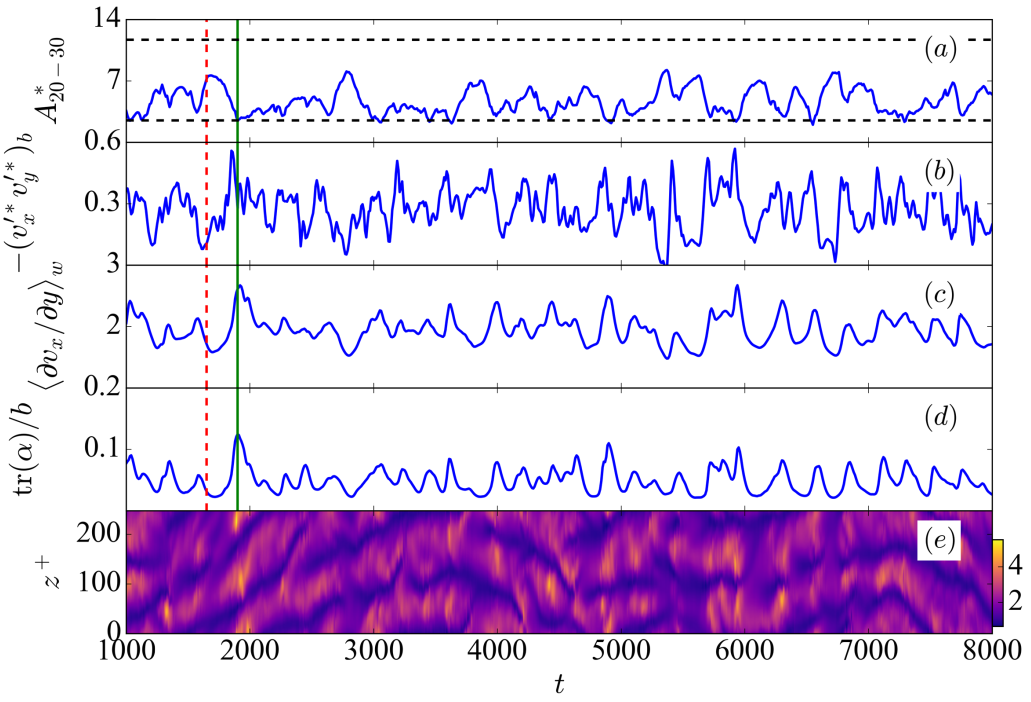

Figure 6.11: Time series of IDT at Wi = 23 obtained by the HM scheme. From top to bottom: (a) instantaneous log-law indicator function in the layer $20 \leq y^* \leq 30$; (b) bulk-average Reynolds shear stress; (c) area-average wall shear rate; (d) normalized trace of polymer conformation tensor; (e) the wall spatial-temporal shear rate patterns along $x^+ = 0$. The vertical solid and dash lines respectively mark an instance of active and hibernation turbulence.

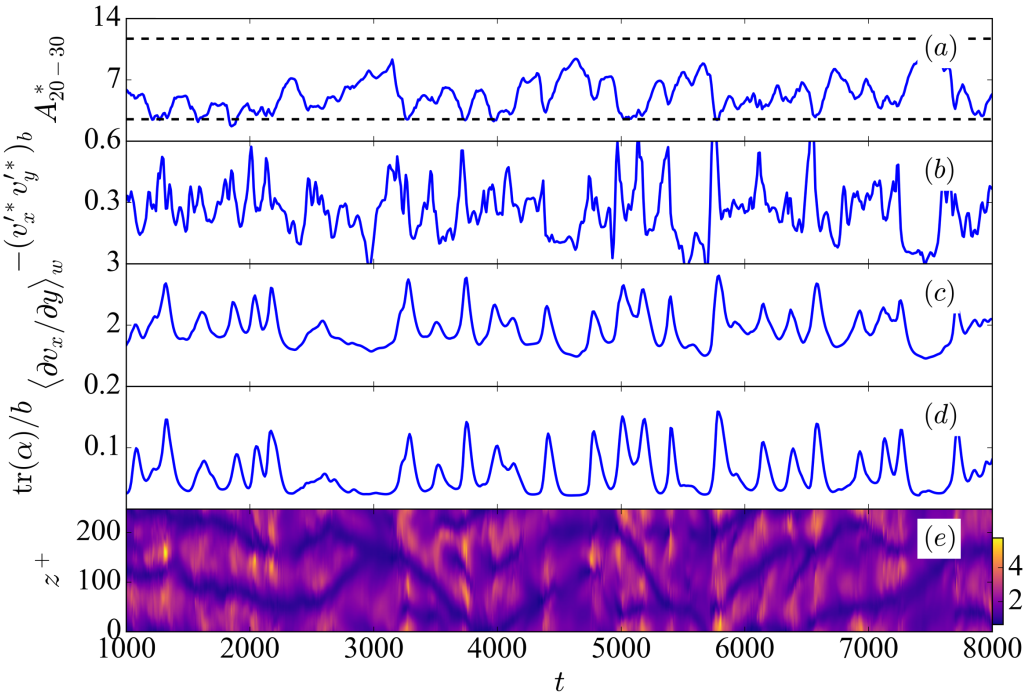

Figure 6.12: Time series of IDT at Wi = 23 obtained by the SM scheme. From top to bottom: (a) instantaneous log-law indicator function in the layer $20 \leq y^* \leq 30$; (b) bulk-average Reynolds shear stress; (c) area-average wall shear rate; (d) normalized trace of polymer conformation tensor; (e) the wall spatial-temporal shear rate patterns along $x^+ = 0$.

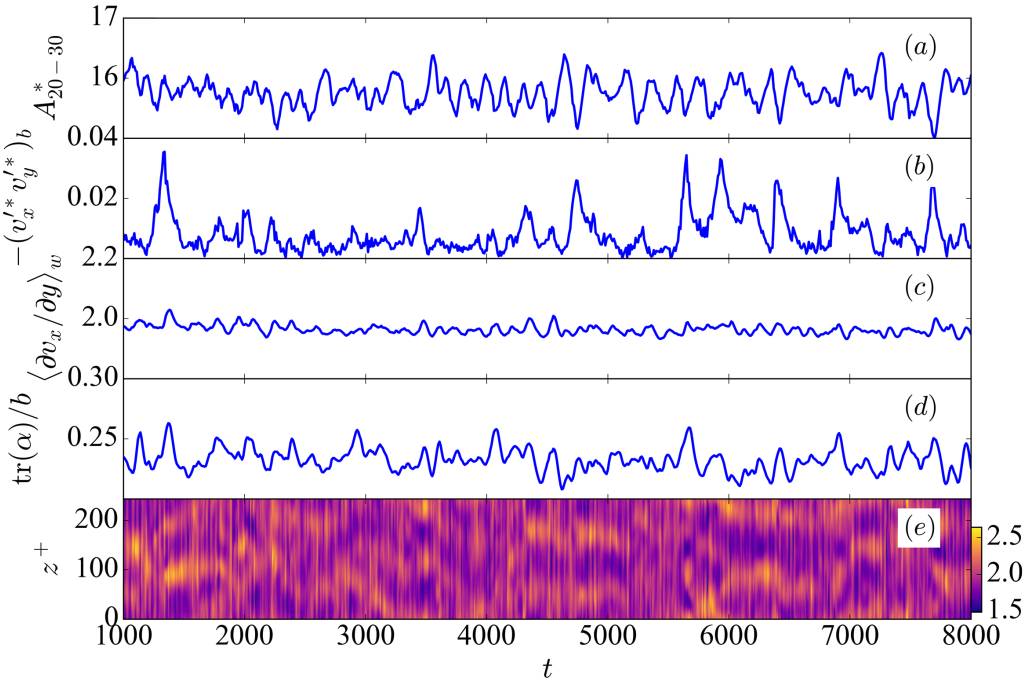

Figure 6.13: Time series of EDT at Wi = 64 obtained by the HM scheme. From top to bottom: (a) instantaneous log-law indicator function in the layer $20 \leq y^* \leq 30$; (b) bulk-average Reynolds shear stress; (c) area-average wall shear rate; (d) normalized trace of polymer conformation tensor; (e) the wall spatial-temporal shear rate patterns along $x^+ = 0$.

are visualized in fig. 6.14. As mentioned by Xi and Graham (2012b), the IDT flow at a relatively high Wi can alternate between two distinctly different stages, i.e., the active and hibernation stages. In the active stage, the intensity of turbulence is high, strong streamwise vortical structures occupy the entire domain (fig. 6.14(a) and (b)). Polymers in this stage also become highly stretched which start to suppress the intensive turbulence. Due to the influence of the polymers, most of the vortices in the flow will be killed, and the flow will become quiescent, indicating the occurrence of the hibernation stage (fig. 6.14(c) and (d)). Both HM and SM are able to capture phase alternation between the active and hibernation stages. The vortical structures obtained by the two schemes are also similar: they align along the streamwise direction with the upstream side (also called "leg") attaching to the wall while the downstream side ("head") lifting up. Interestingly, in the hibernation stage, vortices tend to form a vortex string as the head of upstream vortices connects with the leg of downstream vortices. This type of vortex configuration was also observed by Zhu *et al.* (2018) and was corresponding to one of the known self-sustaining cycles of turbulence – the "parent-offspring" cycle. This cycle is believed to be the dominant mechanism to maintain turbulence in the HDR stage (Zhu *et al.*, 2018).

Despite the overall similarity of vortical structures between HM and SM, differences can be observed in the polymer extension (measured by $\mathrm{tr}(\boldsymbol{\alpha})/b$) contours (fig. 6.14). In the active stage, the polymer extension contours obtained by the two schemes are similar. This similarity may due to the rapidly changing of local velocity field caused by the intensive vortical structures. In this case, a local region of high polymer stress gradient will soon been destroyed by a different local velocity field which minimizes the effect of artificial diffusion in the SM scheme. However, in the

hibernation stage, the flow is quiescent and the IDT vortices are weak. The turbulent convection is thus weak and the influence of GAD is amplified. Especially, in the turbulent inner layer ($y^+ < 10$), the high gradient of polymer conformation can lead to a strong AD under the same Sc. As a result, the extension of polymers changes faster in the HM case than the SM case as it leaves the wall. Note that the EDT-like structures were also observed in the IDT-dominated flow fields by Zhu *et al.* (2019). In the HM case, we can also observe the sheet-like EDT polymer structures near the wall. However, these EDT-like structures are restricted in the turbulent inner layer and have a negligible influence on the vortex dynamics. On the other hand, the spanwise vortical structures that are typically observed in EDT flows, do not show up in the current HM IDT flow. In the SM case, the sheet-like structures are completely eliminated due to the effect of GAD. Despite these differences between HM and SM, we note that the nature of the self-sustaining process has not been changed by GAD in the SM case. In both HM and SM, the active-hibernation process is observed with similarly vortical structures.

Figure 6.15 shows the instantaneous flow structures at the EDT state. Note that EDT is captured by HM only. The vortical structures of EDT are spanwise-like which are greatly different from the IDT vortices. Spanwise vortices were also reported by Samanta *et al.* (2013) and are widely accepted as the characteristic structures of EDT. In addition, unlike the IDT vortices which often extend to the center of the channel (at least in the active stage of IDT), the EDT structures prefer to attach to the wall. This is also supported by observations in the polymer extension contour that the sheet-like polymer structures concentrate in the near wall region.

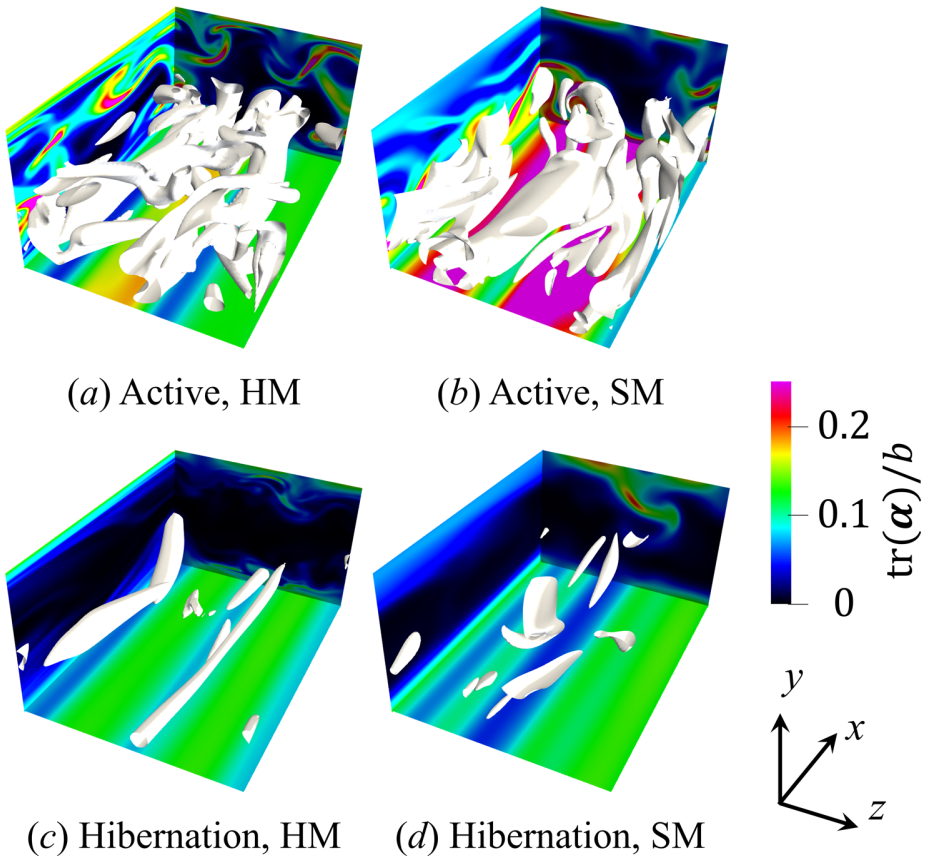

Figure 6.14: Instantaneous flow structures in IDT captured by the HM and SM schemes: (a) active turbulence by HM; (b) active turbulence by SM; (c) hibernation turbulence by HM;(d) hibernation turbulence by SM. Iso-surfaces are vortices identified by $Q = 0.008$. Only vortices in the bottom half of the channel are presented. Color contours are polymer extension normalized the maximum extension b, $\mathrm{tr}(\boldsymbol{\alpha})/b$.

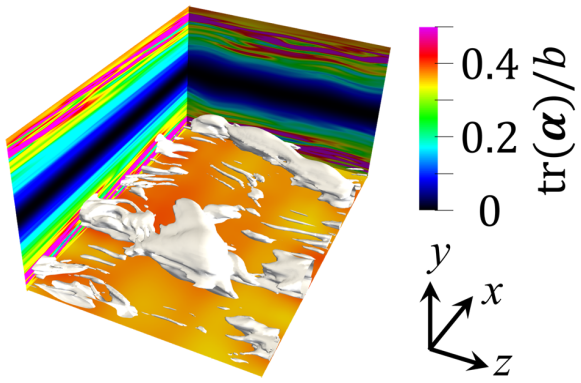

Figure 6.15: Instantaneous flow structures in EDT captured by the HM scheme. Iso-surfaces are vortices identified by $Q = 0.008$. Only vortices in the bottom half of the channel are presented. Color contours are polymer extension normalized the maximum extension b, $\mathrm{tr}(\boldsymbol{\alpha})/b$.

In fig. 6.16, we show the one-dimensional spectra of the streamwise velocity fluctuation and the x-diagonal component of the polymer conformation tensor, as respectively defined by

$$E_{u,b}(k_x) = \frac{1}{2l\Delta T}\int_{\Delta T}\int_{2l}\int_{k_z} \tilde{v}_x'^{\circledast}\tilde{v}_x' dk_z dy dt, \tag{6.48}$$

$$E_{\alpha,b}(k_x) = \frac{1}{2l\Delta T}\int_{\Delta T}\int_{2l}\int_{k_z} \tilde{\alpha}_{xx}'^{\circledast}\tilde{\alpha}_{xx}' dk_z dy dt, \tag{6.49}$$

("$\circledast$" indicates the complex conjugate and ΔT is the time averaging window). In fig. 6.16(a), the velocity spectra of the two schemes merge in the large-scale regime but differ in the small-scale regime. That is, only the small-scale flow structures are changed when adding GAD to the SM scheme, whereas the large-scale flow structures can be largely preserved. Recall that IDT is driven by the large-scale structures.

Thus the influence of GAD on the dynamics of IDT is mild. In fig. 6.16(b), difference between the HM and SM cases is larger. The spectrum profile of the SM case is generally lower than that of the HM case due to the dissipation caused by GAD. Also, note that the two profiles are close in the large-scale regime but distinctly disparate in the small-scale regime. Therefore, GAD is more efficient to dissipate the small-scale elastic structures, which is consistent with observations in Sid *et al.* (2018).

As for EDT, small-scale elastic structures are responsible for the evolution of turbulence (Dubief *et al.*, 2013; Sid *et al.*, 2018). As GAD can dissipate most of the small-scale elastic structures, it will lead to the relaminarization of flow. In fig. 6.16, only the sustained EDT obtained by HM are presented. The spectrum profile of the conformation tensor of EDT is much higher than the IDT profiles, indicating a large amount of elastic energy is stored in the polymers. The spectrum profile of the streamwise velocity of EDT is far below the IDT profiles, suggesting its weaker turbulent intensity. In the small-scale regime, the EDT profile slightly shifts up which may be attributed to the insufficient resolution to resolve those extremely sharp gradient in the polymer conformation field. However, the resolution adopted by current study ($\delta_x^+ \times \delta_z^+ \times \delta_{y,min}^+/\delta_{y,max}^+ = 2.81 \times 1.98 \times 0.025/2.05$) is already significantly smaller than previous studies on IDT (Li *et al.*, 2015; Xi and Graham, 2010b) and is comparable with other studies on EDT (Dubief *et al.*, 2013; Samanta *et al.*, 2013; Shekar *et al.*, 2019). In fact, the mesh size to fully resolve the sharp gradients is much smaller than what is computationally feasible, as Sid *et al.* (2018) mentioned that the EDT structures have infinite small scales.

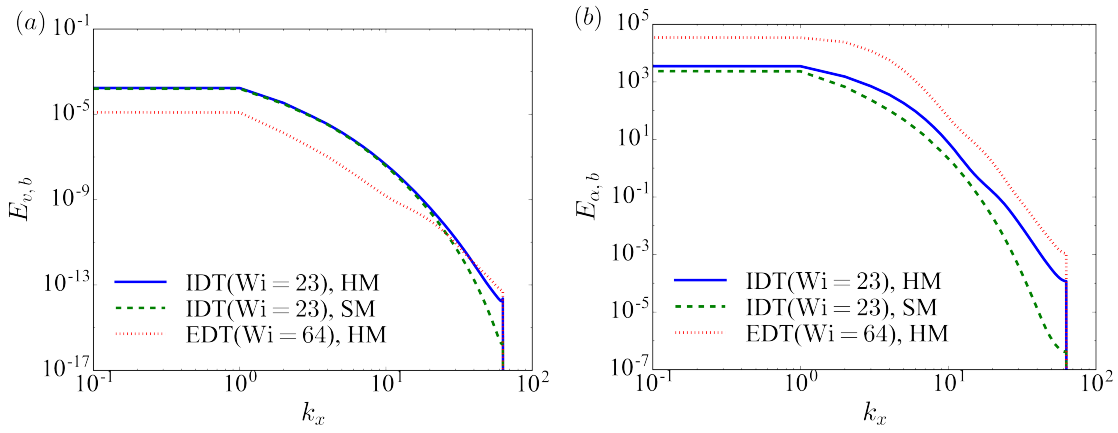

Figure 6.16: The one-dimensional spectra of (a) the streamwise velocity, and (b) the x-diagonal component of the polymer conformation tensor.

6.4 Impact of artificial diffusion

From section 6.3.2, it is found that the additional GAD required by SM damps the small-scale structures but its influence on the dynamics of turbulent flows depends on the immediate state (i.e., EDT or IDT). For IDT, the existence of GAD suppresses the EDT-like structures and decreases the energy in the small scales. However, its influence on the large scales of turbulence is minor. Since IDT is driven by large-scale structures, it will not be significantly changed by GAD. On the other hand, the EDT state is known to be governed by small-scale structures (Sid *et al.*, 2018; Dubief *et al.*, 2013). As GAD is efficient to suppress small-scale structures, EDT is thus significantly erased.

Another factor that affects the roles of GAD in polymeric turbulence is the different influence regions. In fig. 6.17, we plot the average magnitude of the GAD term and the polymer convection term at different wall distance. Here, the GAD

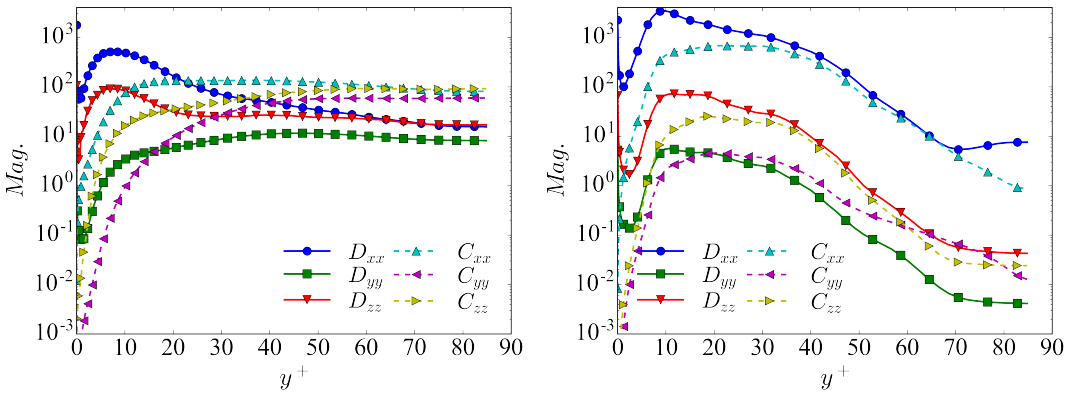

Figure 6.17: Magnitude of diffusion and convection terms in the FENE-P equations (eq. (6.3)) of (a) IDT (Wi = 23) and (b) EDT (Wi = 64), as a function of y^+.

magnitude, defined as

$$\boldsymbol{D} = \frac{1}{\mathrm{ScRe}}|\boldsymbol{\nabla}^2\boldsymbol{\alpha}|, \tag{6.50}$$

(Sc = 0.5 is consistent with the current steady-state simulation using SM) is added to the IDT and EDT solutions of the HM scheme, respectively. The average magnitude of GAD is then obtained by taking average in the x-, z-, and t-dimensions. The three diagonal components of GAD, i.e., D_{xx}, D_{yy}, and D_{zz}, are plotted in fig. 6.17. For comparison, we also compute and plot the magnitude of the three diagonal components (C_{xx}, C_{yy}, and C_{zz}) of the FENE-P convection term in eq. (6.3),

$$\boldsymbol{C} = |\boldsymbol{v}\cdot\boldsymbol{\nabla}\boldsymbol{\alpha}|. \tag{6.51}$$

In the IDT flows (fig. 6.17(a)), the xx- and zz-components of GAD initially increase after leaving the wall and reach a peak at $y^+ \approx 10$. After the peak, the profiles steadily drop till the center of the channel. For the yy-component, after the initial

increase, the profile reaches a plateau and becomes flat afterward. Compared with the diffusion profiles, the convection profiles have a smaller magnitude in the inner layer ($y^+ < 20$) but a much higher magnitude as they approach the channel's center. It is well-known that IDT structures, e.g. the vortex, are generated in the buffer layer ($20 < y^+ < 30$) and are highly active in the log-law and even higher region (Robinson, 1991; Adrian *et al.*, 2000). As GAD is much weaker outside the inner layer, its influence on the IDT structures is minimized. The flow field outside the inner layer is still dominated by turbulent convection. In the inner layer, EDT-like structures can also show up in high Wi IDT flow. However, the strong magnitude of GAD in this region can significantly suppress the EDT-like structures. Therefore, these EDT-like structures are not observed in the SM case.

On the other hand, the shape of the convection and diffusion profiles in EDT flows is similar. After leaving the wall, the convection profiles will first reach a local minimum at $y^+ = 3$. After that they increase along with the convection profiles to a plateau at $y^+ = 10$ and then quickly drop after $y^+ = 40$. Note that the mean velocity of the EDT flow continuously increases as it leaves the wall. Hence the decreasing of the convection profiles is mostly due to the the drastically dropping $\boldsymbol{\nabla\alpha}$. It is well-known that the strong gradient of the polymer conformation tensor is responsible for the generation of EDT structures (Sid *et al.*, 2018). Therefore, the decreasing convection profiles indicate that EDT is intensive near the wall while weaker at the center of the channel, which agrees with previous observations (figs. 6.10 and 6.15). Across the entire channel, the xx- and zz-components of the GAD profiles are everywhere higher than the convection profiles. Especially, in the near-wall region ($y^+ < 20$) where GAD is one-order of magnitude larger than the convection term.

Thus it will significantly smear the strong $\boldsymbol{\nabla\alpha}$ in this region and suppress the EDT structures. The EDT flow is thus vulnerable to GAD in comparison with IDT which also explains why EDT is hard to be captured by the SM scheme.

6.4.1 Effect of mesh resolution

Depending on the flow state (IDT or EDT), the required mesh resolution to obtain a numerically-converged solution is different. Thus we will discuss the effect of resolution in the two flow types separately.

For IDT, we test the resolution dependence of four mesh sizes, as summarized in table 6.2. Despite the mesh, other parameters of the four test cases are the same as that of the standard IDT case in section 6.3.2. The profiles of the bulk one-dimensional spectra of the streamwise velocity $E_{v,b}$, the mean velocity U^+, the Reynolds shear stress $-\langle v_x^+ v_y^+ \rangle$, and the square root of the normalized trace of polymer conformation tensor $\sqrt{\mathrm{tr}(\boldsymbol{\alpha})/b}$ (which is proportional to the average end-to-end distance of polymer chains) at different resolutions are plotted and summarized in fig. 6.18. In general, all of the statistical quantities agree well, suggesting that the lowest mesh size ($40 \times 73 \times 46$) can obtain a numerical converged solution. Note that the lowest resolution is similar to those adopted in the pseudo-spectral DNS by Xi and Graham (2010b); Zhu *et al.* (2018). Hence, the current hybrid scheme largely preserves the precision of SM. As to more detailed observations, the $E_{v,b}$ profiles (fig. 6.18(a)) and the $-\langle v_x^+ v_y^+ \rangle$ profiles (fig. 6.18(c)) of the four cases collapse well onto one another. As the resolution increases, the U^+ profiles (fig. 6.18(b)) and the $\sqrt{\mathrm{tr}(\boldsymbol{\alpha})/b}$ profiles (fig. 6.18(d)) from different resolution fluctuates within a very small range without any obvious pattern. This fluctuation may be due to the statistical uncertainty of

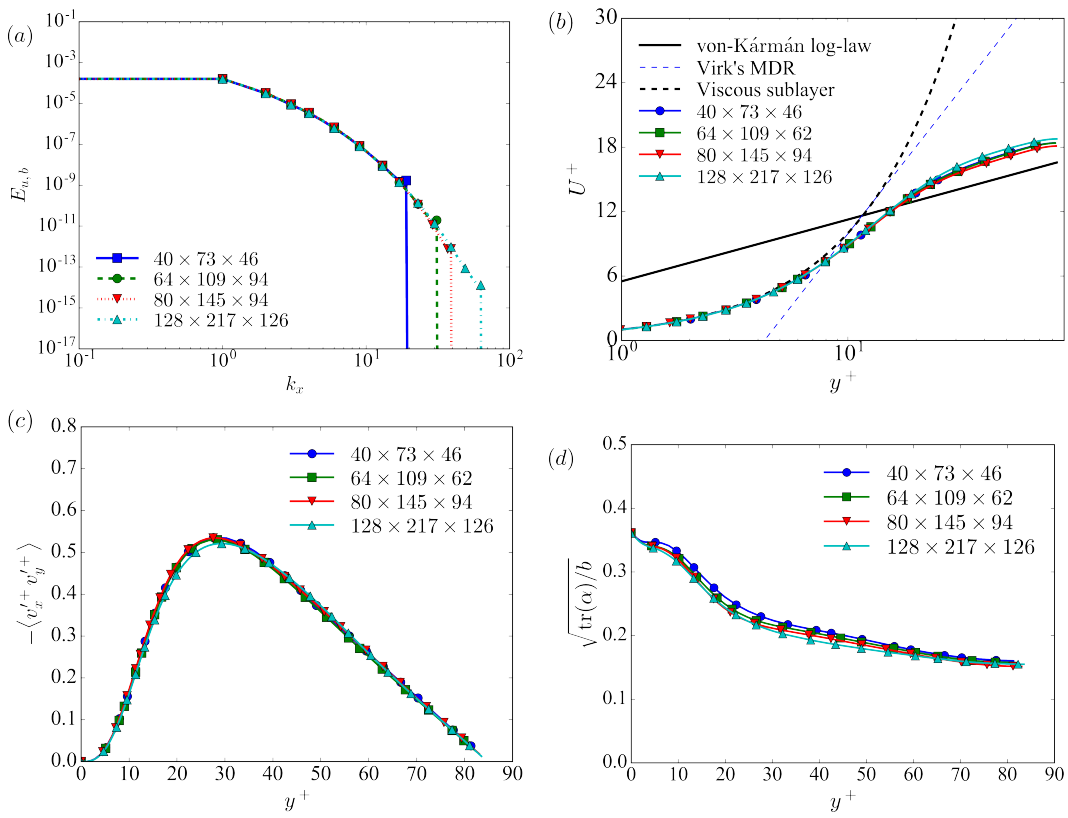

Figure 6.18: Statistical quantities of IDT (Wi = 23) at different mesh sizes: (a) the bulk one-dimensional spectra of the streamwise velocity, (b) the mean velocity profile, (c) the Reynolds shear stress, and (d) the square root of the normalized trace of polymer conformation tensor.

measurement.

As for the EDT flows, strictly converged solutions are difficult to be achieved as the elastic structures have infinitely small scales (Sid *et al.*, 2018). The resolution dependence of EDT in the 2D DNS was tested by Sid *et al.* (2018) who found that energy of the small-scale structures can pile up at the end of the spectrum and change the shape of the spectrum. This effect will confine to smaller scales as the resolution increases. Eventually, the large scales of the energy spectrum can converge under a significantly high resolution. In Sid *et al.* (2018)'s study, $N_x \times N_y = 1280 \times 384$

for the box size of $L_x^+ \times L_y^+ = 720 \times 169.71$ is found to have a converged large-scale spectrum and can provide a reasonable prediction. However, this resolution is already difficult to achieve in 3D DNS due to the extremely high computational cost. To have a reasonable mesh resolution, we tested a series of different mesh sizes in both 2D and 3D simulations. Details about the geometry and mesh of the test runs are listed in tables 6.2 and 6.3. Note that the box size is chosen to be the same as that in (Sid *et al.*, 2018; Zhu *et al.*, 2019).

Figure 6.19(a) and (b) show the streamwise velocity spectra of 2D EDT cases with variate N_y and N_x, respectively. In the y-direction (fig. 6.19(a), $N_x = 512$ is fixed), profiles in the small-scale regime do not converge even at the highest resolutions but the large scales of the profiles converge at $N_y = 369$ (in fact the $N_y = 185$ case is also considerably close to the converged solution), which agrees with the earlier observations by Sid *et al.* (2018). Moreover, after comparing the N_y dependence at different N_x (not shown here), we find that the minimum N_y for numerical convergence is independent of N_x. In the x-direction (fig. 6.19(b), $N_y = 269$ is fixed), the profiles do not converge until $N_x = 1280$ even in the large-scale regime. In fact, at such resolution, the grid size is already 10 times finer than that of traditional DNS for IDT (e.g., (Yu and Kawaguchi, 2004; Li *et al.*, 2005a; Housiadas *et al.*, 2005; Wang *et al.*, 2017; Li *et al.*, 2015; Zhu *et al.*, 2018)). It is difficult to implement 3D DNS under such high resolution as tremendous computational resources are needed. Fortunately, by carefully controlling the $N_x - N_y$ ratio, the spectra could sufficiently converge in the large-scale regime.

Here, we use the $N_x \times N_y = 1280 \times 369$ case as a benchmark which is sufficient close to the converged solution since further increasing mesh size (without fixing the mesh

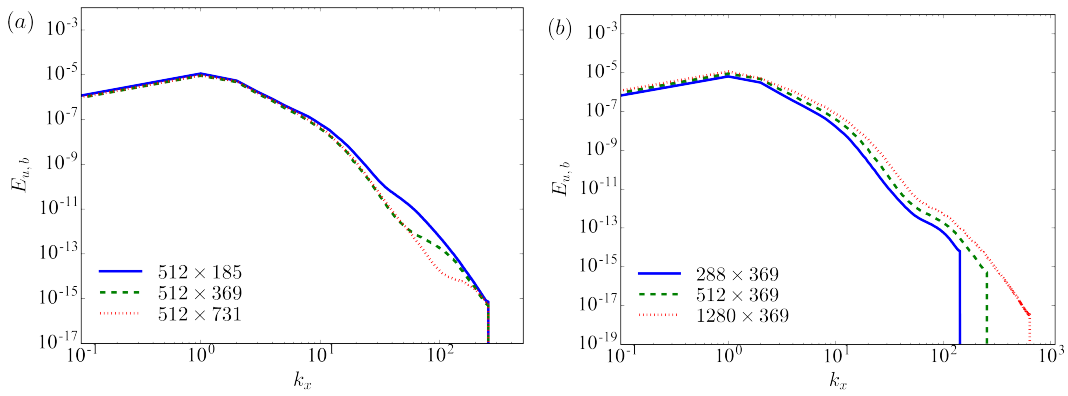

Figure 6.19: The bulk one-dimensional spectra of the streamwise velocity of 2D DNS ($\mathrm{Re}_\tau = 84.85$, $\mathrm{Wi} = 64$) with (a) variate N_y, and (b) variate N_x.

ratio) do not change the spectrum profile in the large-scale regime. Next, a wide range of $N_x - N_y$ mesh ratios is tested. We finally found that by fixing the $N_x - N_y$ ratio to ~ 3, the spectrum profiles of courser mesh cases are largely consistent with the 1280×369 case in the large scale regime (but still deviate in the small-scale regime), as shown in fig. 6.20. Since the 1280×369 case is well close to the converged solution, we could expect that the courser mesh cases can have a reasonable prediction.

It is important to notice that the numerically converged solution of EDT is difficult even in 2D DNS due to the extremely high resolution required. On the other hand, in order to investigate the relationship between EDT and IDT in the high elasticity regime, we have to adopt 3D DNS in which both types of flows can exist. Since 3D EDT solutions cannot quantitatively converge, at least not for the whole spectrum of scales, we need to inspect how the limited resolution affects qualitative aspects of the dynamics. In fig. 6.21, we run some 3D DNS ($\mathrm{Re}_\tau = 84.85$, $\mathrm{Wi} = 64$) with a controlled mesh ratio, and plot the state-space projections of solution trajectories of the 3D DNS onto the $|\langle v_x'^* v_y'^* \rangle|_{\max} - A_{25}^*$ space. Here, A_{25}^* is the slope of the instantaneous mean velocity at $y^* = 25$, $|\langle v_x'^* v_y'^* \rangle|_{\max}$ is the peak of the instantaneous

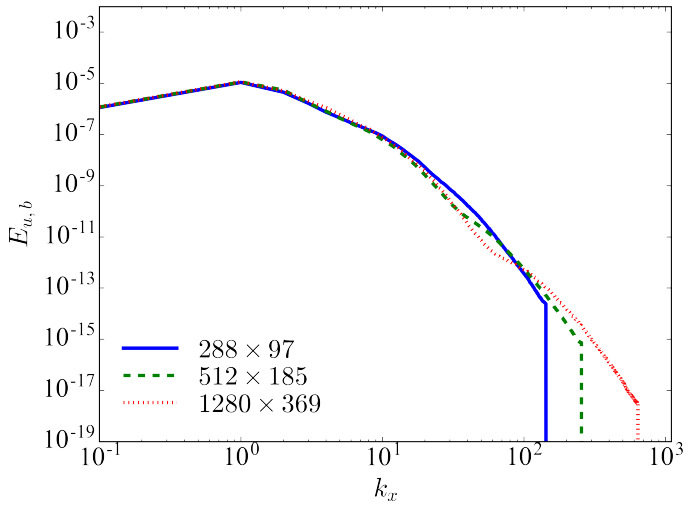

Figure 6.20: The bulk one-dimensional spectra of the streamwise velocity of 2D DNS ($\mathrm{Re}_\tau = 84.85$, $\mathrm{Wi} = 64$) with controlled mesh size ratio.

RSS profile (the shape of the RSS profile can refer to fig. 6.18). The tested meshes are listed in table 6.2. For reference, we also plot the time trajectory of a statistically converged 2D case ($N_x^+ \times N_y^+ = 1280 \times 369$). All of the 3D cases initially shoot up from an initial condition that close to the EDT state (lower right) and reach to the IDT state (upper left). Due to the effect of polymers, these 3D cases can only temporarily stay at the IDT state and then decay after several hundred time units. Note that these cases do not decay to laminar as the IDT structures disappear. Instead, the EDT structures become dominant, indicating the occurrence of the EDT state. In fig. 6.21, the trajectories of the three mesh resolution cases are similar. The locations of the IDT and EDT phases in the three cases are also close. Importantly, the EDT phase of the 3D cases are also close to the converged 2D case, indicating a reasonable prediction of the current mesh for the EDT phase. In summary, a fully converged 3D EDT solution is computationally difficult. However, by controlling the mesh ratio, the trajectories of the simulations are most independent of the resolution, whereas the

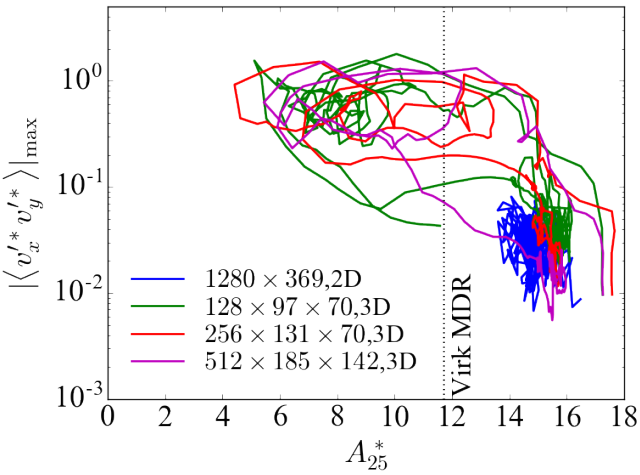

Figure 6.21: State-space projection of solution trajectories at different mesh resolutions.

EDT phase of the 3D cases are reasonable close to the converged 2D EDT. Therefore, the mesh sizes of the 3D EDT DNS are at least suitable for studying the dynamical relationship of IDT and EDT.

6.5 Conclusions

In this study, a new hybrid SM-FDM algorithm is developed for the DNS of viscoelastic turbulent flows. In the hybrid scheme, a TVD finite difference scheme is adopted to discretize the convection term of the FENE-P equation in space, whereas the other spatial derivatives are discretized using a standard Fourier-Chebyshev-Fourier spectral scheme. We choose TVD for its extraordinary performance to eliminate numerical oscillations which are inevitable when discretizing the FENE-P equations using SM. It also has an acceptable accuracy in comparison with other high-order finite-different schemes, e.g., WENO and CUD3, but less computational cost (section 6.2.3).

The HM scheme is validated in the streak transient growth simulation (section 6.3.1)

by comparing with solutions from an artificial-diffusion-free SM. The results are highly consistent, but HM is more stable to capture the sharp polymer structures.

In the full-scale steady-state DNS (section 6.3.2), the HM scheme is capable of capturing two known types of turbulent states: IDT and EDT. In comparison, the SM scheme (with GAD) can only capture the IDT flows. In IDT, the introducing of GAD smears the small-scale structures with sharp stress gradient. However, the dynamics (e.g., figs. 6.11 and 6.12) and statistics (e.g., figs. 6.9 and 6.10) of the IDT flow are not greatly affected. On the other hand, the EDT structures are generated by the sharp polymer stress. Therefore, GAD can quench the EDT structures and lead to flow relaminarization.

The magnitude of GAD depends on the distance from the wall (section 6.4). In both IDT and EDT flows, GAD will have a much larger magnitude in the near-wall region(fig. 6.17), but drastically decreases when approaching to the center of the channel. As IDT structures are likely to become active outside the inner layer while EDT structures tend to attach the wall, GAD thus has minor influence on IDT but strong influence on EDT.

Bibliography

Adrian, R. J., Meinhart, C. D., and Tomkins, C. D. (2000). Vortex organization in the outer region of the turbulent boundary layer. *J. Fluid Mech.*, **422**, 1–54.

Bird, R. B., Armstrong, R. C., and Hassager, O. (1987a). *Dynamics of polymeric liquids*, volume 1. John Wiley & Sons, New York, 2nd edition.

Bird, R. B., Curtis, C. F., Armstrong, R. C., and Hassager, O. (1987b). *Dynamics of polymeric liquids*, volume 2. John Wiley & Sons, New York, 2nd edition.

Canuto, C., Hussaini, M. Y., Quarteroni, A., and Zang, T. A. (1988). *Spectral methods in fluid dynamics*. Springer, Berlin Heidelberg.

Dallas, V., Vassilicos, J. C., and Hewitt, G. F. (2010). Strong polymer-turbulence interactions in viscoelastic turbulent channel flow. *Phys. Rev. E*, **82**(6), 066303.

Delis, A. T., Skeels, C. P., and Ryrie, S. C. (2000). Evaluation of some approximate riemann solvers for transient open channel flows. *J. Hydraul. Res.*, **38**(3), 217–231.

Douglas, J. J. and Russell, T. F. (1982). Numerical methods for convection-dominated diffusion problems based on combining the method of characteristics with finite element or finite difference procedures. *SIAM Journal on Numerical Analysis*, **19**(5), 871–885.

Dubief, Y., White, C. M., Terrapon, V. E., Shaqfeh, E. S. G., Moin, P., and Lele, S. K. (2004). On the coherent drag-reducing and turbulence-enhancing behaviour of polymers in wall flows. *J. Fluid Mech.*, **514**, 271–280.

Dubief, Y., Terrapon, V. E., White, C. M., Shaqfeh, E. S. G., Moin, P., and Lele, S. K. (2005). New answers on the interaction between polymers and vortices in turbulent flows. *Flow Turbul. Combust.*, **74**, 311–329.

Dubief, Y., Terrapon, V. E., and Soria, J. (2013). On the mechanism of elasto-inertial turbulence. *Phys. Fluids*, **25**, 110817.

Gibson, J. F. (2014). Channelflow: A spectral Navier-Stokes simulator in C++. Technical report, U. New Hampshire. `Channelflow.org`.

Gibson, J. F., Reetz, F., Azimi, S., Ferraro, A., Kreilos, T., Schrobsdorff, H., Farano, M., Yesil, A. F., Schütz, S. S., Culpo, M., and Schneider, T. M. (2019). Channelflow 2.0. manuscript in preparation.

Gottlieb, D. and Orszag, S. A. (1977). *Numerical analysis of spectral methods: theory and applications*, volume 26. Siam.

Harten, A. (1983). High resolution schemes for hyperbolic conservation laws. *J. Comput. Phys.*, **49**(3), 357–393.

Housiadas, K. D., Beris, A. N., and Handler, R. A. (2005). Viscoelastic effects on higher order statistics and on coherent structures in turbulent channel flow. *Phys. Fluids*, **17**, 035106.

Hunt, J. C. R., Wray, A. A., and Moin, P. (1988). Eddies, stream, and convergence zones in turbulent flows. In *Proceedings of the Summer Program*, pages 193–208, Stanford, CA. Center for Turbulence Research.

Jeong, J. and Hussain, F. (1995). On the identification of a vortex. *J. Fluid Mech.*, **285**, 69–94.

Kim, J., Moin, P., and Moser, R. (1987). Turbulence statistics in fully-developed channel flow at low Reynolds-number. *J. Fluid Mech.*, **177**, 133–166.

Kolář, V. (2007). Vortex identification: New requirements and limitations. *Int. J. Heat Fluid Flow*, **28**(4), 638–652.

Laizet, S. and Lamballais, E. (2009). High-order compact schemes for incompressible flows: A simple and efficient method with quasi-spectral accuracy. *J. Comput. Phys.*, **228**(16), 5989–6015.

Lee, S. J. and Zaki, T. A. (2017). Simulations of natural transition in viscoelastic channel flow. *J. Fluid Mech.*, **820**, 232–262.

LeVeque, R. J. (1996). High-resolution conservative algorithms for advection in incompressible flow. *SIAM Journal on Numerical Analysis*, **33**(2), 627–665.

Li, C. F., Sureshkumar, R., and Khomami, B. (2006). Influence of rheological parameters on polymer induced turbulent drag reduction. *J. Non-Newton. Fluid Mech.*, **140**(1), 23–40.

Li, C. F., Sureshkumar, R., and Khomami, B. (2015). Simple framework for understanding the universality of the maximum drag reduction asymptote in turbulent flow of polymer solutions. *Phys. Rev. E*, **92**, 043014.

Li, F. C., Kawaguchi, Y., Segawa, T., and Hishida, K. (2005a). Reynolds-number dependence of turbulence structures in a drag-reducing surfactant solution channel flow investigated by particle image velocimetry. *Phys. Fluids*, **17**, 075104.

Li, W., Stone, P., and Graham, M. D. (2005b). Viscoelastic nonlinear traveling waves and drag reduction in plane poiseuille flow. In *IUTAM Symposium on Laminar-Turbulent Transition and Finite Amplitude Solutions*, pages 289–312.

Min, T., Yoo, J. Y., and Choi, H. (2001). Effect of spatial discretization schemes on numerical solutions of viscoelastic fluid flows. *J. Non-Newton. Fluid Mech.*, **100**, 27–47.

Min, T., Yoo, J. Y., Choi, H., and Joseph, D. D. (2003). Drag reduction by polymer additives in a turbulent channel flow. *J. Fluid Mech.*, **486**, 213–238.

Moin, P. and Kim, J. (1982). Numerical investigation of turbulent channel flow. *J. Fluid Mech.*, **118**, 341–377.

Myska, J. and Stern, P. (1998). Significance of shear induced structure in surfactants for drag reduction. *Colloid Polym. Sci.*, **276**, 816–823.

Nesyn, G. V., Sunagatullin, R. Z., Shibaev, V. P., and Malkin, A. Y. (2018). Drag reduction in transportation of hydrocarbon liquids: From fundamentals to engineering applications. *J. Petrol. Sci. Eng.*, **161**, 715–725.

Peyret, R. (2002a). Spectral methods for incompressible viscous flow.

Peyret, R. (2002b). *Spectral methods for incompressible viscous flow*. Springer, New York.

Ptasinski, P. K., Boersma, B. J., Nieuwstadt, F. T. M., Hulsen, M. A., van den Brule, B. H. A. A., and Hunt, J. C. R. (2003). Turbulent channel flow near maximum drag reduction: simulations, experiments and mechanisms. *J. Fluid Mech.*, **490**, 251–291.

Robinson, S. K. (1991). Coherent motions in the turbulent boundary layer. *Annu. Rev. Fluid Mech.*, **23**, 601–639.

Roe, P. L. (1981). Approximate riemann solvers, parameter vectors, and difference schemes. *J. Comput. Phys.*, **43**(2), 357–372.

Rogallo, R. S. and Moin, P. (1984). Numerical simulation of turbulent flows. *Annu. Rev. Fluid Mech.*, **16**(1), 99–137.

Samanta, D., Dubief, Y., Holzner, M., Schäfer, C., Morozov, A. N., Wagner, C., and Hof, B. (2013). Elasto-inertial turbulence. *Proc. Natl. Acad. Sci. U. S. A.*, **110**, 10557–100562.

Schoppa, W. and Hussain, F. (2002). Coherent structure generation in near-wall turbulence. *J. Fluid Mech.*, **453**, 57–108.

Shekar, A., McMullen, R. M., Wang, S. N., McKeon, B. J., and Graham, M. D. (2019). Critical-layer structures and mechanisms in elastoinertial turbulence. *Phys. Rev. Lett.*, **122**(12), 124503.

Shu, C. (1998). Essentially non-oscillatory and weighted essentially non-oscillatory schemes for hyperbolic conservation laws. In *Advanced numerical approximation of nonlinear hyperbolic equations*, pages 325–432. Springer.

Shu, C. W. (2009). High order weighted essentially nonoscillatory schemes for convection dominated problems. *SIAM review*, **51**(1), 82–126.

Sid, S., Terrapon, V. E., and Dubief, Y. (2018). Two-dimensional dynamics of elasto-inertial turbulence and its role in polymer drag reduction. *Phys. Rev. Fluids*, **3**, 011301.

Sod, G. A. (1978). A survey of several finite difference methods for systems of nonlinear hyperbolic conservation laws. *J. Comput. Phys.*, **27**(1), 1–31.

Sureshkumar, R. and Beris, A. N. (1995). Effect of artificial stress diffusivity on the stability of numerical calculations and the flow dynamics of time-dependent viscoelastic flows. *J. Non-Newton. Fluid Mech.*, **60**, 53–80.

Sureshkumar, R., Beris, A. N., and Handler, R. A. (1997). Direct numerical simulation of the turbulent channel flow of a polymer solution. *Phys. Fluids*, **9**, 743–755.

Sweby, P. K. (1984). High resolution schemes using flux limiters for hyperbolic conservation laws. *SIAM journal on numerical analysis*, **21**(5), 995–1011.

Toms, B. A. (1948). Some observations on the flow of linear polymer solutions through straight tubes at large Reynolds numbers. In *Proc. 1st Int'l. Congress on Rheology*, volume 2, pages 135–141, Amsterdam.

Vaithianathan, T., Robert, A., Brasseur, J. G., and Collins, L. R. (2006). An improved algorithm for simulating three-dimensional, viscoelastic turbulence. *Journal of non-newtonian fluid mechanics*, **140**, 3–22.

Virk, P. S. (1975). Drag reduction fundamentals. *AIChE J.*, **21**, 625–656.

Waleffe, F. (1997). On a self-sustaining process in shear flows. *Phys. Fluids*, **9**, 883–900.

Wang, S. N., Shekar, A., and Graham, M. D. (2017). Spatiotemporal dynamics of viscoelastic turbulence in transitional channel flow. *J. Non-Newton. Fluid Mech.* submitted.

Warholic, M. D., Heist, D. K., Katcher, M., and Hanratty, T. J. (2001). A study with particles image velocimetry of the influence of drag-reducing polymers on the structure of turbulence. *Exp. Fluids*, **31**, 474–483.

Waterson, N. P. and Deconinck, H. (2007). Design principles for bounded higher-order convection schemes–a unified approach. *J. Comput. Phys.*, **224**(1), 182–207.

White, C. M., Dubief, Y., and Klewicki, J. (2012). Re-examining the logarithmic dependence of the mean velocity distribution in polymer drag reduced wall-bounded flow. *Phys. Fluids*, **24**, 021701.

Xi, L. (2009). *Nonlinear dynamics and instabilities of viscoelastic fluid flows*. Ph.D. thesis, University of Wisconsin-Madison.

Xi, L. and Graham, M. D. (2010a). Active and hibernating turbulence in minimal channel flow of Newtonian and polymeric fluids. *Phys. Rev. Lett.*, **104**, 218301.

Xi, L. and Graham, M. D. (2010b). Turbulent drag reduction and multistage transitions in viscoelastic minimal flow units. *J. Fluid Mech.*, **647**, 421–452.

Xi, L. and Graham, M. D. (2012a). Dynamics on the laminar-turbulent boundary and the origin of the maximum drag reduction asymptote. *Phys. Rev. Lett.*, **108**, 028301.

Xi, L. and Graham, M. D. (2012b). Intermittent dynamics of turbulence hibernation in Newtonian and viscoelastic minimal channel flows. *J. Fluid Mech.*, **693**, 433–472.

Yu, B. and Kawaguchi, Y. (2004). Direct numerical simulation of viscoelastic drag-reducing flow: a faithful finite difference method. *J. Non-Newton. Fluid Mech.*, **116**, 431–466.

Zhang, D., Jiang, C., Liang, D., and Cheng, L. (2015). A review on tvd schemes and a refined flux-limiter for steady-state calculations. *J. Comput. Phys.*, **302**, 114–154.

Zhu, L. and Xi, L. (2019). Vortex axis tracking by iterative propagation (vatip): a method for analysing three-dimensional turbulent structures. *Journal of Fluid Mechanics*, **866**, 169–215.

Zhu, L., Schrobsdorff, H., Schneider, T. M., and Xi, L. (2018). Distinct transition in flow statistics and vortex dynamics between low- and high-extent turbulent drag reduction in polymer fluids. *J. Non-Newton. Fluid Mech.*, **262**, 115–130.

Zhu, L., Bai, X., Krushelnycky, E., and Xi, L. (2019). Transient dynamics of turbulence growth and bursting: Effects of drag-reducing polymers. *J. Non-Newton. Fluid Mech.*, **266**, 127–142.

Chapter 7

Roles of inertia- and elasticity-driven turbulence in polymeric flow

Polymeric turbulence can be either driven by the inertial and elastic forces and result in two fundamentally different states: the inertia- (IDT) and elasticity-driven turbulence (EDT). Although previous studies (Li *et al.*, 2005; Housiadas *et al.*, 2005; Xi and Graham, 2012b; Samanta *et al.*, 2013; Sid *et al.*, 2018) have found that the two turbulent flows can sustain independently under certain conditions, their relationship in the dynamics of polymeric flows is actually not clear. In this chapter, we will investigate the roles of IDT and EDT in polymeric flows with a wide range of parameters. Particularly, it is found that the two types of turbulent motions can sustain alternatively, leading to a new dynamical flow state.

I was responsible for implementing simulations and collecting data. I also post-processed the data with Dr. Xi Li's suggestions. The manuscript was written by me

and revised by Dr. Li Xi.

This chapter is under preparation for future publication.

7.1 Introduction

It is well-known that a small amount of polymers in the turbulent flows can significantly change the flow structures and reduce the energy dissipation (Toms, 1948; Virk, 1975; Graham, 2014). As a result, nearly 80% of friction drag reduction can be achieved in the turbulent flows. The wide applications of this phenomenon in industry have attracted a considerable amount of attention. However, some key questions still remain to be answered. Especially, as the elasticity of the polymer solution continuously increases, the amount of drag reduction will converge at an asymptotic upper bound. This so-called maximum drag reduction (MDR) asymptote is found to be insensitive to the rheological properties of the polymer solution (Virk, 1975). Understanding of MDR has extraordinary practical importance. However, its origin is still not clear and has been regarded as the most critical unsolved problem in this area.

The elastic sublayer theory proposed by Virk (1975) believed that the increasing DR is a consequence of expanding of the "elastic sublayer" where polymers are highly stretched. Eventually, as the elastic sublayer occupies the entire flow domain, MDR is achieved. This theory benefits from its conceptual simplicity but is soon proven oversimplified to explain the complex polymer-turbulence interactions in viscoelastic fluid. An alternative model for MDR was proposed by Xi and Graham (2012b,a) who suggested that the flow in MDR is dominated by a weak turbulent state (named as "hibernating turbulence") which is sufficiently close to the laminar-turbulence boundary. Stronger turbulent states, i.e. the "active turbulence", in MDR can occasionally appear which drags the flow away from the turbulence edge. The "active-hibernating" theory is supported by large domain DNS (Wang *et al.*, 2017; Zhu *et al.*, 2018) in

which locally stronger and weaker turbulent regions are found alternatively distribute in space. Note that the "active-hibernation" theory interprets the origin of MDR from the Newtonian nature of turbulence. Turbulence, here, is still driven by inertial forces (thus termed as "inertia-driven" turbulence (IDT)) and has those typical Newtonian coherent structures, e.g., the quasi-streamwise streaks and vortices. Therefore, it is insufficient to explain the recent finding of a new type of turbulence in the high elasticity regime. Sid *et al.* (2018) indicated that in the high elasticity flows, Newtonian structures can be completely eliminated by polymers. The flow, instead, is dominated by elastic instability, leading to the so-called "elasticity-driven turbulence" (EDT). Note that EDT was initially considered to be driven by both inertial and elastic forces (Dubief *et al.*, 2013; Samanta *et al.*, 2013) (and thus termed as "elasto-inertial turbulence"(EIT)). However, it was soon found to be purely driven by the elastic force (Sid *et al.*, 2018). Samanta *et al.* (2013) further proposed a potential connection between EDT and the MDR state since EDT can sustain in the high elasticity regime where MDR occurs. The EDT structures are found to be significantly different from the IDT structures (which are mostly Newotnian-like). DNS studies by Sid *et al.* (2018) indicated that EDT has strictly 2-dimensional near-wall structures, e.g. the spanwise vortical structure and the sheet-like polymer structure, whereas IDT structures are mostly 3-dimensional. Moreover, polymers in EDT are not only in charge of suppressing turbulence, but also feed energy to the flows at the small-scale, exhibiting a positive contribution in the turbulent kinetic energy budget (Dallas *et al.*, 2010).

The concept of EDT is quite fresh with a lot of unsolved puzzles. Especially, its roles in the drag reduction phenomenon of polymeric turbulence are remained to be revealed. Previous studies (Samanta *et al.*, 2013; Sid *et al.*, 2018) suggested that as

elasticity increases, EDT will eventually dominate the polymeric flow, whereas IDT is completely erased. However, as will be presented in this study, EDT and IDT both play an important role in the dynamics of high elasticity polymeric turbulence. The turbulent flow, here, is governed by a dynamical state in which the EDT and IDT structures can sustain in an alternative way.

7.2 Methodology

The plane Poiseuille flow driven by a constant pressure drop is investigated in this study. Periodic boundary conditions are applied to the streamwise (x-) and the spanwise (z-)directions while no-slip boundary condition is applied to the walls in the wall-normal (y-)direction. Lengths and velocities are respectively scaled with the half-channel height l and the Newtonian laminar center line velocity U. Pressure p and time t are scaled with ρU^2 (ρ is density) and l/U, respectively. The polymeric flow is governed by

$$\frac{\partial \boldsymbol{v}}{\partial t} + \boldsymbol{v}\cdot\boldsymbol{\nabla}\boldsymbol{v} = -\boldsymbol{\nabla}p + \frac{\beta}{\mathrm{Re}}\nabla^2\boldsymbol{v} + \frac{2\left(1-\beta\right)}{\mathrm{ReWi}}\left(\boldsymbol{\nabla}\cdot\boldsymbol{\tau}_p\right), \tag{7.1}$$

$$\boldsymbol{\nabla}\cdot\boldsymbol{v} = 0. \tag{7.2}$$

$$\frac{\boldsymbol{\alpha}}{1-\frac{\mathrm{tr}(\boldsymbol{\alpha})}{b}} + \frac{\mathrm{Wi}}{2}\left(\frac{\partial\boldsymbol{\alpha}}{\partial t} + \boldsymbol{v}\cdot\boldsymbol{\nabla}\boldsymbol{\alpha} - \boldsymbol{\alpha}\cdot\boldsymbol{\nabla}\boldsymbol{v} - \left(\boldsymbol{\alpha}\cdot\boldsymbol{\nabla}\boldsymbol{v}\right)^{\mathrm{T}}\right) = \frac{b\boldsymbol{\delta}}{b+2}, \tag{7.3}$$

$$\boldsymbol{\tau}_p = \frac{b+5}{b}\left(\frac{\boldsymbol{\alpha}}{1-\frac{\mathrm{tr}(\boldsymbol{\alpha})}{b}} - \left(1-\frac{2}{b+2}\right)\boldsymbol{\delta}\right). \tag{7.4}$$

Equations (7.1) and (7.2) are the conservation equations of momentum and mass, respectively. Equations (7.3) and (7.4) are the FENE-P constitutive equations to

govern the polymer conformation and stress tensors $\boldsymbol{\alpha}$ and $\boldsymbol{\tau}_p$ (Bird *et al.*, 1987). $\mathrm{Re} \equiv \rho U l/\eta$ is Reynolds number (η is the solution viscosity), $\mathrm{Wi} \equiv 2\lambda U/l$ is Weissenberg number (λ defines the polymer relaxation time), b is the upper bound of the polymer extension, i.e., $\mathrm{tr}(\boldsymbol{\alpha}) \leq b$, and $\beta \equiv \eta_s/\eta$ is the viscosity ratio (η_s denotes the solvent viscosity).

A hybrid pseudo-spectral/finite-difference scheme is used to solve the equation system. For spatial discretization, a conservative second-order upwind TVD (total variation diminishing) finite difference scheme (Zhang *et al.*, 2015; Yu and Kawaguchi, 2004) is adopted to discretize the convection term $\boldsymbol{v} \cdot \boldsymbol{\nabla}\boldsymbol{\alpha}$ in eq. (7.3), whereas other spatial derivative terms are discretized using a Fourier-Chebysheve-Fourier pseudo-spectral projection. No artificial diffusion is applied. The time discretization uses a third-order semi-implicit backward-differentiation-Adams-Bashforth scheme (Peyret, 2002). Both 2D and 3D DNS are implemented in this study. Note that the evolution of EDT is independent of the spanwise direction (Sid *et al.*, 2018). Therefore, we also include 2D DNS to study EDT, in order to reduce the computational cost. Typical computational domain sizes for 3D and 2D simulations are $L_x^+ \times L_y^+ \times L_z^+ = 720 \times 2\mathrm{Re}_\tau \times 230$ and $L_x^+ \times L_y^+ = 720 \times 2\mathrm{Re}_\tau$ ("+" indicates quantities normalized by turbulent inner scale, and $\mathrm{Re}_\tau = \rho u_\tau l/\eta = \sqrt{2\mathrm{Re}}$ is the friction Reynolds number, where u_τ is the friction velocity), respectively. This domain size is consistent with those studies for EDT (Dubief *et al.*, 2013; Sid *et al.*, 2018) but may be insufficient to exhibit the full pathway of IDT. However, the extremely high computational cost required by the current study to simulate the EDT flow prevents us to further explore in a larger simulation domain. Besides, it will not alter the critical observations, i.e. the dynamical IDT-EDT state, in this study. In addition, we also choose two mesh

resolutions ($N_x \times N_y \times N_z$) for the 3D simulations. The courser mesh, $72 \times 97 \times 72$, is adopted to explore IDT parameter space which is statistically converged for IDT flow. The refiner mesh, $256 \times 131 \times 142$, for the IDT-EDT dynamics is comparable with those adopted by Dubief *et al.* (2013); Samanta *et al.* (2013); Shekar *et al.* (2019), but is not yet converged for EDT. Note the refiner mesh is already much denser than the typical IDT DNS in the literature (Sureshkumar *et al.*, 1997; Yu and Kawaguchi, 2004; Li *et al.*, 2005; Xi and Graham, 2010; Zhu *et al.*, 2018). In fact, the numerical converged EDT solution is not realistic for the 3D simulation, as a mesh with 30 times (estimated from Sid *et al.* (2018)'s 2D EDT DNS) more grids than current refined mesh may be needed. However, we notice that current resolution can at least maintain the IDT-EDT dynamics qualitatively. As for 2D simulations, the resolution is chosen to be $N_x \times N_y = 1280 \times 369$ which can give a converged solution.

7.3 Results and discussion

In dilute polymer flows, IDT and EDT are found under different conditions. In a number of numerical studies (Xi and Graham, 2010; Housiadas and Beris, 2003; Li *et al.*, 2005), IDT was observed in a moderate elasticity polymeric flow. The characteristics of the IDT flow (e.g., the near-wall coherent structures) are still largely similar to the Newtonian turbulence. Polymers in IDT are mainly responsible for suppressing turbulence, whereas the flow is driven by inertial force. As the elasticity (measured by Wi) increases, IDT becomes difficult to sustain due to the strong polymer effect. In the meantime, the high elasticity of the flow will cause a large elastic force which could trigger the elasticity-driven turbulence. In addition, unlike IDT in which the flow is 3-dimensional, EDT instability is strictly 2-dimensional (Sid *et al.*, 2018), in

the sense that it can sustain in a 2D flow geometry. Although it is well accepted that both IDT and EDT can exist in the polymeric flow, their roles may change with the elasticity level and are far from been fully understood. Particularly, in the high elasticity regime, while Li *et al.* (2005); Zhu *et al.* (2018); Wang *et al.* (2017) observed an IDT-dominated flow motions, Dubief *et al.* (2013); Samanta *et al.* (2013), on the contrary, suggested that the flow should be dominated by EDT structures. Despite the different opinions in the literature, this study (as will be presented later) notices that IDT and EDT can coexist in the high elasticity flow, exhibiting a new dynamical turbulent state.

Before starting to discuss the roles of IDT and EDT in the dynamics of high elasticity polymeric flows, we will first look at the qualitatively different near-wall structures and statistics between these two turbulent motions. To have a sense on the differences between IDT and EDT, we first investigate the turbulent kinetic energy (TKE) budget of the two turbulent motions. The TKE budget equation

$$\frac{\partial k}{\partial t} + \langle \boldsymbol{v} \rangle \cdot \boldsymbol{\nabla} k + \boldsymbol{\nabla} \cdot \boldsymbol{T}^k = \mathcal{P}^k - \epsilon^k - \chi^k, \tag{7.5}$$

is derived from eq. (7.1), which governs the evolution of TKE in the turbulent flow. In eq. (7.5), $\mathcal{P}^k$ is the production of TKE, ϵ^k is the consumption rates of TKE by viscous dissipation, and χ is the elastic conversion. They are respectively define as,

$$\mathcal{P}^k \equiv -\boldsymbol{\nabla}\langle \boldsymbol{v} \rangle : \langle \boldsymbol{v'v'} \rangle, \tag{7.6}$$

$$\epsilon^k \equiv -\frac{2\beta}{\mathrm{Re}} \langle \boldsymbol{\Gamma}' : \boldsymbol{\Gamma}' \rangle. \tag{7.7}$$

$$\bar{\chi}^k \equiv -\frac{2(1-\beta)}{\mathrm{ReWi}}\langle \boldsymbol{\tau}_\mathrm{p}' : \boldsymbol{\Gamma}' \rangle. \tag{7.8}$$

where $\boldsymbol{v}'$, $\boldsymbol{\Gamma}'$ and $\boldsymbol{\tau}_\mathrm{p}'$ are the fluctuating components of the velocity, the rate of strain and the polymer stress tensors, respectively. The transportation terms of the TKE budget are grouped into $\boldsymbol{T}^k$. Since these terms are not responsible for the energy transferring between different energy forms, they will not be further discussed. In fig. 7.1, the spatial average of $\mathcal{P}^k$, χ^k, and ϵ^k (i.e., $\bar{\mathcal{P}}^k$, $\bar{\chi}^k$ and $\bar{\epsilon}^k$, where $\bar{\cdot}$ indicates quantities averaged in all spatial dimensions) in typical IDT and EDT flows are computed and plotted as a function of time t. We choose the 3D DNS at $\mathrm{Re} = 3600$ and $\mathrm{Wi} = 30$ as a representative example of IDT. The resolution is $N_x \times N_y \times N_z = 72 \times 97 \times 72$, which is sufficient for a statistically converged IDT solution. For EDT, a much higher resolution is required to resolve the sharp polymer stress gradients, which is numerically difficult for 3D DNS. Therefore, we adopt a high resolution 2D DNS ($\mathrm{Re} = 3600$, $\mathrm{Wi} = 64$) which has a converged EDT solution (Sid *et al.*, 2018).

In IDT flows (fig. 7.1(a)), TKE is produced by the inertial force and then consumed by viscous dissipation. Therefore, the production term is always positive and the viscous dissipation term is always negative. Note that the elastic conversion can be positive or negative mathematically. In IDT, the elastic conversion term is negative as TKE is converted into the elastic energy. In addition, periodic increases of all profiles are observed. This phenomenon has been observed by Xi and Graham (2012b,a) and was termed as the "active" turbulent stage. Between two active stages, the flow is quiescent and is called "hibernating" stage in contrast to the "active" stage. In Xi and Graham (2012b); Wang *et al.* (2017)'s studies, the active and hibernating stages are both dominated by IDT structures. This opinion is validated in our simulations

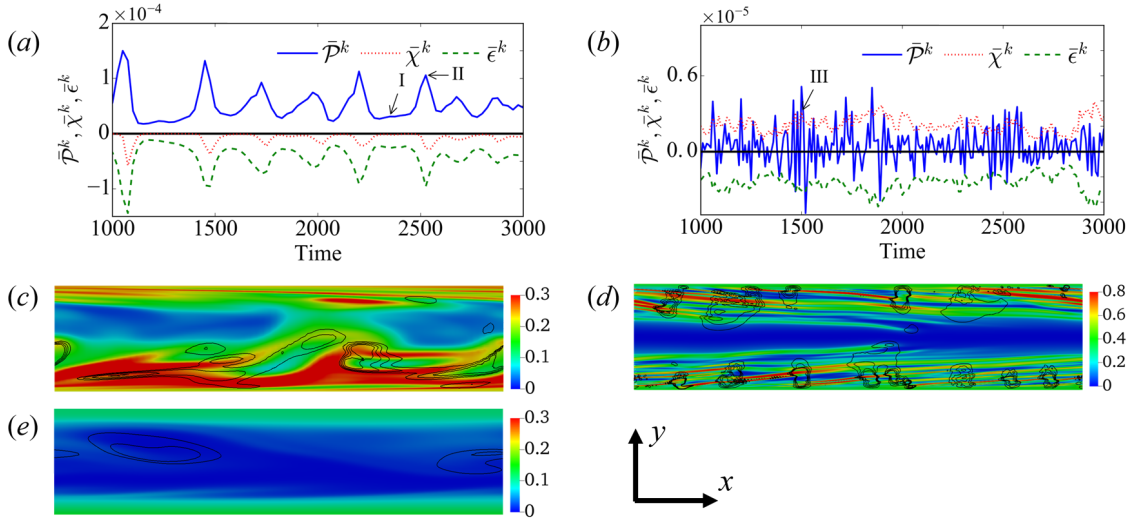

Figure 7.1: Time series of the bulk-average production $\bar{\mathcal{P}}^k$, elastic conversion $\bar{\chi}^k$ and dissipation $\bar{\epsilon}^k$ in the turbulent kinetic energy budget of (a) IDT (Wi = 30, 3D DNS) and (b) EDT (Wi = 64, 2D DNS). Instantaneous 2D snapshots of Q (line contours with equispaced levels from 0.005 to 0.02) and $\mathrm{tr}(\boldsymbol{\alpha})/b$ (color contours) from the (c) active, and (e) hibernating stages of IDT, and (d) EDT.

until Wi = 37 at which IDT cannot sustain itself and starts to decay. As we will discuss later, it could eventually transition to either the laminar or the EDT stage depending on the flow conditions. EDT (fig. 7.1(b)), on the other hand, has positive elastic conversion while its production term fluctuates around zero. Polymers here are responsible for feeding the turbulence while the inertial force has negligible influence. In addition, compared with the IDT case, the magnitude of the profiles in the EDT case is much lower, indicating a weaker intensity of turbulence. Quantities here still slightly fluctuate but do not have a clear period between the active (stronger) and hibernation (weaker) states.

Figure 7.1(c-e) show the instantaneous 2D snapshots of the vortex identification

quantity Q (Jeong *et al.*, 1997; Zhu and Xi, 2019), defined as

$$Q \equiv \frac{1}{2}\left(\| \boldsymbol{\Omega} \|^2 - \| \boldsymbol{S} \|^2\right) \tag{7.9}$$

($\boldsymbol{\Omega} \equiv \frac{1}{2}\left(\boldsymbol{\nabla v} - \boldsymbol{\nabla v}^T\right)$ is the vorticity tensor, $\boldsymbol{S} \equiv \frac{1}{2}\left(\boldsymbol{\nabla v} + \boldsymbol{\nabla v}^T\right)$ is the rate of strain tensor, and $\| \cdot \|$ represents the Frobenius tensor norm), and the trace of polymer conformation tensor $\boldsymbol{\alpha}$ normalized by the maximum polymer extension parameter b, i.e., $\mathrm{tr}(\boldsymbol{\alpha})/b$. In fig. 7.1($c$) and ($e$), the instantaneous contours of the active and hibernating turbulent stages in IDT are plotted which correspond to instance I and II in fig. 7.1(a). Strong quasi-streamwise vortical structures (the contour lines) are observed in the active stage with their upstream side attaching the wall while the downstream side lifting up towards the center of the channel. Polymer configurations (represented by color contours) are strongly correlated with vortices.The polymers near the vortices are highly extended which strongly suppress the intensity of the vortices in the flow field (Zhu *et al.*, 2019; Li and Graham, 2007; Dubief *et al.*, 2005). In the hibernating stage, only a few weak streamwise vortices are observed. The extension of polymers are thus smaller than the active stage. In the near wall region, a larger magnitude of $\mathrm{tr}(\boldsymbol{\alpha})/b$ is observed, polymers here are stretched mainly by the mean shear. The instantaneous EDT structures are significantly different from those of IDT. As shown in fig. 7.1(d), a series of thin bands of large polymer extensions are found extending from the walls to the channel's center with an angle of ~ 5 degree to the wall. Induced by these polymer structures, an array of spanwise vortices occurs near the wall, which is consistent with Samanta *et al.* (2013). Note that the spanwise EDT vortical structures can also been observed in the near-wall region of the IDT flow but are much weaker comparing with the dominated IDT structures. Thus they

are mostly hidden in the IDT flows.

In fig. 7.2, we explore the existence of IDT and EDT in the Re – Wi parameter space. Still, IDT is obtained by a low resolution 3D DNS while EDT is simulated in 2D DNS. The initial condition of EDT/IDT uses a statistically converged solution at a slightly higher/lower Wi. The initial condition is designed to maximally expand the region of each turbulent state in the parameter space, as it is easiest to converge to a similar new state from the state with similar parameters. The "sustained turbulence" is determined when turbulent motions can persist for a pre-defined time interval (Xi and Graham, 2010). For IDT, this interval is 5000 time units , while the interval of EDT is 1000 time units. Three Re (i.e., Re_τ = 66.33, 84.85, and 169.70) are investigated in this study. Starting from the lowest Re (Re_τ = 66.33), the highest Wi (0, 36, and 66 for Re_τ = 66.33, 84.85, and 169.70) for a sustained IDT quickly increases with Re. This phenomenon is also observed by Zhu *et al.* (2018). In the meantime, EDT can also sustain at a fairly low Wi. The lowest Wi (21, 16, and 14 for Re_τ = 66.33, 84.85, and 169.70) decreases as Re increases, but the Re-dependence is considerably weaker than that of IDT. It is of great interest to note that there is a window of Wi for the co-existence of these two types of turbulence and the window widens with increasing Re. In this overlapping region, both IDT and EDT can sustain by themselves and the destination of the flow depends on the initial condition.

To understand the relationship of IDT and EDT with the MDR stage, we investigate the Wi-dependence of the mean velocity profiles in the two types of turbulence in fig. 7.2(b). Cases in this plot are taken at Re_τ = 84.85. As Wi gradually increases, the mean velocity profiles of the IDT cases lift up but eventually converge at Wi = 36. The converged velocity profile (i.e. the Wi = 36 case) is far below Virk's MDR. Note

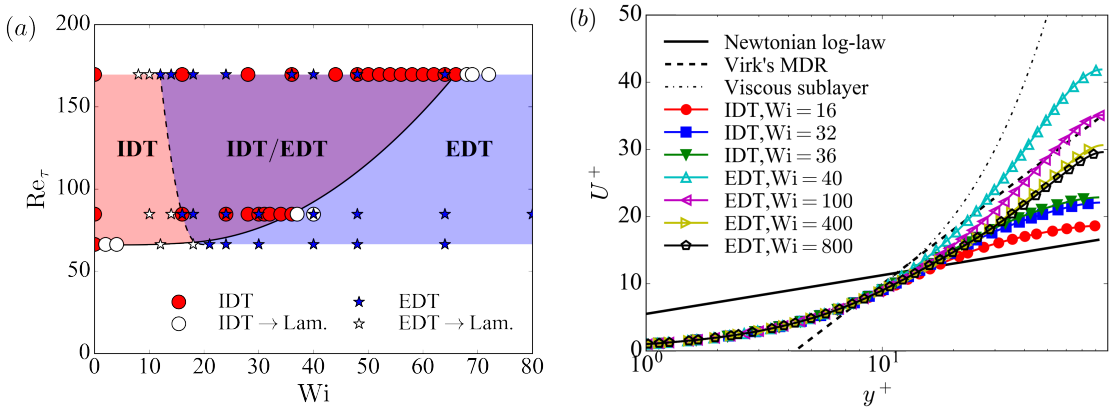

Figure 7.2: (a) Existence of IDT and EDT in the Re – Wi parameter space. Solid and dash lines are boundaries of sustained IDT and EDT drawn according to the B-spline interpolation between the critical Wi of the transitions at different Re. (b) Mean velocity profiles of IDT and EDT cases at $\mathrm{Re}_\tau = 84.85$.

that this may be because of the restriction of the current domain size, as Zhu *et al.* (2018); Wang *et al.* (2017) had obtained a converged velocity profile much closer to the Virk's MDR asymptote in a larger domain. On the other hand, the mean velocity profile of the Wi = 40 case of EDT is significantly higher than the Virk's MDR profile. As Wi increases, the mean velocity profile gradually drops down below the Virk's MDR profile. Note that it is intuitive to relate EDT to the MDR stage, as EDT can sustain at a high Wi where the MDR stage occurs (Sid *et al.*, 2018). However, as found here, the mean velocity of EDT do not converge to the Virk's MDR profile. Moreover, it even does not converge at Wi = 400 where polymers are close to their fully extension limit. In fact, it is found that the average velocity and the average polymer extension in EDT have a strong linear relationship at least until current highest Wi = 800. Therefore, we could expect that the mean velocity profile will not converge until polymers reaching the maximum extension. Thus the convergence of EDT will depend on specific rheological properties of the polymer solution (e.g.,

polymer length), which contradicts experimental observations (Virk, 1975).

In figs. 7.1 and 7.2, simulations are designed to expose one type of turbulence. Once the turbulent flow cannot sustain, it will decay directly to the laminar state. In the meantime, by changing the initial condition, we found another type of trajectories in which one type of turbulence can directly transition to the other. Next, we will try to probe this type of trajectories.

In fig. 7.3, we plot the projections of trajectories of the high resolution 3D DNS cases on to the $|\langle v_x'^* v_y'^* \rangle|_{\max} - A_{25}^*$ and the $|\langle v_x'^* v_y'^* \rangle|_{\max} - Q_{\rm rms}$ state-spaces. Here, $|\langle v_x'^* v_y'^* \rangle|_{\max}$ defines the peak of the instantaneous Reynolds shear stress (RSS) profile, A_{25}^* is the value of the log-law slope of the instantaneous mean velocity profile (White *et al.*, 2012; Zhu *et al.*, 2019)

$$A^* \equiv y^* \frac{\partial U_m^*}{\partial y^*}, \tag{7.10}$$

measured at $y^* = 25$, and $Q_{\rm rms}$ is the root-mean-square value of Q. Note that in figs. 7.1 and 7.2, we adopted a relatively low resolution ($N_x \times N_y \times N_z = 72 \times 97 \times 70$) to simulate IDT. This resolution is enough for the simulation of IDT and will not change the statistics (e.g. the mean velocity) and dynamics (e.g. the time series of TKE budget, and the the existence of solution) of IDT. However, capturing EDT requires much higher resolution than that of IDT to resolve the sharp stress gradient. The EDT structures will not be captured in those low resolution cases once IDT is erased from the flow. Therefore, we adopt a higher resolution ($N_x \times N_y \times N_z = 256 \times 131 \times 142$) here compared with previous 3D DNS for IDT. This resolution is comparable to that in previous studies (Dubief *et al.*, 2013; Shekar *et al.*, 2019), but is still not converged for the EDT flows. In fact, a converged mesh resolution for EDT is difficult

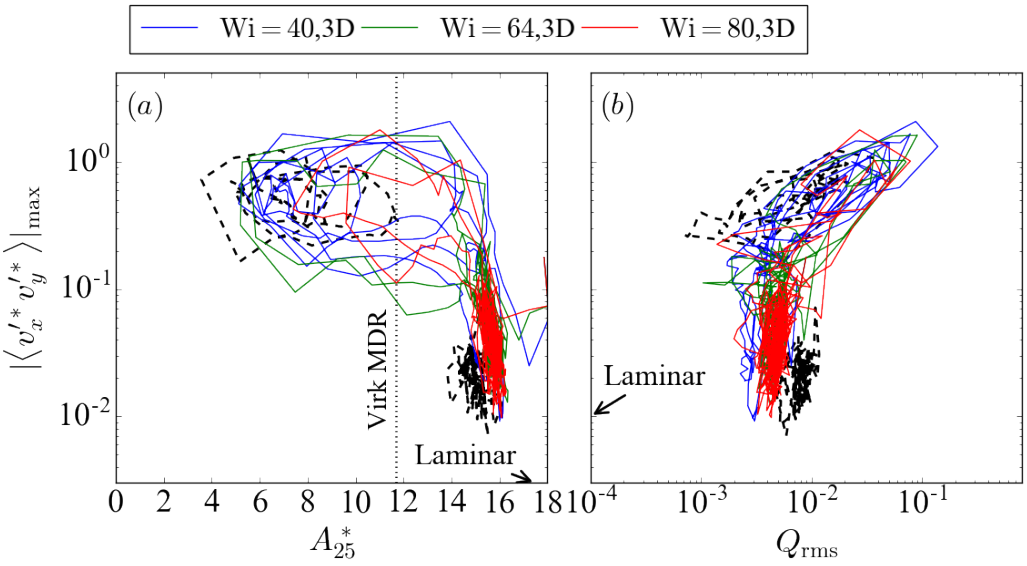

Figure 7.3: State-space projections of solution trajectories on to different coordinate combinations: (a) instantaneous RSS profile peak, $|\langle v_x'^* v_y'^* \rangle|_{\max}$, versus log-law slope of the instantaneous mean velocity profile at $y^* = 25$, A_{25}^*, and (b) $|\langle v_x'^* v_y'^* \rangle|_{\max}$ versus the root-mean-square of the Q field, $Q_{\rm rms}$. Black dash lines occupying the upper and lower halves (in both panels) are trajectories of the 3D IDT (Wi = 30) and 2D EDT (Wi = 64) described in fig. 7.1

as mentioned by Sid *et al.* (2018), since EDT has infinitely small scale structures. Although quantitative statistics of EDT do not converge, the dynamics, in terms of the existence of solutions and their transition, has been tested and is largely independent of the resolutions.

In fig. 7.3, three Wi cases (Wi = 40, 64, and 80) that are above the critical Wi for a sustaining IDT at $\mathrm{Re}_\tau = 84.85$, are tested. We also plot the trajectory projections of the 3D low resolution IDT and the 2D EDT flows that has been discussed in fig. 7.1, to indicate the location of the IDT and EDT states in the state space. It is necessary to mention that the initial conditions of the cases in fig. 7.3 are different than that discussed in fig. 7.2. Cases in fig. 7.3 choose a manually designed perturbation that distinctly deviates from the two turbulent states, whereas the initial condition in

fig. 7.1 is a statistically converged solution at slightly different parameters. In fig. 7.3, the significant differences between the IDT and EDT states are clearly manifested by the big gap between them in the state-space. Starting from the initial condition, the trajectories of all these cases initially approach the EDT state. However, all of them do not stay at the EDT state and quickly jump up to the IDT state. They can stay at the IDT state for several hundred time units during which intermittent cycles similar to that of the active-hibernating cycles are observed. Also, the location of intermittent cycles of the three cases is close to that of the sustaining IDT case in the two state-spaces. As the IDT structures are eliminated by polymers at the high Wi, the three cases start to decay. Interestingly, all of them do not decay to laminar (in fact, they never go to laminar in current time interval of 8000 time units) but transition back to the EDT state. As the three cases reach the EDT state, they will stay there for several thousands of time units. During this period, disturbances of the flow are accumulated and another shooting to IDT can be triggered, which are observed in all three cases. The alternation of turbulent flow states between the two distinctly different states provides a new perspective for the dynamics of polymeric flow at the high elasticity regime. In this dynamically changing turbulent flow, EDT and IDT (and thus the inertial and elastic forces) both play an important role. This is different from previous theories (e.g., the active-hibernation theory (Xi and Graham, 2012b,a) and the EDT-dominated theory (Samanta *et al.*, 2013; Sid *et al.*, 2018)) which depicted the high elasticity polymer turbulence solely from one type of turbulent states.

The alternation between IDT and EDT states in the high elasticity polymeric flow will be further discussed in fig. 7.4. Here, the Wi = 40 case in fig. 7.3 is picked as

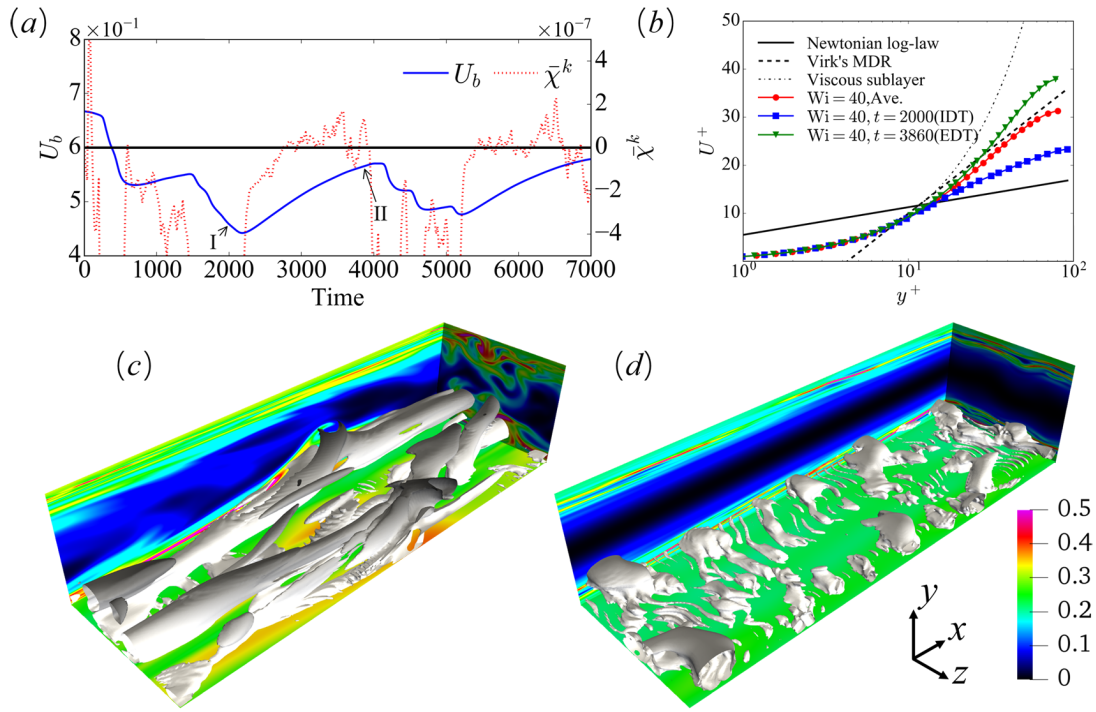

Figure 7.4: (a) Time series of bulk velocity U_b and polymer contribution to TKE budget $\bar{\chi}^k$, (b) time averaged and instantaneous mean velocity profiles, and instantaneous coherent structures at (c) instance I and (d) instance II in the Wi = 40 case described in fig. 7.3. The iso-surfaces in (c,d) are vortices identified by $Q = 0.004$, and color contours are $\mathrm{tr}(\boldsymbol{\alpha})/b$. Only vortices in the bottom half of the channel are presented.

a representative example. Figure 7.4(a) shows the time series of the bulk velocity U_b and the polymer contribution to TKE budget $\bar{\chi}^k$. After the initial evolution, the bulk velocity starts to follow a clear periodic pattern with the period of 2500 time units. Interestingly, the time-averaged mean velocity profile (fig. 7.4(b)) taken from one period (e.g., $t \approx 1500 - 4000$) of the Wi = 40 case, is considerably close to the Virk's MDR profile, which indicates its potential relation to the MDR stage. The decreasing period ($t \approx 1500 - 2200$) of the U_b profile is corresponding to the IDT period. Polymers in the IDT period have strongly negative contribution to the TKE and thus responsible for dissipating turbulence. In the increasing period (e.g., $t \approx 2200 - 4000$), the flow is dominated by elastic structures and is referred to as the EDT state. The polymer contribution in the EDT period is sufficiently close to zero but continuously increasing. Unlike the 2D EDT DNS in which IDT is restricted by its 3D nature, in the 3D simulation, the inhibition of IDT is mainly due to the suppression effect of polymers. Thus polymers in the EDT period are responsible for both the suppression of IDT and the generation of EDT. As time in the EDT period advances, more and more IDT structures (e.g. the streamwise vortical structures in fig. 7.4(c)) are eliminated while EDT structures (e.g. the spanwise vortical structures in fig. 7.4(d)) become stronger, the polymer contribution thus gradually grows and eventually becomes positive. To intuitively see these two qualitative different states, we pick two time instances, labels by I and II, which immediately precede the IDT-EDT and EDT-IDT transitions. The instantaneous mean velocity profiles and the flow structures are shown in fig. 7.4(b-d). At instance I, the flow is dominated by the streamwise vortical structures (fig. 7.4(c)), while the mean velocity profile is far below the time-averaged profile and is close the pure IDT flow (e.g., the Wi = 30

case in fig. 7.2(b)). For instance II, the IDT structures are mostly eliminated in the flow and the spanwise vortex trains and the band-like polymer structures show up (fig. 7.4(d)) as a distinct sign of the EDT state. The mean velocity profile is higher than the Virk's MDR and is consistent with the 2D EDT DNS.

7.4 Conclusions and discussion

The dilute polymeric flow can be driven by the inertial and elastic forces. As a result, two clearly different turbulent types: IDT and EDT, can be triggered and could sustain independently or interactively.

There is a clear region in the Re − Wi parameter space where IDT and EDT coexist. The terminal state of the flow in the overlap regime will depend on the initial condition and the relative attractiveness of each state. IDT and EDT both share some common features with the MDR stage but also have some differences. As Wi increases, the mean velocity of IDT eventually converges to an asymptotic upper limit, which is consistent with MDR. However, IDT cannot sustain as we further increase Wi and will decay to the laminar, which is different from MDR. In the meantime, EDT can sustain at a high Wi (same feature as that of MDR), but the convergence of EDT will depend on the maximum extension of polymers, which is also different from MDR.

As Wi is larger than the critical Wi of sustained IDT, the turbulent flow can periodically alternate between the IDT and EDT states. This newly discovered dynamical state may relate to the MDR stage since the time average of this dynamical state gives a mean velocity that is close to that of Virk's MDR.

Bibliography

Bird, R. B., Curtis, C. F., Armstrong, R. C., and Hassager, O. (1987). *Dynamics of polymeric liquids*, volume 2. John Wiley & Sons, New York, 2nd edition.

Dallas, V., Vassilicos, J. C., and Hewitt, G. F. (2010). Strong polymer-turbulence interactions in viscoelastic turbulent channel flow. *Phys. Rev. E*, **82**(6), 066303.

Dubief, Y., Terrapon, V. E., White, C. M., Shaqfeh, E. S. G., Moin, P., and Lele, S. K. (2005). New answers on the interaction between polymers and vortices in turbulent flows. *Flow Turbul. Combust.*, **74**, 311–329.

Dubief, Y., Terrapon, V. E., and Soria, J. (2013). On the mechanism of elasto-inertial turbulence. *Phys. Fluids*, **25**, 110817.

Graham, M. D. (2014). Drag reduction and the dynamics of turbulence in simple and complex fluids. *Phys. Fluids*, **26**, 101301.

Housiadas, K. D. and Beris, A. N. (2003). Polymer-induced drag reduction: effects of variations in elasticity and inertia in turbulent viscoelastic channel flow. *Phys. Fluids*, **15**, 2369–2384.

Housiadas, K. D., Beris, A. N., and Handler, R. A. (2005). Viscoelastic effects on higher order statistics and on coherent structures in turbulent channel flow. *Phys. Fluids*, **17**, 035106.

Jeong, J., Hussain, F., Schoppa, W., and Kim, J. (1997). Coherent structures near the wall in a turbulent channel flow. *J. Fluid Mech.*, **332**, 185–214.

Li, F. C., Kawaguchi, Y., Segawa, T., and Hishida, K. (2005). Reynolds-number dependence of turbulence structures in a drag-reducing surfactant solution channel flow investigated by particle image velocimetry. *Phys. Fluids*, **17**, 075104.

Li, W. and Graham, M. D. (2007). Polymer induced drag reduction in exact coherent structures of plane Poiseuille flow. *Phys. Fluids*, **19**, 083101.

Peyret, R. (2002). *Spectral methods for incompressible viscous flow*. Springer, New York.

Samanta, D., Dubief, Y., Holzner, M., Schäfer, C., Morozov, A. N., Wagner, C., and Hof, B. (2013). Elasto-inertial turbulence. *Proc. Natl. Acad. Sci. U. S. A.*, **110**, 10557–100562.

Shekar, A., McMullen, R. M., Wang, S. N., McKeon, B. J., and Graham, M. D. (2019). Critical-layer structures and mechanisms in elastoinertial turbulence. *Phys. Rev. Lett.*, **122**(12), 124503.

Sid, S., Terrapon, V. E., and Dubief, Y. (2018). Two-dimensional dynamics of elasto-inertial turbulence and its role in polymer drag reduction. *Phys. Rev. Fluids*, **3**, 011301.

Sureshkumar, R., Beris, A. N., and Handler, R. A. (1997). Direct numerical simulation of the turbulent channel flow of a polymer solution. *Phys. Fluids*, **9**, 743–755.

Toms, B. A. (1948). Some observations on the flow of linear polymer solutions through straight tubes at large Reynolds numbers. In *Proc. 1st Int'l. Congress on Rheology*, volume 2, pages 135–141, Amsterdam.

Virk, P. S. (1975). Drag reduction fundamentals. *AIChE J.*, **21**, 625–656.

Wang, S. N., Shekar, A., and Graham, M. D. (2017). Spatiotemporal dynamics of viscoelastic turbulence in transitional channel flow. *J. Non-Newton. Fluid Mech.* submitted.

White, C. M., Dubief, Y., and Klewicki, J. (2012). Re-examining the logarithmic dependence of the mean velocity distribution in polymer drag reduced wall-bounded flow. *Phys. Fluids*, **24**, 021701.

Xi, L. and Graham, M. D. (2010). Turbulent drag reduction and multistage transitions in viscoelastic minimal flow units. *J. Fluid Mech.*, **647**, 421–452.

Xi, L. and Graham, M. D. (2012a). Dynamics on the laminar-turbulent boundary and the origin of the maximum drag reduction asymptote. *Phys. Rev. Lett.*, **108**, 028301.

Xi, L. and Graham, M. D. (2012b). Intermittent dynamics of turbulence hibernation in Newtonian and viscoelastic minimal channel flows. *J. Fluid Mech.*, **693**, 433–472.

Yu, B. and Kawaguchi, Y. (2004). Direct numerical simulation of viscoelastic drag-reducing flow: a faithful finite difference method. *J. Non-Newton. Fluid Mech.*, **116**, 431–466.

Zhang, D., Jiang, C., Liang, D. F., and Cheng, L. (2015). A review on tvd schemes and a refined flux-limiter for steady-state calculations. *J. Comput. Phys.*, **302**, 114–154.

Zhu, L. and Xi, L. (2019). Vortex axis tracking by iterative propagation (VATIP): a method for analyzing three-dimensional turbulent structures. *J. Fluid Mech.*, **886**, 169–215.

Zhu, L., Schrobsdorff, H., Schneider, T. M., and Xi, L. (2018). Distinct transition in flow statistics and vortex dynamics between low- and high-extent turbulent drag reduction in polymer fluids. *J. Non-Newton. Fluid Mech.*, **262**, 115–130.

Zhu, L., Bai, X., Krushelnycky, E., and Xi, L. (2019). Transient dynamics of turbulence growth and bursting: Effects of drag-reducing polymers. *J. Non-Newton. Fluid Mech.*, **266**, 127–142.

Chapter 8

Conclusions and contributions

A small amount of polymers in turbulence can cause distinct changes in statistics and lead to drastic drag reduction. This phenomenon is studied in a plane-Poseuille channel using direct numerical simulation (DNS). With different parameter settings, turbulent flows can exhibit qualitatively different behaviors. Especially, polymeric turbulence can be driven by both the inertial force and the elastic force, resulting in two completely different flow states: the inertia- and elasticity-driven turbulence (IDT and EDT). In this dissertation, we discussed the behaviors of the two types of turbulence.

DNS of IDT in a large box ($L_x^+ \times L_z^+ = 4000 \times 800$) is first investigated. Several intermediate stages with qualitative differences are observed in IDT. The flow statistics, e.g., the mean velocity profile, the Reynolds shear stress, and the energy spectrum, are drastically changed in the log-law layer during the LDR-HDR transition. Despite these apparent changes in flow statistics, turbulent coherent structures are also modified. Vortices homogeneously distribute across the flow field at LDR, but strongly cluster at HDR. Turbulence hence becomes localized, creating laminar-like

regions between these vortex clusters. Demonstrated by these changes are the different polymer-turbulence interactions in the LDR and HDR stages. The first interaction starts at the onset of DR, where the coil-stretch transition of polymers indiscriminately suppresses all turbulent fluctuations. The second mechanism occurs during the LDR–HDR transition but its origin is unknown. Therefore, we proposed a mechanism based on two typical vortex regeneration cycles. In the streak-instability cycle, new vortices are generated from small-scale disturbances that come from the bursting events of the existing lifted-up vortices. On the other hand, a vortex can also be generated immediately next to an existing one, which forms the parent-offspring cycle. At the HDR stage, polymers are capable of suppressing the lift-up and bursting of vortices which substantially block the steak-instability pathway, leaving the parent-offspring pathway the main mechanism of turbulence self-sustenance. As a consequence, energy feeding to the log-law layer through the bursting process is blocked, which changes the flow behaviors at the HDR stage.

Direct evidence to support the hypothesis requires the statistical analysis of vortex configurations. This can be achieved by the newly developed vortex tracking algorithm – VATIP. The VATIP algorithm connects vortex axis-points using the cone-detective criterion by Jeong *et al.* (1997) and iteratively propagates the vortex axis over all spatial dimensions. A classification procedure is also proposed to classify vortices captured by the VATIP algorithm into several categories, including quasi-linear, hairpins, hooks, and various branched vortices.

Implementation of the VATIP algorithm and the corresponding vortex classification procedure to the inertia-driven polymeric turbulence supports our hypothesis about the polymer-turbulence interactions during the LDR-HDR transition. At LDR,

polymers can weaken vortex motions and suppress turbulent fluctuations. But the distribution and the balance between different classes of vortices are not affected. At HDR, the effect of polymers on the vortex motions becomes different in two aspects: first, polymers start to suppress the lift-up of quasi-streamwise vortices; second, the generation pathway of curved vortices are interrupted. Both activities reduce the group of the highly lifted vortices which is efficient for the momentum and energy transfer between the buffer layer and log-law layer. This directly explains the changing flow statistics in the log-law layer at HDR.

The hypothesis of suppressing lift-up of vortices in HDR is also investigated in a conditional sampling analysis. Here, we adopt Jeong *et al.* (1997)'s cone-detective method to extract the axis-line of vortices. The reference points to align individual vortex realizations are chosen to be the x-axis-point located at $y^+ = 50$ and only the realizations with the same sense of rotation are picked to form the conditional eddy. The lifting angle of conditional eddy of the HDR case is considerably smaller than the Newtonian case, indicating the weaker lift-up trend of vortices in HDR. These observations also support our hypothesis.

When the elasticity of polymeric flow is high, IDT cannot sustain independently and EDT becomes dominant in the flow. DNS of EDT requires a numerically stable scheme that does not require the global artificial diffusion (GAD) – a widely adopted strategy to avoid numerical oscillations when solving the polymeric turbulent system. In our study, a new hybrid pseudo-spectral/finite-difference scheme (HM) is developed. This method uses a TVD scheme to deal with the convection term of the FENE-P equation which efficiently eliminates the numerical oscillations introduced due to the hyperbolic nature of the polymer constitutive equations. The hybrid method is

tested in steady-state DNS and is compared with the pseudo-spectral method (SM) with artificial diffusion. Although IDT obtained by the HM and SM schemes at low Wi are largely consistent, only the HM scheme can obtain EDT at high Wi. The artificial diffusion in SM is highly active in the near-wall region while weaker near the center of the channel. Therefore it significantly affects the EDT structures which attach to the wall. On the other hand, the IDT structures are mostly intensive in regions away from the wall and the effect of GAD is weaker.

Exploring the $\mathrm{Re} - \mathrm{Wi}$ parameter space of the dilute polymeric turbulence finds that parameter regions where IDT and EDT can respectively sustain have substantial overlap region. IDT and EDT both share some common features with the MDR stage but also have some differences. As IDT cannot sustain independently at the high elasticity, the flow starts to periodically alternate between the IDT and EDT states, indicating a new dynamical polymeric turbulence.

As a summary, this dissertation investigated the statistics and dynamics of polymeric flows at different levels of elasticity, in order to understand the complex polymer-turbulence interactions that lead to the drastic drag reduction. The major contributions of this dissertation are:

- We proposed a new mechanism that explains the qualitative LDR-HDR transition from the perspective of vortex dynamics. Starting from the LDR-HDR transition, the lift-up process of vortices in the polymeric turbulence is suppressed by polymers, which results in the modification of vortex regeneration cycles and the abrupt changes of flow statistics.

- We developed a powerful tool, i.e. VATIP, to efficiently track the axis lines of individual vortical structures in both Newtonian and viscoelastic turbulence.

This new tool helps us analyze the vortex statistics at the LDR and HDR stages of polymer turbulence and confirms our hypothesis of polymer-turbulence interactions.

- A new hybrid SM-FDM DNS method was also developed to simulate the highly elastic polymeric turbulence. This method successfully simulates the polymeric turbulence without requiring an artificial diffusion. It is highly efficient and accurate, ans is potable to be embedded into the widely used pure pseudo-spectrum method.

- In the high elasticity polymeric turbulence, a new type of turbulent state was found in which the flow motions is alternated between the IDT and EDT states.

Bibliography

Jeong, J., Hussain, F., Schoppa, W., and Kim, J. (1997). Coherent structures near the wall in a turbulent channel flow. *J. Fluid Mech.*, **332**, 185–214.